

**MATHEMATICAL MODELLING OF GAS
AND GAS-LIQUID JETS INJECTED INTO A
FLUIDIZED BED**

by

Konstantin Pougatch

M.Sc. in Eng., St. Petersburg State Technical University, Russia, 1993

A THESIS SUBMITTED IN PARTIAL FULFILLMENT OF THE
REQUIREMENTS FOR THE DEGREE OF

DOCTOR OF PHILOSOPHY

in

The Faculty of Graduate Studies
(Mechanical Engineering)

The University of British Columbia
(Vancouver)

April 2011

© Konstantin Pougatch, 2011

ABSTRACT

This thesis presents the development of novel mathematical models of jet injection into fluidized beds. Two types of injections are considered: the first is gas-assisted liquid atomization including flow through a variable cross-section nozzle, followed by spray dispersion and interaction with fluidized bed particles (jet-bed interaction), and the second is a high speed injection of a gas jet with a purpose to break down solid particles (particle attrition). Both models are based on a multi-fluid Eulerian-Eulerian treatment and include the system of the ensemble-averaged Navier-Stokes equations together with the particle number density equation for each phase written independently of the local nature of the continuous phase. The models rely on a number of sub-models that form constitutive equations. Some of the sub-models, such as ones used for atomization, moisture and heat transport in a bed due to particle collisions, heat conduction through the particle core, multiphase wall functions, and breakage frequency, are developed during the course of this project.

The jet-bed interaction model includes break-up and coalescence of bubbles and droplets due to interfacial (mean and turbulent) shear and collisions in order to account for spatial variations of the average diameters. Atomization is considered as a catastrophic phase inversion triggered by a critical local volume fraction. The jet-bed interaction model is applied to gas-liquid flow through a nozzle, spray dispersion in open air, and spray injection into the bed. Modelling results are compared with experimental data for pressure variation along the nozzle wall, radial profiles of the liquid flow rate and average droplet diameter, and cumulative liquid distribution in a fluidized bed. It is demonstrated that there is an overall satisfactory agreement.

The particle attrition model connects the solid phase properties and the granular temperature with the breakage rate. Modelling results allow calculation of the grinding efficiency – a quantitative measure of the attrition performance. For validation purposes, the model is applied to a number of cases that have been previously investigated experimentally with a good agreement.

Both models are also applied to cases of practical interest, and a detailed flow analysis is conducted.

PREFACE

Most of the research presented in this thesis has been previously published (or is currently under consideration) in a number of peer-reviewed journals. Below we list the published (or submitted) articles and indicate their use in the present manuscript. In addition, contributions of various authors of the papers are outlined.

- Pougatch, K., Salcudean, M., Chan, E., Knapper, B., 2008. Modelling of compressible gas-liquid flow in a convergent-divergent nozzle. *Chemical Engineering Science* 63, 4176-4188. The part of the paper that describes a mathematical model is used in Chapter 2, and the application part is used in Chapter 3. Note that there are some minor discrepancies between models and simulation results presented in this thesis and published in a journal. They arise from new developments included in the current work that increase the generality of model application.
- Pougatch, K., Salcudean, M., Chan, E., Knapper, B., 2009. A two-fluid model of gas-assisted atomization including flow through the nozzle, phase inversion, and spray dispersion. *International Journal of Multiphase Flow* 35, 661-675. The part of the paper that describes a mathematical model appears in Chapter 2, and the application part is used in Chapter 4. Note that similar to the previous paper, there are some minor discrepancies between models and simulation results presented in this thesis and published in a journal. They arise from new developments included in the current work that increases the generality of model application.
- Pougatch, K., Salcudean, M., 2010. Numerical simulation of liquid spray dispersion in a fluidized bed. *Canadian Journal of Chemical Engineering* 88, 648-654. Some parts of this paper are included in Chapter 2.
- Pougatch, K., Salcudean, M., McMillan, J., 2011. 3D numerical modelling of interactions between a gas-liquid jet and a fluidized bed. Submitted to *Chemical Engineering Science*.

The part of the paper that describes a mathematical model is used in Chapter 2, and the application part in Chapter 5.

- Pougatch, K., Salcudean, M., McMillan, J., 2010. Simulation of particle attrition by supersonic gas jets in fluidized beds. *Chemical Engineering Science* 65, 4829-4843. The part of the paper that describes a mathematical model appears in Chapter 2, and the application part in Chapter 7.
- Pougatch, K., Salcudean, M., McMillan, J., 2011. Nozzle design influence on particle attrition by a supersonic steam jet. *Powder Technology* 209, 35-45. The material from this paper is included in Chapter 7.
- Pougatch, K., Salcudean, M., McMillan, J., 2010. Average droplet diameter spatial distribution in a spray after gas-assisted atomization. *ASME2010 International Mechanical Engineering Congress and Exposition IMECE2010*, Vancouver, BC, Canada, November 12-18. Some parts of this paper are utilized in Chapter 2 and the rest in Chapter 4.
- Pougatch, K., Salcudean, M., 2011. Computational investigation of liquid spray dispersion modification by conical nozzle attachments. *Journal of Fluids Engineering* 133, 031301. This paper is included in Chapter 6.
- Pougatch, K., Salcudean, M., McMillan, J., 2011. Influence of conical nozzle attachments on horizontal spray dispersion in a fluidized bed. In preparation. This paper is used in Chapter 6.

For all publications, the research plan was designed jointly by KP and MS; KP conducted model and code development, computer simulation and analysis of the results under the supervision of MS; the manuscript was initially drafted by KP and subsequently edited by all authors. EC and BK conducted experiments related to liquid spraying; JM provided experimental data and collaborated on some interpretations of results.

TABLE OF CONTENTS

ABSTRACT	ii
PREFACE	iv
TABLE OF CONTENTS	vi
LIST OF TABLES	xii
LIST OF FIGURES	xiii
NOMENCLATURE	xxi
ACKNOWLEDGEMENTS	xxvi
DEDICATION	xxviii
CHAPTER 1. INTRODUCTION	1
1.1. PROBLEM DESCRIPTION	1
1.1.1. Injection into the fluidized bed	1
1.1.2. Fluid coker reactor	2
1.2. LITERATURE REVIEW	6
1.2.1. Bubbles-dispersed two-phase flow	6
1.2.2. Atomization and spray dispersion.....	9
1.2.3. Jet-bed interaction.....	11
1.2.4. Particle attrition.....	14
1.3. OBJECTIVES	17
1.4. RESEARCH METHODOLOGY	17
1.4.1. Jet-bed interaction.....	18
1.4.2. Particle attrition.....	19

1.5.	OUTLINE	19
CHAPTER 2. MATHEMATICAL MODEL DESCRIPTION		22
2.1.	MODEL OF SPRAY INJECTION INTO FLUIDIZED BED INCLUDING FLOW THROUGH THE NOZZLE AND ATOMIZATION	22
2.1.1.	Mass, momentum, energy and components balance.....	23
2.1.2.	Interfacial forces	25
2.1.3.	Fluctuating motion of gas and liquid phases.....	28
2.1.3.1.	Mixture turbulence model.....	29
2.1.3.2.	Turbulence response coefficient	32
2.1.4.	Fluctuating motion of particulate phase.....	33
2.1.5.	Diameter of bubbles and droplets	35
2.1.5.1.	Bubble break-up and coalescence	36
2.1.5.2.	Droplet break-up and coalescence	37
2.1.6.	Atomization (phase inversion).....	46
2.1.7.	Diameter of particulate phase	47
2.1.8.	Interactions between droplets and particles	48
2.1.9.	Heat transfer within a particulate phase.....	50
2.1.10.	Moisture and heat transport in the particulate phase	52
2.1.11.	Interfacial heat transfer	56
2.1.12.	Interfacial and boundary conditions.....	56
2.1.12.1.	A wall function model for multiphase flows	57
2.1.12.2.	Wall conditions for the particulate phase.....	60
2.2.	MODEL OF PARTICLE ATTRITION BY HIGH SPEED GAS JET IN FLUIDIZED BED.....	60
2.2.1.	Mass, momentum and energy balance	61
2.2.2.	Interfacial forces	62
2.2.3.	Fluctuating motion of gaseous phase.....	62
2.2.4.	Fluctuating motion of solid particles	63
2.2.5.	Heat transfer closure	65
2.2.6.	Boundary conditions	66
2.2.7.	Attrition modelling.....	67

2.2.7.1.	Particle number density.....	67
2.2.7.2.	Attrition criterion	68
2.2.7.3.	Breakage frequency	71
2.2.7.4.	Grinding efficiency	72
2.3.	NUMERICAL METHOD.....	73
CHAPTER 3. GAS-LIQUID FLOW IN A CONVERGENT-DIVERGENT NOZZLE		
.....		75
3.1.	MODEL COMPARISON WITH EXPERIMENT	76
3.1.1.	Experimental set-up	76
3.1.2.	Modelling geometry and solution details.....	77
3.1.3.	Gravity influence	78
3.1.4.	Grid independence	80
3.1.5.	Comparison with experiment.....	81
3.2.	FLOW ANALYSIS	83
3.3.	SUMMARY	89
CHAPTER 4. GAS-ASSISTED ATOMIZATION INCLUDING FLOW THROUGH		
THE NOZZLE, PHASE INVERSION, AND SPRAY DISPERSION..		90
4.1.	STUDY A – LIQUID FLOW RATES	91
4.1.1.	Experimental set-up	91
4.1.2.	Computational domain.....	92
4.1.3.	Comparison with experimental results.....	94
4.1.3.1.	Influence of the phase inversion critical liquid volume fraction values	97
4.1.4.	Flow analysis	98
4.1.4.1.	Volume fraction distribution.....	98
4.1.4.2.	Velocity variations	101
4.1.4.3.	Discrete phase diameter variations	104
4.2.	STUDY B – DROPLET DIAMETER	107
4.2.1.	Experimental set-up	107

4.2.2.	Interpretation of experimental results	108
4.2.3.	Computational domain.....	109
4.2.4.	Comparison with experimental results.....	110
4.2.4.1.	Model adjustment.....	110
4.2.4.2.	Average droplet diameter comparison.....	111
4.2.5.	Flow analysis	113
4.3.	SUMMARY	117
CHAPTER 5. INTERACTIONS BETWEEN A GAS-LIQUID JET AND A FLUIDIZED BED		119
5.1.	MODEL COMPARISON WITH EXPERIMENT.....	119
5.1.1.	Draft tube addition (McMillan et al., 2005).....	119
5.1.1.1.	Experimental set-up and computational domain.....	120
5.1.1.2.	Computational procedure.....	122
5.1.1.3.	Grid independence	123
5.1.1.4.	Liquid to solid (<i>L/S</i>) mass ratio comparison.....	124
5.1.1.5.	Flow analysis	126
5.1.1.6.	2D and 3D solution comparison	133
5.1.2.	Penetration distance (Ariyapadi et al., 2004).....	134
5.1.2.1.	Model set-up	136
5.1.2.2.	Penetration distance comparison.....	137
5.1.2.3.	Penetration distance for cases with and without a draft tube.....	138
5.2.	VARIATION OF SUPERFICIAL GAS VELOCITY.....	139
5.3.	SUMMARY	141
CHAPTER 6. LIQUID SPRAY DISPERSION MODIFICATION BY CONICAL NOZZLE ATTACHMENTS		142
6.1.	AIR – WATER SPRAY IN OPEN AIR.....	143
6.1.1.	Description of cases	143
6.1.2.	Computational grid	144
6.1.3.	Transient effects.....	145

6.1.4.	Numerical accuracy	145
6.1.5.	Flow analysis	147
6.2.	STEAM-BITUMEN SPRAY INJECTED INTO A FLUIDIZED BED	156
6.2.1.	Description of cases	156
6.2.2.	Steam dispersion without particles	158
6.2.3.	Steam dispersion in a fluidized bed	159
6.2.3.1.	Transient behaviour	159
6.2.3.2.	Flow analysis	160
6.2.3.3.	Grid independence	164
6.3.	SUMMARY	165
CHAPTER 7. PARTICLE ATTRITION		167
7.1.	SMALL SCALE FLUIDIZED BED	167
7.1.1.	Grinding efficiency model	167
7.1.2.	Calculation procedure	168
7.1.3.	Model comparison with experiments	170
7.1.3.1.	Experimental set-up	170
7.1.3.2.	Computational domain, initial and process conditions	172
7.1.3.3.	Comparison with experimental results	174
7.1.3.4.	Numerical accuracy	175
7.1.4.	Flow analysis	176
7.1.4.1.	Transient features of the flow	176
7.1.4.2.	Time-averaged solution	179
7.1.4.3.	Comparison between cases	181
7.2.	INDUSTRIAL SCALE ATTRITION	185
7.2.1.	Model calibration	186
7.2.2.	Computational domain	188
7.2.3.	Grid independence	190
7.2.4.	Flow analysis	190
7.2.4.1.	Influence of nozzle area ratio	190
7.2.4.2.	Influence of nozzle expansion angle	201

7.2.4.3. Influence of superficial gas velocity	202
7.3. SUMMARY	203
CHAPTER 8. CONCLUSIONS AND RECOMMENDATIONS.....	205
8.1. MAIN CONTRIBUTIONS	205
8.1.1. Jet-bed interactions	205
8.1.2. Particle attrition.....	207
8.2. RESEARCH FINDINGS.....	208
8.2.1. Jet-bed interactions	208
8.2.2. Particle attrition.....	210
8.3. FUTURE RESEARCH DIRECTIONS.....	211
8.3.1. Model application to cases of practical and/or research interest	211
8.3.2. Improvements of existing model	212
8.3.3. Further development	214
REFERENCES.....	216

LIST OF TABLES

Table 2-1. Droplet fragmentation modes classification.....	39
Table 2-2. Constants in Eq. (2-72).....	40
Table 3-1. Summary of experimental flow rates.	77
Table 4-1. Air and water flow rates for investigated cases in flow rates experiments.	91
Table 4-2. Air and water flow rates for investigated cases in droplet diameter experiments.	107
Table 4-3. Comparison between experimental and predicted results for $C_{vel} = 3$	110
Table 5-1. Nozzle diameters and flow rates for investigated cases (from Ariyapadi et al., 2004).	136
Table 5-2. Jet penetration distance for cases with and without the draft tube.	138
Table 6-1. Attachment expansion angle and exit height of the investigated cases.	143
Table 6-2. Estimated convergence order and solution error for different cut-off values of liquid volume fraction.....	146
Table 7-1. Process parameters for small-scale computations.	186
Table 7-2. Nozzle dimensions for various cases.....	190
Table 7-3. Process parameters for industrial scale cases.	191

LIST OF FIGURES

Figure 1-1. Schematic of fluid coking process (Reprinted from House et al. (2004) with permission from Elsevier).....	4
Figure 2-1. Various droplet collision outcomes schematic; (a) – bouncing, (b) – reflective separation, (c) – stretching separation, (d) – coalescence.....	43
Figure 2-2. Droplet collision regimes after Ashgriz and Poo (1990) and our approximation.....	45
Figure 2-3. Solid particles with a gradient of liquid film mass fraction.....	54
Figure 2-4. Particle collision schematic.....	68
Figure 2-5. Typical breakage probability function.....	71
Figure 3-1. TEB Nozzle geometry (all dimensions are in mm; not to scale).....	76
Figure 3-2. Schematic diagram of the experimental set-up.....	76
Figure 3-3. 3D computational domain with grid.....	78
Figure 3-4. Air bubble volume fraction profiles in radial direction from bottom (negative distance) to top (positive distance) before and after the nozzle.....	79
Figure 3-5. Pressure profiles along the centreline for different resolution grids.....	81
Figure 3-6. Comparison of the pressure profiles along the nozzle wall obtained by the model with experimental data.....	82
Figure 3-7. Liquid volume fraction contours in the nozzle. Computational domain is extended from axisymmetric to a full axial cross-section for better presentation.....	83
Figure 3-8. Velocity profiles along the centreline.....	84
Figure 3-9. Turbulence intensity variation along the centreline.....	85
Figure 3-10. Bubble diameter profile along the centreline.....	86

Figure 3-11. Average bubble diameter contours inside the entrance pipe and the nozzle (in mm).....	87
Figure 3-12. Comparison of pressure profiles along the centreline between the present model, the homogeneous model, and the model without an added mass force.....	88
Figure 4-1. Schematic diagram of spraying experiment set-up.....	91
Figure 4-2. Computational domain and boundary conditions (the area around the nozzle is magnified and shown in the upper part of the figure).....	93
Figure 4-3. Computational grid and domain segmentation.....	94
Figure 4-4. Comparison between model predictions and pressure measurements along the wall of the inlet pipe and the nozzle.....	95
Figure 4-5. Comparison between model predictions and water flux measurements in radial direction at different distances from the nozzle exit.....	96
Figure 4-6. Profiles of the water flow rate that correspond to the various values of the critical volume fraction α_d^{\max}	97
Figure 4-7. Liquid volume fraction distribution for Case A1. (a) in the spray; (b) in the nozzle.....	98
Figure 4-8. Liquid volume fraction distribution for Case A2. (a) in the spray; (b) in the nozzle.....	99
Figure 4-9. Pressure contours in and around the nozzle (in MPa). (a) Case A1; (b) Case A2.....	100
Figure 4-10. Air velocity magnitude contours (in m s^{-1}). (a) Case A1; (b) Case A2.....	102
Figure 4-11. Water droplets velocity magnitude contours (in m s^{-1}). (a) Case A1; (b) Case A2.....	103
Figure 4-12. Air and droplets axial velocity profiles along the centreline for Case A1 (left) and Case A2 (right). The nozzle orifice is located at $x = 0$	103
Figure 4-13. Average diameter of the discrete phase (bubbles or droplets) profiles along the centreline for both cases.....	104

Figure 4-14. Profiles of the droplet average diameter at different distances from the nozzle orifice for Case A1 (left) and Case A2 (right). The curves are shown only if the local droplets volume fraction exceeds 0.001.	105
Figure 4-15. TEB1.25 nozzle geometry (All dimensions are in mm; not to scale.)	107
Figure 4-16. PSD density of water droplets at 0.3556 m axial distance from the nozzle orifice for Case 1 at different radial distances; number based (above), volume based (below).	108
Figure 4-17. Computational grid.....	109
Figure 4-18. Average droplet diameter cross-sectional profile for various cases and distances from the nozzle orifice. (a) – Case B1, 0.3556 m; (b) – Case B1, 0.6096 m; (c) – Case B2, 0.3556 m; (d) – Case B2, 0.6096 m; (e) – Case B3, 0.3556 m; (f) – Case B3, 0.6096 m. ...	112
Figure 4-19. Average droplet diameter contours (in mm). (a) – Case B1; (b) – Case B2; (c) – Case B3.	113
Figure 4-20. Mixture turbulent kinetic energy contours (in $m^2 s^{-2}$). (a) – Case B1; (b) – Case B2; (c) – Case B3.....	114
Figure 4-21. Liquid volume fraction contours. (a) – Case B1; (b) – Case B2; (c) – Case B3.	115
Figure 4-22. Average bubble diameter profiles along the centerline of the nozzle.....	116
Figure 4-23. Pressure profile along the centerline of the nozzle.	117
Figure 5-1. Experiment schematic (Reprinted from McMillan et al. (2005))	120
Figure 5-2. Nozzle schematics (in mm).....	120
Figure 5-3. Computational grid for jet-bed interaction case.....	121
Figure 5-4. Cumulative liquid distribution profiles at 30 cm from the nozzle orifice for regular and coarse grid cases.	123
Figure 5-5. Cumulative liquid distribution profiles at various distances from the nozzle orifice obtained from model prediction and McMillan et al. (2005) experiment; (a) $l = 3.27$ cm; (b) $l = 5.27$ cm; (c) $l = 7.27$ cm.....	125
Figure 5-6. Transient variations of the particulate phase volume fraction.	127

Figure 5-7. Contours of volume fraction of the particulate phase; (a) – Case without a draft tube; (b) – Case with a draft tube.....	129
Figure 5-8. Volume fraction of liquid (droplets and liquid layer); (a) – Case without a draft tube; (b) – Case with a draft tube.....	130
Figure 5-9. Predicted cumulative liquid distribution profiles at various distances from the nozzle orifice. (a) $l = 10$ cm; (b) $l = 30$ cm.	130
Figure 5-10. Volume fraction of droplets; (a) – Case without a draft tube; (b) – Case with a draft tube.	131
Figure 5-11. Axial velocity of the particulate phase (in m s^{-1}); (a) – Case without a draft tube; (b) – Case with a draft tube.....	131
Figure 5-12. Phase and component temperature profiles along the centreline; (a) – Case without a draft tube; (b) – Case with a draft tube.	132
Figure 5-13. Cumulative liquid distribution for 3D and 2D axisymmetric solutions at different axial distances from the nozzle exit.	133
Figure 5-14. Instantaneous profiles of minimal cross-sectional liquid film temperature and maximum particle velocity with an example of penetration depth determination.....	135
Figure 5-15. Jet penetration distance time variations for Case 2 (from Table 5-1) as determined by temperature and velocity methods.	137
Figure 5-16. Time averaged jet penetration distance for cases from Table 5-1 compared with experimental values of Ariyapady et al. (2004). Error bars on modelling results show \pm one standard deviation. (a) lower flow rates; (b) higher flow rates.....	138
Figure 5-17. Contours of volume fraction of the particulate phase; (a) – superficial velocity 0.02 m s^{-1} ; (b) – superficial velocity 0.1 m s^{-1}	139
Figure 5-18. Cumulative liquid distribution profiles at various distances from the nozzle orifice for different fluidization velocities. (a) $l = 10$ cm; (b) $l = 30$ cm.	140
Figure 6-1. Schematic drawing of nozzle with an attachment (mm, not to scale).....	143

Figure 6-2. Computational grid and domain segmentation (full domain – above, and nozzle attachment area – below).	144
Figure 6-3. Pressure profiles along the nozzle centerline for various cases.	147
Figure 6-4. Droplets volume fraction contours in the nozzle and spray modifier (above) and in the spray area (below) for (a) - stand alone nozzle, (b) - 80°, (c) - 60°, (d) - 40°, (e) - 20°, (f) - 10°. Note the different scale for the upper and lower plots.	148
Figure 6-5. Phase inversion surfaces for all investigated cases.	150
Figure 6-6. Air velocity magnitude contours in the spray area for (a) - stand alone nozzle, (b) - 80°, (c) - 60°, (d) - 40°, (e) - 20°, (f) - 10° (in $m s^{-1}$).	150
Figure 6-7. Air velocity vectors and magnitude contours in the nozzle exit area for (a) – stand-alone nozzle, (b) - 60°, (c) - 20° (in $m s^{-1}$).	152
Figure 6-8. Water flow rate profiles in a radial cross-sectional plane located at 0.3048 m from the nozzle exit.	153
Figure 6-9. Average droplet diameter variation in a radial cross-sectional plane located at 0.3048 m from the nozzle exit.	154
Figure 6-10. Turbulence kinetic energy contours in the spray area for (a) - stand alone nozzle, (b) - 80°, (c) - 60°, (d) - 40°, (e) - 20°, (f) - 10° (in $m^2 s^{-2}$).	155
Figure 6-11. Droplet volume fraction contours for the case with 20° attachment angle.	158
Figure 6-12. Water flow rate profiles in a radial cross-sectional plane located at 0.3048 m from the nozzle exit.	159
Figure 6-13. Snapshots of volume fraction of the particulate phase; (a) - TEB nozzle, (b) - 80°, (c) - 60°, (d) - 40°, (e) - 20°, (f) - 10°.	160
Figure 6-14. Time-averaged particulate phase volume fraction contours; (a) - TEB nozzle, (b) - 80°, (c) - 60°, (d) - 40°, (e) - 20°, (f) - 10°.	161
Figure 6-15. Bitumen droplets volume fraction contours; (a) - TEB nozzle, (b) - 80°, (c) - 60°, (d) - 40°, (e) - 20°, (f) - 10°.	162

Figure 6-16. Bitumen film volume fraction; (a) - TEB nozzle, (b) - 80°, (c) - 60°, (d) - 40°, (e) - 20°, (f) - 10°.	163
Figure 6-17. Cumulative liquid distribution profiles at 10 cm (a) and at 30 cm (b) from the nozzle exit.	164
Figure 6-18. Cumulative liquid distribution profile for the case with 20° attachment at 30 cm from the nozzle exit for three different grid resolutions.	165
Figure 7-1. Schematic of the experiment (Reprinted from McMillan et al. (2007a) with permission from Elsevier).	170
Figure 7-2. Investigated nozzle geometries (Reprinted from McMillan et al. (2007b) with permission from Elsevier).	171
Figure 7-3. Computational domain with grid.	172
Figure 7-4. Variation of the predicted grinding efficiency with the inlet pressure for A and B nozzle configurations together with experimentally measured values (McMillan et al., 2007a).	174
Figure 7-5. Variation of the predicted grinding efficiency with inlet pressure for C nozzle configurations with different exit diameters together with experimentally measured values (McMillan et al., 2007a).	174
Figure 7-6. Particulate phase volume fraction contours in the axial cross-sectional plane passing through the axis for the C2.4 nozzle at 150 psi (1.034 MPa) inlet pressure. Plots are arranged in a time sequence left to right and top to bottom. Time interval between each successive plots is 25 ms.	177
Figure 7-7. Grinding efficiency variation with time for the C2.4 nozzle at 150 psi (1.034 MPa).	178
Figure 7-8. Time-averaged volume fraction contours of the particulate phase for nozzle C2.4 at 150 psi (1.034 MPa) inlet pressure.	179
Figure 7-9. Time-averaged particle diameter contours for the nozzle C2.4 at 150 psi (1.034 MPa) inlet pressure (in mm).	180

Figure 7-10. Time-average increase of the particles surface area (in $\text{m}^2 \text{s}^{-1}$) due to breakage for nozzle C2.4 at 150 psi (1.034 MPa) inlet pressure.....	180
Figure 7-11. Contours of the Mach number for the nozzle A (top) and the nozzle C2.4 (bottom) at 100 psi (0.689 MPa).....	182
Figure 7-12. Particle volume fraction along the centreline for the nozzles A and C2.4.....	183
Figure 7-13. Variation of jet penetration length with pressure for the nozzles A and B (top) and for the nozzles C (bottom) together with the estimated values from Benjelloun et al. (1995) empirical correlation.	184
Figure 7-14. Nozzle schematic.	186
Figure 7-15. Grinding efficiency variation with pressure in a small scale fluidized bed. Error bars show \pm one standard deviation for modelling results and for experimental data. (a) Comparison with experimental values; (b) Parametric study for different breakage constants.	187
Figure 7-16. Domain segmentation, computational grid and boundary conditions (nozzle walls not shown here are treated as walls).....	188
Figure 7-17. Average particle volume fraction contours for Case 1.....	192
Figure 7-18. Contours of steam temperature ($^{\circ}\text{C}$) (above) and temperature difference between particles and steam ($^{\circ}\text{C}$) (below).....	193
Figure 7-19. Contours of average particle diameter for Case 1 (mm).....	193
Figure 7-20. Grinding efficiency variation with time for Case 1.	194
Figure 7-21. Grinding efficiency variation with nozzle area ratio. Error bars show \pm one standard deviation.	195
Figure 7-22. Solid flow rate dependence on the borderline velocity definition.	196
Figure 7-23. Solid particle entrainment for nozzles of different exit areas.	197
Figure 7-24. Steam velocity contours (m/s) for Cases 1 – 4. (a) – Case 1, (b) – Case 2, (c) – Case 3, (d) – Case 4.	198

Figure 7-25. Particle velocity contours for Cases 1 – 4. (a) – Case 1, (b) – Case 2, (c) – Case 3, (d) – Case 4 (in m s^{-1}).	199
Figure 7-26. Jet penetration distance for nozzles of different exit areas.	200
Figure 7-27. Particle volume fraction variations along the axis for Cases 1 – 4.	200
Figure 7-28. Grinding efficiency variation with nozzle expansion angle.....	202
Figure 7-29. Grinding efficiency variation with superficial gas velocity.	203

NOMENCLATURE

A	Area, m^2
B	Dimensionless number, see Eq. (2-96)
c_p	Specific heat, $\text{J kg}^{-1} \text{K}^{-1}$
C_{br}	Breakage constant, see Eq. (2-193)
C_D	Drag coefficient
C_t	Turbulence response coefficient
C_{vm}	Virtual mass coefficient
C_β	Geometric parameter, see Eq. (2-44)
$C_{\varepsilon 1}$	Constant in Eq. (2-28), 1.44
$C_{\varepsilon 2}$	Constant in Eq. (2-28), 1.92
$C_{\varepsilon 3}$	Constant in Eq. (2-28), 1.2
$C_{\varepsilon 4}$	Constant in Eq. (2-28), 1.2
C_μ	Coefficient in turbulent viscosity model, dimensionless, 0.09
d	Locally averaged bubble diameter, m
D	Diffusion coefficient, $\text{m}^2 \text{s}^{-1}$
e	Restitution coefficient, 0.95
f	Frequency, s^{-1}
\mathbf{F}	Force, N
Fo	Fourier number
\mathbf{g}	Gravitational acceleration, m s^{-2}
g_0	Radial distribution function
G	Strength of particle, Pa

H	Enthalpy, J kg^{-1}
h	Interfacial heat transfer coefficient, $\text{W K}^{-1} \text{m}^{-3}$
\mathbf{I}	Unit tensor
I	Turbulence intensity
J	Mass flow rate, $\text{kg m}^{-2} \text{s}^{-1}$
k	Turbulence kinetic energy, $\text{m}^2 \text{s}^{-2}$
k_θ	Granular temperature diffusion coefficient, $\text{kg m}^{-1} \text{s}^{-1}$
K	Constant in Eq. (2-59), 0.25
Lp	Laplace number, see Eq. (2-96)
M	Molar mass, kg mol^{-1}
\dot{m}	Mass flow rate of droplets that collide with particles, $\text{kg m}^2 \text{s}^{-1}$
\dot{m}_{st}	Mass flow rate from liquid phase to particulate phase, $\text{kg m}^2 \text{s}^{-1}$
\dot{m}_r	Mass flow rate of droplets that rebound after collision with particles, $\text{kg m}^2 \text{s}^{-1}$
n	Particle number density, m^{-3}
N	Number of collisions, $\text{m}^{-3} \text{s}^{-1}$
Nu	Nusselt number
P	Pressure, Pa
Pr	Prandtl number
q	Heat flow rate, W
q_{gp}	Gas-particle turbulent correlation, $\text{m}^2 \text{s}^{-2}$
Q	Turbulence production by shear, $\text{kg m}^{-1} \text{s}^{-3}$
r	Radial coordinate, m
R	Universal gas constant, $8.314 \text{ J mol}^{-1} \text{ K}^{-1}$
Re	Reynolds number
S	Turbulence source term due to interfacial interactions, $\text{kg m}^{-1} \text{s}^{-3}$
S	Surface area, m^2
Sc^t	Turbulent Schmidt number, 0.7
t	Time, s
T	Temperature, K

u	Axial velocity, m s^{-1}
\mathbf{V}, V	Velocity, m s^{-1}
V	Volume, m^3
We	Weber number
x	Mass fraction
x	Distance, m
y	Normal distance from the wall, m

Greek letters

α	Volume fraction
α	Thermal diffusivity, $\text{m}^2 \text{s}^{-1}$
β	Constant in Eq. (2-59), 8.2
γ	Interfacial momentum transfer coefficient, $\text{kg m}^3 \text{s}^{-1}$
δ_{ij}	Kronecker's delta
Γ	Granular temperature dissipation, $\text{kg m}^{-1} \text{s}^{-3}$
ε	Turbulence dissipation rate, $\text{m}^2 \text{s}^{-3}$
θ	Granular temperature, $\text{m}^2 \text{s}^{-2}$
κ	von Karman constant, see Eq. (2-141)
κ	Thermal conductivity, $\text{W K}^{-1} \text{m}^{-1}$
μ	Dynamic viscosity, $\text{kg m}^{-1} \text{s}^{-1}$
ζ	Parameter, see Eq. (2-43)
ξ	Averaged tangential velocity, m s^{-1}
ρ	Density, kg m^{-3}
σ	Surface tension, N m^{-1}
σ_k	Constant in Eq. (2-27), 1.0
σ_ε	Constant in Eq. (2-28), 1.3
$\boldsymbol{\tau}$	Stress tensor, Pa
τ_{cd}^t	Eddy-droplet interaction time, s

τ_c^t	Scale of the energetic turbulent eddies, s
τ_{cd}^F	Characteristic time of particle entrainment by fluid motion, s
$\Delta\tau_{br}$	Break-up time, s
φ	Friction angle, rad
Φ	Stickiness ratio
ψ	Angle, rad, see Eq. (2-114)

Subscripts

1p	One particle
br	Break-up
c	Continuous
coal	Coalescence
coll	Collision
d	Dispersed
f	Film
g	Gas
l	Liquid
m	Mixture
p	Particles
s	Solid core
w	Wall

Superscripts

eff	Effective
fric	Frictional
max	Maximum
rel	Relative
t, turb	Turbulent

t	Tangential
T	Transpose
vm	Virtual mass

ACKNOWLEDGEMENTS

I would like to express my gratitude to many people who were either directly or indirectly involved in the presented work.

First of all, my heartfelt thanks are due to my supervisors during my tenure at UBC: Martha Salcudean and Ian Gartshore. Even though Ian was not my advisor at the time this research was conducted – his illness and death in 2006 preceded my enrolment as a student – his influence stayed with me without the need for a physical presence. Thus, I can still count myself as his student – the last one. I am grateful to Martha and Ian for recognizing my potential and offering me a place in their group ten long years ago. It is from them that I learned what academic research is, and acquired a taste for it. Their willingness to let me do things in my own way, yet being always there to provide guidance and support when needed, is greatly appreciated. Overall, Martha and Ian’s mentorship facilitated an enormous progress in my career, and I can only hope that I can keep up the momentum and one day return the investment by making them proud.

While I am grateful to all members of our industrial CFD group at UBC and at PSL, I would like to single out Paul Nowak, who was the developer of the original curvilinear code. Paul’s wealth of knowledge in CFD and numerical methods in general helped me greatly during the code development part of this work. His readiness to share many nitty-gritty details of the numerical code that are usually overlooked in the books on the subject is greatly appreciated. In addition, I extend my thanks to the graduate students I co-advised – Tingwen Li and Pirooz Darabi. Providing them with guidance on their projects broadened my horizons and taught me about research leadership as an art to balance between hands-on experience, critique, and encouragement.

My gratitude is also due to our industrial collaborators. Ed Chan, Jennifer McMillan, Eb Mueller, and Brian Knapper at Syncrude Canada Ltd., Darwin Kiel and Jonathan Tyler at

Coanda Research and Development Corporation provided experimental results and participated in many useful discussions that advanced our understanding of the investigated processes.

I appreciate the time and effort of several unnamed reviewers who provided critical feedback to papers that formed the basis of this thesis. The work on the revisions inspired by their comments allowed me to see the problems from a different perspective and, as a result, become a better researcher.

I am thankful to John Grace for many discussions and helpful suggestions for manuscript improvement. Also, I acknowledge support and feedback of the other members of my advisory committee: Dana Grecov and James Olson.

I am also grateful to many members of the Department of Mechanical Engineering with whom I have interacted during these years. Thanks are due to Ian Frigaard for reintroducing me to classical fluid dynamics through his courses and subsequent work on a research project, and to Carl Ollivier-Gooch for showing me how classes should be taught in university. During all these years, Alan Steeves proved that there is no computer-related problem he cannot solve; Jan Marsden and Yuki Matsumura helped with organizational matters in such a smooth way that left an impression that things were getting done by themselves. A special thank you is owed to Maureen Phillips who proofread this thesis as well as many other papers written by the author.

The funding from Natural Sciences and Engineering Research Council (NSERC) of Canada and Syncrude Canada Ltd. is gratefully acknowledged.

Finally, I owe gratitude to my family for supporting me through many difficult years without getting back all the love they deserve.

To Irina and Andrew

Chapter 1. INTRODUCTION

In this chapter we present the problem of single and two-phase jet injection into the fluidized bed that will be studied in the subsequent chapters. We also provide some of the background on the targeted industrial application – bitumen upgrading by a fluid coking process. Next, a literature review will cover all major areas that are related to the problem, i.e. dispersed bubble flows, sprays, interactions between the bed and the liquid injection, and particle attrition. Finally, we outline the research objectives and provide details on the thesis layout.

1.1. Problem description

1.1.1. Injection into the fluidized bed

Fluidized bed technology is at the core of many processes in chemical, pharmaceutical, petroleum, food and a number of other industries. Due to the high mixing rates of solid particles, fluidized beds are used whenever there is a need to quickly distribute reagents. Superior heat and mass transfer rates make fluidization the process of choice to handle reactions that are highly exo- or endothermic and require the rapid removal of the products. The fluidized bed itself is basically a layer of granular material located in the enclosed space above the distribution plate that is penetrable to the fluidization agent but not to the granular particles. As the fluidization agent (usually gas) flows upward, particles become suspended in the flow because their weight is balanced by the drag force exerted on them. The behaviour of the particles is similar to the fluid behaviour as they fill the shape of the vessel they are in; this explains the origin of the term “fluidized” beds. With the increase of the velocity of the fluidization fluid, the fluidization regime, loosely defined based on the particle motion, changes from the fixed bed to dispersed particle flow. Depending on the particle size, material and bed geometry, several intermediate stages, such as homogeneous

bed, bubbling and turbulent regimes are possible. This diversity of fluidization regimes also increases the variety of bed industrial applications.

There are several ways to introduce the reactants and particulate media to the fluidized bed reactor. While solid particles are usually delivered by screw-like mechanisms, gaseous materials can be mixed with the fluidization agent or injected through the nozzles, and liquid materials are typically sprayed into the reactor. The arrangement of nozzles that inject liquid or gas into the reactor can vary. The nozzles can be directed upwards to form a spout, downwards from above the bed surface, or horizontally either from above or from the side of the bed. Also, some other angular alignments are possible. Naturally, after the injection, the gas or liquid interacts with the bed. Depending on the injection location and direction, some physics of the interaction changes. For example, liquid sprayed over the top of the bed has little influence on bed hydrodynamics.¹ On the other hand, fluid injecting nozzles that are located below the bed surface, either vertical or horizontal, have a substantial influence on the bed itself. Depending on the momentum of the injected components, such influence can be observable in large parts of the whole bed. Thus, there is also a potential to use injections as a means to control the bed. They can help by producing favourable flow patterns or assisting with the mixing. Also, high speed jets may facilitate particle collision breakage that can be used to process advantage. All in all, there is a rich variety of applications that involve jet injection into the fluidized bed making the subject worthy of many in-depth investigations.

1.1.2. Fluid coker reactor

Among many applications where the jet injections into the fluidized bed can be found, the present study is motivated by the fluid coking reactor. The purpose of the fluid coking process is a bitumen upgrade by means of thermal cracking (Gray, 2002). The bitumen obtained from oil sands in the Athabasca region in northern Alberta by either open pit mining with subsequent separation or in-situ gravity drainage requires additional upgrading before further processing in a conventional distillation column because the

¹ Note, however, that while the spray itself has little influence, the liquid that ends up on the particle surface may change the collision dynamics and, hence, the motion of particles within a bed.

bitumen consists mostly of heavy non-distillable hydrocarbons. The thermal cracking (or fluid coking) is one of the upgrading options², and it is currently employed by Syncrude Canada Ltd. The upgrade process is associated with significant energy requirements and environmental impacts. As world conventional oil and other fossil fuel reserves are gradually being depleted, non-traditional energy sources are slow to emerge, nuclear fission has serious opposition in many countries, and controlled nuclear fusion is yet to materialize, it is inevitable that the share of heavy oils in total energy consumption will increase to satisfy ever-growing demand, driven mostly by economic development. In such a situation, the importance of the upgrading process optimization remains one of the available means to reduce additional energy consumption and mitigate the environmental impact. The optimization is usually based on the detailed understanding of the process. The presented research attempts to take a step in the direction of this understanding.

The fluid coking reactor, shown on the left-hand side of Figure 1-1, is a large cylindrical vessel with increasing diameter from bottom to top. The hot coke particles (510-530°C) are fluidized by steam that is supplied from the bottom. Bitumen is injected through several rows of nozzles by steam-assisted atomization. In this process, the compressed steam (~ 1 MPa) is injected into the liquid and the mixture passes through a nozzle consisting of two convergent and one divergent sections (Base et al., 1999). Close to the nozzle exit, the gas rapidly expands because of a large pressure drop. This expansion makes it unsustainable for the liquid to remain a continuous phase due to the decrease of its volume fraction, and, thus, a catastrophic phase inversion, i.e. the change of the continuous phase from liquid to gas, takes place across a certain surface. The resulting droplets inherit liquid momentum and continue their motion, forming a spray.

Upon contact between bitumen droplets and coke particles, a liquid layer is formed on the particle surface. As this bitumen layer heats up due to heat transferred from the particle, cracking reactions start to take place. Lighter hydrocarbons evaporate from the surface to be collected for further processing downstream of the reactor to produce so-called “synthetic

² The others are delayed coking, flexicoking, fluid catalytic cracking, and hydrocracking

crude,” which is a mixture of hydrocarbons similar to what is found in conventional oils, and heavier hydrocarbons remain on the particle eventually forming an additional layer of coke.

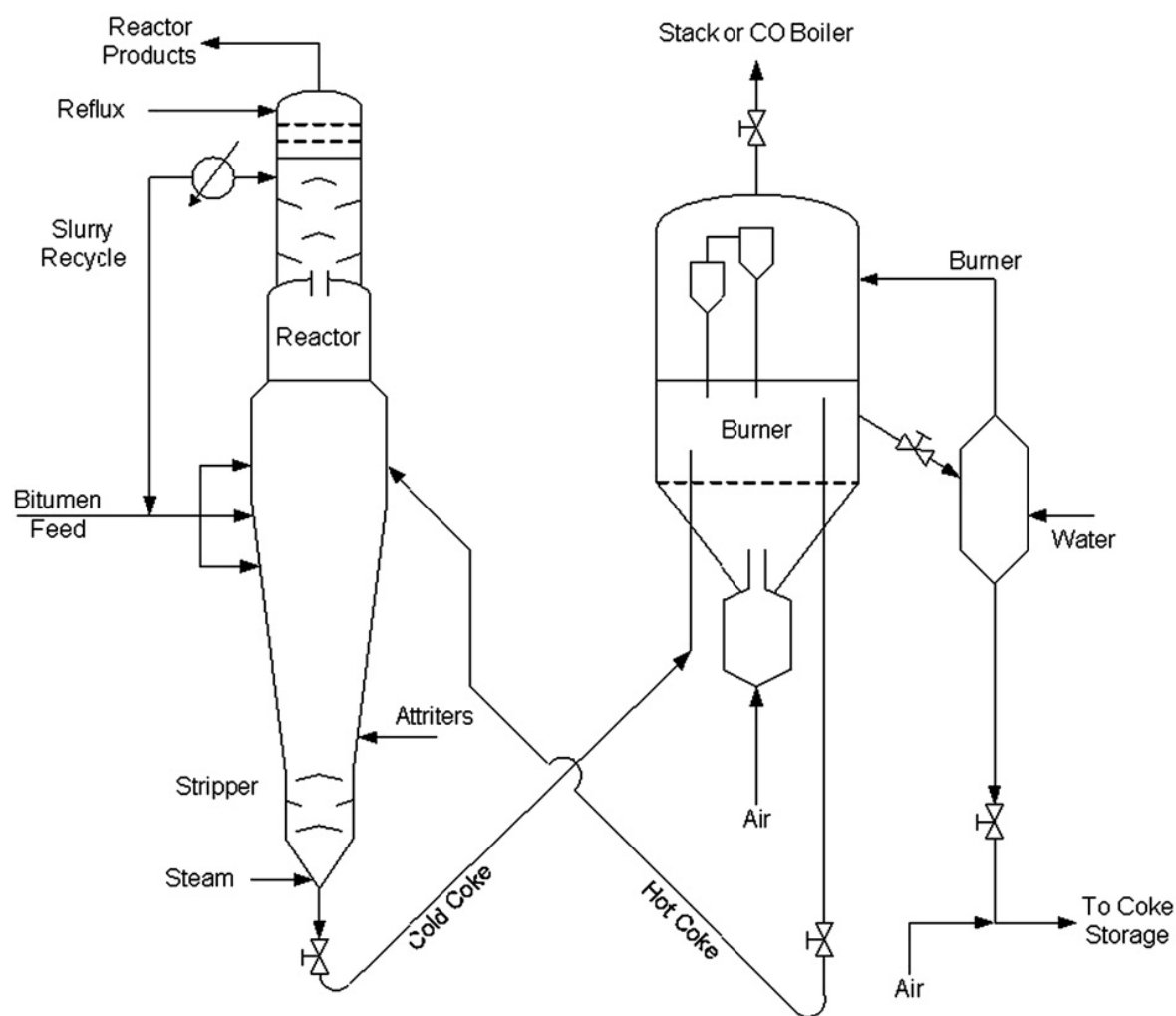


Figure 1-1. Schematic of fluid coking process (Reprinted from House et al. (2004) with permission from Elsevier).

Generally, the faster the reaction, the more yield of the favourable products such as lighter hydrocarbons and vice versa (Gray, 2002). The speed of the reaction is controlled by temperature and, hence, by heat transfer. Therefore, it is beneficial to have a thinner bitumen layer, as it can heat up more quickly. Thus, for a constant bitumen flow rate, it is desirable to distribute liquid as evenly as possible among the available coke particles (House et al., 2004).

Spraying bitumen droplets into the hot coke particles ensures a fast contact that facilitates heat transfer and subsequent cracking reactions. However, the process operating

Chapter 1. Introduction

window is limited. For example, a large thickness of liquid film would result in a decreased yield due to the mass transport limitations because of the trapping of cracked products inside (Gray et al., 2001). In addition, poor agitation may lead to undesired agglomeration. Thus, the tasks of process control and optimization are far from trivial. To achieve progress, it is necessary to develop a good physical understanding of complex multi-phase and multi-scale interactions. Such understanding can be accomplished through both experimental and numerical methods.

Evidently, the particle size tends to grow naturally during the process. In addition, some of the particles may stick together because of the formation of the liquid bridge that does not rupture when they rebound after a collision. This way agglomerates are formed from several particles. This process also accelerates growth and if left unchecked, such growth would result in poor fluidization and, subsequently, in bed collapse.

There are two methods in use to control particle size growth in the coking reactor. In the first method, some particles are continuously taken out of the reactor and directed to the burner, which is shown on the right-hand side of Figure 1-1, where some coke is oxidized providing heat for the process, and then hotter and smaller particles are returned to the reactor. Note that there are inherent limitations to this method arising from the coke recirculation ratio and usable heat consumption. In the second method, particles are broken up inside the reactor. This is achieved by an array of supersonic nozzles located circumferentially in the lower part of the reactor (note that larger particles are usually segregated towards the bottom of the bed) and directed towards the reactor axis. Steam, supplied through these nozzles, accelerates coke particles entrained in the jet and facilitates inter-particle collisions with high impact velocity. Such collisions result in particle (or agglomerate) breakage, thus effectively reducing the size of the bed particles, which is called attrition.

Currently, attrition nozzles require a large quantity of steam, and account for a large percentage of the total steam usage in the fluid coker. Improving the efficiency of the attrition nozzles would reduce steam consumption, which would decrease sour water treatment, and allow for more throughput in the reactor. The gas flow rate in the coker is limited by capacity, and therefore, if less steam is used in the attrition nozzles, more

hydrocarbons can be put through the reactor. Simple jet attritors require large amounts of gas to grind the particles effectively. If these attrition jets were improved, they may be able to achieve the same attrition rates while operating at a much lower gas flow rate.

While the quite well known jet mills are designed primarily for particle breakage, (see Akunov, 1966), the attrition in the fluid coking reactor is a secondary process. The primary process is the dispersion of bitumen into the fluidized bed and its cracking on the surface of coke particles. Therefore, the design options to ensure the best possible attrition are fairly limited. Due to significant operational constraints, detailed understanding of the particle attrition mechanism and factors that have an influence on it becomes extremely important.

1.2. Literature review

In this section we examine the previous work that is related to jet injection into fluidized beds. As Li (2009) has already presented a thorough review of work that pertains to generic jets issuing into the bed, our investigation focuses on the studies that consider conditions similar to the ones found in the fluid coking reactor and on other studies that are generally relevant to modelling of the gas-assisted atomization. Due to the complexity of the problem, we separate it into four parts:

- 1) Bubbles-dispersed flow in the nozzle
- 2) Atomization and droplet-dispersed flow in the open space
- 3) Droplets interaction with a fluidized bed, called jet-bed interaction
- 4) Particle attrition

The following review is structured accordingly.

1.2.1. Bubbles-dispersed two-phase flow

The interest in the research community in the two-phase flow through the converging nozzle has been demonstrated for a long time. The majority of work was published in the 1970s and 80s, most likely due to demands from the nuclear industry. Initially, researchers attempted to adapt a well developed single phase flow passing through the nozzle theory to two-phase flow. Assuming choking conditions at the nozzle end, the pressures and flow rates

Chapter 1. Introduction

were calculated. However, the dependency of the speed of sound in the multiphase mixture on the flow parameters makes the problem much more complex. Thus, the critical flow conditions become dependant on the interfacial interactions. As long as the air volume fraction and the bubble diameter are small, the homogeneity assumption of the two phase flow produces acceptable results (Romstedt and Werner, 1986). However, when the drag between the phases decreases with the increase of the bubble diameter, the slip velocity, which is the difference between the velocities of the gas and the liquid, needs to be taken into account. Hench and Johnston (1972) investigated the performance of a two-dimensional diffuser for different gas volume fractions and different nozzle geometries. They showed experimentally that the similarity between the single phase and the two phase flow behaviour exists only for small values of the air volume fractions. With the increase of the gas volume fraction, the flow becomes less homogeneous and, hence, the slip velocity between the phases increases. Chisholm (1968) proposed utilizing an effective velocity and effective density of the mixture together with an empirical correlation for the phase velocity ratios in order to derive analytically critical flow conditions at the nozzle throat. Maxwell et al. (1975) presented a differential model for a nozzle flow. Even though the model was one-dimensional and steady state, it required less empirical input, as the model solved the momentum equations for each phase velocity. The authors also introduced a variable bubble diameter that changed according to the surrounding pressure and temperature.

There is a wealth of publications devoted to the applications of the numerical modelling of two-phase flows with bubbles dispersed in liquid. However, the majority of them are directed towards the bubble column simulations, where the flow is generally incompressible and has a relatively low speed. While there are some successful applications of direct numerical simulations (DNS) methods and Eulerian-Lagrangian modelling, the approach of choice for practical computations is the multi-fluid Eulerian-Eulerian model, as it is less computationally expensive than the former two. The treatment of the gas bubbles can be different. Pan et al. (1999) considered all bubbles to be of the same mean diameter. Krishna et al. (1999) proposed to separate bubbles into two phases: small bubbles and large bubbles. The mass transfer between these two phases and the bubble sizes are determined by a semi-empirical algebraic equation. Another approach represented by Sheung et al. (2007) is to model bubble size by solving a particle number density differential equation. The bubble

Chapter 1. Introduction

distribution is assumed to be monodispersed, that is, the bubble size varies depending on the time and location in the flow field, but is considered constant at each local point. This methodology allows the inclusion of the bubble coalescence and break-up processes into the model. Finally, there is population balance modelling which considers a variety of bubble sizes that may coexist locally. Chen et al. (2005) demonstrated that a bubble population balance model with 16 distinct classes of bubbles separated according to their diameter provides better agreement with experimental data than the use of the mean bubble size. However, the researchers have not compared their results with a monodispersed model, which is more realistic than the monosized model, but less computationally expensive than the population balance one.

The continuity and momentum balance equations for the multi-fluid Eulerian model are obtained from ensemble averaging of the instantaneous equations (Zhang and Prosperetti, 1994). These equations are commonly accepted for the gas-liquid modelling. Still, there are also other averaging approaches, for example, one presented by Boisson and Malin (1996) results in the appearance of the diffusion source term in the bubble continuity equation. At the same time, there is less agreement in the exact form of the constitutive relationships, which determine interfacial forces and phase stress tensors that are necessary to close the system of equations. Monahan et al. (2005) presented a thorough review of the variety of model closures used by different researchers. While comprehensive two phase turbulence models do exist, e.g. Kataoka and Serizawa, (1989), their practical usage is limited due to the lack of knowledge about the modelling of production and dissipation terms. Most of the applications use the turbulence model for a continuous phase only, e.g. Sha et al. (2006). In order to take into account additional turbulence generated by the bubbles, a term called bubble induced turbulent viscosity proposed by Sato and Sekoguchi (1975) is often added to the viscosity of the continuous phase. Behzadi et al. (2004) developed a mixture turbulence model, which was obtained by summation of the corresponding equations for each phase and assuming direct proportionality between the Reynolds stresses in the continuous and dispersed phases.

We need to note that the flow rates and the volume fractions of the gaseous phase represented in the current gas-liquid flow models are generally low. The study of Wang et al. (2005), who attempted to model the flow regime transition with a population balance model,

considers the highest bubble fraction – up to 40%. However, this value represents only a lower range of the values typically encountered in the gas-liquid nozzles, where the gas volume fraction usually varies from about 40% in the conduit leading to the nozzle entrance, up to 85% at the nozzle exit.

1.2.2. Atomization and spray dispersion

Liquid sprays are widely used in various industrial applications where either the increase of the surface area of the liquid is desired, or some other properties of spray, for example, the droplet size distribution and the spraying angle and pattern, play a critical role in the process.

There are two major types of atomization devices: pressure jets and two-fluid atomizers (Nasr et al, 2002). The pressure jet is basically a pipe with an orifice at the end, through which the liquid is pushed, while the two-fluid atomizers bring gas and liquid together in a more sophisticated nozzle design. The two-fluid atomizers are also called gas-assisted because of an additional shear created by the gas injection. Depending on where the gas and liquid come into contact, two-fluid atomizers can be internal or external: in the internal atomization, gas is injected someplace upstream of the nozzle orifice, and in the external – downstream. It is known that gas-assisted atomization produces more finely dispersed droplets (Nasr et al, 2002). One of the various designs of the internal atomization device (Base et al., 1999) employs the continuous phase inversion, which is the change of the continuous phase from liquid to gas, as a primary method of obtaining liquid droplets. In this device the compressed gas is injected into the liquid, then the mixture travels through the variable cross-section nozzle; near the nozzle exit the gas rapidly expands causing catastrophic phase inversion, and thus forming the droplets. The nozzle is usually operated in the choked regime; therefore, the exit velocity is determined by the speed of sound in the two-phase mixture. As noted by Chawla (1985), the advantage of this method is that due to the reduction of the sonic velocity in the presence of the second phase, lower energy consumption is required to achieve similar atomization results, as for a single phase nozzle, because of the lessening of the wall friction. There are a number of processes that take place simultaneously or sequentially during the operation of the described atomizer, such as compressible gas-liquid flow through the nozzle at high gas volume fraction, bubble

Chapter 1. Introduction

coalescence and break-up, phase inversion and primary droplets formation, droplet dispersion, and secondary droplet break-up and coalescence.

In order to simplify modelling, the sprays are often decoupled from the atomizer, so that only the spray dispersion is modelled. Such models usually employ the Lagrangian description of the droplet's movement, i.e. direct tracking of each droplet, as the concentration of the dispersed phase is relatively small and the description of the droplet's properties is significantly easier. One of the first such models was proposed by Dukowicz (1980). Even though the original model did not consider secondary break-up, coalescence, and size variations of droplets, it can be generalized to include these phenomena, e.g. Shi and Kleinstreuer (2007). The Eulerian description of the spray as a continuum is also possible, but it is not very popular in the spray-only computations. There are also attempts to improve the Eulerian scheme by building on its advantages in predicting the chaotic motion of the particles. Beck and Watkins (2003) proposed a model that utilizes moments of the droplet distribution function, making the computations more efficient. Nijdam et al. (2006) considered both the Lagrangian and Eulerian approaches and confirmed that the results they produced are similar, provided the same sub-models are used; however, the ease of the implementation and a wider range of applicability make the Lagrangian method a preferred choice.

All separate spray models require the inlet boundary conditions to determine the initial droplet size distribution, the mass and momentum flux distributions, etc. While in some situations these values can be estimated or measured with sufficient accuracy, more often they are not well known. This makes necessary the inclusion of the atomization (or primary break-up) region into the modelling domain. The high liquid volume fractions in those regions make the Lagrangian approach not applicable. Vallet et al. (2001) proposed a simplified model for liquid jet atomization. They assumed that the large scale features of the flow, such as velocity, depend on the density ratio only, while the small scale features, such as droplet diameter, depend on the surface tension and turbulence. In addition, a single phase momentum equation with a variable density is used to represent the flow motion following the Eulerian approach. This model was applied to predict the droplets' flow rates and the mean droplet diameter distribution throughout the spray area.

Chapter 1. Introduction

Von Berg et al. (2005) developed the first coupled model that includes the nozzle and the spray regions. The authors demonstrated two coupling approaches: first, the sequential applications of the nozzle flow model, primary break-up model, and discrete droplet model; and second, the fully coupled approach, where the multi-fluid (Eulerian) model equations are applied to the whole domain with different interfacial exchange terms. Even though the description of the break-up rate was significantly simplified in the second approach, the authors concluded that it has better potential than the first one due to improved resolution of the flow features.

Another coupled spray atomization model of Deux and Sommerfeld (2006) divides the computational domain in dense and dilute spray regions. In the dense region the two-fluid model is applied together with the atomization model based on the structure formation process, and in the dilute region the Lagrangian droplet tracking is employed. A good agreement with experimental data was reported, but still more work is required on the treatment of the boundary between the two regions.

The existing models consider the liquid jet break-up as a mechanism for the primary atomization. However, in the case of the premixed atomization under consideration, it is the phase inversion that is responsible for this process. Even though the phase inversion has been studied by many researchers, e.g. Vaessen et al. (1996), to the best of our knowledge the phase inversion theory has not been previously applied to the premixed atomizers.

In the existing coupled nozzle spraying models the flow through the nozzle itself is fairly straightforward, even though it might be complicated by cavitation, as is the case for Von Berg et al. (2005). However, in the gas-assisted premixed atomization the solution for the compressible high gas volume fraction flow is nontrivial.

1.2.3. Jet-bed interaction

There is a substantial amount of research carried out to investigate the granulation process. For example, liquid propagation in the fluidized bed has been studied rather extensively (see a review paper by Iveson et al., 2001), but in a general framework of granulation applications. However, in granulation, liquid is generally delivered vertically into the fluidized bed. It can be done either from the bottom of the reactor through the spout, e.g.

Chapter 1. Introduction

Becher and Schlunder (1997), or through the top by spraying in the freeboard region of the bed, e.g. Jimenez et al. (2006). Evidently, for these cases the interactions between the bed and spray are different from the ones that take place during the horizontal injection. In addition, the jet velocity is orders of magnitude smaller than the one encountered in the fluid coking process. Moreover, the atomization device used in the coking process (Base et al., 1999) is fairly unique and not similar to nozzles used for spray granulation. The above arguments make the direct applicability of the granulation research to the horizontal high speed spray injection rather questionable. Therefore, more process specific research is required.

As actual process conditions are characterized by relatively high pressure and temperature, e.g. House et al. (2004), and bitumen is rather difficult material to work with, the experimental studies are therefore usually conducted at room conditions with more handling-friendly materials. At the same time, researchers tried to preserve some characteristic dimensionless numbers to ensure relevance to the industrial case. House et al. (2004) injected sucrose solution into a small-scale bed of coke particles. As sucrose binds coated particles together, liquid-solid contact can be evaluated after the bed was dried out so that water can evaporate. The authors discovered that an addition to the cylindrical tube coaxially downstream from the nozzle improves uniformity of liquid distribution. A year later, McMillan et al. (2005) also investigated a similar tube insertion and came to similar conclusions. However, they used a different experimental technique. They inserted an array of thermocouples into the bed and estimated contact properties in real time based on the temperature difference between liquid and solid. House et al. (2008) investigated several nozzle designs including the addition of a conical attachment to the nozzle orifice. It turned out that such an attachment improved the nozzle performance in terms of better contact between liquid droplets and solid particles.

Ariyapadi et al. (2004, 2005) investigated jet penetration and stability for a variety of nozzle designs. The jet penetration length was detected by either axial temperature measurements or triboelectric probes. Quite naturally, jet penetration distance correlations established for gas jet are not valid for gas-liquid jets; therefore, the authors proposed a new generalized correlation which incorporates the influence of the second phase. That

Chapter 1. Introduction

correlation included a nozzle geometry parameter that somewhat limits the applications outside the tested designs.

Portoghese et al. (2008) studied the influence of various operating parameters, such as the ratio of the gas to the liquid mass flows (so-called GLR – Gas to Liquid Ratio or ALR – Air to Liquid Ratio) and nozzle size on nozzle performance in terms of a nozzle performance index, which is a measure of liquid distribution uniformity obtained from triboelectric signals. Their experiments were also done for a small scale fluidized bed of glass beads. They found that an increase of GLR improved nozzle performance, as did a reduction in the size of the nozzle.

Similar to the experimental work, the majority of simulation studies pertain to granulation conditions, e.g. Heinrich and Morl (1999). At the same time, some researchers did target liquid injection by means of a horizontal jet. Due to the complexity of the problem, modelling studies are usually focused only on certain parts of it. The majority of the researchers concentrated on the chemistry and mass transfer, which means ignoring the details of the particle motion. Usually, such approaches result in a one-dimensional approximation of the reactor. Gupta and Rao (2001) investigated feed injection in Fluid Catalytic Cracking (FCC) riser reactors. They assumed that droplets travel through the gas with their terminal velocity and solid particles are arranged into clusters, with its volume fraction calculated based on the flow rate and the drag force. These assumptions allow them to include the reaction kinetic and heat and mass transfer mechanisms into the model to obtain axial profiles of species concentrations and volume fractions that are compared with limited industrial data. Nayak et al. (2005) presented a model based on a commercial code for a FCC riser including an oil injection. The model is focused mostly on the heat transfer and chemical reactions taking place after the injection, while modelling of particle motion received a less rigorous approach. Okasha and Miccio (2006) modelled the injection of evaporative fuel jet into the fluidized bed. They did not solve the motion of phases and relied on a large number of empirical correlations, such as gas and solid velocities, temperatures, jet penetration, etc. instead. Nevertheless, they were able to investigate the process qualitatively by utilizing the model.

Chapter 1. Introduction

A smaller number of published works resolves the motion of the phases in greater detail, making it the central part of their models. Zhu et al. (2002) simulated the nozzle region of Circulating Fluidized Bed (CFB) reactors. As the nozzle injection was vertical, they used an axial symmetry assumption to reduce the problem to two dimensions. The authors solved the equations of motion and energy for each phase together with a correlation for the droplet evaporation rate. They chose a combination of methods for the solution: the gaseous and solid phases are calculated using an Eulerian approach, while liquid droplets are traced in the Lagrangian coordinates, which simplified the treatment of various droplet diameters. The researchers obtained detailed distribution profiles of flow properties and compared some average values to the experimental data. A more detailed model of jet bed interaction was developed by Li et al. (2009, 2010). It utilized an Eulerian description of flow of each of the three phases—gas, droplets and wet particles—together with the kinetic theory of granular flow and a collision-based mass transfer model to close the equations. The model application to a jet injection into the CFB riser with a relatively low solid loading provided reasonable agreement with the experimental data. It has to be noted that all these jets were in the area of the fairly low solid loading, making interaction between particles less important. Recently, Nowak et al. (2010) developed a mixed Eulerian-Lagrangian model for spray injection into the bed. This model combines Lagrangian tracking for representative liquid droplets with an Eulerian treatment of gaseous phase and wet solid particles. None of the described models include liquid atomization. That is, the liquid spray with a certain velocity, volume fraction, and droplet diameter distribution is assumed as a boundary condition. However, in many industrially relevant cases these parameters are not known *a priori*. Moreover, it has been reported by House et al. (2004) that jet bed interaction depends significantly on the nozzle design. Therefore, it is necessary to develop a comprehensive model that includes the nozzle in the computational domain in order to avoid uncertain assumptions and increase model predictive capabilities.

1.2.4. Particle attrition

It is well known that solid particles can break-up upon a collision. This breakage can play a significant role in many processes that utilize a large number of solid particles such as fluidized beds, pneumatic transport, or granular flows. Sometimes, particle fracture is

Chapter 1. Introduction

beneficial for a process, for example, it is used to control particle sizes in the jet mills (Bentham et al., 2004). However, sometimes, it is detrimental, for example, catalyst attrition is undesirable in fluidized bed reactors. (Werther and Xi, 1993).

Historically, the work on particle breakage focused on analytical and experimental studies. This work can be separated into micro-scale studies that investigate the impact between two particles or between one particle and another surface, and macro-scale studies that look at overall attrition performance inside a reactor. The first group is represented by a number of researchers. Yashima et al. (1987) investigated crushing under compression of fairly large spherical particles made from different materials. They confirmed that crushing resistance increases with the decrease of the particle size. In addition, they proposed an analytical relationship that connects the fracture energy with the particle size and properties. Kapur et al. (1997) developed a probability based model to connect the particle breakage with the impact energy. Ghadiri and Zhang (2002) proposed an attrition propensity parameter, a dimensionless number that characterizes the possibility of attrition; this number contains properties of the particulate material such as the hardness and the fracture toughness, particle diameter, and impact velocity. Note that the authors considered only a semi-brittle failure mode, where the initial plastic deformation is followed by failure when the stresses exceed the yield point. Meier et al. (2009) proposed empirical relations for the breakage function based on some test data of particle impact on the rigid target.

Macro-scale attrition is also well studied. Shamlou et al. (1990) studied the hydrodynamic influences on particle breakage in a fluidized bed due to particle-particle and particle-wall interactions. No gas jets were injected into the bed. They found that during normal fluidized bed operation breakage could still take place. They attributed it to chipping of small pieces from the particle surface. At the same time, almost no large-scale fragmentation was observed. Benz et al. (1996) investigated the performance of a jet mill. They focused on finding the optimum spin number, which is the ratio of the circumferential speed of the classifier to the radial velocity of the gas. Werther and Xi (1993) tested attrition dependency on a number of fluidized bed properties, such as the bed height, the superficial and jet velocity, orifice diameter, bed geometry, and jet orientation. Similarly, Palaniandy et al. (2008) conducted a number of experimental runs to determine the influence of the feed rate, the classifier rotational speed, and the jet pressure. McMillan et al. (2007a) investigated

Chapter 1. Introduction

jet attrition using high speed nozzles in an experimental set-up that is representative of fluid coking. The authors obtained the grinding “efficiency”, which they defined as the ratio of the new particle surface created by the attrition to the mass of the required attrition gas, for a variety of materials, gas pressures, fluidization velocities, and nozzle configurations. They demonstrated that increased inlet pressure with a constant exit diameter and an increased exit diameter with constant inlet pressure results in better grinding efficiency. In addition, it was shown that larger superficial velocities were also beneficial for particle attrition. They proposed also a model to predict the final particle size distribution, and the breakage frequency (McMillan et al., 2007b). Jiang et al. (2009) presented a model based on the collision energy dissipation and applied it to a circulating fluidized bed. Their model connects macroscopic bed parameters, such as superficial gas velocity and particle diameter, to the attrition rate.

More recently, numerical models of the particle attrition started to appear. Eskin et al. (1999) simulated the flow in a jet-vortex mill. They modelled the two-phase flow of gas and particles inside the nozzle one-dimensionally accounting for a polydispersed particle size distribution. Even though the attrition was not directly modelled, the mill performance efficiency can be inferred from the flow dynamics data. Han et al. (2002) developed a comprehensive model that combines the discrete element model (DEM) for the motion of solid particles in the gas flow with Ghadiri’s attrition model (Papadopoulos et al., 1998). The trends predicted with the model correspond to the ones observed experimentally. It is important to note that while DEM provides a very good representation of the particle motion, its practical application is restricted to a relatively small system with a limited number of particles. Cocco et al. (2010) utilized a more practical multiphase particle-in-cell method (Andrews and O’Rourke, 1996) implemented in a commercial software for attrition modelling. In the framework of this method, only the selected representative particles are tracked, instead of tracking all the particles in DEM. Even though the attrition was not directly simulated, the model provided the flow field results in the cylindrical jet cup, which are in agreement with the experiments and were indicative of the attrition performance. Use of an Eulerian-Eulerian approach for gas-particle mixture was adopted by Rajniak et al. (2008). They also utilized a commercial software package to model the flow in laser diffraction equipment with a population balance model. The authors adjusted parameters of

the breakage kernel, a source term function used in the population balance equation, to obtain reasonable agreement between modelling and experimental results.

1.3. Objectives

Overall, the purpose of this work is to build a modelling foundation for an optimization of jet injection processes related to a fluid coking reactor. As outlined in Section 1.1.2, such optimization would have a significant economic and environmental impact. The work to achieve the stated intentions can be structured in the following way:

- Develop mathematical models for jet-bed interaction and particle attrition based on flow physics
 - Choose main model assumptions and a corresponding set of conservation equations
 - Find available sub-models to quantify processes taking place in a system
 - Develop sub-models for phenomena that were not investigated previously
- Adapt and modify numerical tools to ensure robustness of calculations
- Adjust models and compare their performance with available experimental data
- Demonstrate models applicability to industrial process conditions
- Analyse the flow based on the modelling results

1.4. Research methodology

The project splits into two parts: modelling of gas-liquid injections and modelling of high speed gas injections.

1.4.1. Jet-bed interaction

This part of the work is aimed at the improvement of initial spreading of liquid bitumen in the fluidized bed of coke particles. The improvement comes from advanced understanding of the complex processes taking place inside and near the nozzle. This understanding, in turn, can be achieved by experimental or modelling means. As process conditions in fluid coking do not allow direct observation due to high temperature and pressure, and they are not reproducible in a lab setting in a controlled experiment for the same reasons, modelling has to bridge the gap between the experimental studies and industrial application. We chose to use mathematical modelling that relies on the process physics that is independent of most of the process conditions. Thus, we adjust and verify the model based on the available experimental results for small scale devices that utilize other materials, and then extrapolate its applicability to actual process conditions. The problem physics is extremely complex. It involves liquid-continuous flow with high volume fraction of the dispersed compressible gas through the nozzle with a variable cross-section; phase inversion or atomization, as the gas volume fraction rapidly grows; spray dispersion; granular flow of solid particles that may have a layer of liquid on their surface; interactions between droplets and wet particles; and possible break-up and/or coalescence of droplets or bubbles. The main focus of this work is the mathematical model development. While some applications to industrial conditions are also presented here, specifically spray modifications by nozzle attachments, they serve as examples without being a comprehensive study of the process.

The models of sprays and spray interaction with bed particles, described in Sections 1.2.2 and 1.2.3, require the knowledge of the initial spray characteristics before it enters the fluidized bed. However, due to a particular nozzle design for the gas-assisted atomization in the fluid coking process, such characteristics are highly dependent on flow rates, temperatures, material properties, and nozzle geometry and generally are not known *a priori*. Therefore, it is desirable for a model to rely only on the available integral values, e.g. inlet flow rates of gas and liquid and their corresponding physical properties. In order to achieve this, the model has to include the nozzle itself in the computational domain.

Chapter 1. Introduction

Due to the complexity of the problem, we divided the work into three stages: at first, we consider only two-phase flow through the nozzle; second, we add to the nozzle flow the atomization and spray dispersion; and third, we add to the previous model the fluidized bed and interactions between droplets and solid particles. During each stage, modelling predictions are compared with available experimental data and any adjustable parameters, if present, are chosen to ensure a best fit.

1.4.2. Particle attrition

This part of the work is aimed at improving efficiency of coke particle attrition by high speed steam jets. In particular, we are interested in the determination of the optimal area ratio of the expansion section of the convergent-divergent (Laval-type) nozzle to provide the best attrition efficiency and in the investigation of the influences of the nozzle expansion angle and the superficial gas velocity. These issues are addressed by means of the mathematical modelling that can complement experimental studies.

We develop a comprehensive attrition model utilizing an Eulerian-Eulerian modelling of gas-solid flow and a granular temperature approach to describe collisions between solid particles. The particle breakage is modelled based on the collision frequency and break-up probability, which in turn depends on the impact velocity, the particle diameter, and the material properties. Similar to modelling jet-bed interactions, we apply the model to conditions for which experimental data are available. Next, after the determination of the coefficient that depends on particle material, the model can be applied to industrially relevant conditions. The model allows a quantifiable characterization of nozzle efficiency, and it can be applied to the various configurations encountered in the fluid coking process as well as in other industrial applications.

1.5. Outline

Chapter 2 presents two novel mathematical models; the first simulates liquid spray dispersion in the fluidized bed of solid particles, and the second models particle attrition by a high speed gas jet. The jet-bed interaction model includes flow through the atomization device (nozzle), phase inversion and formation of the spray, its interaction with the solid particles, and liquid propagation within the bed. (For brevity, we will call this model jet-bed

Chapter 1. Introduction

interaction.) All these processes are modelled simultaneously to reflect the couplings between them. The model utilizes an Eulerian description for all three phases to allow for the continuous computations throughout the whole domain. To adequately represent the variety of local bubble and droplet sizes, the particle number density approach is chosen. The constitutive equations that depend on the flow regime are obtained from many sub-models that have been developed alongside the main model. Droplet and bubble size is represented by an average diameter that can vary in the flow field. Bubble and droplet break-up and coalescence models are adapted to the flow conditions. The proposed model for atomization treats it as a catastrophic phase inversion that takes place over the infinitely thin surface determined by the local values of phase volume fractions. A mathematical model for particle attrition by high velocity gas jets also utilizes an Eulerian-Eulerian approach for the gaseous and particulate phases coupled with the Kinetic Theory of Granular Flow (KTGF) and a novel attrition model connecting the solid phase properties and the granular temperature with the breakage rate. In addition, the numerical methods utilized to obtain converged solution are presented. It is shown that for numerical stability, it is necessary to discretize implicitly the virtual mass term and solve the momentum equations for two phases simultaneously in a coupled way.

In Chapter 3, a two-fluid model for compressible flow of gas bubbles dispersed in liquid is applied to air-water flow through a convergent-divergent nozzle. Curvilinear body fitted grids are utilized to represent the nozzle shape accurately. The comparison between the experimentally measured and the predicted pressure profiles along the nozzle wall demonstrate good overall agreement. Gravitational effects are analysed by modelling a three-dimensional case. The examination of the flow through the nozzle reveals the non-uniformities of the bubble size and volume fraction distributions. The role that the virtual mass force plays in accelerating/decelerating flows with a relatively low interfacial drag is also analysed.

The model application to simulate the premixed air-assisted atomization of water in a nozzle-type device is presented in Chapter 4. The computational domain includes the nozzle and the surrounding area of the spray dispersion. The model performance is verified by comparing the predicted and measured liquid flow rates in the spray and the average droplet

Chapter 1. Introduction

diameters, as well as the pressures along the nozzle wall. Computational results are analyzed, and the main flow features are presented.

Chapter 5 presents application of the full jet-bed interaction model to the experiments conducted for a small scale fluidized bed. Experimentally measured Liquid to Solid (L/S) ratio radial profiles are compared with model prediction for two different cases. Next, the model is utilized to determine jet penetration distances for various flow conditions. The obtained distances are compared with experimental values. In addition, we analyse the influence of the superficial gas velocity on initial liquid spreading. Finally, we discuss advantages and disadvantages of an axial symmetry assumption over full three-dimensional calculations that are employed in this chapter.

In Chapter 6 we investigate addition of the conically shaped attachment to the premixed gas-assisted high-pressure atomizer. We numerically study attachments with three different expansion angles and compare them with the case without any attachments. Our investigation reveals spray patterns average droplet diameter distributions that can be obtained with the use of the attachments.

The particle attrition model is applied in Chapter 7 to a large number of cases that have been previously investigated experimentally. Simulation results are compared with model predictions. We study the influence of the gas inlet pressure on grinding efficiency. Also, we examine how attrition is affected by the nozzle exit diameter. Next, numerical simulations are conducted for industrial conditions to investigate various nozzle designs, i.e. a range of area ratios (indicative of the jet being over- or under-expanded) and nozzle expansion angles, and different bed fluidization velocities.

Finally, in Chapter 8 we summarize our research, reiterate main findings, and present conclusions pertaining to both jet-bed interaction studies and particle attrition. We also provide some practical recommendations that can be drawn from this work. In addition, we outline areas that may benefit from further research, suggest ways for additional model improvements and further model development, and recommend model application to certain conditions of practical and/or research interest.

Chapter 2. MATHEMATICAL MODEL DESCRIPTION

In this chapter we present the development of two numerical models that form the core of this work. We introduce full models for jet-bed interaction as well as for particle attrition. The presentation follows a logical path of model development: from problem formulation through major assumptions to main conservation equations. Next, all closure equations (or sub-models) are described. The degree of detail in sub-model description varies depending on whether it is a previously known model, or it is developed by us specifically for this project. In the former case, the reader is referred to the corresponding sources. Finally, the numerical method that is utilized to solve the modelling equations is presented.

Since the modelling work was done in stages, as described in Section 1.4.1, some parts of the models were not used during certain studies. Throughout the text we point readers' attention to the actual subset of equations used during each particular investigation if they differ from the model presented in this chapter.

2.1. Model of spray injection into fluidized bed including flow through the nozzle and atomization

As mentioned in Section 1.4.1, the flow through the nozzle has to be explicitly modelled to avoid the introduction of boundary conditions at the beginning of the spray. Therefore, the problem to be modelled includes the liquid-continuous flow with bubbles through the convergent-divergent nozzle, atomization, the gas-continuous flow with droplets, and the surrounding fluidized bed. We assume that there are three phases in the computational domain: compressible gas (denoted by 'g'), which can exist either in continuous or bubble form, liquid ('l'), which can exist either in continuous or droplet form, and spherical solid particles ('p'), which consist of two components: a solid core ('s') and a liquid film ('f'). In order to reflect the variation in particulate size and, at the same time, keep

Chapter 2. Mathematical model description

the solution economical, particle size distribution is considered locally monodispersed. That means that size variations are permitted throughout the flow field, but only one average diameter is used to represent particle sizes within a control volume. This average diameter is obtained by solving a particle number density equation. Both bubbles and droplets can undergo break-up and coalescence. The size of solid particles can also vary due to the changing mass fraction of the liquid layer. The atomization is treated as a catastrophic phase inversion that depends only on the local values of the volume fractions. The kinetic theory of granular flow is employed to describe the motion of solid particles. Collisions between the droplets and solid particles can lead to either rebound or coalescence. Thus, there can be mass transfer between liquid and solid particles phase. In addition, heat transfer is also included in the model. That is, the enthalpy equation is solved for gas and liquid phases and for each of the two components of the particulate phase.

An Eulerian multi-fluid description is adopted for both continuous and dispersed phases. The advantage of this approach is that it can be applied to any flow region regardless of the local values of the volume fraction; also our implementation allows its application regardless of which phase is locally continuous. It is assumed that both phases are interpenetrating; either the gas bubbles are dispersed in the liquid or the liquid droplets are dispersed in the gas, and particles are always dispersed in gas.

2.1.1. Mass, momentum, energy and components balance

The conservation equations for the model are obtained with ensemble averaging of the Navier-Stokes equations (Drew and Passman, 1999; Zhang and Prosperetti, 1994). Only the final forms are presented here, where all the variables are already averaged, unless noted otherwise. For convenience of presentation and for ease of implementation into the computer code, the equations are written in a phase independent way whenever possible. Because the model is applied to the curvilinear geometry, a coordinate independent form is used. To streamline the presentation of the equations, we make use of Kronecker's delta, i.e. δ_{ij} equals unity when i and j are the same and equals zero otherwise. The mass conservation takes the following form.

$$\frac{\partial}{\partial t} \alpha_i \rho_i + \nabla \cdot \alpha_i \rho_i \mathbf{V}_i = \delta_{ip} \dot{m}_{st} - \delta_{il} \dot{m}_{st} \quad i = g, l, p \quad (2-1)$$

Similarly, the momentum conservation can be written as

$$\begin{aligned} \frac{\partial}{\partial t} \alpha_i \rho_i \mathbf{V}_i + \nabla \cdot \alpha_i \rho_i \mathbf{V}_i \mathbf{V}_i = \nabla \cdot \boldsymbol{\tau}_i - \alpha_i \nabla P_i - \delta_{ip} \nabla P_s + \rho_i \mathbf{g} + \mathbf{F}_i + \\ + \delta_{ip} (\dot{m} \mathbf{V}_l - \dot{m}_r \mathbf{V}_p) - \delta_{il} (\dot{m} \mathbf{V}_l - \dot{m}_r \mathbf{V}_p) \quad i = g, l, p \end{aligned} \quad (2-2)$$

Note that the source terms appearing at the right hand side of the equations have their origin in mass transfer during droplets-particles interactions. They will be described below in greater detail. Density of the particulate phase can be obtained through mass fractions and densities of the solid core and the liquid layer.

$$\frac{1}{\rho_p} = \frac{x_s}{\rho_s} + \frac{x_f}{\rho_f} \quad (2-3)$$

The Boussinesq approximation extended to multiphase flow is utilized to calculate Reynolds stresses.

$$\boldsymbol{\tau}_i = \alpha_i \left(\delta_{ic} \mu_i + \mu_i^t \right) \left(\nabla \mathbf{V}_i + \nabla \mathbf{V}_i^T \right) - \frac{2}{3} \mathbf{I} \nabla \mathbf{V}_i - \frac{2}{3} \alpha_i \rho_i k_i \mathbf{I} \quad i = g, l \quad (2-4)$$

$$\boldsymbol{\tau}_p = \alpha_p \left(\mu_p (\nabla \mathbf{V}_p + \nabla \mathbf{V}_p^T) + \left(\lambda_p - \frac{2}{3} \mu_p \right) \mathbf{I} \nabla \mathbf{V}_p \right) \quad (2-5)$$

In Eq. (2-4), ‘c’ represents a locally continuous phase, which can be either gas or liquid. Next, the energy conservation is written separately for gas and liquid phases and for components of the particulate phase.

$$\begin{aligned} \frac{\partial}{\partial t} \alpha_i \rho_i H_i + \nabla \cdot \alpha_i \rho_i \mathbf{V}_i H_i = \alpha_i \frac{\partial p}{\partial t} - \nabla \cdot (\delta_{ic} \kappa_i + \kappa_i^t) \nabla T_i + \sum_k^{k \neq i} h_{ki} (T_k - T_i) + \\ + \delta_{ig} h_{fg} (T_f - T_g) - \delta_{il} (\dot{m} H_l - \dot{m}_r H_f) \quad i, k = g, l \end{aligned} \quad (2-6)$$

$$\begin{aligned} \frac{\partial}{\partial t} \alpha_p \rho_p x_j H_j + \nabla \cdot \alpha_i \rho_i \mathbf{V}_i x_j H_j = \nabla \cdot \kappa_j^{eff} \nabla T_j + \delta_{jf} h_{gf} (T_g - T_f) + \\ + \sum_k^{k \neq j} h_{kj} (T_k - T_j) + \delta_{if} (\dot{m} H_l - \dot{m}_r H_f) \quad j, k = s, f \end{aligned} \quad (2-7)$$

The enthalpy in Eqs. (2-6 and (2-7) is defined as follows

$$H_g = c_{p_g} T_g + \frac{\mathbf{V}_g^2}{2} + k_g \quad (2-8)$$

$$H_i = c_{p_i} T_i \quad i = l, s, f \quad (2-9)$$

In order to connect the gas density with the pressure, an ideal gas equation of state is applied.

$$P_g = \frac{\rho_g R T_g}{M_g} \quad (2-10)$$

Next, we add equations for conservation of the components of the particulate phase, i.e. solid core and liquid film.

$$\frac{\partial}{\partial t} \alpha_p \rho_p x_j + \nabla \cdot \alpha_p \rho_p \mathbf{V}_p x_j = \nabla \cdot (D_p \nabla x_j) + \delta_{jf} \dot{m}_{st} \quad j = s, f \quad (2-11)$$

The above balance equations alone do not provide a sufficient description of the flow. Additional closure relationships need to be developed in order to provide missing links between micro-scale physical phenomena and macro-scale variables. This development is presented in subsequent sections.

2.1.2. Interfacial forces

Only the drag, turbulent drag, and the virtual mass forces are considered in the model. The drag force accounts for the friction resulting from the difference of mean phase velocities. We consider drag between bubbles and liquid, droplets and gas, and solid particles and gas. Note that interactions between droplets and particles are treated separately. The drag force is proportional to the difference of the mean phase velocities (Drew and Passman, 1999).

$$\mathbf{F}_d^{drag} = \gamma_{cd} (\mathbf{V}_c - \mathbf{V}_d); \quad \mathbf{F}_c^{drag} = -\sum_i^{i \neq c} \mathbf{F}_i^{drag} \quad i = g, l, p \quad (2-12)$$

where γ_{cd} is the interfacial momentum transfer coefficient defined as

$$\gamma_{cd} = \frac{3}{4} \frac{\alpha_c \rho_d C_D}{d_d} |\mathbf{V}_c - \mathbf{V}_d| \quad (2-13)$$

The drag coefficient C_D^d depends on the flow regime. According to the existing flow regime maps, e.g. Taitel and Dukler (1976), flow in the pipe leading to the nozzle is in the dispersed bubble or churn-turbulent flow regime. We assume that the same flow regime persists through the length of the nozzle. Therefore, the Ishii and Zuber (1979) correlation can be applied for the drag coefficient of the deformed gas bubbles.

$$C_D^g = \frac{8}{3} (1 - \alpha_d)^2 \quad (2-14)$$

After the atomization, the flow is in the dispersed droplets flow regime. When the gaseous phase is continuous, the widely used model of Schiller and Naumann (1935) is employed:

$$C_D^l = \begin{cases} \frac{24(1 + 0.15 \text{Re}^{0.687})}{\text{Re}} & \text{Re} \leq 1000 \\ 0.44 & \text{Re} > 1000 \end{cases} \quad (2-15)$$

where Re is the droplet Reynolds number, which is calculated as

$$\text{Re} = \frac{\rho_g |\mathbf{V}_g - \mathbf{V}_l| d_l}{\mu_g} \quad (2-16)$$

The interfacial drag force between the particulate and gaseous phases is modelled by Gidaspow (1992) model.

$$\begin{cases} \text{if } \alpha_p \geq 0.2 & \gamma_p = 150 \frac{\alpha_p^2}{\alpha_g} \frac{\mu_g}{d_p^2} + 1.75 \frac{\alpha_p \rho_g}{d_p} |\mathbf{V}_g - \mathbf{V}_p| \\ \text{if } \alpha_p < 0.2 & \gamma_p = \frac{3}{4} C_D \frac{\alpha_p \alpha_g \rho_g}{d_p} \alpha_g^{-2.65} |\mathbf{V}_g - \mathbf{V}_p| \end{cases} \quad (2-17)$$

$$C_D = \begin{cases} \frac{24(1 + 0.15 \text{Re}^{0.687})}{\text{Re}} & \text{Re} \leq 1000 \\ 0.44 & \text{Re} > 1000 \end{cases} \quad \text{Re} = \frac{\rho_g |\mathbf{V}_g - \mathbf{V}_p| d_p}{\mu_g}$$

Chapter 2. Mathematical model description

To calculate the turbulent drag force, we utilize the model of Viollet and Simonin (1994).

$$\mathbf{F}_d^{turb} = \frac{3}{4} \frac{\alpha_c \alpha_d \rho_c C_D}{d_d} |\mathbf{V}_c - \mathbf{V}_d| \mathbf{V}_{drift} \quad \mathbf{F}_c^{turb} = -\mathbf{F}_d^{turb} \quad (2-18)$$

where \mathbf{V}_{drift} is the drift velocity, calculated as

$$\mathbf{V}_{drift} = \frac{\mu_m^t}{\rho_m Sc^t} \left(\frac{\nabla(\rho_c \alpha_c)}{\rho_c \alpha_c} - \frac{\nabla(\rho_d \alpha_d)}{\rho_d \alpha_d} \right). \quad (2-19)$$

The turbulent Schmidt number Sc^t in this equation is assumed 0.7.

The virtual mass force appears due to the acceleration of the continuous phase that is carried away together with the accelerating discrete particle. It is important when the density of the continuous phase is significantly larger than the one of the dispersed phase. In our case, it is important in the nozzle area, where there are dispersed bubbles flowing in the liquid. There are several relationships for the virtual mass force in the published literature with minor variations. We adopt the most commonly used one (Drew and Passmann, 1999).

$$\mathbf{F}_d^{vm} = C_{vm} \alpha_d \rho_c \left[\left(\frac{\partial \mathbf{V}_c}{\partial t} + \mathbf{V}_c \cdot \nabla \mathbf{V}_c \right) - \left(\frac{\partial \mathbf{V}_d}{\partial t} + \mathbf{V}_d \cdot \nabla \mathbf{V}_d \right) \right]; \quad \mathbf{F}_c^{vm} = -\mathbf{F}_d^{vm} \quad (2-20)$$

The virtual mass coefficient C_{vm} generally depends on the volume fraction of the dispersed phase. Laurien and Niemann (2004) proposed a polynomial correlation by analysing the results from the direct numerical simulations.

$$C_{vm} = 0.5 + 1.63\alpha_g + 3.85\alpha_g^2 \quad (2-21)$$

This correlation has been established for volume fractions of the dispersed phase up to 40%. However, in the case of the nozzle flow, the encountered bubble volume fractions can be much higher. A simple extrapolation of Eq. (2-21) would result in extremely high values of the coefficient. Considering that the virtual mass is the mass of the continuous phase that is carried along with the bubble, it becomes obvious that the virtual mass cannot exceed the value of the remaining mass of the continuous phase. That is:

$$\rho_{vmMAX} = \alpha_l \rho_l \quad (2-22)$$

This would correspond to a coefficient

$$C_{vmMAX} = \frac{\alpha_l}{\alpha_g} \quad (2-23)$$

Therefore, the following model is proposed. As long as the value provided by Eq. (2-21) does not exceed the limit established by Eq. (2-23), this value is used in the virtual mass force calculations; otherwise, the limiting value provided by Eq. (2-23) is used instead.

There are also other interfacial forces that have not been included in the model. The lift force is applied to the bubble while it travels through the shearing field of liquid. Similar to virtual mass, it may be important for the flow inside the nozzle. However, the physical mechanisms of the lift force acting on a single bubble are still an active research area, e.g. Legendre and Magnaudet (1998). Needless to say, there is even less clarity for the multitude of bubbles. Some of the researchers include the lift force in the computations of the bubbly flow, e.g. Cheung et al. (2007), while others do not, e.g. Pan et al. (1999). However, it has been shown by Behzadi et al. (2004), who proposed a correlation for the lift coefficient, that this coefficient decreases with increasing bubble volume fraction. The values obtained by their correlation are negligibly small for the range of the volume fractions encountered in the region of liquid-continuous flow. Thus, we decided to neglect the lift force in the model. Other forces, such as the Faxén force and the Basset force are also ignored, as their influence in the investigated process conditions seems to be negligible.

2.1.3. Fluctuating motion of gas and liquid phases

The fluctuating motion of the phases plays an extremely important role in determining the microscopic structures in the two-phase flow. These structures influence the break-up and coalescence processes as well as momentum dissipation through the Reynolds stresses, which, in turn, have a significant influence on the macroscopic flow parameters. Thus, it is crucial for the success of the simulations to have a turbulence model that adequately represents the complex nature of the process. It is possible to obtain the equations for Reynolds stresses in a similar way as for single phase flow, e.g. Besnard and Harlow

(1988), Kataoka and Serizawa (1989). However, not dissimilar to single phase flow, these equations are only a starting point in the turbulence model development as most of the terms cannot be directly implemented into the computations.

2.1.3.1. Mixture turbulence model

The widely used single phase k - ϵ model can be extended to multiphase flows. Kataoka and Serizawa (1989) obtained the equations for the turbulent kinetic energy (k) and its dissipation rate (ϵ) for each phase, using the same approach as for the single phase equations. However, the well-known problem of finding appropriate closures for the equations due to the inability to model some terms becomes even more difficult for multiphase flow turbulence. The equations need to be substantially simplified for practical use. Thus, the mixture turbulence model approach proposed by Gosman et al. (1992) and further developed by Behzadi et al. (2004) was chosen. In this approach, the turbulence kinetic energy and its dissipation rate equations for both phases are added, and the final equations are written in terms of the mixture variables. This is made possible due to an assumption that the velocity fluctuations in the dispersed phase are directly proportional to the velocity fluctuations in the continuous phase:

$$\mathbf{v}'_d = C_t \mathbf{v}'_c \quad (2-24)$$

where C_t is turbulence response coefficient, which depends on the flow parameters. It follows from Eq. (2-24) that the turbulence kinetic energy and the dissipation rate are also directly proportional:

$$k_d = C_t^2 k_c \quad (2-25)$$

$$\epsilon_d = C_t^2 \epsilon_c \quad (2-26)$$

We also have to modify the original model in order to take into consideration the influence of the particulate phase. Additional terms are added to the conservation equation to account for the turbulence transfer between the mixture and solid particles (see Das et al., 2004) and for the turbulence transfer associated with the mass transfer. The resulting equation for turbulent kinetic energy takes the following form:

Chapter 2. Mathematical model description

$$\begin{aligned} \frac{\partial}{\partial t}(\rho_m k_m) + \nabla \cdot (\rho_m \mathbf{V}_m k_m) = \nabla \cdot \frac{\mu_m}{\sigma_k} \nabla k_m + Q - \rho_m \varepsilon_m - \\ - \gamma_{cp} (2k_m - q_{cp}) + \sum_{i=1}^2 S_i + \left(\frac{3}{2} \dot{m}_r \theta - \dot{m} k_l \right) \end{aligned} \quad (2-27)$$

And for its dissipation rate

$$\begin{aligned} \frac{\partial}{\partial t}(\rho_m \varepsilon_m) + \nabla \cdot (\rho_m \mathbf{V}_m \varepsilon_m) = \nabla \cdot \frac{\mu_m}{\sigma_\varepsilon} \nabla \varepsilon_m + \\ + \frac{\varepsilon_m}{k_m} \left(C_{\varepsilon 1} Q - C_{\varepsilon 2} \rho_m \varepsilon_m - C_{\varepsilon 3} \gamma_{cd} (2k_m - k_{cd}) + C_{\varepsilon 4} \sum_{i=1}^2 S_i \right) \end{aligned} \quad (2-28)$$

In the above equations all constants are assumed to take their standard values; an additional coefficient, $C_{\varepsilon 3}$, specific to the multiphase flow is assumed 1.2, according to Simonin and He (1992).

Knowing values of k and ε for each phase, the turbulent viscosities in Eq. (2-4) can be calculated in the usual way:

$$\mu_i^t = C_\mu \rho_i \frac{k_i^2}{\varepsilon_i} \quad i = c, d \quad (2-29)$$

The weighted mixture properties, used in Eqs. (2-27) and (2-28) are calculated as follows (Behzadi et al., 2004):

$$\rho_m = \frac{\alpha_c \rho_c + \alpha_d \rho_d}{\alpha_c + \alpha_d} \quad (2-30)$$

$$k_m = \frac{\alpha_c \rho_c k_c + \alpha_d \rho_d k_d}{\rho_m} \quad (2-31)$$

$$\varepsilon_m = \frac{\alpha_c \rho_c \varepsilon_c + \alpha_d \rho_d \varepsilon_d}{\rho_m} \quad (2-32)$$

$$\mu_m = \frac{(\alpha_c \mu_c + \alpha_d \mu_d C_t^2) \rho_m}{\alpha_c \rho_c + \alpha_d \rho_d C_t^2} \quad (2-33)$$

$$\mathbf{V}_m = \frac{\alpha_c \rho_c \mathbf{V}_c + \alpha_d \rho_d \mathbf{V}_d C_t^2}{\alpha_c \rho_c + \alpha_d \rho_d C_t^2} \quad (2-34)$$

The production of turbulence due to the flow shear is obtained as a sum of each phase production terms:

$$Q = \boldsymbol{\tau}_c^t \cdot \nabla \mathbf{V}_c + \boldsymbol{\tau}_d^t \cdot \nabla \mathbf{V}_d \quad (2-35)$$

The additional production term S in Eq. (2-28) consists of two parts. The first part, S_1 , is the turbulence dissipation by the dispersed phase, and the second, S_2 , is the so-called bubble/droplet induced turbulence. In order to find S_1 , the interfacial force terms in the instantaneous phase momentum balance equation are multiplied by the fluctuating velocity of the corresponding phase and averaged. This way the drag induced dissipation is obtained:

$$S_1^{drag} = -2\gamma_{cd} k_c (C_t - 1)^2 \quad (2-36)$$

Similarly, the virtual mass induced dissipation can also be obtained. It can be written as

$$S_1^{vm} = \alpha_d \rho_c (C_t - 1) F(\mathbf{V}_c, \mathbf{V}_d), \quad (2-37)$$

where F is a function, which depends on the phase velocity. The exact expression for this function is quite lengthy, and for the sake of brevity is not presented. Also, it is shown in the discussion in the following section that this function is not required in the model.

The bubble or droplet induced turbulence S_2 is calculated following Troshko and Hassan (2001b), who using the results of Kataoka and Serizawa (1989) demonstrated that

$$S_2 = (\mathbf{F}_d^{drag} + \mathbf{F}_d^{turb} + \mathbf{F}_d^{vm}) \cdot (\mathbf{V}_d - \mathbf{V}_c) \quad (2-38)$$

The effective thermal conductivity for gas and liquid phases is calculated based on Reynolds' analogy between heat and momentum transfer.

$$\kappa_i^t = \frac{c_{p_i} \mu_i^t}{Pr_t} \quad i = c, d \quad (2-39)$$

2.1.3.2. Turbulence response coefficient

The response coefficient defined in Eq. (2-24) depends on the flow regime. It has been shown experimentally by Garnier et al. (2002) and also reported by Behzadi et al. (2004) that for the bubble volume fractions above 6%, the bubbles and the surrounding liquid have the same values of the fluctuating velocities; that means that the value of the response coefficient is unity. Inside the nozzle, where the liquid phase is continuous, the volume fraction of the discrete phase is expected to be much higher than 6%; therefore, the unity value of the response coefficient for the bubbles can be adopted. Now, we can note that for $C_t = 0$, the virtual mass induced dissipation is also zero (see Eq. (2-38)). On the other hand, when gas is the continuous phase, this dissipation is negligibly small because the density of the gas is significantly lower than the density of the liquid. Therefore, the virtual mass induced dissipation is always negligible, and the exact form of the function F in Eq. (2-37) is indeed not required.

In the flow areas where the gaseous phase is continuous (dispersed droplet flow regime) the Viollet and Simonin (1994) model is applied to determine the turbulence response coefficient. The model is based on the analysis of time scales for the turbulence in the dispersed phase. The response coefficient is calculated as

$$C_t = \sqrt{\frac{\tau_{cd}^t}{\tau_{cd}^F + \tau_{cd}^t}} \quad (2-40)$$

The eddy-droplet interaction time, τ_{cd}^t is obtained from

$$\tau_{cd}^t = \frac{\tau_c^t}{\sqrt{1 + C_\beta \zeta^2}} \quad (2-41)$$

where τ_c^t is the time scale of the energetic turbulent eddies is

$$\tau_c^t = \frac{3}{2} C_\mu \frac{k_c}{\varepsilon_c} \quad (2-42)$$

and the parameter ζ is given by

$$\xi = \frac{|\mathbf{V}_c - \mathbf{V}_d|}{\sqrt{\frac{2}{3}k_c}} \quad (2-43)$$

Comparison with the experimental results of Wells and Stock (1963) led Viollet and Simonin (1994) to find that the coefficient C_β depends on the angle between the velocity of the particulate phase and the relative velocity: when they are parallel $C_\beta = 1.8$, and when they are perpendicular $C_\beta = 0.45$. Therefore, it can be written as a continuous function:

$$C_\beta = 1.8 - 1.35 \left(\frac{\mathbf{V}_d \cdot (\mathbf{V}_c - \mathbf{V}_d)}{|\mathbf{V}_d| |\mathbf{V}_c - \mathbf{V}_d|} \right)^2 \quad (2-44)$$

Finally, the characteristic time of particle entrainment by the fluid motion, τ_{cd}^F , is calculated as

$$\tau_{cd}^F = \frac{4}{3} \frac{\rho_d}{\rho_c} \frac{d_d}{C_D |\mathbf{V}_c - \mathbf{V}_d|} \quad (2-45)$$

2.1.4. Fluctuating motion of particulate phase

Fluctuating motion of the particulate phase is described by the kinetic theory of granular flow (Jenkins and Savage, 1983; Lun et al., 1984; Gidaspow, 1994). The granular temperature, which loosely corresponds to the turbulent kinetic energy of particles, is introduced based on the ideal gas kinetic theory analogy. The conservation equation for the granular temperature (Das et al., 2004) is augmented by source terms arising from the interactions between droplets and particles.

$$\begin{aligned} \frac{3}{2} \left(\frac{\partial}{\partial t} \alpha_p \rho_p \theta + \nabla \cdot \alpha_p \rho_p \theta \mathbf{V}_p \right) = & \left(-P_s \mathbf{I} + \boldsymbol{\tau}_p \right) : \nabla \mathbf{V}_p + \nabla \cdot (k_\theta \nabla \theta) - \Gamma + \\ & + \gamma_{gp} q_{gp} - 3\gamma_{gp} \theta + \left(\dot{m} k_l - \frac{3}{2} \dot{m}_r \theta \right) \end{aligned} \quad (2-46)$$

where the granular temperature diffusion coefficient (Gidaspow, 1992)

$$k_\theta = \frac{75}{192} \frac{\rho_p d_p \sqrt{\pi\theta}}{(1+e)g_0} \left(1 + \frac{6}{5}(1+e)g_0\alpha_p\right)^2 + 2\alpha_p^2 \rho_p d_p g_0 (1+e) \sqrt{\frac{\theta}{\pi}} \quad (2-47)$$

and the granular temperature dissipation is obtained following Jenkins and Savage (1983)

$$\Gamma = 3(1-e^2)\alpha_p^2 \rho_p g_0 \theta \left(\frac{4}{d_p} \sqrt{\frac{\theta}{\pi}} - \nabla \cdot \mathbf{V}_p \right) \quad (2-48)$$

Following Simonin and He (1992) we assume that the gas particle velocity covariance q_{gp} is equal to the fluctuating energy of the particular phase, i.e.

$$q_{gp} = 3\theta \quad (2-49)$$

The closure equations for viscosity and pressure are obtained through the use of this granular temperature. In doing so, we assume that the liquid influence on the inter-particle collisions is small. This should be acceptable, as the liquid content in the bed is generally very small everywhere except in the jet area. In this area, however, the solid loading is minimal and the collision velocity is very high making the collision outcome less dependent on the liquid layer (see Darabi et al., 2009). Even though the presence of liquid film has some influence on the coefficient of restitution, we still use a constant value (0.95) in the model as a first approximation. The solid pressure is modelled according to Lun et al. (1984).

$$P_s = \alpha_p \rho_p \theta (1 + 2g_0\alpha_p(1+e)) \quad (2-50)$$

The solid shear viscosity is calculated with Gidaspow's (1992) model

$$\mu_p = \frac{4}{5} \alpha_p^2 \rho_p d_p g_0 (1+e) \sqrt{\frac{\theta}{\pi}} + \frac{5}{48} \frac{\rho_p d_p \sqrt{\pi\theta}}{(1+e)g_0} \left(1 + \frac{4}{5}(1+e)g_0\alpha_p\right)^2 + \mu_p^{fr} \quad (2-51)$$

where μ_p^{fric} is an additional frictional viscosity (Schaeffer, 1987) to account for tangential stresses at high solid loading. This frictional viscosity term is included only for $\alpha_p > 0.5$. It is obtained as

$$\mu_p^{fric} = \frac{\alpha_p P_s \sin \varphi}{2\sqrt{I_2}} \quad (2-52)$$

where φ is the contact angle and I_2 is the second invariant of the strain rate tensor, defined as

$$I_2 = \frac{1}{6} \left((D_{11} - D_{22})^2 + (D_{22} - D_{33})^2 + (D_{33} - D_{11})^2 + D_{12}^2 + D_{23}^2 + D_{31}^2 \right) \quad (2-53)$$

$$\mathbf{D} = \frac{1}{2} (\nabla \mathbf{V}_p + \nabla \mathbf{V}_p^T)$$

The bulk viscosity is calculated by the Lun et al. (1984) model.

$$\lambda_p = \frac{4}{5} \alpha_p^2 \rho_p d g_0 (1 + e) \sqrt{\frac{\theta}{\pi}} \quad (2-54)$$

The Ma and Ahmadi (1986) correlation that is applicable for both low and high solid volume fractions is used to calculate the radial distribution function.

$$g_0 = 1 + 4\alpha_p \frac{1 + 2.5\alpha_p + 4.5904\alpha_p^2 + 4.515439\alpha_p^2}{\left(1 - \left(\frac{\alpha_p}{\alpha_p^{\max}} \right)^3 \right)^{0.67802}} \quad (2-55)$$

2.1.5. Diameter of bubbles and droplets

The dispersed phase, bubbles or droplets, consists of different size particles. They can undergo break-up or coalescence under certain conditions. There are a number of approaches to represent a variety of particle sizes in the two-phase flow. In this model the assumption of monodispersed particles is made. This way an average particle diameter represents the actual particles within each control volume. The average diameter can change from one point in the flow field to another. The variation of the average particle diameter introduced above is determined by the particle number density conservation. The particle number density is defined as a number of particles per unit volume.

$$n = N/V \quad (2-56)$$

As N can be calculated from the volume occupied by all particles and the volume of one particle with an average diameter, and also using the definition of the volume fraction we have

$$n = \frac{V_d}{V_{lp} V} = \frac{6\alpha_d}{\pi d_d^3} \quad (2-57)$$

The conservation equation for the particle number density was derived by Kolev (2002a).

$$\frac{\partial n}{\partial t} + \nabla \cdot (\mathbf{V}_d n) = \nabla \cdot \left(\frac{\mu_d^t}{\rho_d S c^t} \nabla n \right) + n(f_{br} - f_{coal}) \quad (2-58)$$

It is a convection-diffusion transport equation with the source and sink terms on the right-hand side that are described by means of the frequencies of break-up, f_{br} , and coalescence, f_{coal} . Note that the break-up frequency is defined for a single particle (bubble or droplet). In order to solve this equation, it is necessary to find appropriate models for these frequencies. As there are two distinct flow regimes under consideration, bubbles in liquid and droplets in gas, each of them needs to be analysed separately.

2.1.5.1. Bubble break-up and coalescence

The conditions, generally encountered in such systems, are different from the compressible flow in the nozzle in terms of the lower values of gas volume fraction and lower flow rates. However, most of the models for bubble break-up and coalescence were developed either for individual bubbles or for bubble column reactors. Thus, in order to make progress we extrapolate the use of the existing models to the region of our interest.

Bubble stability is determined by the ratio between the shear forces and the surface tension forces. The shear forces can arise due to the fluctuating motion or to the interfacial drag. The Martinez-Bazan et al. (1999) break-up frequency relationship is used

$$f_{br} = K \frac{\sqrt{(V^{rel})^2 - \frac{12\sigma}{\rho_c d_d}}}{d_d} \quad (2-59)$$

where $K = 0.25$. Depending on the dominant break-up mechanism, V^{rel} can be either the mean value of the turbulent velocity fluctuations, obtained using Kolmogorov's (1949) theory of turbulence, or the difference between the velocities of the continuous and discrete phases.

$$(V^{rel})^2 = \max \left\{ \beta (\varepsilon_c d_d)^{\frac{2}{3}}; (\mathbf{V}_c - \mathbf{V}_d)^2 \right\} \quad (2-60)$$

where $\beta = 8.2$ is the constant given by Batchelor (1956).

Coalescence frequency is the product of the collision frequency, f_{coll} , and coalescence probability, P_{coal} :

$$f_{coal} = f_{coll} P_{coal} \quad (2-61)$$

The collision frequency relationship can be obtained considering the elastic collisions of hard spheres with uniform spatial distribution (see Kolev, 2002b) with the Hibiki and Ishii (1999) proposed modification to take into account the volume reduction due to the presence of the dispersed phase:

$$f_{coal} = \frac{3}{2} \frac{\alpha_d}{(\alpha_d^{\max} - \alpha_d) d_d} V^{rel} \quad (2-62)$$

where α_d^{\max} is the maximum volume fraction of the dispersed phase (bubbles), before the flow regime changes due to the catastrophic phase inversion.

For the collision probability Chesters (1991) model is applied:

$$P_{coal} = \exp\left(-c\sqrt{0.5We_g}\right) \quad (2-63)$$

where We_d is the Weber number defined as:

$$We_g = \frac{\rho_c (\varepsilon_c d_d)^{2/3} d_d}{2\sigma} \quad (2-64)$$

and $c = 0.4$ is the model constant.

2.1.5.2. Droplet break-up and coalescence

Similar to the bubble break-up, the droplet break-up also depends on the balance between the surface stresses, determined by the surface tension σ , and the external stresses that can be different in nature. For the high speed jets, the dynamic forces associated with the relative motion of the droplet and with the fluctuating velocities around the droplet play the dominant role because the viscous effects are relatively small. In this case, the droplet Weber number can be introduced, as the ratio of the shear to surface tension forces:

$$We_d = \frac{\rho_c (V^{rel})^2 d_d}{\sigma} \quad (2-65)$$

Kolmogorov (1949) and Hinze (1955) proposed a Weber number based droplet break-up model. It postulates that if the droplet Weber number is below the critical value, $We_d \leq We_{cr}$, the droplet is stable, and if it is above, $We_d > We_{cr}$, the droplet will break up. Thus, the maximum stable droplet diameter can be found from the critical Weber number:

$$d_d^{st} = \frac{We_{cr} \sigma}{\rho_c (V^{rel})^2} \quad (2-66)$$

Both of these researchers considered only the turbulence induced break-up. The same theory can be extended to the drag induced break-up as well, provided an appropriate value for the relative velocity V^{rel} is used. Kocamustafaogullari et al. (1994) showed that the critical Weber numbers differ depending on the break-up mechanism considered. The researchers obtained the relationship, which connects both critical Weber numbers:

$$We_{cr}^{turb} = k_{We} \left(\frac{\rho_c}{\rho_d} \right)^{\frac{2}{3}} \frac{(\rho_d - \rho_c)}{\rho_d} We_{cr}^{drag} \quad (2-67)$$

where k_{We} is the coefficient, which for the air-water flow at about atmospheric pressure is close to unity. We assume that it is close to unity for other materials as well.

Let us first consider the drag induced break-up. In this case, the relative velocity is the absolute value of the difference between the average velocities of the phases:

$$V^{rel} = |\mathbf{V}_c - \mathbf{V}_d| \quad (2-68)$$

It was found by Brauer (1992) and reported by Kolev (2002b) that the critical Weber number for the drag induced break-up is also Reynolds number-dependent. If the droplet Reynolds number is defined as

$$Re_d = \frac{\rho_c |\mathbf{V}_c - \mathbf{V}_d| d_d}{\mu_c} \quad (2-69)$$

then the dependency correlation takes the following form:

$$We_{cr}^{drag} = \begin{cases} 25, & \text{for } Re_d < 200 \\ 55 \left(\frac{24}{Re_d} + \frac{20.1807}{Re_d^{0.615}} - \frac{16}{Re_d^{0.667}} \right), & \text{for } 200 \leq Re_d < 2000 \\ 5.48, & \text{for } Re_d \geq 2000 \end{cases} \quad (2-70)$$

The critical Weber number criterion determines whether or not the droplet will break up; in addition, it is also required to know how the droplet will break up. In contrast with the bubble break-up, where the bubble most often just splits into two daughter bubbles, there are several fragmentation modes for the droplet break-up. There are some variations between different authors regarding the classifications of the modes, e.g. Kolev (2002b), Lee and Reitz (2001), Shi and Kleinstreuer (2007); however, the general features of the break-up do not change. In this work we will use the Kolev (2002b) classification. The different break-up regimes are summarized in Table 2-1.

Table 2-1. Droplet fragmentation modes classification

Weber number	Fragmentation mode
$We_d \leq 12$	Vibration break-up
$12 < We_d \leq 18$	Bag break-up
$18 < We_d \leq 45$	Bag and stamen break-up
$45 < We_d \leq 350$	Stripping break-up
$We_d > 350$	Catastrophic break-up

Vibration break-up is characterised by droplet oscillation with its natural frequency and its subsequent decomposition into two parts. Bag break-up happens when the droplet is deformed into the hollow semi-spherical shape, and then, when the wall becomes too thin, bursts into droplets of various sizes. Bag and stamen break-up is the variation of the previous mode; the difference is that during the “bag” formation, a column of liquid parallel to the flow is also formed along the axis of the droplet. This column bursts after the “bag.” As the name implies, during the stripping break-up, small droplets are stripped from the surface of the original droplet. Finally, in catastrophic break-up the droplet disintegrates into large fragments, which in turn, instantly break down further.

The time it takes for a droplet to break, the break-up time $\Delta\tau_{br}$, depends on the fragmentation mode. By analysing experimental data, Pilch et al. (1981) developed a correlation for the dimensionless break-up time, $\Delta\tau_{br}^*$, defined as

$$\Delta\tau_{br}^* = \Delta\tau_{br} \frac{|\mathbf{V}_c|}{d_d} \sqrt{\frac{\rho_c}{\rho_d}} \quad (2-71)$$

This correlation connects the break-up time to the droplet Weber number in the following form:

$$\Delta\tau_{br}^* = c(We_d - 12)^m \quad (2-72)$$

where the constants c and m are determined from Table 2 depending on the droplet Weber number.

Table 2-2. Constants in Eq. (2-72)

c	m	Weber number
7	0	$We_d \leq 12$
6	-0.25	$12 < We_d \leq 18$
2.45	0.25	$18 < We_d \leq 45$
14.1	-0.25	$45 < We_d \leq 350$
0.766	0.25	$350 < We_d \leq 2670$
5.5	0	$We_d > 2670$

Evidently, the break-up frequency depends on the break-up time and the fragmentation mode. In the vibration break-up, two new droplets are produced instead of one. Thus, the frequency can be calculated as

$$f_{br} = \frac{1}{\Delta\tau_{br}}, \quad We_d \leq 12 \quad (2-73)$$

For bag, bag and stamen, and stripping break-ups the frequency depends on the number of droplets produced. Unfortunately, the process is not investigated or understood well enough to provide a definite value of this number. Kolev (2002b) reported that it varies from 30 to 110, while Beck and Watkins (2002) assumed the value of 8 for their model. In

Chapter 2. Mathematical model description

the presented model a general approach proposed by Kolev (2002b) is used that does not employ the number of daughter droplets directly. (However, this number can be easily deduced from the model.) The break-up frequency is obtained from the stable droplet diameter (Eq. (2-66)), current droplet diameter, and the break-up time:

$$f_{br} = \frac{\left(\left(\frac{d_d}{d_{st}} \right)^3 - 1 \right)}{\Delta\tau_{br}} \quad (2-74)$$

In addition, to prevent the frequency from reaching unreasonably high values, the maximum number of daughter droplets is limited to 101. Thus, the maximum frequency f_{br}^{\max} is calculated as:

$$f_{br}^{\max} = \frac{100}{\Delta\tau_{br}} \quad (2-75)$$

On the other hand, the number of the resulting droplets cannot be less than two. So, the minimum frequency f_{br}^{\min} can also be obtained.

$$f_{br}^{\min} = \frac{1}{\Delta\tau_{br}} \quad (2-76)$$

Therefore, the following procedure is adopted. If the value obtained in Eq. (2-74) exceeds the maximum calculated by Eq. (2-75) or drops below the minimum calculated by Eq. (2-76), the maximum or minimum values respectively are used in the model. Similar ideas are used to predict the catastrophic break-up frequency. However, no limiting maximum value is used in this case as the number of daughter bubbles can be very large.

In the turbulent break-up the relative velocity is connected to the variation of the fluctuating velocity around the droplet. Using Kolmogorov's (1949) theory, the velocity change over the distance d is

$$V^{rel} = (\varepsilon_c d_d)^{\frac{1}{3}} \quad (2-77)$$

Substituting V^{rel} in Eq. (2-66), one can obtain the relationship for the stable droplet diameter:

$$d_d^{st} = \varepsilon_c^{-0.4} \left(\frac{We_{cr}^{turb} \sigma}{\rho_c} \right)^{0.6} \quad (2-78)$$

The time needed for break-up is estimated according to Kolev (2002b)

$$\Delta\tau_{br}^{turb} = \left(\frac{d_d^2}{\varepsilon_d} \right)^{\frac{1}{3}} \quad (2-79)$$

In order to find the break-up frequency, f_{br}^{turb} , Eqs. (2-74) - (2-76) are used with the stable droplet diameter from Eq. (2-78) and the break-up time from Eq. (2-79).

Finally, knowing the frequencies for the interfacial drag and turbulence induced break-ups, the largest one is assumed to determine the dominant mechanism under the particular flow conditions,

$$f_{br} = \max \{ f_{br}^{drag}; f_{br}^{turb} \} \quad (2-80)$$

and this frequency value is used in Eq. (2-58).

The coalescence frequency for a droplet is obtained as a combination of collision frequency and coalescence probability (see Eq. (2-61)). The collision frequency relationship from Kolev (2002b) is adopted for droplets.

$$f_{coal} = \frac{3}{2} \frac{\alpha_d}{d_d} V_d^{rel} \quad (2-81)$$

where V_d^{rel} is the average relative velocity between two droplets. Note, that as the droplet volume fraction is generally low, there is no additional multiplier in the denominator opposing Eq. (2-62). In line with Kolmogorov's (1949) theory, the change of the droplet fluctuating velocity over a distance d can be approximated as

$$V_d^{rel} = C_{vel} (\varepsilon_d d_d)^{0.333} \quad (2-82)$$

In the above equation, the turbulent kinetic energy dissipation rate of the discrete phase is used and the constant C_{vel} has an order of one. In the present model we propose that its value be determined based on droplet size measurements.

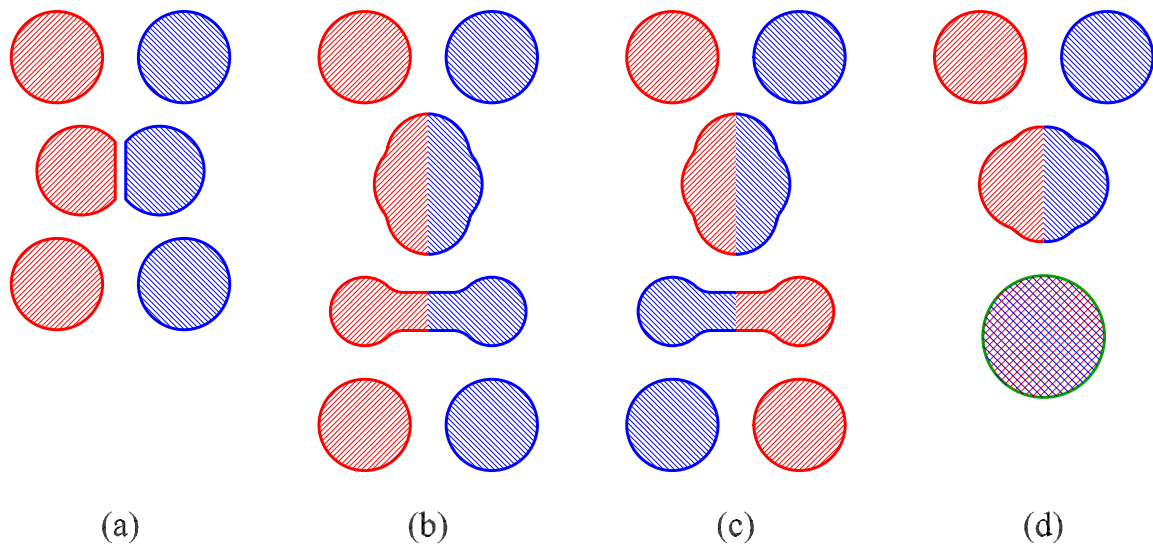


Figure 2-1. Various droplet collision outcomes schematic; (a) – bouncing, (b) – reflective separation, (c) – stretching separation, (d) – coalescence.

There is an extensive amount of experimental work that investigates collisions of two droplets. Ashgriz and Poo (1990) identified three possible collision outcomes. First, the droplets may undergo a reflective separation, i.e. a separation caused by liquid from each droplet changing the direction of their momentum by 180° ; second, they may experience a stretching separation, i.e. a separation caused by liquid from each droplet keeping its original momentum, and third, the droplets may coalesce. These types of collision outcomes are schematically shown in Figure 2-1 (b), (c), and (d) correspondingly. Furthermore, during stretching separations, additional daughter droplet (or droplets) may form either due to the capillary instability of the liquid cylinder connecting two droplets, or by the end pinching caused by liquid inertia. The authors also developed a collision regime map based on the analytical model that marked a boundary between the coalescence and two different separation collision outcomes depending on the Weber number (a ratio of inertial to surface tension forces) and the impact parameter (a sine function of an angle between the line connecting the centres of two droplets and the direction of the relative velocity vector at the moment immediately before the droplet contact). Also, in more recent years, the problem of droplet collision has been studied numerically. Pan and Suga (2005) conducted extensive numerical studies of droplet collisions. They were able to reproduce computationally the collisions that were previously experimentally observed with a high degree of temporal

Chapter 2. Mathematical model description

accuracy. In addition to the three regimes already mentioned, they also investigated a more elusive bouncing outcome, which is analogous to the bouncing of hard spheres that takes place at low Weber numbers (see Figure 2-1 (a)).

Clearly, the phenomenon is extremely complex. Some simplifications are necessary before its implementation into the numerical model. We assume that there are no daughter particles forming during collisions. In effect, this means that we ignore collision-associated break-up. Also, we do not distinguish between stretching and reflecting separations. And, finally, we do not account for the variations of the impact parameter considering all collisions in an average and probabilistic sense. Thus, after colliding the droplets may bounce off, separate, or coalesce. Accordingly, the coalescence probability can be written as

$$P_{coal} = 1 - P_{bounce} - P_{sep} \quad (2-83)$$

The bouncing probability is obtained from the Lasheras et al. (1998) model as a balance between the critical drainage time defined as

$$t_{dr} = \frac{\mu_c}{\rho_d (V_d^{rel})^2} \quad (2-84)$$

And the droplet contact time is

$$t_{con} = \frac{d_d}{V_d^{rel}} \quad (2-85)$$

Basically, by comparing two time scales, we evaluate whether two droplets would stay together long enough for a thin film of gas separating them to break.

$$P_{bounce} = 1 - \exp\left(-\frac{t_{dr}}{t_{con}}\right) \quad (2-86)$$

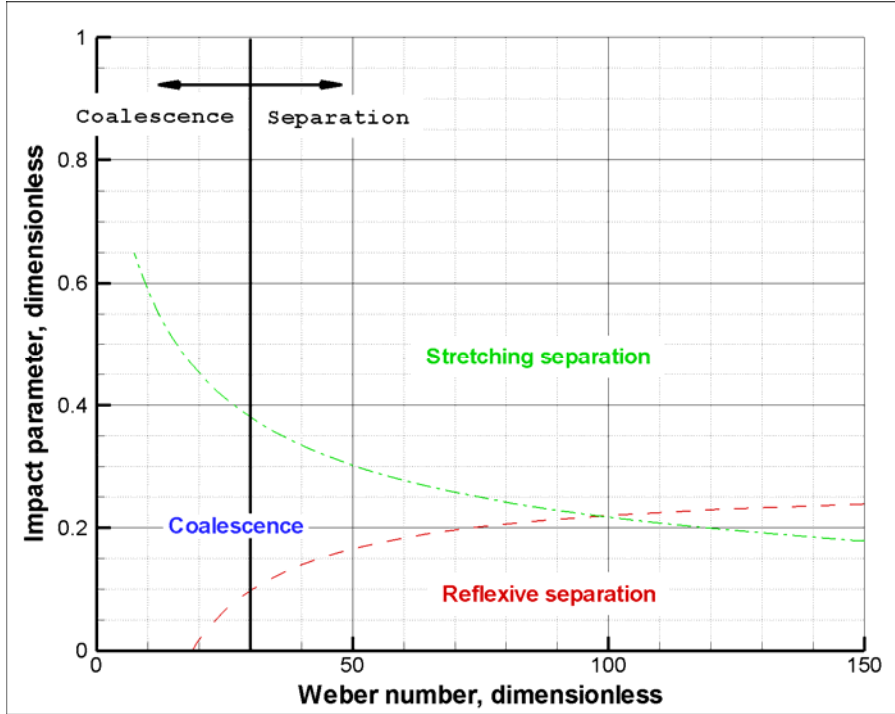


Figure 2-2. Droplet collision regimes after Ashgriz and Poo (1990) and our approximation.

Next, we need to determine the separation probability. As it depends on the Weber number, $We = \rho_d d_d (V_d^{rel})^2 / \sigma$, we can write the probability in a general form

$$P_{sep} = 1 - \exp(-c\sqrt{We}) \quad (2-87)$$

where a constant c has to be determined. Based on the collision outcome maps presented in Ashgriz and Poo (1990) and Pan and Suga (2005), and reproduced in Figure 2-2, we can approximate that below $We = 30$ droplets coalesce, and above it they separate. Assuming that for this number, the probability equals 0.5, we can obtain from Eq. (2-87) that $c \approx 0.127$.

After substitution of Eqs. (2-86) and (2-87) into Eq. (2-83), we obtain

$$P_{coal} = 1 - \exp\left(-\frac{t_{dr}}{t_{con}}\right) + \exp(-0.127\sqrt{We}) \quad (2-88)$$

This equation together with Eq. (2-81) fully determines the droplet coalescence frequency calculated by Eq. (2-61).

2.1.6. Atomization (phase inversion)

As the flow progresses through the nozzle, the gaseous phase expands and at a certain point, which can be located inside or outside the nozzle, the volume fraction of the liquid phase becomes too small to sustain the liquid-continuous flow regime, and the gaseous phase assumes continuity. That is, the flow from the churn-turbulent/dispersed bubble flow regime transits to a dispersed droplet flow regime. This phenomenon is called the phase inversion. It can happen extremely quickly, over a very thin surface, or there can be some transitional area where the parcels of various flow regimes are intertwined in time and space. Clearly, the interfacial interactions during the phase inversion are complex and not well understood; investigating those interactions will constitute by itself a very significant challenge to researchers in the future. Meanwhile, in order to make further progress with the model, it is necessary to introduce a number of assumptions that simplify the problem at the cost of losing details in the representation of the phase inversion. First, we assume that the phase inversion takes place over an infinitely thin surface; such phase inversion is called catastrophic. While there is some work investigating the catastrophic phase inversion for emulsions, e.g. Vaessen et al. (1996), for the oil-water mixture, a comprehensive model for the gas-liquid flows is yet to be developed. Therefore, further assumptions are required. A simplified approach is proposed below that allows the model to switch from one flow regime to another based on intuitive considerations. We assume that the location for the catastrophic phase inversion surface depends only on the local volume fraction values. If all the bubbles were round spheres of the same diameter, then the maximum volume fraction value for the ordered packing is well established and equals 0.74. However, in the high speed compressible flow in the nozzle, the bubbles can be deformed and, most importantly, their distribution is in reality polydispersed, which means that the gaps between the bigger bubbles can be filled with the smaller ones. Santiso and Muller (2002) investigated the packing of the polydispersed mixtures and concluded that the packing limit can reach values above 0.9. Wang et al. (2005) used the value of 0.8 to describe the transition from the churn-turbulent flow regime in the bubble column reactor. In addition, the experimental results of Deichsel and Winter (1990) suggest that for high speed critical flow in pipes, the transition from the churn-turbulent regime is delayed up to a volume fraction of 0.92. Evidently, there is a difference between the critical values of the volume fraction for a free shear flow and for a

Chapter 2. Mathematical model description

pipe flow. However, in the case under consideration, the transition happens in the immediate vicinity of the nozzle exit either upstream (in the nozzle) or downstream (outside the nozzle). Thus, it is more logical to use the pipe value for the description of the phase inversion. Also, an introduction of an additional unknown parameter would make the model application less convenient and create another non-trivial task of defining the extent of the influence of the nozzle wall boundaries downstream of the exit orifice. Therefore, it is assumed that the transition happens as soon as the local value of the gas volume fraction reaches $\alpha_d^{\max} = 0.8$ (80%). As the selection of this value is somewhat arbitrary (only the range is established), some additional studies are presented and discussed later in Section 4.1.3.1.

In order to determine the diameter of the newly formed droplets, it is assumed that the particle number density (or the number of particles) remains the same during the phase inversion. This assumption can be illustrated by a honeycomb structure where the cells represent the bubbles and the nodes represent the new droplets that will be formed when the bubbles simultaneously coalesce, resulting in the catastrophic phase inversion. The increase of the surface area can be estimated as

$$\frac{S_{droplet}}{S_{bubble}} = \left(\frac{\alpha_d^{\max}}{1 - \alpha_d^{\max}} \right)^{\frac{2}{3}} \quad (2-89)$$

This is not a very large value compared with jet atomizers; therefore, the pressure drop across the phase inversion surface, associated with the energy loss due to the increase of the surface area, can be ignored.

It is assumed that other phase parameters, such as the velocity and the turbulence parameters do not change as the flow passes through the phase inversion plane.

2.1.7. Diameter of particulate phase

Size distribution of the particular phase is also represented by the average diameter. However, instead of solving a differential equation, the diameter value is determined from a fixed core diameter and an additional thickness of the liquid film that can be obtained through its volume fraction.

$$d_p = d_s \left(x_s \frac{\rho_p}{\rho_s} \right)^{\frac{1}{3}} \quad (2-90)$$

2.1.8. Interactions between droplets and particles

As the liquid spray is injected into the fluidized bed, droplets inevitably collide with solid particles. The interactions between the particulate and liquid phases are treated as mass and/or momentum transfer. We assume that the collisions between the liquid droplets and solid particles are inelastic. The number of collisions per unit volume and time can be calculated (Kolev, 2002a)

$$\dot{n}_{coll} = n_p n_l \frac{\pi}{4} \left(\frac{d_p + d_l}{2} \right)^2 |\mathbf{V}_l - \mathbf{V}_p| \quad (2-91)$$

where the particle number density for the particulate phase n_p is calculated in a similar way as for the liquid phase, see Eq. (2-57), but using the particle diameter instead of the droplet one. The total mass transferred to the particular phase can then be obtained.

$$\dot{m} = m_{drop} \dot{n}_{coll} \quad (2-92)$$

As the single droplet mass is $m_{drop} = \pi d_l^3 \rho_l / 6$, the resulting mass transfer can be obtained from Eqs. (2-57), (2-91), and (2-92).

$$\dot{m} = \frac{3}{2} \frac{\alpha_p \alpha_l}{d_p^3} \left(\frac{d_p + d_l}{2} \right)^2 \rho_l |\mathbf{V}_l - \mathbf{V}_p| \quad (2-93)$$

We assume that a droplet-particle collision can produce two outcomes: either liquid sticks to the particle, or it separates or rebounds. Also, part of the liquid may stick and the rest separates. Thus, the total mass can be split into two parts

$$\dot{m} = \dot{m}_{st} + \dot{m}_r \quad (2-94)$$

In order to determine the ratio at which the mass is split, it is better to rely on some empirical evidence. Even though it is possible to construct a model based on some general considerations, such approach would still require the knowledge of an adjustable parameter

that has to be obtained from indirect comparison with experiments. Thus, we have to look for direct experimental measurements that eliminate the need for model adjustment. While there are many published works that experimentally investigate collision outcomes for droplets, the droplet-solid particle collisions have generated much less interest in experimental studies so far. Nevertheless, some studies were done by Dubrovskiy et al. (1984) and Podvysotskiy and Dubrovskiy (1986) to investigate the mass transfer when droplets collide with a spherical particle. They obtained correlations for the stickiness ratio ($\Phi = \dot{m}_{st}/\dot{m}$) in two forms: average and depending on the impact angle. In our model we use the average form, as we do not simulate the impact angle.

$$\Phi = \begin{cases} 1 - 0.35B, & B < 2.86 \\ 0, & B \geq 2.86 \end{cases} \quad (2-95)$$

$$B = \frac{Re^{0.37}}{Lp^{0.1}} \sqrt{\frac{d_l}{d_s}}; \quad Re = \frac{\rho_l |\mathbf{V}_l - \mathbf{V}_p| d_l}{\mu_l}; \quad Lp = \frac{\sigma \rho_l d_l}{\mu_l^2} \quad (2-96)$$

While the actual values of the diameters at which the measurements were conducted are about an order of magnitude larger than the ones encountered in our problem, their ratio and the dimensionless numbers used in the correlation are about the same order of magnitude. In the absence of other reliable data, the extrapolation of the applicability region seems to be the best option. In addition, there is a time-dependency issue: clearly, as a particle continues to be bombarded by droplets, the ratio cannot be constant (otherwise the liquid layer would grow to infinity). Yet, keeping in mind that solid particles are removed from the jet zone fairly quickly by convection, we chose to ignore this problem in the present study.

Knowing the mass of droplets that sticks to and rebounds from solid particles, we can determine the source terms in the conservation equations. Assuming non-elastic collisions, the colliding droplets transfer their momentum to the particular phase ($\dot{m}\mathbf{V}_l$), and the particular phase loses some of its newly gained momentum with rebound droplets ($\dot{m}_r\mathbf{V}_p$) (see Eq. (2-2)). Thus, the collision results in the exchange of mass and momentum or of the momentum only. Similar exchange takes place for the enthalpy and fluctuating components

of the velocity that is transferred with the mass, i.e. turbulence (Eq. (2-27)) and granular temperature (Eq. (2-46)).

2.1.9. Heat transfer within a particulate phase

The particulate phase consists of two parts: the solid core and the liquid film. Both components are considered together from the mechanical motion point of view, i.e. they have the same velocity and granular temperature. However, it would not be correct to extend a similar treatment to the heat transfer. As droplets generally have a lower temperature than solid core particles, there would be some heat exchange following the collision. While the temperature of liquid film can be considered uniform because the liquid is well mixed due to multiple collisions and rebounds, the same cannot be said about the core itself because the heat conduction (the only mode available) is not an instantaneous process. The Fourier number ($Fo = \alpha_s t / d_s^2$) is expected to be about 0.1 in the vicinity of the nozzle; this means that the heat distribution inside the solid core cannot be considered uniform. Therefore, we allow the liquid film and the solid core to have different temperatures and model the heat transfer between them.

As mentioned above, we can assume the liquid layer temperature uniform throughout the film, and the solid core is characterized by an average temperature (T_s) and a presence of temperature gradients. For a solid sphere we can write a heat conduction equation

$$\frac{1}{r} \frac{\partial^2}{\partial r^2} (rT) = \frac{1}{\alpha} \frac{\partial T}{\partial t} \quad (2-97)$$

The spatial boundary conditions reflecting the liquid film temperature on the surface and the symmetry at centre are as follows

$$T|_{r=r_s} = T_l; \quad \left. \frac{\partial T}{\partial r} \right|_{r=0} = 0 \quad (2-98)$$

After separation of variables and application of boundary conditions, the solution, which is a transient radial temperature distribution, is obtained in a straightforward manner

$$T = T_l + \sum_{n=1}^{\infty} C_0(t_0) \frac{(-1)^{n+1}}{nr} \sin\left(n\pi \frac{r}{r_s}\right) \exp(-n^2\pi^2 Fo) \quad (2-99)$$

where $C(t_0)$ is a constant to be determined by initial conditions. Let us consider the temperature distribution at a given time. First, we note that for $Fo > 0.1$, the second term of the sum is less than 3% of the first one. Therefore, we can simplify the equation by retaining only the first term. Thus, the temperature can be written as

$$T = T_l + \frac{C}{r} \sin\left(\pi \frac{r}{r_s}\right) \quad (2-100)$$

where C is a time and initial conditions dependent constant. We are going to connect this constant with the average solid core temperature at the same time. By definition, the average temperature is

$$T_s = \frac{1}{V} \iiint_V T dV \quad (2-101)$$

Substituting T from Eq. (2-100) and taking a volume integral, we obtain

$$\iiint_V T dV = \int_0^{r_s} \left[T_l + \frac{C}{r} \sin\left(\pi \frac{r}{r_s}\right) \right] 4\pi r^2 dr = 4\pi r_s^2 \left(\frac{T_l r_s}{3} + \frac{C}{\pi} \right) \quad (2-102)$$

Next, substituting again into Eq. (2-101) together with the expression for the volume of sphere, we can determine C

$$C = \frac{\pi r_s}{3} (T_s - T_l) \quad (2-103)$$

Therefore, the temperature distribution (Eq. (2-100)) becomes

$$T = T_l + \frac{\pi r_s}{3r} (T_s - T_l) \sin\left(\pi \frac{r}{r_s}\right) \quad (2-104)$$

Now, we can determine the heat flux at the surface of the sphere by differentiating the temperature distribution

$$q = -\kappa_s A \frac{\partial T}{\partial r} \Big|_{r=r_s} = \frac{4}{3} \kappa_s \pi^3 r_s (T_s - T_l) \quad (2-105)$$

This heat flux is for a single particle; to find a total value, we use the particle number density (Eq. (2-57)). Finally, the heat transfer coefficient between the solid core and the liquid layer can be obtained after some basic algebra and using the diameter instead of the radius.

$$h_{sf} = \frac{qn_p}{(T_s - T_l)} = \frac{4\pi^2 \alpha_p \kappa_s d_s}{d_p^3} \quad (2-106)$$

This coefficient is used in Eqs. (2-6) and (2-7). Note that the enthalpy transfer associated with droplet-particle collisions occurring as described for other quantities in the previous section takes place between the droplets and the liquid layer part of the particulate phase.

2.1.10. Moisture and heat transport in the particulate phase

The equations of heat and mass transfer for the components of the particular phase (Eqs. (2-7) and (2-11)), i.e. for the solid core and liquid film, require the knowledge of the mass diffusion coefficient and thermal conductivity. These parameters represent the transport of the moisture or heat within the particular phase. As the physics for both moisture and heat diffusion is essentially the same, we consider the moisture spreading first, and then present analogous relationships for thermal conductivity.

There are two mechanisms of liquid spreading in the fluidized bed: first, by random motion of particles, and second, by liquid exchange during collisions, i.e. $D_p = D_p^{kin} + D_p^{coll}$. The first mechanism is well investigated as it pertains not only to the liquid layer, but to any scalar associated with the particles. Hsiau and Hunt (1993) derived a relation that is widely used to model such diffusion.

$$D_p^{kin} = \frac{d_p \rho_p \sqrt{\pi \theta}}{8(1+e)g_0} \quad (2-107)$$

The second mechanism is much less studied. Here, we present a rigorous approach to derive a collisional diffusion coefficient.

Chapter 2. Mathematical model description

Let us first consider liquid transport during a single collision of two particles with slightly different liquid volume fractions. The first particle has a liquid mass fraction $x - \delta x/2$, and the second - $x + \delta x/2$ (note that we do not include the subscript 'f' to avoid cluttering). By definition, the liquid mass of the particle with the mass fraction x is

$$m_x = \frac{\pi}{6} \rho_p d_p^3 x \quad (2-108)$$

However, variables ρ_p and d_p also depend on the liquid mass fraction. To obtain a functional dependence of the liquid mass from the volume fraction, we involve relationships connecting properties of the particulate phase and its components (Eqs. (2-3) and (2-90)). Finally, we get

$$m_x = \frac{\pi}{6} \rho_s d_s^3 \frac{x}{1-x} \quad (2-109)$$

We assume that after the collision, the particles would end up with equal mass of the film. Therefore, we can calculate the mass transferred during a collision

$$\delta m_x = \frac{1}{2} (m_{x+\delta x/2} - m_{x-\delta x/2}) = \frac{\pi}{12} \rho_s d_s^3 \left(\frac{x + \delta x/2}{1 - x - \delta x/2} - \frac{x - \delta x/2}{1 - x + \delta x/2} \right) \quad (2-110)$$

As δx is small, the expression in brackets can be simplified by keeping only first order terms

$$\delta m_x = \frac{\pi}{12} \rho_s d_s^3 \frac{\delta x}{(1-x)^2} \quad (2-111)$$

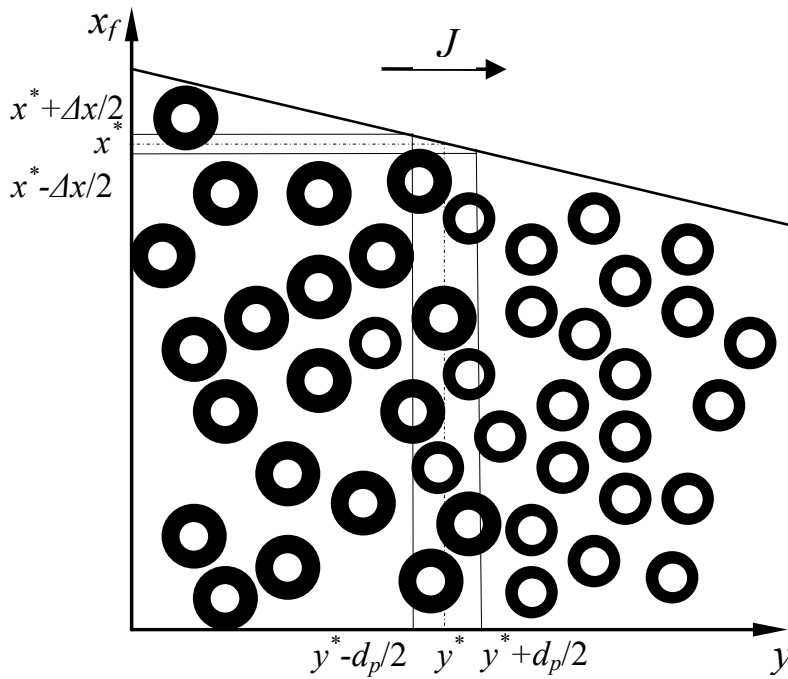


Figure 2-3. Solid particles with a gradient of liquid film mass fraction.

Let us now consider an assembly of particles that in the y -direction have a certain gradient of liquid film mass fraction as shown in Figure 2-3. In all other directions, the distribution is uniform. Consider a plane, normal to the y -axis, at y^* . The mass fraction of the liquid layer at the plane location would be x^* . We can generally write the liquid mass flow rate through this plane as

$$J = D_p^{coll} \frac{\partial x_f}{\partial y} \quad (2-112)$$

The centres of particles, collisions of which result in mass transfer through the defined plane can be located in the interval from $y^* - d_p/2$ to $y^* + d_p/2$. In this interval, the liquid mass fraction varies from $x^* - \Delta x/2$ to $x^* + \Delta x/2$. Depending on the angle ψ between the line connecting the centres of colliding particles and the y -axis, the difference in liquid content would vary according to the following

$$\delta x = \Delta x \cos \psi \quad (2-113)$$

At the same time, the distance that the liquid travels from one particle to another in the y -direction can be determined as

$$s = d_p \cos \psi \quad (2-114)$$

The number of particle collisions per unit volume can be calculated according to the kinetic theory (see Goldschmidt et al., 2002)

$$N = 4n_p^2 d_p^2 g_0 \sqrt{\pi \theta} \quad (2-115)$$

Assuming that all collision directions are equally possible, we can integrate for all collisions to obtain the total mass flux transported through the plane.

$$J = \int_{-\pi/2}^{\pi/2} \frac{N}{\pi} \cdot \delta m_x \cdot s \cdot d\psi \quad (2-116)$$

After substitution of Eqs. (2-57), (2-111), (2-113) - (2-115) and subsequent integration, we arrive at

$$J = \frac{\pi}{6} n_p^2 d_p^3 g_0 \sqrt{\pi \theta} \rho_s d_s^3 \frac{\Delta x}{(1-x)^2} \quad (2-117)$$

Using Eqs. (2-3, (2-57) and (2-90), we return to the particulate phase variables

$$J = \frac{6\alpha_p^2 g_0 \rho_p \Delta x}{(1-x)} \sqrt{\frac{\theta}{\pi}} \quad (2-118)$$

Next, by comparing Eq. (2-118) with Eq. (2-112) and keeping in mind that $dx_f/dy \approx \Delta x/d_p$, we obtain the relationship for the collisional diffusion.

$$D_p^{coll} = \frac{6\alpha_p^2 g_0 \rho_p d_p}{(1-x_f)} \sqrt{\frac{\theta}{\pi}} \quad (2-119)$$

The same argument applies to the heat diffusion in the particulate phase – after all, the heat is transported by liquid. However, while the liquid film has both the kinetic and collisional components, the solid core has only the kinetic component. The kinetic thermal conductivity is determined by

$$\kappa_j^{kin} = \frac{d_p \rho_p c_{pj} \sqrt{\pi \theta}}{8(1+e)g_0} \quad j = s, f \quad (2-120)$$

And the collisional thermal conductivity is analogously

$$\kappa_f^{coll} = \frac{3\alpha_p^2 g_0 \rho_p d_p c_{p_f}}{(1-x_f)} \sqrt{\frac{\theta}{\pi}} \quad (2-121)$$

2.1.11. Interfacial heat transfer

Interfacial heat transfer between continuous and dispersed phases is obtained through the use of the Nusselt number correlation by Ranz and Marshall (1952).

$$Nu = 2 + 0.6Re_p^{0.5} Pr^{0.33} \quad (2-122)$$

where

$$Re_p = \frac{\rho_c |\mathbf{V}_c - \mathbf{V}_d| d_d}{\mu_c}; \quad Pr = \frac{c_{p_c} \mu_c}{\kappa_c} \quad (2-123)$$

The heat transfer coefficient is then found as

$$h_{cd} = \frac{6Nu \alpha_c \alpha_d \kappa_c}{d_d^2} \quad (2-124)$$

2.1.12. Interfacial and boundary conditions

At the interface between gaseous and liquid phases the normal stresses are balanced

$$(-P_d + \tau_d^n) - (-P_c + \tau_c^n) = \frac{4\sigma}{d_d} \quad (2-125)$$

It is assumed that there is no pressure jump between gaseous and particulate phases

$$P_p = P_g \quad (2-126)$$

Constant flow rates of the gas and the liquid are assumed at the inlet. The inlet velocities are assumed to be the same for both phases. These velocities and the volume fractions are calculated during the solution procedure based on the pressure, which is extrapolated from the inside of the domain. The turbulence parameters (k and ε) are calculated based on the velocity and the value of the turbulence intensity, which is estimated from the relationship extended from the single phase theory as follows;

$$I = 0.16(\text{Re}_m)^{\frac{1}{8}}; \quad \text{Re}_m = \frac{\rho_m |\mathbf{V}_m| D}{\mu_m} \quad (2-127)$$

The constant values of the temperature and of the average bubble diameter are set across the inlet. The inlet pressure, velocities, and volume fractions are found as part of the solution.

Other boundary conditions are specific to the cases studied, i.e. single nozzle, nozzle issuing in open air, and nozzle in the fluidized bed, and will be discussed in the corresponding sections.

2.1.12.1. A wall function model for multiphase flows

At the walls, a non-slip condition is assumed for liquid and gaseous phases. It is well known that the presence of the bubbles in the boundary layer reduces the drag between the liquid and the wall, e.g. Sanders et al. (2006). Troshko and Hassan (2001a) developed the wall functions for the two-phase flow boundary layers, but their model is only valid for bubble volume fractions less than 10%, which is far below the levels encountered in the nozzle (40-85%). Politano et al. (2003) proposed corrections to the wall functions to account for the presence of the second phase; however, in the derivations they ignored turbulence in the dispersed phase. We obtain the relationships for wall functions for the multiphase flow by following a procedure similar to that used for the single phase flow (Wilcox, 1998).

We extend a popular wall functions approach for turbulent flows near walls to the multiphase flow. In the layer near the wall the momentum equations for continuous and dispersed phases (Eq. (2-2)) can be simplified as the convective and pressure gradient terms are relatively small. In addition, the turbulent diffusion is much higher than the molecular diffusion. We also assume that the interfacial momentum exchange term can be neglected.

$$\frac{\partial}{\partial y} \left(C_\mu \alpha_i \rho_i \frac{k_m}{\varepsilon_m} \frac{\partial U_i}{\partial y} \right) = 0 \quad i = g, l \quad (2-128)$$

Analogously, the turbulence model (Eqs. (2-27) and (2-28)) can be simplified into the following form

$$\frac{\partial}{\partial y} \left(\frac{C_\mu}{\sigma_k} \rho_m \frac{k_m^2}{\varepsilon_m} \frac{\partial k_m}{\partial y} \right) + C_\mu \alpha_l \rho_l \frac{k_m^2}{\varepsilon_m} \left(\frac{\partial U_l}{\partial y} \right)^2 + C_\mu \alpha_g \rho_g \frac{k_m^2}{\varepsilon_m} \left(\frac{\partial U_g}{\partial y} \right)^2 - \varepsilon_m \rho_m = 0 \quad (2-129)$$

Chapter 2. Mathematical model description

$$\frac{\partial}{\partial y} \left(\frac{C_\mu}{\sigma_\varepsilon} \rho_m \frac{k_m^2}{\varepsilon_m} \frac{\partial \varepsilon_m}{\partial y} \right) + C_{\varepsilon 1} C_\mu \alpha_l \rho_l k_m \left(\frac{\partial U_l}{\partial y} \right)^2 + C_{\varepsilon 1} C_\mu \alpha_g \rho_g k_m \left(\frac{\partial U_g}{\partial y} \right)^2 - C_{\varepsilon 2} \rho_m \frac{\varepsilon_m^2}{k_m} = 0 \quad (2-130)$$

Note that the turbulence generation due to the presence of the second phase is omitted from the equations.

Let us assume that k does not depend on y , then from Eq. (2-129)

$$C_\mu \frac{k_m^2}{\varepsilon_m} \left(\alpha_l \rho_l \left(\frac{\partial U_l}{\partial y} \right)^2 + \alpha_g \rho_g \left(\frac{\partial U_g}{\partial y} \right)^2 \right) = \varepsilon_m \rho_m \quad (2-131)$$

Integrating Eq. (2-128) and defining $u_{i\tau} = \sqrt{\tau_{iw}/\rho_i \alpha_i}$ for $i = g, l$ we obtain

$$\frac{\partial U_i}{\partial y} = \frac{u_{i\tau}^2}{C_\mu} \frac{\varepsilon_m}{k_m^2} \quad i = l, g \quad (2-132)$$

From Eqs. (2-131) and (2-132), it follows that

$$C_\mu \frac{k_m^2}{\varepsilon_m} \left(\alpha_l \rho_l \frac{u_{l\tau}^4}{C_\mu^2} \frac{\varepsilon_m^2}{k_m^2} + \alpha_g \rho_g \frac{u_{g\tau}^4}{C_\mu^2} \frac{\varepsilon_m^2}{k_m^2} \right) = \varepsilon_m \rho_m \quad (2-133)$$

then

$$k_m = \sqrt{\frac{\sum_{i=g,l} \alpha_i \rho_i u_{i\tau}^4}{C_\mu \rho_m}} \quad (2-134)$$

After introducing a parameter ζ

$$\zeta = \sqrt[4]{\frac{\sum_{i=g,l} \alpha_i \rho_i u_{i\tau}^4}{\sum_{i=g,l} \alpha_i \rho_i}} \quad (2-135)$$

Eq. (2-134) can be written as

$$k_m = \frac{\zeta^2}{\sqrt{C_\mu}} \quad (2-136)$$

After substitution of Eq. (2-131) into Eq. (2-130), one can obtain

$$\frac{\partial}{\partial y} \left(\frac{C_\mu}{\sigma_\varepsilon} \rho_m \frac{k_m^2}{\varepsilon_m} \frac{\partial \varepsilon}{\partial y} \right) = (C_{\varepsilon 2} - C_{\varepsilon 1}) \frac{\varepsilon_m^2}{k_m} \rho_m \quad (2-137)$$

Making use of Eq. (2-136) and rearranging Eq. (2-137) produces

$$\frac{1}{\varepsilon_m^2} \frac{\partial}{\partial y} \left(\frac{1}{\varepsilon_m} \frac{\partial \varepsilon_m}{\partial y} \right) = \frac{\sigma_\varepsilon (C_{\varepsilon 2} - C_{\varepsilon 1}) \sqrt{C_\mu}}{\zeta^6} \quad (2-138)$$

Let us look for a solution to Eq. (2-138) in a form $\varepsilon_m = Ay^n$. The equation would then change to:

$$-\frac{n}{A^2 y^{2n+2}} = \frac{\sigma_\varepsilon (C_{\varepsilon 2} - C_{\varepsilon 1}) \sqrt{C_\mu}}{\zeta^6} \quad (2-139)$$

As the right-hand side does not depend on y , n has to equal -1. After that, A can be calculated from Eq. (2-139) and an epsilon equation is obtained.

$$\varepsilon_m = \frac{\zeta^3}{\kappa y} \quad (2-140)$$

where

$$\kappa^2 = \sigma_\varepsilon (C_{\varepsilon 2} - C_{\varepsilon 1}) \sqrt{C_\mu} \quad (2-141)$$

Next, Eqs. (2-140) and (2-136) are substituted to Eq. (2-132) to get

$$\frac{\partial U_i}{\partial y} = \frac{u_{i\tau}^2}{\zeta \kappa y} \quad i = g, l \quad (2-142)$$

Finally, Eq (2-142) is integrated to obtain the logarithmic velocity profile

$$U_i = \frac{u_{i\tau}^2}{\zeta \kappa} \ln(y) + C \quad i = g, l \quad (2-143)$$

The shear stress at the wall is calculated as

$$\tau_{iw} = u_{i\tau}^2 \rho_i \alpha_i \quad i = g, l \quad (2-144)$$

2.1.12.2. Wall conditions for the particulate phase

For the particulate phase at walls, partial slip conditions proposed by Sinclair and Jackson (1989) are adopted. The shear stress near the wall for the solid phase is calculated as

$$\mu_p \left. \frac{\partial \mathbf{V}_p}{\partial n} \right|_{wall} = - \frac{\varphi \sqrt{3\theta} \pi \alpha_p \rho_p g_0}{6\alpha_p^{\max}} \left| \mathbf{V}_p \right| \quad (2-145)$$

where φ is the specularity coefficient that is assumed to be equal to 0.05. The flux of the granular temperature near the wall can be evaluated as

$$k_\theta \left. \frac{\partial \theta}{\partial n} \right|_{wall} = \frac{\sqrt{3}\theta^{\frac{3}{2}} \pi \alpha_p \rho_p g_0 (1 - e_w)}{4\alpha_p^{\max}} \left| \mathbf{V}_p \right| \quad (2-146)$$

2.2. Model of particle attrition by high speed gas jet in fluidized bed

In order to describe gas jet injection into a fluidized bed, an Eulerian multi-fluid model is utilized together with a kinetic theory of granular flow (KTGF) used to close equations for the particulate phase. The choice of the Eulerian treatment of the solid phase over the more accurate Lagrangian Discrete Element Model (DEM) is dictated by the number of solid particles encountered in a typical application. Even in a fairly small experimental set-up considered in Section 7.1, this number is more than 3 million, which is well above any practical possibility of applying DEM at the present time. Instead of considering the particle size distribution with the full population balance approach, an average diameter that can vary throughout the flow field represents all sizes of particles in each local area. In essence, it is the population balance with only one bin of particles.

In this model, some of the equations are shared with the jet-bed interaction model described in Section 2.1. In most of the cases, we repeat them here for complete model presentation.

2.2.1. Mass, momentum and energy balance

The conservation equations are obtained by ensemble averaging of the Navier-Stokes equations (e.g. Drew and Passman, 1999; Zhang and Prosperetti, 1994) in the same manner as Eqs. (2-1) and (2-2). The mass and momentum conservation can be written for gas (g) and solid particles (s) phases as

$$\frac{\partial}{\partial t} \alpha_i \rho_i + \nabla \cdot \alpha_i \rho_i \mathbf{V}_i = 0 \quad i = g, s \quad (2-147)$$

$$\frac{\partial}{\partial t} \alpha_i \rho_i \mathbf{V}_i + \nabla \cdot \alpha_i \rho_i \mathbf{V}_i \mathbf{V}_i = \nabla \cdot \boldsymbol{\tau}_i - \alpha_i \nabla P - \delta_{is} \nabla P_s + \rho_i \mathbf{g} + \mathbf{F}_i \quad i = g, s \quad (2-148)$$

In the above equations, it is assumed that the pressure is shared between the phases. The stress tensor of the gaseous phase consists of the laminar and turbulent parts with the latter being evaluated with the Boussinesq approximation

$$\boldsymbol{\tau}_g = \alpha_g \left(\mu_g + \mu_g^t \right) \left(\nabla \mathbf{V}_g + \nabla \mathbf{V}_g^T \right) - \frac{2}{3} \mathbf{I} \nabla \mathbf{V}_g - \frac{2}{3} \alpha_g \rho_g k_g \mathbf{I} \quad (2-149)$$

The stress tensor of the solid phase arises due to the fluctuating motion of solid particles, and is written in a form similar to the gaseous phase.

$$\boldsymbol{\tau}_s = \alpha_s \left(\mu_s \left(\nabla \mathbf{V}_s + \nabla \mathbf{V}_s^T \right) + \left(\lambda_s - \frac{2}{3} \mu_s \right) \mathbf{I} \nabla \mathbf{V}_s \right) \quad (2-150)$$

Next, the energy conservation equation is written for the gaseous phase

$$\frac{\partial}{\partial t} \alpha_g \rho_g H_g + \nabla \cdot \alpha_g \rho_g \mathbf{V}_g H_g = \alpha_g \frac{\partial p}{\partial t} - \nabla \cdot \kappa_g \nabla T_g + h(T_s - T_g) + \boldsymbol{\tau}_g : \nabla \mathbf{V}_g \quad (2-151)$$

And for the solid phase

$$\frac{\partial}{\partial t} \alpha_s \rho_s H_s + \nabla \cdot \alpha_s \rho_s \mathbf{V}_s H_s = \alpha_s \frac{\partial p}{\partial t} - \nabla \cdot \kappa_s \nabla T_s + h(T_g - T_s) \quad (2-152)$$

In the above equations the enthalpy H is defined differently for gas and solid phases

$$H_g = c_{p_g} T_g + \frac{\mathbf{V}_g^2}{2} + k_g \quad (2-153)$$

$$H_s = c_{p_s} T_s \quad (2-154)$$

In order to connect the gas density with the pressure, an ideal gas equation of state is applied.

$$P_g = \frac{\rho_g R T_g}{M_g} \quad (2-155)$$

Evidently, the above equations by themselves are not sufficient for simulating the flow.

Therefore, a number of sub-models describing constitutive equations for unknown variables are required to close the model.

2.2.2. Interfacial forces

The interfacial drag force between the particulate and gaseous phases is modelled by the Gidaspow (1992) approach.

$$\mathbf{F}_s = \gamma(\mathbf{V}_g - \mathbf{V}_s); \quad \mathbf{F}_g = -\mathbf{F}_s \quad (2-156)$$

$$\left\{ \begin{array}{l} \text{if } \alpha_s \geq 0.2 \quad \gamma = 150 \frac{\alpha_s^2}{\alpha_g} \frac{\mu_g}{d^2} + 1.75 \frac{\alpha_s \rho_g}{d} |\mathbf{V}_g - \mathbf{V}_s| \\ \text{if } \alpha_s < 0.2 \quad \gamma = \frac{3}{4} C_D \frac{\alpha_s \alpha_g \rho_g}{d} \alpha_g^{-2.65} |\mathbf{V}_g - \mathbf{V}_s| \end{array} \right. \quad (2-157)$$

$$C_D = \begin{cases} \frac{24(1 + 0.15 \text{Re}^{0.687})}{\text{Re}} & \text{Re} \leq 1000 \\ 0.44 & \text{Re} > 1000 \end{cases} \quad \text{Re} = \frac{\rho_g |\mathbf{V}_g - \mathbf{V}_s| d}{\mu_g}$$

Note that other interfacial forces, such as the lift, virtual mass, and turbulent dispersion are ignored because the density of the continuous phase (gas) is much smaller than the one of the discrete phase (solid particles). The Faxén and the Basset forces are also neglected.

2.2.3. Fluctuating motion of gaseous phase

The fluctuating motion (turbulence) in the gaseous phase is modelled with the $k-\varepsilon$ model modified for multiphase and high speed flows. Taking into account the volume taken by the particulate phase (Das et al., 2004), the equations for the turbulent kinetic energy and its dissipation rate can be written as

$$\begin{aligned} \frac{\partial}{\partial t} \alpha_g \rho_g k + \nabla \cdot \alpha_g \rho_g \mathbf{V}_g k = \nabla \cdot \left(\mu_g + \frac{\mu_g^t}{\sigma_k} \right) \nabla k + \boldsymbol{\tau}_g : \nabla \mathbf{V}_g - \alpha_g \rho_g \varepsilon \\ - \gamma(2k - q_{gs}) - 2\alpha_g \rho_g \varepsilon \frac{k}{a^2} \end{aligned} \quad (2-158)$$

$$\begin{aligned} \frac{\partial}{\partial t} \alpha_g \rho_g \varepsilon + \nabla \cdot \alpha_g \rho_g \mathbf{V}_g \varepsilon = \nabla \cdot \left(\mu_g + \frac{\mu_g^t}{\sigma_\varepsilon} \right) \nabla \varepsilon \\ + \frac{\varepsilon}{k} \left(C_{1\varepsilon} \boldsymbol{\tau}_g : \nabla \mathbf{V}_g - C_{2\varepsilon} \alpha_g \rho_g \varepsilon - C_{3\varepsilon} \gamma(2k - q_{gs}) \right) \end{aligned} \quad (2-159)$$

The term $\gamma(2k - q_{gs})$ represents the transfer of the fluctuating energy between the phases, where q_{gs} is the fluid-particle velocity covariance. While it is possible to formulate a differential equation for this covariance (see Das et al., 2004), it would still require some empirical closures. A simplified approach proposed by Simonin and He (1992) is utilized instead. They assumed that for two-phase flows where the density of the particulate phase is much larger than the density of the continuous phase, q_{gs} equals the fluctuating energy of the particulate phase. The latter can be expressed through the granular temperature, which is introduced in Section 2.2.4. Therefore,

$$q_{gs} = 3\theta \quad (2-160)$$

The last term in Eq. (2-158) is an additional dilatational dissipation proposed by Sarkar et al. (1991) for high speed flows (a is the speed of sound). While there is some controversy surrounding this addition, it was shown by Birkby and Page (2001) that this correction improves the predicted results for the high speed jet flows. In addition to the dissipational term, Sarkar et al. (1991) scaling for the turbulent viscosity is also implemented.

$$\mu_g^t = C_\mu \rho_g \frac{k^2}{\left(1 + \frac{2k}{a^2}\right) \varepsilon} \quad (2-161)$$

2.2.4. Fluctuating motion of solid particles

Particle-particle interactions are described with the Kinetic Theory of Granular Flow (KTGF), which is an extension of the kinetic theory of dense gases by Chapman and Cowling

Chapter 2. Mathematical model description

(1970) to the ensemble of solid particles. The KTGF was developed in the early 1980s by Savage and Jeffrey (1981) and Jenkins and Savage (1983). Its use became widespread after the work of Gidaspow (1994). The theory is based on the analogy between the random motion of the molecules and solid particles. Similar to the thermodynamic temperature, the granular temperature $\theta = \frac{1}{3}(\mathbf{v}'_s \mathbf{v}'_s)$, is introduced as a measure of the energy associated with this motion (see Goldhirsch, 2008). The balance equation for granular temperature can be written in the following form (Gidaspow, 1994)

$$\frac{3}{2} \left(\frac{\partial}{\partial t} \alpha_s \rho_s \theta + \nabla \cdot \alpha_s \rho_s \theta \mathbf{V}_s \right) = (-P_s \mathbf{I} + \boldsymbol{\tau}_s) : \nabla \mathbf{V}_s + \nabla \cdot (k_\theta \nabla \theta) - \Gamma + \gamma q_{gs} - 3\gamma \theta \quad (2-162)$$

The terms on the right-hand side represent respectively, generation, diffusion, dissipation, production due to the gas-solid fluctuating motion, and loss due to the gas friction of the granular temperature. Note that taking into account Eq. (2-160), the last two terms cancel one another. The diffusion coefficient is modelled according to Gidaspow (1992) as a sum of the two terms for the dilute and dense regions.

$$k_\theta = \frac{75}{192} \frac{\rho_s d \sqrt{\pi \theta}}{(1+e)g_0} \left(1 + \frac{6}{5}(1+e)g_0 \alpha_s \right)^2 + 2\alpha_s^2 \rho_s d g_0 (1+e) \sqrt{\frac{\theta}{\pi}} \quad (2-163)$$

According to Jenkins and Savage (1983), the dissipation, Γ , is calculated as

$$\Gamma = 3(1-e^2) \alpha_s^2 \rho_s g_0 \theta \left(\frac{4}{d} \sqrt{\frac{\theta}{\pi}} - \nabla \cdot \mathbf{V}_s \right) \quad (2-164)$$

The Ma and Ahmadi (1986) correlation is adopted for the radial distribution function, g_0

$$g_0 = 1 + 4\alpha_s \frac{1 + 2.5\alpha_s + 4.5904\alpha_s^2 + 4.515439\alpha_s^2}{\left(1 - \left(\frac{\alpha_s}{\alpha_s^{\max}} \right)^3 \right)^{0.67802}} \quad (2-165)$$

This form is more favourable than others because the radial distribution approaches unity as the volume fraction approaches zero. It makes the correlation applicable for both dilute and

Chapter 2. Mathematical model description

dense flows. The solid pressure, which is a normal force due to the particle interactions, analogous to the hydrostatic pressure, is modelled according to Lun et al. (1984).

$$P_s = \alpha_s \rho_s \theta (1 + 2g_0 \alpha_s (1 + e)) \quad (2-166)$$

Gidaspow's (1992) model is used to calculate the solid shear viscosity

$$\mu_s = \frac{4}{5} \alpha_s^2 \rho_s d g_0 (1 + e) \sqrt{\frac{\theta}{\pi}} + \frac{5}{48} \frac{\rho_s d \sqrt{\pi \theta}}{(1 + e) g_0} \left(1 + \frac{4}{5} (1 + e) g_0 \alpha_s \right)^2 \quad (2-167)$$

and the bulk viscosity is calculated by the Lun et al. (1984) model.

$$\lambda_s = \frac{4}{5} \alpha_s^2 \rho_s d g_0 (1 + e) \sqrt{\frac{\theta}{\pi}} \quad (2-168)$$

For dense flow it is necessary to add an additional term, the frictional viscosity, to the solid shear viscosity to account for yielding of the material at high solids concentrations.

Schaeffer's (1987) model is utilized

$$\mu_s^{fric} = \frac{\alpha_s P_s \sin \varphi}{2\sqrt{I_2}} \quad (2-169)$$

where φ is the friction angle, and I_2 is the second invariant of the rate of deformation tensor, which is calculated as follows

$$I_2 = \frac{1}{6} \left((D_{11} - D_{22})^2 + (D_{22} - D_{33})^2 + (D_{33} - D_{11})^2 + D_{12}^2 + D_{23}^2 + D_{31}^2 \right) \quad (2-170)$$

$$\mathbf{D} = \frac{1}{2} (\nabla \mathbf{V}_s + \nabla \mathbf{V}_s^T)$$

This frictional viscosity term is included only for $\alpha_s > 0.5$.

2.2.5. Heat transfer closure

In order to close energy equations (Eqs. (2-151) and (2-152)), we need to determine the interfacial heat transfer coefficient and the effective thermal diffusion coefficients for both phases. We adopted an approach from Schmidt and Renz (1999). The interfacial heat transfer coefficient is obtained through the Nusselt number (Nu) as

$$h = \frac{6\alpha_s \kappa_g \text{Nu}}{d^2} \quad (2-171)$$

by utilizing a correlation proposed by Gunn (1978)

$$\text{Nu} = (7 - 10\alpha_g + 5\alpha_g^2) \left(1 + 0.7 \text{Re}^{0.2} \text{Pr}^{0.33}\right) + (1.33 - 2.4\alpha_g + 1.2\alpha_g^2) \text{Re}^{0.7} \text{Pr}^{0.33} \quad (2-172)$$

The gas effective thermal conductivity expression is taken from Kuipers et al. (1992).

$$\kappa_g = \kappa_{gas} \left(1 - \sqrt{1 - \alpha_g}\right) \quad (2-173)$$

For the solid phase, the relation obtained by Hunt (1997) (Eq. (T2.5)) connects the solid effective thermal conductivity with the random movement of particles.

$$\kappa_s = \alpha_s \rho_s c_{p_s} d \frac{\pi \sqrt{\pi \theta}}{32 g_\kappa} \quad (2-174)$$

where

$$g_\kappa = \frac{16 - 7\alpha_s}{16(1 - \alpha_s)^2} \quad (2-175)$$

2.2.6. Boundary conditions

At the nozzle entrance and at the top of the freeboard (upper part of the fluidized bed that generally contains no particles) a constant pressure is assumed. For the gaseous phase a no-slip condition is applied at all walls. Following De Wilde et al. (2002), it is assumed that solid particles do not have a substantial influence in the viscous sub-layer, and the regular gas phase wall functions are applied. For the solid phase near walls, partial slip conditions proposed by Sinclair and Jackson (1989) are adopted. The shear stress and the flux of the granular temperature near the wall for the solid phase are calculated as (see Eqs. (2-145) and (2-146))

$$\mu_s \left. \frac{\partial \mathbf{V}_s}{\partial n} \right|_{wall} = - \frac{\sqrt{3\theta} \pi \alpha_s \rho_s g_0}{6\alpha_s^{\max}} |\mathbf{V}_s| \quad (2-176)$$

$$k_{\theta} \frac{\partial \theta}{\partial n} \Big|_{wall} = \frac{\sqrt{3} \theta^2 \pi \alpha_s \rho_s g_0 (1 - e_w)}{4 \alpha_s^{\max}} |\mathbf{V}_s| \quad (2-177)$$

2.2.7. Attrition modelling

While there are a variety of attrition mechanisms, such as abrasion and thermal stresses, in this work we consider only the attrition due to inter-particle collisions as it dominates the process under consideration.

2.2.7.1. Particle number density

As solid particles experience breakage, their diameter changes. In order to account for this change, a particle number density approach, similar to the one presented in Section 2.1.5, is adopted. It is assumed that the local particle size distribution can be represented by the local average diameter. A partial justification for this assumption comes from the observation that the particle size distribution for a targeted application is not very wide (McMillan et al., 2007b). Moreover, the probability of break-up reduces with the reduction of the particle diameter; thus, the boundary of the low range of the particle size would not decrease very significantly during attrition, and the range would not grow very substantially. Additionally, as the main objective of the current modelling is to investigate the optimal grinding conditions, as determined by grinding efficiency, the particle size distribution plays a somewhat secondary role in this context. That is, if a certain nozzle configuration performs better with our assumption of monodispersed particle distribution, it would perform better with the polydispersed particle distribution as well. It is more convenient to formulate a transport equation for the total number of particles, instead of one for the diameter itself. The particle number density, the number of solid particles per unit volume, can be obtained from the volume fraction and the average diameter

$$n = \frac{6 \alpha_s}{\pi d^3} \quad (2-178)$$

The conservation equation for the particle number density can be written in the following form (e.g. Kolev, 2002a).

$$\frac{\partial n}{\partial t} + \nabla \cdot n \mathbf{V}_s = n f_{br} \quad (2-179)$$

where f_{br} is a break-up frequency.

2.2.7.2. Attrition criterion

It is necessary to determine whether particle collision leads to breakage or not. We follow the approach of Yashima et al. (1987) to connect the impact velocity with the breakage. Consider the axial collision of two identical spherical particles as shown in Figure 2-4.

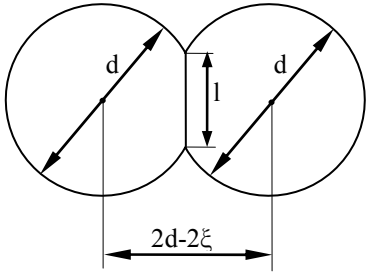


Figure 2-4. Particle collision schematic.

The particle strength depends on the presence of small flaws or cracks that are randomly distributed in the material. Thus, the strength depends on the volume (or the diameter) of the particle. It was shown by Weibull (1939) that the strength is inversely proportional to the particle diameter

$$G = \frac{C_s}{d^m} \quad (2-180)$$

where m is the Weibull's coefficient of uniformity. According to the Hertz model (see Thornton and Ning, 1998), the normal contact force acting on a sphere during elastic collision is proportional to its diameter and the deformation

$$F = \frac{4}{3} d^{\frac{1}{2}} \xi^{\frac{3}{2}} \frac{E}{1 - \nu^2} \quad (2-181)$$

where E and ν are the Young's modulus and Poisson's ratio respectively. The work of the contact force required to obtain the deformation, can then be calculated as

$$E_{coll} = 2 \int_0^{\alpha} F d\alpha = \frac{16}{15} d^{\frac{1}{2}} \zeta^{\frac{5}{2}} \frac{E}{1 - \nu^2} \quad (2-182)$$

Note that the integral is multiplied by two because there are two spheres involved in the collision. The kinetic energy of the two colliding particles is

$$E_{kin} = \frac{1}{6} \pi d^3 \rho_s v^2 \quad (2-183)$$

where v is the approach velocity. The fracture energy is defined as the energy necessary for the particle rupture. We assume that the particles are brittle and the rupture follows after some initial elastic deformation. Therefore, the maximum deformation marks the point of rupture; it can be determined from the energy balance

$$E_{kin} = E_{coll} \quad (2-184)$$

At the same time, at the point of rupture, the load per unit area is equal to the particle strength.

$$\frac{F}{A} = G \quad (2-185)$$

From Figure 2-4, the contact area is

$$A = \pi l^2 \quad (2-186)$$

As the particle indentation is generally small compared to the particle diameter, we can use a parabolic approximation

$$l^2 = d\zeta \quad (2-187)$$

For this contact area, we obtain from Eqs. (2-180), (2-181), and (2-185)

$$\frac{4}{3\pi} d^{-\frac{1}{2}} \zeta^{\frac{1}{2}} \frac{E}{1 - \nu^2} = \frac{C_s}{d^{\frac{3}{m}}} \quad (2-188)$$

From this equation we can retrieve particle deformation ζ

$$\zeta^{\frac{1}{2}} = \frac{3\pi}{4} \frac{C_s}{d^{\frac{3}{m}}} d^{\frac{1}{2}} \frac{1-v^2}{E} \quad (2-189)$$

Next, from Eqs. (2-184) and (2-189) we can find a minimum velocity required for the particle breakage.

$$c_* = \sqrt{\frac{81}{80} \pi^2 C_s^{\frac{5}{2}} \left(\frac{1-v^2}{E} \right)^2} \frac{1}{\rho_s^{\frac{1}{2}} d^{\frac{15}{2m}}} \quad (2-190)$$

It can be seen that $c_* d^{\frac{15}{2m}}$ is a constant that depends only on the particle material properties. The value of m varies somewhat depending on the material and particle size. From the work of Ghadiri et al. (2002), who proposed an attrition propensity parameter

$$\eta = \frac{\rho_s c_*^2 d H}{K^2} \quad (2-191)$$

it follows that m is equal to 15. (In the above equation, H is the hardness and K is the fracture toughness.) We adopted this value for use in the model. It was noted above that the distribution of the material flaws is random, making the derivation valid only in the statistical sense. That is, some particles would break up when the approach velocity is less than c_* , while others would not break up when the approach velocity is larger than c_* . Therefore, we introduce the breakage probability function to account for such behaviour,

$$P_{br} = e^{-\frac{C_{br}}{dc^2}} \quad (2-192)$$

where C_{br} is the breakage constant

$$C_{br} = \frac{81\pi^4}{80} C_s^5 \left(\frac{1-v^2}{E} \right)^4 \frac{1}{\rho_s} \quad (2-193)$$

This constant depends on the material properties and needs to be determined empirically. The choice of the probability function (Eq. (2-192)) is arbitrary provided the value is close to zero for small values of the velocity and approaches unity as the velocity increases to infinity. The selection was guided by the general simplicity and subsequent ease of the integration (see Eq.

(2-195)). The shape of this function for the parameter values used in the Section 7.1 simulations, $C_{br} = 0.21 \text{ m}^3 \text{ s}^{-2}$ and $d = 1.9 \cdot 10^{-4} \text{ m}$ (initial value), is shown in Figure 2-5.

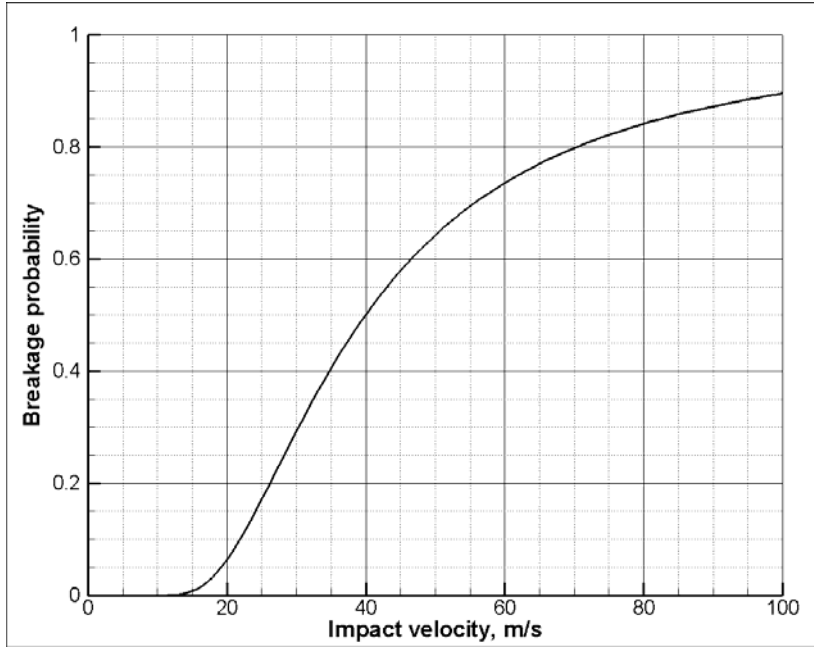


Figure 2-5. Typical breakage probability function.

2.2.7.3. Breakage frequency

According to the kinetic theory (see Chapman and Cowling, 1970 and Goldschmidt et al., 2002) the zero order approximation of the impact velocity distribution is given by

$$f^{(0)} = n^2 d^2 g_0 \sqrt{2\pi} (2\theta)^{-\frac{3}{2}} e^{-\frac{v^2}{4\theta}} v^3 \quad (2-194)$$

The number of collisions per unit volume that end up with the particle break-up can be found by integration over all impact velocities.

$$N = \int_0^{\infty} f^{(0)} P_{br} dv \quad (2-195)$$

Note that each collision is counted twice as it involves two particles. After substitution of Eqs. (2-192) and (2-194) and integration, we obtain

$$N = 2n^2 d^2 g_0 \sqrt{\pi} \sqrt{\frac{C_{br}}{d\theta}} \left(\sqrt{\frac{C_{br}}{d}} K_0 \left(\sqrt{\frac{C_{br}}{d\theta}} \right) + 2\sqrt{\theta} K_1 \left(\sqrt{\frac{C_{br}}{d\theta}} \right) \right) \quad (2-196)$$

where K_0 and K_1 are the modified Bessel functions of the second kind. Next, we assume that if a particle breaks, it produces two daughter particles. Even though the number of daughter particles can be larger, we do not follow the approach by Rajniak et al. (2008), who implemented daughter distribution functions to account for multi-particle splits because of the uncertainties involved in determining the parameters of such functions. Instead, we chose to simulate particle breakage to more than two daughters by a series of successive binary splits. Thus, the breakage frequency to be used in Eq. (2-179) can be determined.

$$f_{br} = \frac{N}{n} = \frac{12\alpha_s}{\sqrt{\pi}d} g_0 \sqrt{\frac{C_{br}}{d\theta}} \left(\sqrt{\frac{C_{br}}{d}} K_0 \left(\sqrt{\frac{C_{br}}{d\theta}} \right) + 2\sqrt{\theta} K_1 \left(\sqrt{\frac{C_{br}}{d\theta}} \right) \right) \quad (2-197)$$

2.2.7.4. Grinding efficiency

In order to compare the attrition performance during different operating conditions, we use the grinding “efficiency” to quantify the reduction in size of the particulate phase. The grinding efficiency terminology was introduced by McMillan et al. (2007a, 2007b) as a ratio of the new surface area created during the unit time to the inlet gas mass flow rate.

$$\kappa = \frac{\Delta S}{Q\Delta t} \quad (2-198)$$

For consistency with published literature, we continue using this terminology in the present work.

While the flow rate, Q , is a known variable, the increase of the surface area needs to be calculated. We assume that the particle always split in half, ignoring the mass distribution between the daughter particles. Note that an assumption of the particle breaking in two parts does not prevent modelling of the particle disintegrating into many daughter particles. Such situations are characterized by high values of the breakage frequencies, and it would mean that the particle undergoes a series of subsequent breakages resulting in multiple daughter particles, albeit all daughter particles would have the same diameter. The surface area of all the particles within each computational cell can be easily determined

$$S_i = \pi d_i^2 n V_i = \frac{6\alpha_s}{d_i} V_i \quad (2-199)$$

where i is the cell number. Next, during each time step we can calculate a total increase of the particle surface area as

$$\Delta S = 6 \left(\sum_i \frac{\alpha_i V_i}{d_i} - \sum_i \frac{\hat{\alpha}_i V_i}{\hat{d}_i} \right) \quad (2-200)$$

where caps denote the values from the previous time step and the summation is for all computational cells. Due to the transient nature of the process, the attrition efficiency values need to be averaged over a sufficient period of time that is longer than the timescale of the process.

2.3. Numerical method

The conservation equations together with the closure equations have to be solved for a number of geometries. We extended the numerical code previously developed at the University of British Columbia for single phase flows (He and Salcudean, 1994; Nowak and Salcudean, 1996) to multiphase flows. In order to truthfully represent model geometry, non-orthogonal non-uniform structured curvilinear grids with domain segmentation are utilized. The staggered grid arrangement, where the pressure and all the scalars are defined in the centre of the cell and the velocity components—in the centre of the cell face—is utilized together with a control volume approach (Nowak and Salcudean, 1996). The transient equations are discretized in time by the first order fully implicit Euler method. The second order upwind approximations are used for all convective terms, except the one for the volume fraction and particle number density equations in the jet-bed interaction model, for which a flux limiter approach is utilized. Vinokur's (1974) method is employed for discretizing coordinate independent transport equations in the physical space. The contravariant velocity components are used in the momentum equations. The discretization procedure developed by Karki and Patankar (1988) allows for obtaining the equations for the curvilinear velocities by algebraic manipulation of the discretized momentum equations for the Cartesian velocity components without the explicit discretization of the curvilinear momentum component equations.

There is a strong coupling between the velocities for different phases due to the interfacial forces. In high speed multiphase flows the slip velocity between the phases can be

Chapter 2. Mathematical model description

very significant and, hence, the drag and the virtual mass forces can be extremely large. Although for a lower velocity flow through the nozzle, the virtual mass forces produce a very small difference in the final results (Lahey et al, 1980), in our case the difference can be substantial. In order to improve the numerical stability of the solution algorithm, the momentum component equations for each phase are solved coupled together, with the drag and virtual mass terms implicitly discretized.

The pressure-velocity coupling is achieved with a modified IPSA (Inter-Phase Slip Algorithm) procedure developed by Spalding (1980) which is an extension of the well-known SIMPLE (Semi-Implicit Method for Pressure Linked Equations) algorithm (see Patankar, 1980) to multiphase flows. This procedure is also applicable to the supersonic flow encountered in the attrition nozzle because it was shown by Birkby and Page (2001) that pressure-based methods can be used for computations for flows that contain high and low Mach number zones provided the Mach number is not very large. A total mass conservation equation is constructed by the summation of the all phase density weighted mass balance equations. The result is simplified, as the sum of all the volume fractions equals unity. Velocity corrections relationships that implicitly account for the drag and virtual mass terms are obtained from the momentum equations for all phases. These corrections are substituted into the total mass conservation equation to form an equation for the pressure corrections. This equation is iteratively solved in a procedure analogous to the PISO (Pressure Implicit with Split Operator) algorithm (Issa, 1986) to account for the neighbouring velocities and the non-orthogonal pressure components. The number of PISO iterations during each pressure-velocity correction step is controlled to obtain a converged solution. From 10 to 20 iterations are performed during each time step.

For the solution of the system of linear equations the GMRES (Generalized Minimal RESidual) algorithm (Saad, 1996) from the family of Krylov subspace methods with ILU(0) (Incomplete Lower Upper decomposition of degree zero) preconditioning is used. The code of the matrix solver was obtained from the Netlib depository (SLATEC, 1993).

Chapter 3. GAS-LIQUID FLOW IN A CONVERGENT-DIVERGENT NOZZLE

This chapter describes the jet-bed interaction model application during the first stage in its development, i.e the gas-liquid flow through the nozzle. We assume that the atomization takes place outside of the nozzle. This means that we consider only the liquid-continuous flow without a phase inversion. There are no particles in the domain, no heat or mass transfer. Instead of solving a full energy equation (Eq. (2-6)), a constant total enthalpy is assumed because of the adiabatic nature of the process and negligibly small viscous heat dissipation.

$$\frac{dH_g}{dt} = \frac{d}{dt} \left(c_{p_g} T_g + \frac{\mathbf{V}_g^2}{2} + k_g \right) = 0 \quad (3-1)$$

Therefore, only a subset of the whole model is used. We simulate the flow through the convergent-divergent nozzle under conditions similar to the experimental cases in order to verify model performance by comparing pressure profiles along the nozzle walls. In addition, we analyse two-phase flow through the nozzle based on the insights that numerical modelling can provide.

3.1. Model comparison with experiment

3.1.1. Experimental set-up

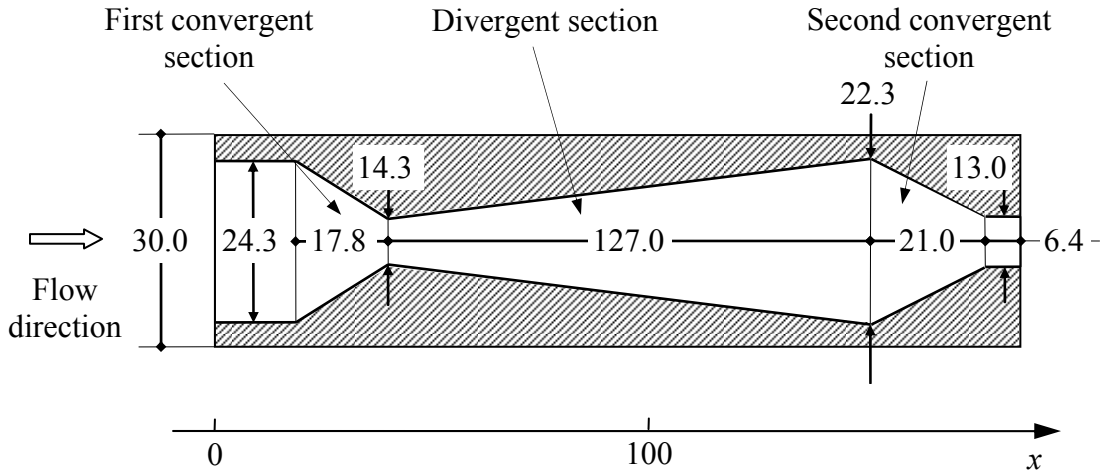


Figure 3-1. TEB Nozzle geometry (all dimensions are in mm; not to scale).

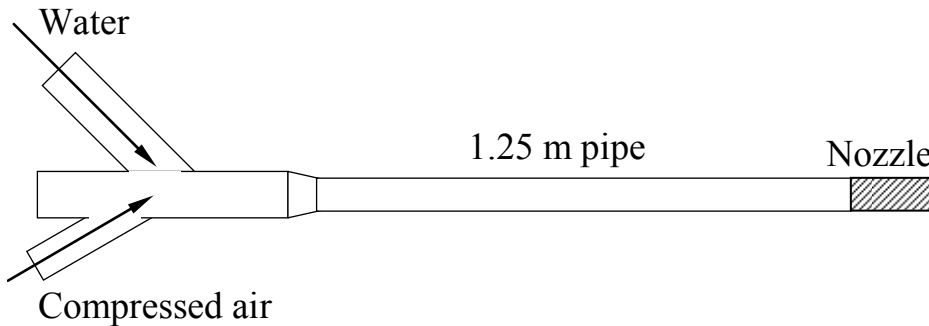


Figure 3-2. Schematic diagram of the experimental set-up.

As noted above, most of the experiments for the two-phase nozzle flow consider air and water as gas and liquid phases. The experiments presented in this section were conducted at the spray test research facility at Syncrude Canada Ltd.. The standard TEB-type (Base et al., 1999) nozzle geometry is sketched in Figure 3-1. It consists of the pipe connector, the initial convergent section (31°) with the slightly divergent section to follow (4°), and the second convergent section (25°) that ends with a small straight piece. This type of nozzle is used in the fluid coking process to inject the steam-bitumen mixture into the reactor. However, as already noted in Section 1.2.3, the steam and bitumen are not very suitable for experimental runs. Water spraying tests in open air were performed instead. The

Chapter 3. Gas-liquid flow in a convergent-divergent nozzle

experimental set-up is shown schematically in Figure 3-2. After the compressed air is injected into the water, the mixture travels through a long pipe (~ 1.25 m) before entering the nozzle. A similar set-up of the scaled down version of the nozzle has been described in detail by Ariyapadi et al. (2005). The nozzle has multiple pressure taps and transducers installed, so that the pressure measurements can be taken along the nozzle wall. Six test cases with the Gas to Liquid mass Ratio (GLR) varied from 1.02% to 2.38% were considered. A summary of the flow rates of the air and the water corresponding to the different test conditions is presented in Table 3-1.

Table 3-1. Summary of experimental flow rates.

Case number	Air flow rate, kg s^{-1}	Water flow rate, kg s^{-1}	GLR, %
1	$5.933 \cdot 10^{-2}$	2.498	2.38
2	$4.417 \cdot 10^{-2}$	2.504	1.76
3	$2.9 \cdot 10^{-2}$	2.498	1.16
4	$5.9 \cdot 10^{-2}$	2.832	2.08
5	$4.433 \cdot 10^{-2}$	2.839	1.56
6	$2.9 \cdot 10^{-2}$	2.832	1.02

3.1.2. Modelling geometry and solution details

Because our intent is to compare the modelling and experimental results, the computational domain mimics the experimental conditions described in the previous subsection. At the inlet we assume the known flow rates of the phases. As we do not know the bubble diameter at the inlet, we have to assume a certain value that is constant across the inlet plane; in all our cases it is 3 mm. Similarly, we assume that turbulent intensity is 0.1. Also, we assume that the radial distribution of phases is uniform. In addition, we model the nozzle together with the inlet pipe in order to reduce the influence that the unknown inlet boundary conditions (diameter and phase distribution) might have on the nozzle flow. The numerical domain starts right after the mixing device shown in Figure 3-2. In all empirical and semi-empirical correlations the models employed are used in their original form, as they were obtained by the respective authors. No coefficient adjustments or other data fitting procedures have been performed. Physical properties of air and water are used in the

Chapter 3. Gas-liquid flow in a convergent-divergent nozzle

simulations; the inlet mixture temperature is 20°C. The calculations are carried out time-dependently with a time step typically being 10^{-4} s, and ten outer iterations are performed per each time step. The forward time marching continued until a steady state solution has been reached. Note that a steady state is used here in a practical sense, as minute fluctuations of the flow parameters are always present in the computational results for the nozzle flow. However, these fluctuations are visually indistinguishable.

3.1.3. Gravity influence

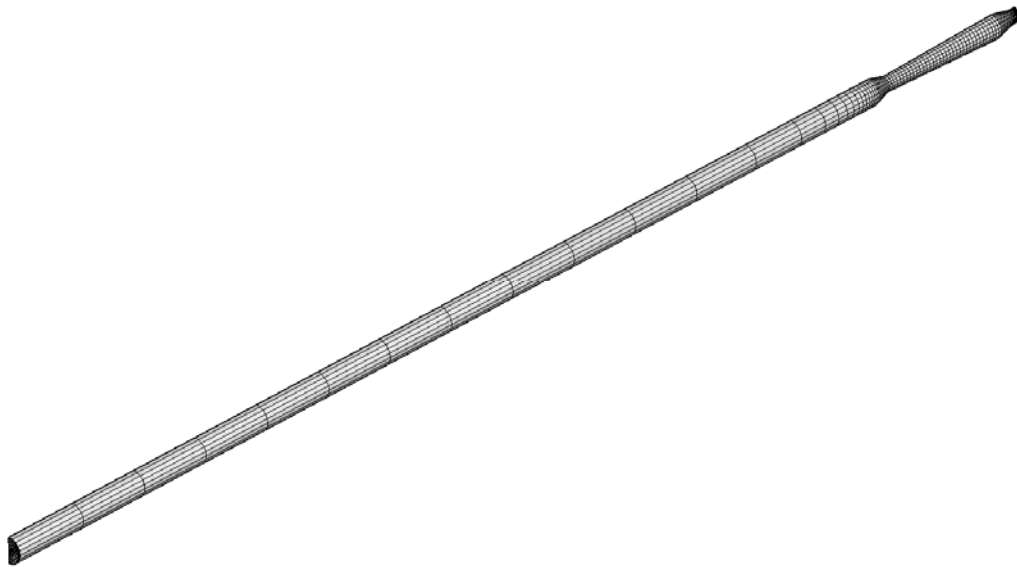


Figure 3-3. 3D computational domain with grid.

First, we investigate the influence that the gravity force has on the flow through the nozzle. The main interest is to assess whether phase separation occurs during the horizontal flow of the gas and liquid. As the likelihood of phase separation increases with the reduction of the flow rate, we chose the flow conditions corresponding to the Case 3 from Table 3-1 because it has the lowest flow rate of the mixture. If the separation does take place, it would be more pronounced in this case. Due to planar symmetry the computational domain can be reduced to half of the pipe and the nozzle cut vertically along the centreline. It is shown in Figure 3-3 with the body-fitted grid. The grid is relatively coarse for practical three-dimensional computations; however, during this stage it is sufficient for evaluating the gravity effects.

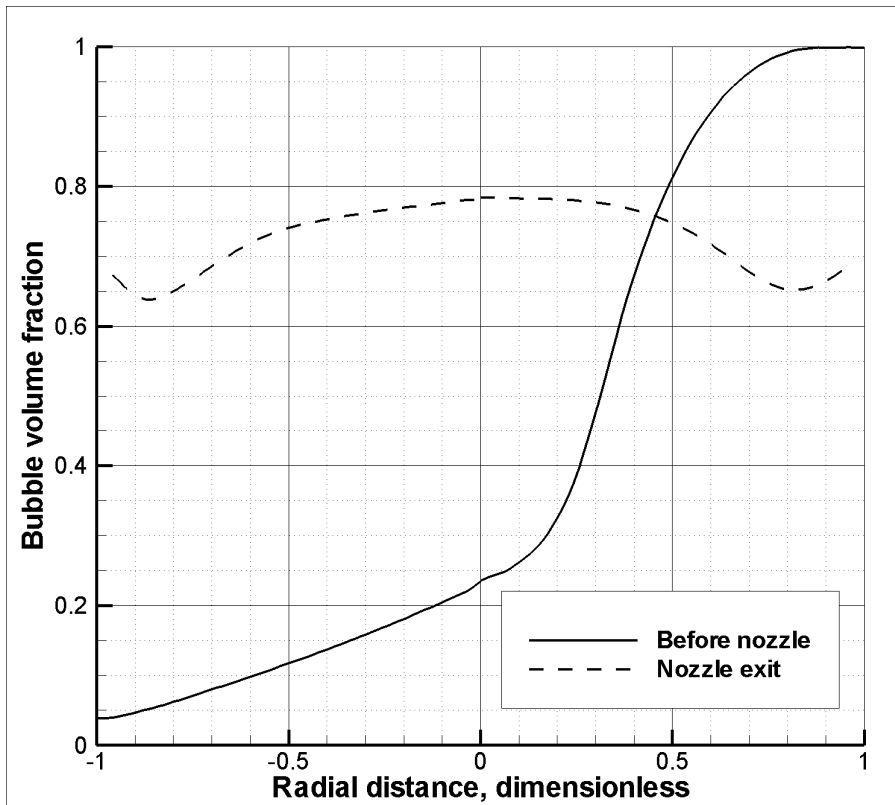


Figure 3-4. Air bubble volume fraction profiles in radial direction from bottom (negative distance) to top (positive distance) before and after the nozzle.

The analysis of the results demonstrates that the distribution of the bubbles in the vertical direction is indeed affected by gravity. However, the nozzle acts as an equalizer of bubble distribution. Figure 3-4 illustrates the bubble volume fraction cross-sectional profiles in the vertical direction before the nozzle inlet (after the full length of the entrance pipe) and at the nozzle exit for the calculated case. Note that the radial distance is non-dimensionalised by the nozzle/pipe radius. It is evident that a substantial top to bottom gradient of the volume fraction has formed as the flow moves along the entrance pipe. It is the consequence of the balance between the gravity force, which moves the bubbles upward, and the turbulence, which works to disperse them evenly. As the flow enters the nozzle, the turbulence is increased due to the introduction of an additional shear to the flow and the increase of the interfacial forces. Thus, the balance is shifted towards turbulence. As a result, the non-symmetry of the bubble volume fraction vertical distribution at the nozzle end is barely distinguishable in the plot. Variations of the other flow parameters, such as pressure and velocity, along the circumferential direction are generally small. As pointed out earlier, the

chosen case has the most important gravity effect because of the low flow-rate; therefore, one can conclude that it is possible to neglect the influence of gravity for nozzle simulations. Thus, in all subsequent simulations Eq. (2-2) is solved without the gravity term. This assumption allows for the two-dimensional axisymmetric treatment of the problem, so that the number of cells in the computational domain required for adequate resolution can be substantially reduced.

3.1.4. Grid independence

An important step in the verification of the numerical model is to ensure that the discretization errors obtained on a chosen computational mesh are sufficiently low. These errors are analysed by comparing the solutions obtained on grids with different degrees of refinement. Four separate grid sets have been constructed for this purpose: the coarse grid contained 1 104 (92×12 , grid size near the nozzle exit is about 0.54 mm) cells, the medium grid – 2 040 (102×20 , 0.33 mm) cells, the fine grid – 4 672 (146×32 , 0.2 mm) cells, and the extra fine grid – 8 840 (221×40 , 0.16 mm) cells. The total number of cells is approximately doubled for the next size up. Most of the refinement is done in the radial direction, with some in the axial direction, mostly in the area closer to the nozzle exit. Similar to the previous investigation of the initial diameter influence, the flow rates for this study are assumed from Case 1. The converged solution is obtained for all grid sizes. For comparison, we plot pressure values along the centreline for all four cases (Figure 3-5). It is evident that the profiles for the fine and the extra fine grid cases are very close, whilst there is an appreciable difference between them and other cases, as well as between the coarse and the medium grid cases. Thus, it can be concluded that only the fine and extra fine grids provide sufficient accuracy of the discretization. We will use the fine grid (4 672 cells) for simulations of the following cases for comparison with experimental data.

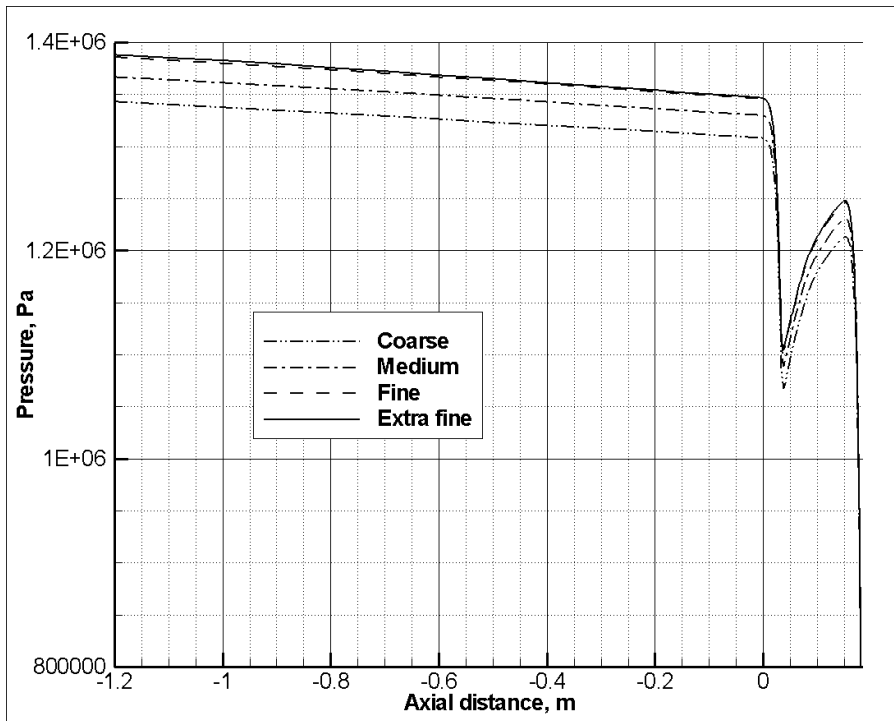


Figure 3-5. Pressure profiles along the centreline for different resolution grids.

3.1.5. Comparison with experiment

The model has been applied to predict pressure measurements obtained during the experimental run of the cases listed in Table 3-1. Figure 3-6 shows the simulated pressure curves along the nozzle wall together with the measurement points for all calculated cases on separate graphs. The pressure drop through the second convergent section has been predicted very well; the difference is less than 1%. The pressure recovery curve along the divergent section has also very good agreement with the experimental data; the difference is less than 1-2% also. However, the pressure drop at the first convergent section is under-predicted by 10% to 18% depending on the case. The simulation results demonstrated great consistency between the cases: the locations of good and fair agreement with the test data are the same regardless of the inlet flow rates. This feature can make an adjustment of the closure coefficients to match experimental points easier. However, we refrained from doing so because there are not enough experimental data available to support the modifications of the many sub-models. As there is much more than one coefficient to adjust in this complex model, a variety of specially targeted experiments needs to be designed. Moreover, we believe that for such a complex process that involves interfacial physics which is not entirely

Chapter 3. Gas-liquid flow in a convergent-divergent nozzle

understood, the agreement between the predicted and experimental results is certainly satisfactory.

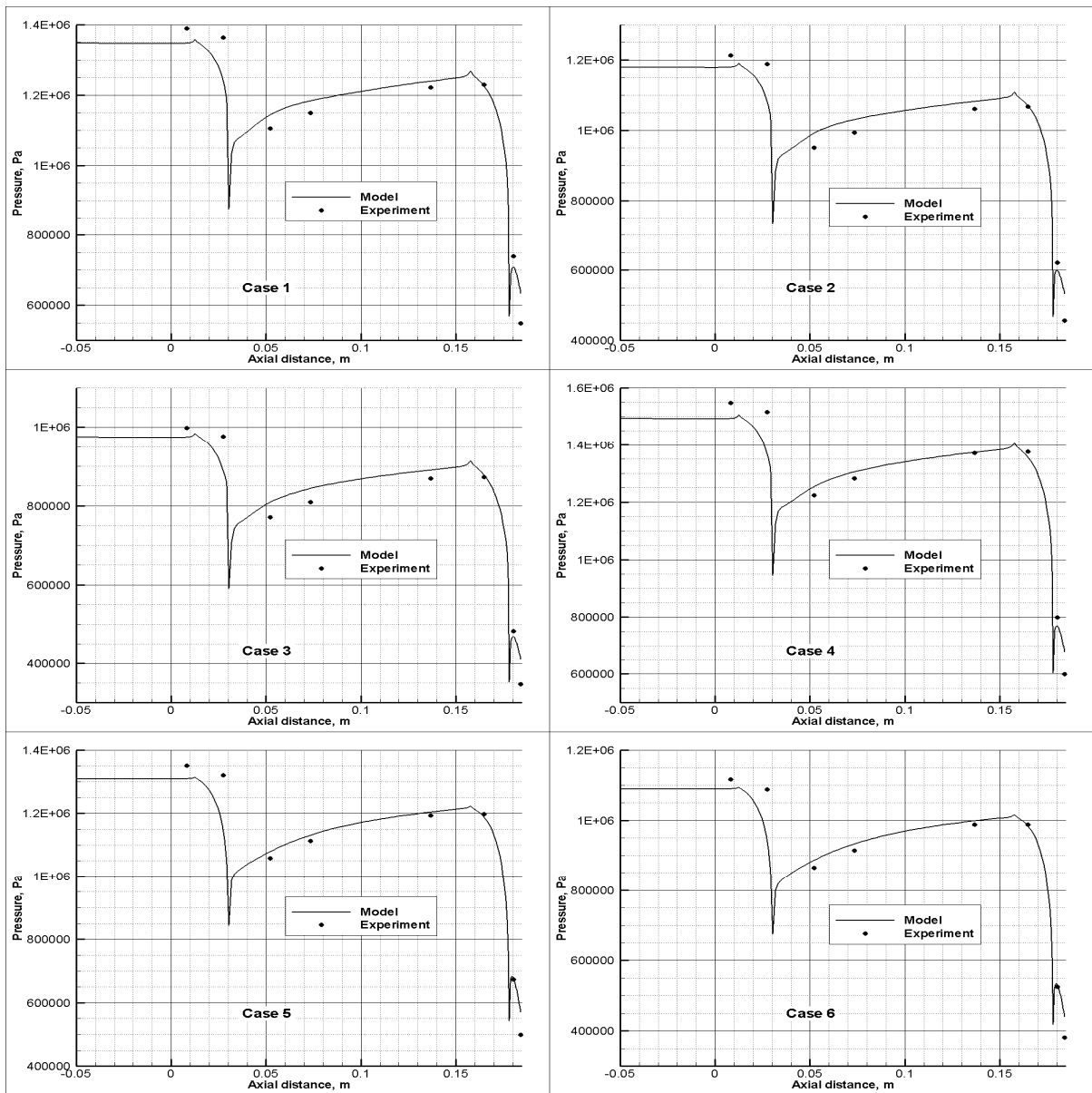


Figure 3-6. Comparison of the pressure profiles along the nozzle wall obtained by the model with experimental data.

3.2. Flow analysis

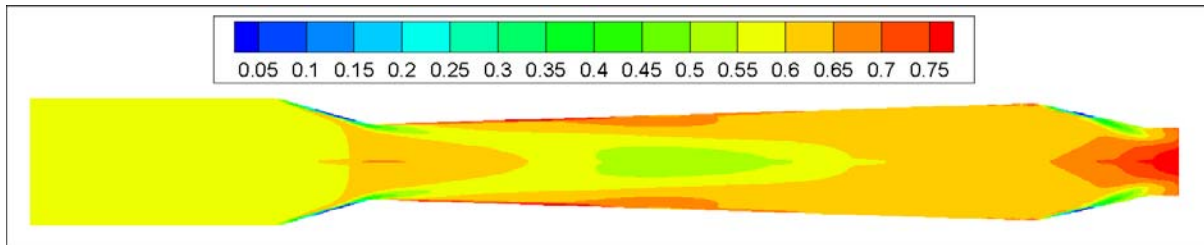


Figure 3-7. Liquid volume fraction contours in the nozzle. Computational domain is extended from axisymmetric to a full axial cross-section for better presentation.

The Case 1 results are used as an example for the analysis of the nozzle flow. As the the air-water mixture moves along the entrance pipe in the absence of gravity, the bubble volume fraction distribution remains uniform across the pipe cross-section. (Gravity influence has been discussed above in Section 3.1.3.) This uniformity changes as soon as the flow enters the nozzle. Figure 3-7 demonstrates the contours of the liquid volume fraction inside the nozzle. It is evident that there is an accumulation of the liquid along the wall of the first convergent section. It happens because of a higher inertia of the liquid which has a higher density. This creates the bubbles rich central area and the liquid rich peripheral area. After the first convergent section, the liquid moves back towards the centreline making the cross-sectional distribution close to a uniform one before the start of the second convergent section. As the flow passes through the second contraction, liquid again accumulates near the wall. Thus, by the nozzle exit the bubble distribution is non-uniform; the area around the centreline is full of bubbles, while the periphery is rich in liquid. In addition, along this convergent section and the small straight piece that follows, the pressure drops dramatically (see Figure 3-6). This change of pressure results in air expansion and, hence, rapid growth of the bubble volume fraction takes place. However, its value reaches only about 80%, which confirms our assumptions of the churn-turbulent flow inside the nozzle till the end, and that the phase inversion happens some place outside the nozzle.

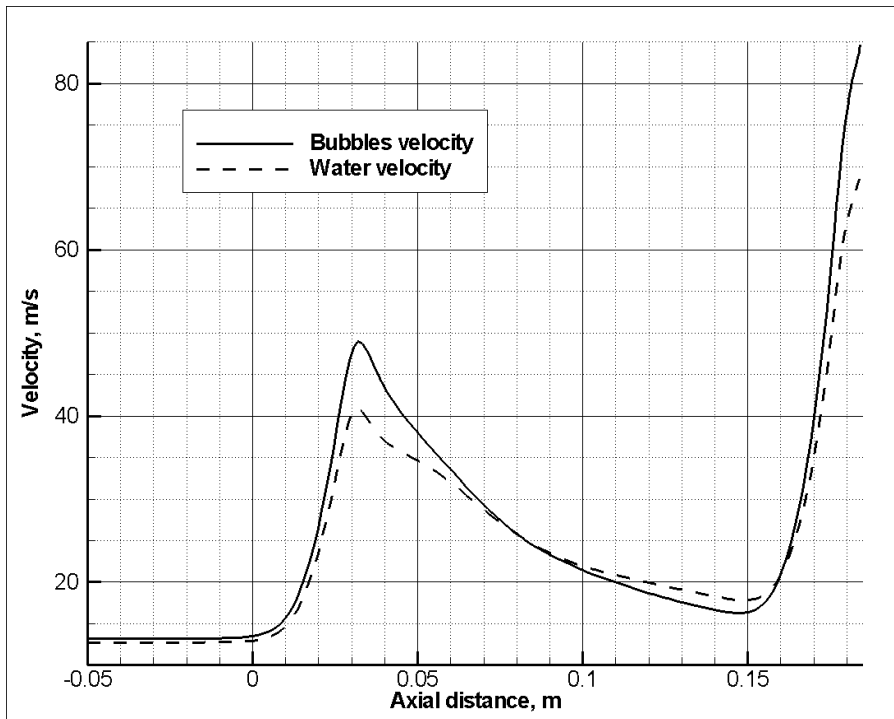


Figure 3-8. Velocity profiles along the centreline.

It is interesting to examine the changes of the velocities of each phase inside the nozzle. Figure 3-8 displays profiles of the air bubbles and water velocities along the centreline. In order to improve the plot resolution in the nozzle area, only a small section corresponding to the entrance pipe is included in the graph together with the nozzle, since there are few changes to the axial velocities of phases in the entrance pipe. As can be seen from the figure, the velocity of the air bubbles in the pipe is slightly higher than the velocity of the water. This is probably the result of the higher shear and the wall friction in the liquid phase. At the start of the first convergent section, the bubbles begin to accelerate faster than the liquid, fuelled not only by the reduction of the cross-sectional area, but also by the air expansion due to the drop in pressure. However, the drag and virtual mass forces restrain the growth of the slip velocity. Still, the difference between the phase velocities reaches about 8 m/s at the end of the first convergent section. In the divergent section, the bubbles and water velocities decrease with the increase of the area. At the same time, the bubble velocity decreases faster than the liquid, due to its lower inertia. At some point the liquid velocity becomes larger than the velocity of the air bubbles. This situation continues until the flow reaches the second convergent section. Then, again, the bubbles are accelerated faster than

Chapter 3. Gas-liquid flow in a convergent-divergent nozzle

the water and their velocity eventually exceeds that of the water. Even though the bubble diameter is somewhat smaller during the second contraction (see Figure 3-11) leading to a higher drag force, the maximum difference between the phase velocities reaches higher values because the acceleration is larger than that encountered in the first contraction section due to the air expansion.

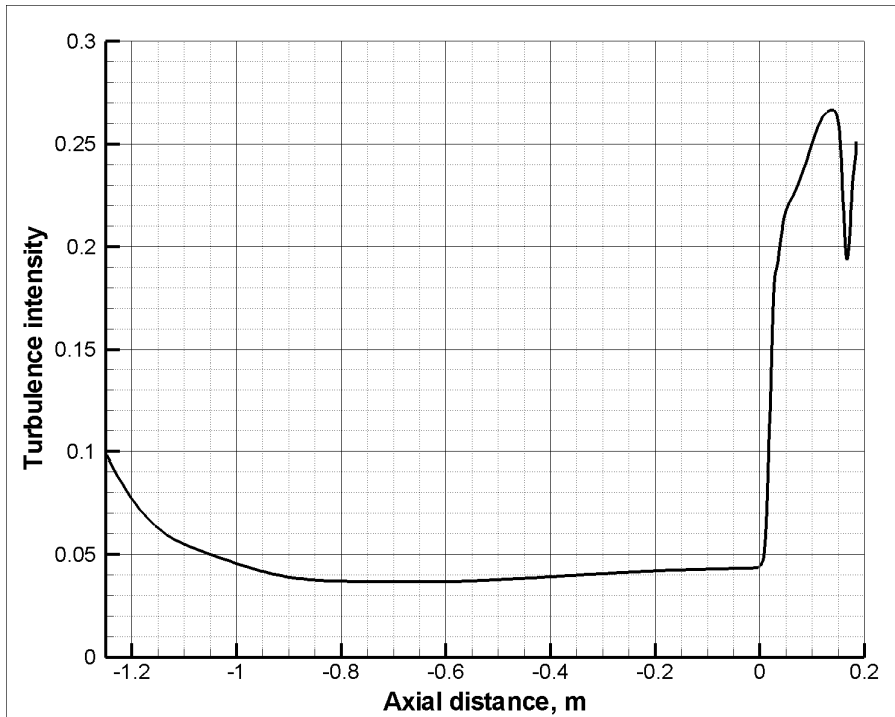


Figure 3-9. Turbulence intensity variation along the centreline.

The turbulence intensity defined as

$$I = \frac{\sqrt{0.67k_m}}{|\mathbf{V}_m|} \quad (3-2)$$

changes along the centreline is illustrated in Figure 3-9. It can be seen that with the development of the flow in the inlet pipe, the intensity reaches a steady value at which the production of turbulence is balanced by the dissipation. However, this balance is shifted as soon as the mixture enters the nozzle. At the beginning of the first convergent section, the intensity increases sharply because the velocity difference between the phases starts to increase (see Figure 3-8). This in turn causes an increase in turbulence production. Even though the absolute value of the velocity also increases, the turbulence generation is much

Chapter 3. Gas-liquid flow in a convergent-divergent nozzle

more significant. In addition, at the end of the convergent section, the flow experiences free shear that increases turbulence. It can be observed in Figure 3-8 that after a certain distance into the divergent section, the slip velocity decreases. This reduction manifests itself in the turbulence intensity graph (Figure 3-9) as the change of the rate of increase after the initial quick increase. It is evident that without very substantial production such high intensity levels are not sustainable, and the flow gradually readjusts itself. With the progression of the flow along the divergent section, the slip velocity starts to increase again (see Figure 3-8). This growth again results in the increase of the turbulence production, represented by a moderate increase of the incline of the profile curve. At the beginning of the second convergent section, the slip velocity falls to zero, which produces the drop of the turbulence intensity for the same reasons that have already been discussed. However, this time the decrease is more prolonged because of the larger influence of the flow acceleration due to the rapid growth of the bubble volume fraction in this area. This decrease results not only in changes of the growth rate, but also in the decline of the turbulent intensity. Only very close to the nozzle orifice, as can be seen from the graph, does the intensity start to increase again because the production of the turbulence by the interfacial forces becomes dominant.

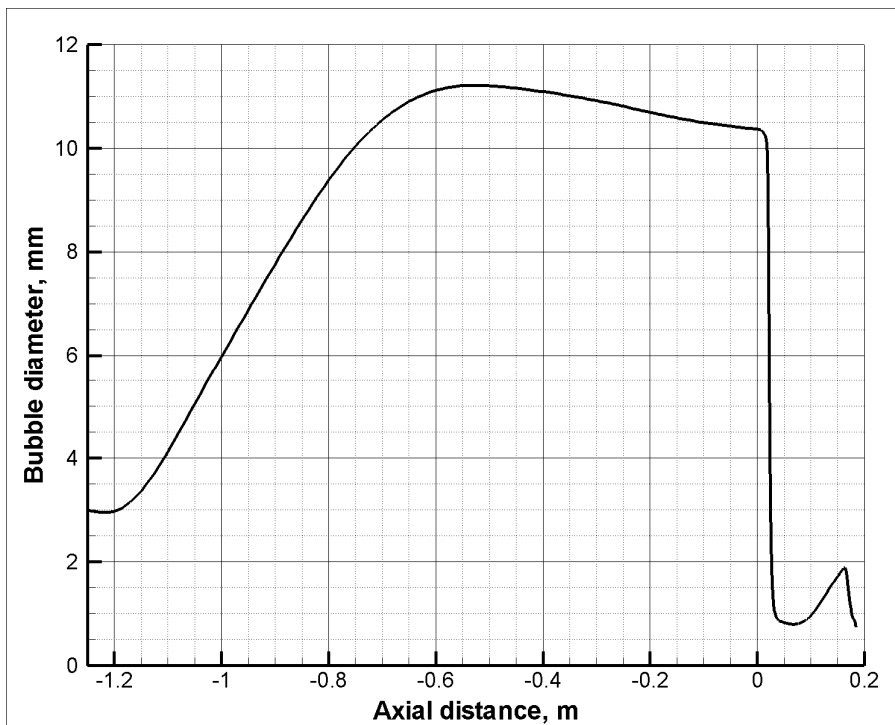


Figure 3-10. Bubble diameter profile along the centreline.

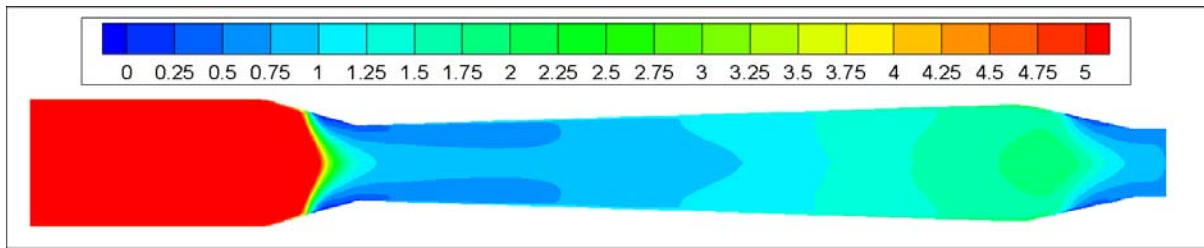


Figure 3-11. Average bubble diameter contours inside the entrance pipe and the nozzle (in mm).

The bubble diameter is closely linked to the turbulence. The development of the bubble diameter in the entrance pipe is shown in Figure 3-10. Let us recall that the churn-turbulent flow at the entrance of the modelling domain is obtained after the injection of the compressed air into the water (see Figure 3-2). The mixing process itself cannot be simulated with the present model, as it involves the air jet disintegration in water. Thus, the knowledge of the flow parameters at the model entrance is limited. While the flow rates of each phase are measured, there is more uncertainty with the determination of the average bubble diameter at the entrance. From Figure 3-10, we can see that the bubble diameters converge to about 11 mm, by the middle of the entrance pipe. It is evident that with the progress of the flow along the pipe, the influence of the initial bubble diameter diminishes as the diameter becomes more and more determined by the balance between the break-up and coalescence processes, i.e. $f_{br} = f_{coal}$, which mainly depend on the local turbulence parameters. Most importantly, the bubbles undergo massive break-up as the flow enters the nozzle, making the development in the pipe less relevant.

Let us consider the evolution of the average bubble diameter inside the nozzle (Figure 3-11). It has already been demonstrated that with the flow entering the nozzle, a large amount of turbulence is generated. This causes rapid acceleration of the bubble break-up process. It can be seen that the area with the lowest bubble diameter is located in the middle of the nozzle divergent section and corresponds to the “inclined plateau” of the turbulence intensity profile (Figure 3-9). After this area, the diameter grows somewhat up to about 2 mm. Even though there is a growth of the turbulent intensity near the second convergent section, the average diameter does not react to it strongly because the growth of the break-up rate is compensated by the growth of the coalescence rate due to an increase in the bubble volume fraction. The cross-sectional distribution of the average bubble diameter is fairly uniform, except inside the convergent sections, due to the uniformity of the turbulence parameters and

the large turbulent dispersion of bubbles. It is interesting to note that the observations of the nozzle flow with high speed photography show that the average bubble size in the area of the divergent section is in the order of 1 mm. This value correlates well with the model predictions.

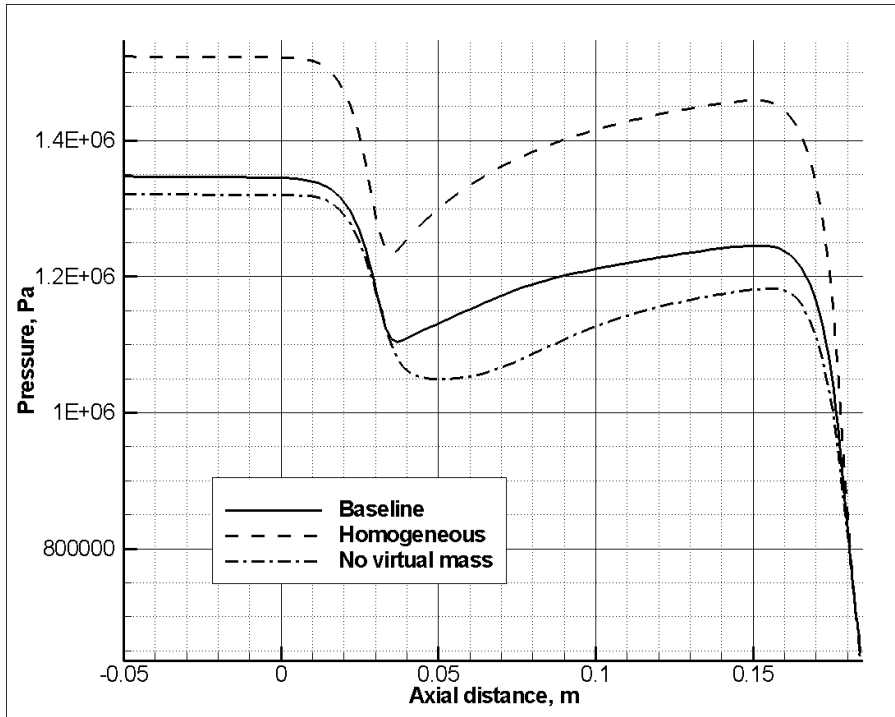


Figure 3-12. Comparison of pressure profiles along the centreline between the present model, the homogeneous model, and the model without an added mass force.

Our analysis has shown that the flow through the nozzle is far from being homogeneous (see Figure 3-7 and Figure 3-8). It can be instructive to see the difference of the pressure profiles obtained with our model and with the homogeneity assumption that would lead to a Bernoulli-type connection between pressure and velocity. This comparison is shown in Figure 3-12; again, the flow conditions of Case 1 are used for both cases. It is clear that the pressure loss through the nozzle obtained with the homogeneous model is much higher than that obtained with the present two-fluid model, which has been experimentally confirmed. The reasons for such dissimilarity are similar to the ones discussed by Hench and Johnston (1972). The equality of the phase velocities means that the liquid must accelerate through the convergent section to keep the same velocity as the gas bubbles, while allowing the slip velocity means that the gas can go faster and the liquid slower, thus reducing the drag encountered in the nozzle. The assumption of the homogeneity can produce acceptable

results only when the bubble size is small enough and the high interfacial drag makes the slip velocity relatively small. Evidently, it is not the case in the assisted atomization nozzle we have considered.

It is also instructive to evaluate the influence of the virtual mass force, as it is sometimes ignored in the dispersed bubble flow modelling. The obtained pressure curve, which is also shown in Figure 3-12, is positioned lower than the curve for the baseline case (Case 1). The reduction of the interfacial interaction increases the slip velocity and, hence, as was discussed above, reduces the pressure drop. In addition, with the removal of the turbulence production by the virtual mass force, the turbulence levels inside the nozzle drop, and the bubble break-up frequency decreases. As a result, the range of the bubble diameter inside the nozzle is significantly larger than that obtained with a full model, contradicting the experimental observations reported above. Therefore, one can conclude that including the virtual mass in this calculation is very important.

3.3. Summary

A two-fluid computational model for the gas-liquid flow through the convergent-divergent nozzle has been developed. The model constitutive equations are consistent with the high void fraction churn-turbulent flow that takes place in the nozzle and in the pipe leading to it. All the closure relationships were used in the exact form they were obtained, without any adjustment of the parameters to fit the data. The model demonstrates robust performance for the investigated range of the flow parameters. It is demonstrated that it is necessary to discretize implicitly the virtual mass term, which is very large; otherwise, the problem becomes numerically unstable. The comparison of the predicted and measured values of the pressure along the wall yields very good agreement for the divergent and the second convergent sections of the nozzle, and satisfactory agreement for the first convergent section. The developed multi-phase flow wall functions model for calculating the tangential shear stress and turbulent quantities near the wall produces plausible results in the vicinity of the wall, and reasonably good agreement of the pressure loss along the pipe length. Modelling results enabled the analysis of the flow through the nozzle to understand the mechanisms of the phase interactions.

Chapter 4. GAS-ASSISTED ATOMIZATION INCLUDING FLOW THROUGH THE NOZZLE, PHASE INVERSION, AND SPRAY DISPERSION

After model application to the flow through the nozzle described in Chapter 3, we now extend the modelling domain to include atomization and spray dispersion. This would constitute the second, intermediate, stage of the project. While some of the model features related to the phase inversion and droplet break-up and coalescence are now included in simulations, others related to the particulate phase and heat and mass transfer are not. As in Chapter 3, total enthalpy is assumed constant instead of solving Eq. (2-6).

All of the closure relationships for included sub-models are taken from the published literature without any adjustments, except for the value of the volume fraction that triggers phase inversion and the relative velocity constant from Eq. (2-82). The model is applied to the experimental cases that were investigated at Syncrude facilities. The predictions of the pressure in the nozzle, the liquid mass flow rate and the droplet average diameter in the spray at different distances from the nozzle orifice are compared with experimental results and flow features are analysed. This chapter comprises two parts that correspond to two different sets of experiments. The first (denoted A) was aimed at liquid flux measurement, and the second (denoted B), at droplet diameter measurement. As these experiments utilize different nozzles (one is a scaled up version of another), we simulated and analysed them separately.

4.1. Study A – Liquid flow rates

4.1.1. Experimental set-up

The experiments were conducted at the same spray test facilities at Syncrude Canada Ltd. that were used to obtain the detailed pressure measurements along the nozzle wall in Chapter 3. The experiments were conducted at room temperature (20°C) and at ambient pressure (0.1013 MPa). All physical properties of the materials, such as water surface tension (0.0727 N m⁻¹) and water density (1000 kg m⁻³), are taken at these conditions.

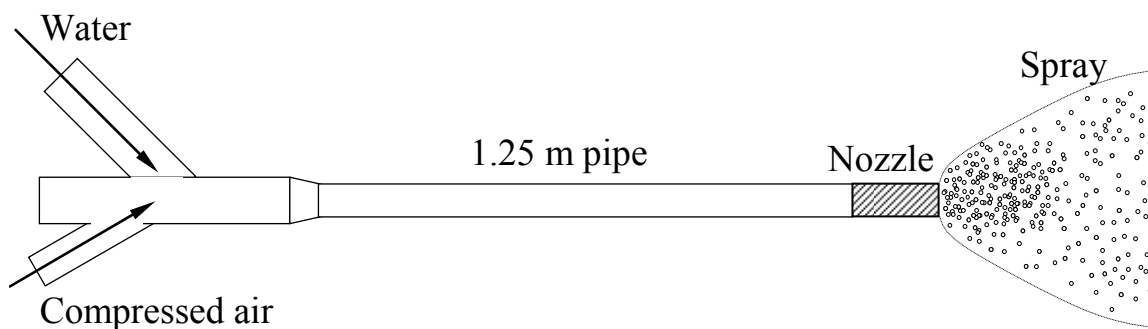


Figure 4-1. Schematic diagram of spraying experiment set-up.

Table 4-1. Air and water flow rates for investigated cases in flow rates experiments.

Case #	A1	A2
Air flow rate, kg s ⁻¹	0.0442	0.0883
Water flow rate, kg s ⁻¹	2.2	2.2
GLR, %	2	4

The nozzle, previously studied and shown in Figure 3-1, is attached to the end of a 1.25 m pipe that connects it to the mixing device where the compressed air is injected into the water. The whole assembly is schematically illustrated in Figure 4-1. The main focus of the described experiment was to obtain the water volume flux profiles across the jet at various distances. A probe, which was a 1 cm (³/₈ in) diameter cylinder with one end open and the other connected to a container that collected water, was placed in the spray to gather water at a certain position during a given amount of time. Knowing the water volume and time, an average flow rate can be calculated. By moving the probe from one position to another, the area of interest can be mapped. During the experiments, the cross-sectional

Chapter 4. Gas-assisted atomization including flow through the nozzle, phase inversion, and spray dispersion

profiles at distances 15.25 cm (6 in.) and 30.5 cm (12 in.) from the nozzle exit were obtained. In addition, the pressure was also measured at three points along the nozzle wall: after the mixer, before the nozzle, and right after the second convergent section of the nozzle. Two sets of the experimental conditions that represent two different gas to liquid mass ratios (GLR) were considered. The values of the flow rates of the air and water are presented in Table 4-1.

4.1.2. Computational domain

Axial symmetry is assumed for all simulated cases. For the flow inside the nozzle, the influence of the gravitational forces has been investigated in Chapter 3 by modelling a three-dimensional case. We have concluded that the influence is small enough to be neglected. Let us consider the droplet moving outside of the nozzle. Assuming it has an average velocity of 50 m/s, its trajectory will deflect only about 2 mm after 1 m distance due to the action of the gravitational acceleration. Clearly, we can neglect gravity outside the nozzle as well. Therefore, the gravity term is omitted from the right-hand side of Eq. (2-2). In addition, we assume that the nozzle is issuing in quiescent air. Thus, no wind influence is considered at this stage. With these assumptions all the flow equations and boundary conditions are axisymmetric; therefore, an axisymmetric simplification is warranted. As the model equations are written in terms of the generalized curvilinear coordinates, the actual shape of the computational domain will be a small angle wedge.

The modelling area starts right after the gas injection device. It includes the pipe leading to the nozzle, the nozzle itself, and the region of spray dispersion, which is about 80 cm long and has 20 cm radius. The whole computational domain is shown in Figure 4-2. Note that the outside area does not start at the nozzle exit plane: it extends about 30 cm beyond it. The reason for this extension is to avoid having a boundary too close to the nozzle exit, where the gradients of pressure and velocity are still quite substantial.

Chapter 4. Gas-assisted atomization including flow through the nozzle, phase inversion, and spray dispersion

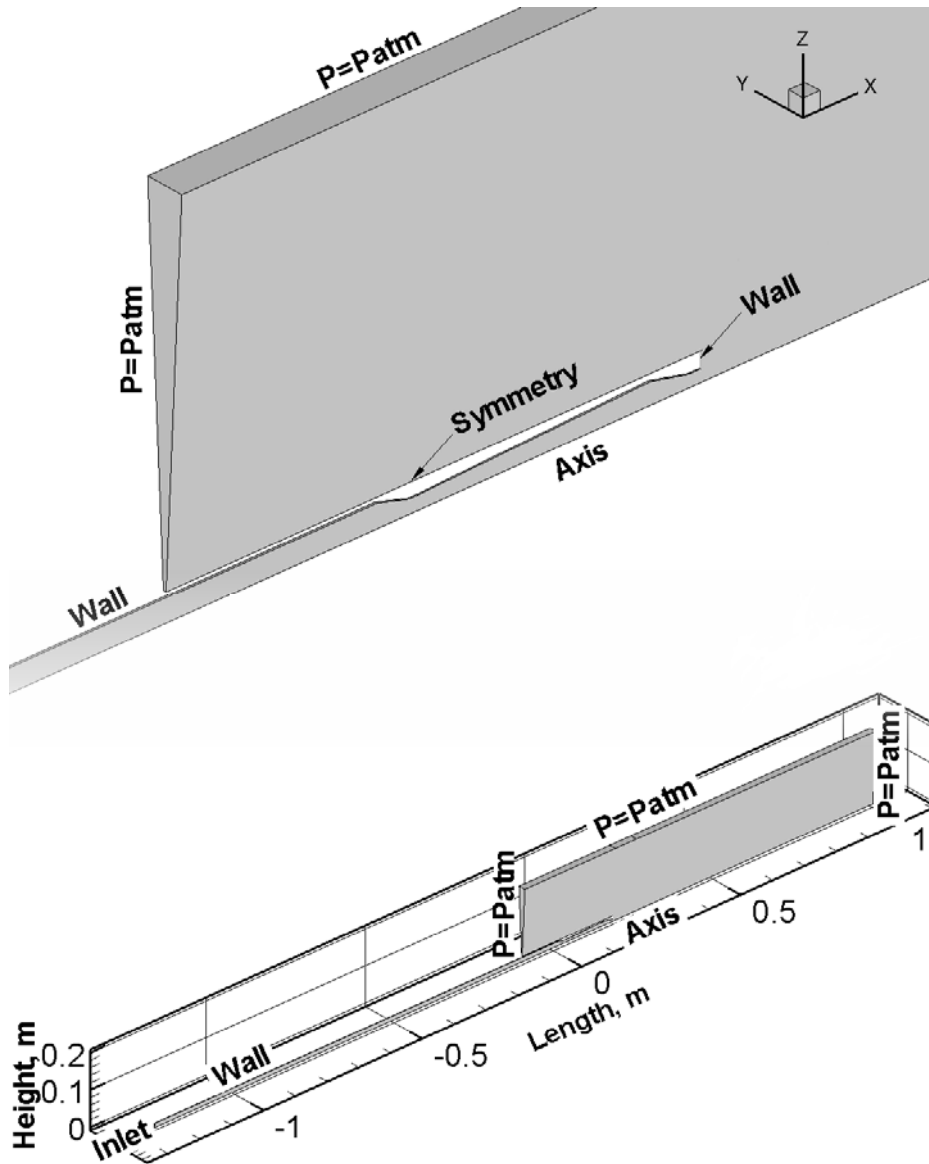


Figure 4-2. Computational domain and boundary conditions (the area around the nozzle is magnified and shown in the upper part of the figure).

The boundary conditions utilized in the simulations are also marked in Figure 4-2. At the nozzle inlet, the air and water flow rates from Table 4-1 or Table 4-2 are assigned. The volume fraction is calculated based on the pressure, which is extrapolated from the inside of the domain during the solution. It was shown in Chapter 3 that no matter what bubble diameter we chose at the inlet, by the half length of the pipe it reaches the value determined by the balance between the break-up and coalescence processes. In this study the value of 10 mm is used. Nozzle walls, inside and outside, are treated according to the procedure

Chapter 4. Gas-assisted atomization including flow through the nozzle, phase inversion, and spray dispersion

described in Section 2.1.12.1. All outside boundaries are equal pressure boundaries, and the pressure is atmospheric. If there is an inflow through these boundaries, then it is assumed that there are no droplets in the entering gas. The sides of the wedge are treated as symmetry boundaries, that is, no flux of any parameter can come through them.

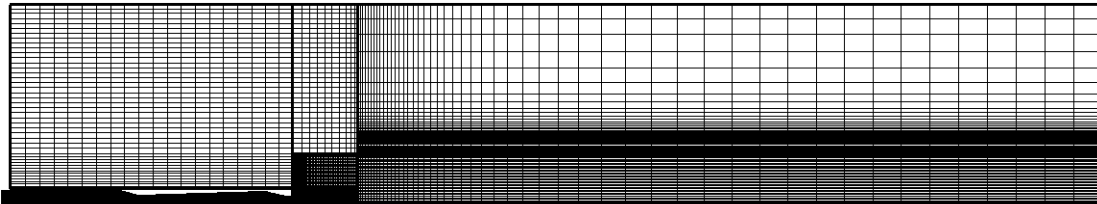


Figure 4-3. Computational grid and domain segmentation.

It is shown in Figure 4-3 that for the discretization, the computational domain was split into five segments. Note that only a small part of the entrance pipe is included in this figure. The mesh is highly non-uniform in order to provide a good resolution in the areas of high gradients, i.e. near the nozzle exit and around the edges of the spray. In order to assess grid independence, the solution for different grids needs to be evaluated. First of all, the grid independence of the solution of the flow inside the nozzle has already been investigated in Section 3.1.4. Therefore, the current study focuses on the grid refinement outside the nozzle in the spray area, leaving the nozzle grid the same. Three sets of numerical grids were considered: small (8 524 grid cells), medium (11 164 grid cells), and fine (15 904 grid cells). The flow conditions, for which the grid independence study was conducted, correspond to Case A1 from Table 4-1. Even though the equations are transient and are solved in a fully transient mode, the final solution exhibits very limited time-dependence. Therefore, the converged results will be time-averaged and analysed as steady state. While there are some observable differences between the solutions for coarse and medium grids, the variations between the medium and fine grid solutions are rather small. Thus, in all subsequent simulations presented in this section, the medium grid is used.

4.1.3. Comparison with experimental results

The numerical solutions for Case A1 and Case A2 described in Table 4-1 are compared with data obtained during the test runs. Note that the model of the gas-liquid flow

Chapter 4. Gas-assisted atomization including flow through the nozzle, phase inversion, and spray dispersion

through the nozzle (see Chapter 3) is part of the more comprehensive model presented in the current chapter. This part has already been validated based on detailed pressure measurements along the nozzle wall in Section 3.1.5. Therefore, the current investigation is focussing on the spray area. However, for the sake of completeness, some pressure data are also presented and compared with the measurements obtained during the spraying experiments. Figure 4-4 demonstrates both the simulated pressure profiles along the nozzle wall and the test values. It is evident that the agreement is excellent for Case A1 (2% GLR) and satisfactory for Case A2 (4% GLR).

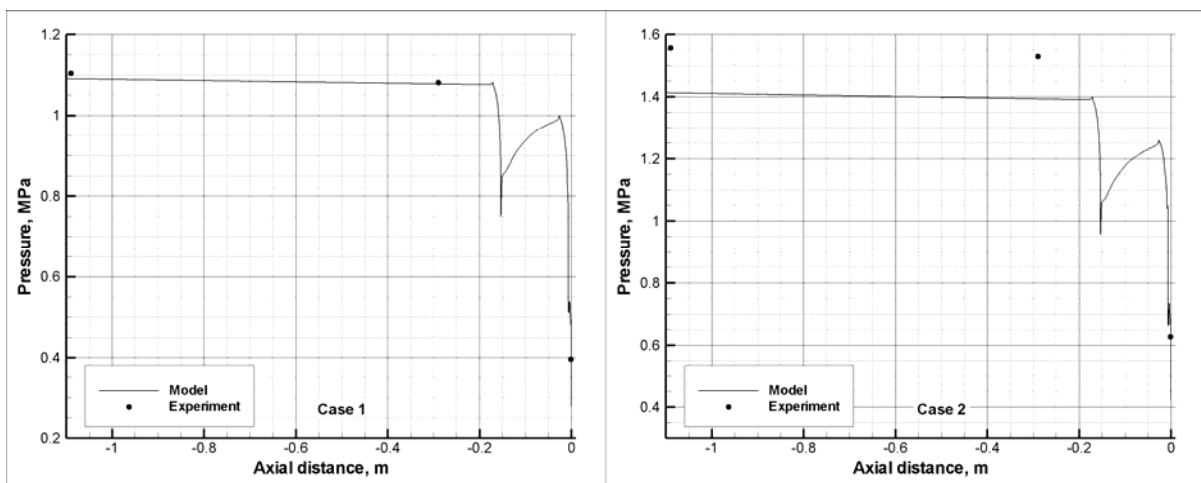


Figure 4-4. Comparison between model predictions and pressure measurements along the wall of the inlet pipe and the nozzle.

Next, the radial profiles of the water fluxes ($\alpha_i \rho_i \mathbf{V}_i \cdot \mathbf{k}$, where \mathbf{k} is the vector collinear with the axis of symmetry) are compared at two different distances from the nozzle end. During the experiments, the measurements were taken across the full cross-section. However, it was observed that the circumferential variations were minimal and within the range of experimental uncertainty. Because of the axisymmetric simplification employed during modelling, the results have to be averaged along the circumferential coordinate before comparison. Figure 4-5 presents the predicted and measured profiles. It can be seen that the predicted curves represent the distribution of fluxes qualitatively correctly. While at 15.25 cm the flow in Case A1 exhibits a strong axial maximum and a smaller peripheral maximum, the flow in Case A2 has a weak central maximum and a larger maximum closer to the periphery. With the increase of the distance from the nozzle, both cases demonstrate that the

Chapter 4. Gas-assisted atomization including flow through the nozzle, phase inversion, and spray dispersion

higher liquid content area shifts towards the periphery of the spray. This area of high liquid volume fraction is more pronounced for Case A2. Even though there is some disagreement between the measured points and modelling profiles, the quantitative comparison is reasonably good, especially considering the very complex nature of the modelled process and the fact that while many closure correlations were used in the model, only the values of the critical volume fraction and the relative velocity constant were adjusted to match experimental data.

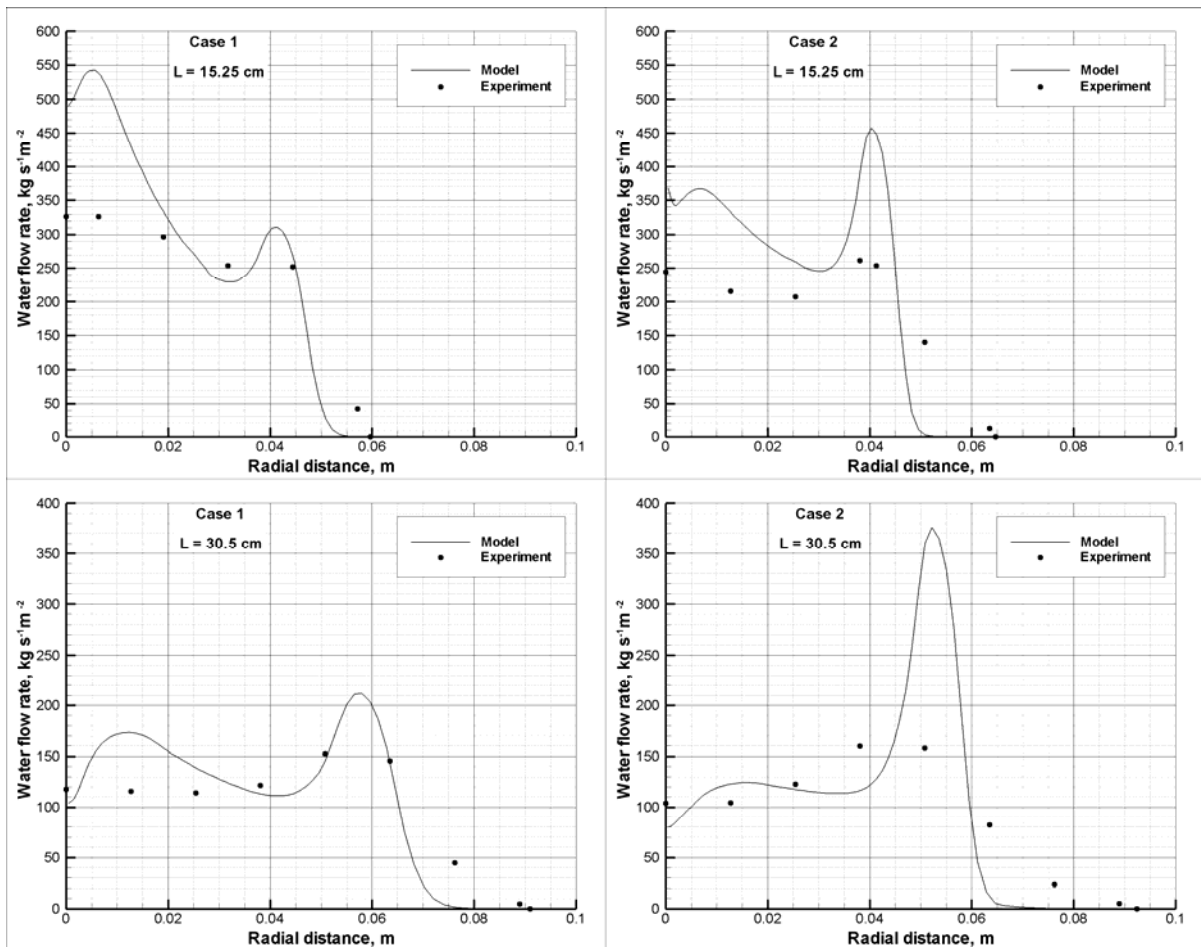


Figure 4-5. Comparison between model predictions and water flux measurements in radial direction at different distances from the nozzle exit.

4.1.3.1. Influence of the phase inversion critical liquid volume fraction values

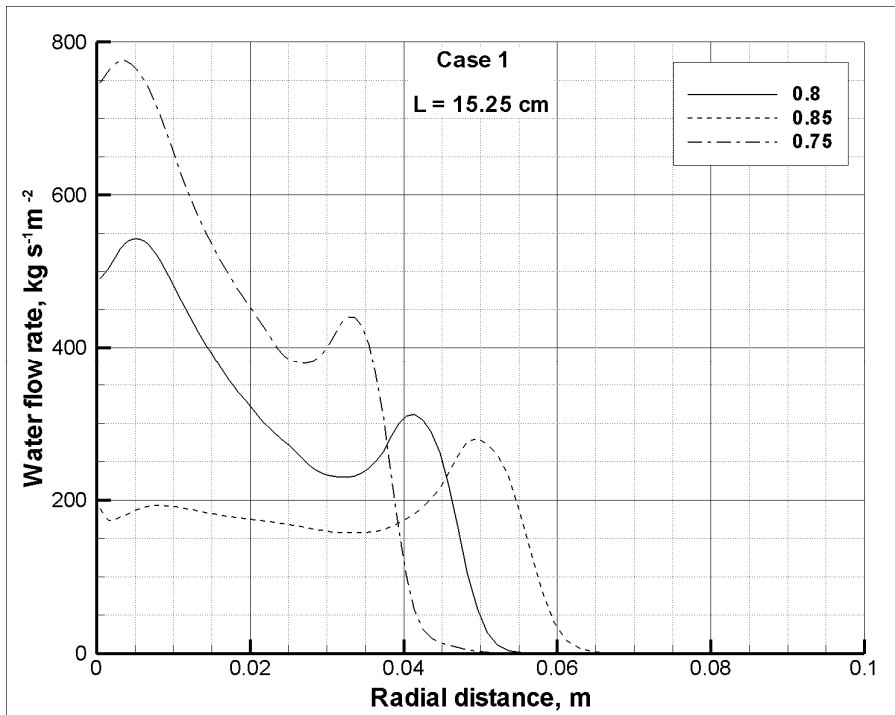


Figure 4-6. Profiles of the water flow rate that correspond to the various values of the critical volume fraction α_d^{\max} .

It is instructive to investigate the influence of the choice of the critical volume fraction value on the solution. We constructed two additional cases that use the same flow parameters as Case A1 (see Table 4-1), but different values of the critical volume fraction α_d^{\max} —0.75 and 0.85. Next, we compare the results with the original Case A1 that uses the value of 0.8. The comparison of liquid flow rate distributions shown in Figure 4-6 reveals substantial dependence of the profile on the critical volume fraction value. The reduction of the volume fraction moves the phase inversion surface upstream in the nozzle; this affects the spray shape by making it less dispersed. Alternatively, the increase of the volume fraction causes the phase inversion surface to move downstream resulting in a wider jet of liquid droplets. In addition, for the critical volume fraction of 0.85, the axial maximum disappears, leaving only the peripheral one. The importance of the selection of the critical volume fraction is substantial, and further studies are required. Meanwhile, the sprays resulting from gas-assisted atomization can be successfully modelled with the critical volume fraction value chosen according to the indirect experimental data.

Chapter 4. Gas-assisted atomization including flow through the nozzle, phase inversion, and spray dispersion

4.1.4. Flow analysis

In order to understand the nozzle operation, the solutions for both cases are closely examined. As the flow inside the nozzle has already been investigated and described in Chapter 3, the present analysis focuses mostly on the spray formation and dispersion; however, some features of the nozzle flow related to the atomization are also presented to facilitate understanding.

4.1.4.1. Volume fraction distribution

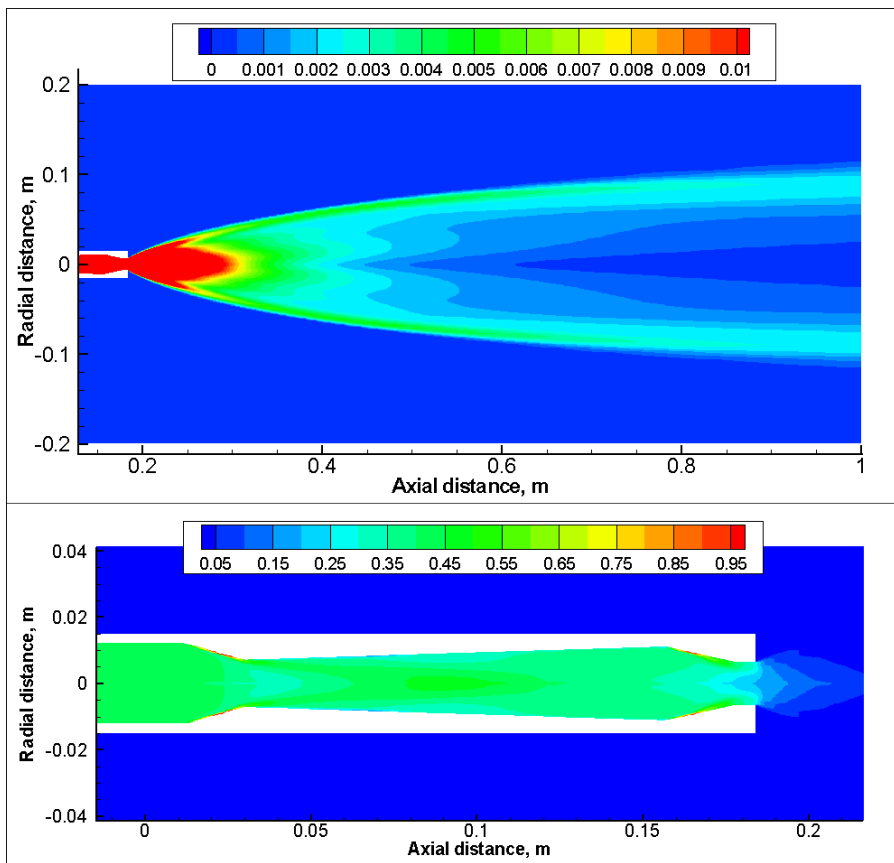


Figure 4-7. Liquid volume fraction distribution for Case A1. (a) in the spray; (b) in the nozzle.

Chapter 4. Gas-assisted atomization including flow through the nozzle, phase inversion, and spray dispersion

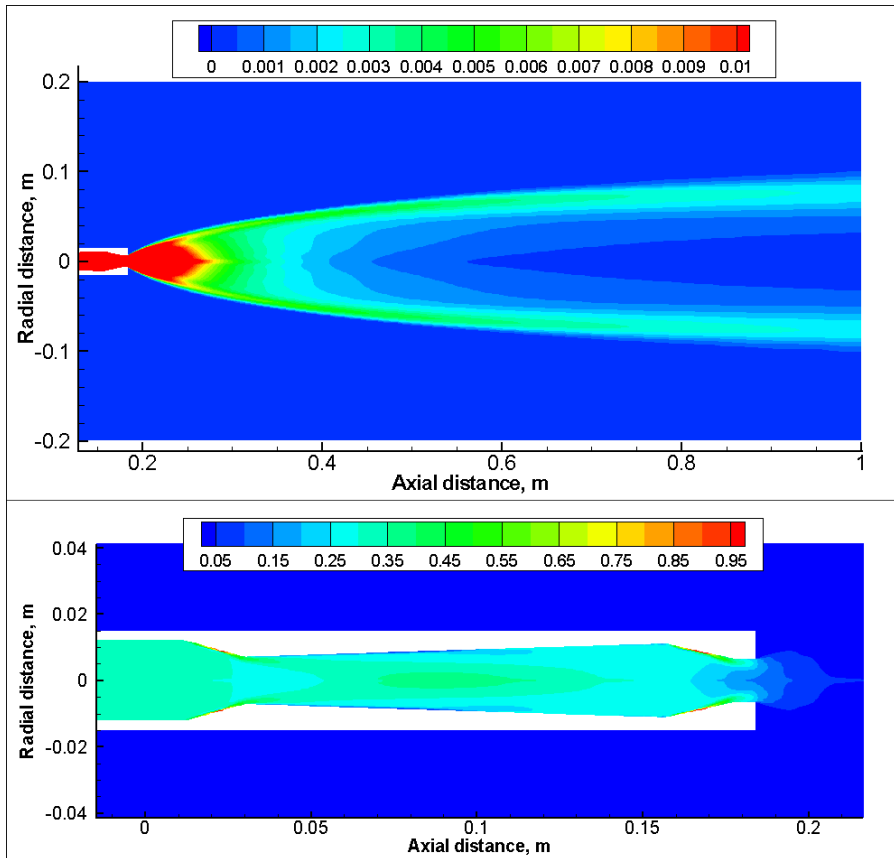


Figure 4-8. Liquid volume fraction distribution for Case A2. (a) in the spray; (b) in the nozzle.

The contour plots of the liquid volume fractions (water, before the phase inversion surface, and droplets, after) for Case A1 are presented in Figure 4-7. For viewing convenience in this and all subsequent contour plots, a cross-sectional view, which was obtained by mirroring an axisymmetric solution, is shown. The lower part of the figure shows the nozzle area, and the upper, the spray area. Note that the scales of the contour maps are different to improve presentation. It can be seen that at each convergent section of the nozzle, the phases separate due to the inertial forces. At the nozzle exit, the gradient of the volume fraction is clearly visible: there is more liquid on the periphery of the nozzle near the wall than around the centreline. According to the definition of the catastrophic phase inversion from Section 2.1.6 and the liquid volume fraction distribution inside the nozzle (Figure 4-7), it is evident that the atomization happens near the nozzle exit plane. Thus, inside the nozzle the air is dispersed into the water as bubbles, and outside the nozzle the droplets are dispersed in the air. The spray fills the so-called tulip shape that has been observed

Chapter 4. Gas-assisted atomization including flow through the nozzle, phase inversion, and spray dispersion

experimentally. This shape reflects the physics of the air-assisted atomization process under consideration. Due to the rapid pressure drop in the area around the nozzle exit (Figure 4-9), the air expands as its density decreases. Because of the interfacial forces, the drag and virtual mass for the water-continuous flow and the drag for the air-continuous flow, liquid has to be accelerated together with the gas, resulting in a more gradual pressure drop than for the pure gaseous flow. It can be seen that the areas of higher pressure extend slightly downstream from the nozzle orifice. While inside the nozzle the gas acceleration is limited to the axial direction, after the exit, a significant portion of the momentum is directed radially. This radial momentum is transferred to the droplets that begin flowing outwards; at the same time, due to continuity, air from the outside fills in the central part of the spray. This entrained air reduces the radial momentum of the droplets; therefore, their trajectories become curved towards the axis.

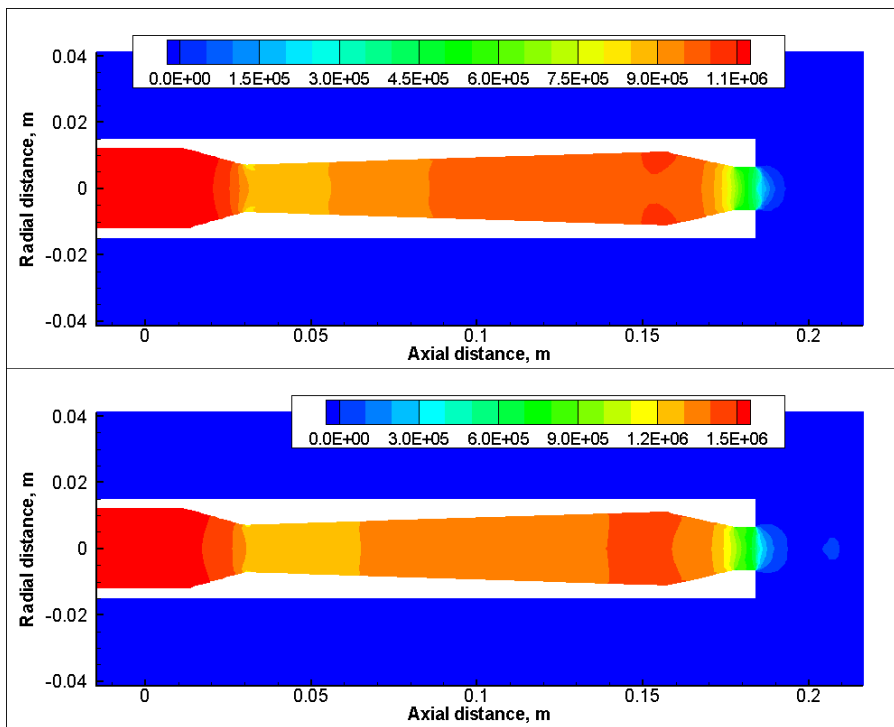


Figure 4-9. Pressure contours in and around the nozzle (in MPa). (a) Case A1; (b) Case A2.

It is important to note that the droplets distribution across the spray is far from uniform. As it observed before in the mass flow rate profiles (Figure 4-5), after a certain distance from the nozzle exit, there are more droplets in the periphery of the spray than in the

Chapter 4. Gas-assisted atomization including flow through the nozzle, phase inversion, and spray dispersion

centre. There are two contributing factors to this distribution. Firstly, it is connected to the non-uniformity of the phase distribution already formed before the phase inversion surface. Secondly, the influence of the air entrainment, explained above, increases with the distance from the centreline due to the larger difference between the phase velocities. Thus, the droplets in the outer part of the spray are pushed towards the centre more than those in the middle. It has to be noted that while plots show some discontinuity right at the centreline, which is the axis of symmetry, this is probably a numerical artefact of the coordinate transformations due to the axis singularity and does not have a physical meaning. The overall features of the water volume fractions distribution in Case A2, shown in Figure 4-8, are similar. However, some important differences are noticeable. The spray is visibly less dispersed and the peripheral maximum is formed at a shorter distance downstream from the nozzle than in the previous case (see also Figure 4-5). The reason for such behaviour is discussed below, after examining of the average droplet diameter. In addition, it can be inferred from the contour plot that in the central area of the nozzle, the phase inversion takes place inside the nozzle upstream from the exit plane.

4.1.4.2. Velocity variations

Next, let us analyse the velocity distribution for both phases. Figure 4-10 shows the air velocity magnitude contours for both cases. The plots demonstrate a rapid increase of the velocity right after the nozzle exit. That happens because of the significant reduction of the drag and the virtual mass forces after the atomization. Even though the air still transfers some momentum to the water droplets, this transfer is less than for the liquid-continuous flow inside the nozzle, and the gas acceleration can be higher. Downstream from the intensive expansion area, which coincides with the high pressure gradients, the air slows down due to the interfacial friction with the droplets, which in the absence of the source terms from the density decrease, becomes the dominant force in the momentum equation. As expected, comparison of the two plots for the different cases shows a substantially higher gas velocity for the higher GLR case (Case A2). The reason lies in a higher inlet air flow rate that results in a higher pressure drop, and, hence, in higher acceleration.

Chapter 4. Gas-assisted atomization including flow through the nozzle, phase inversion, and spray dispersion

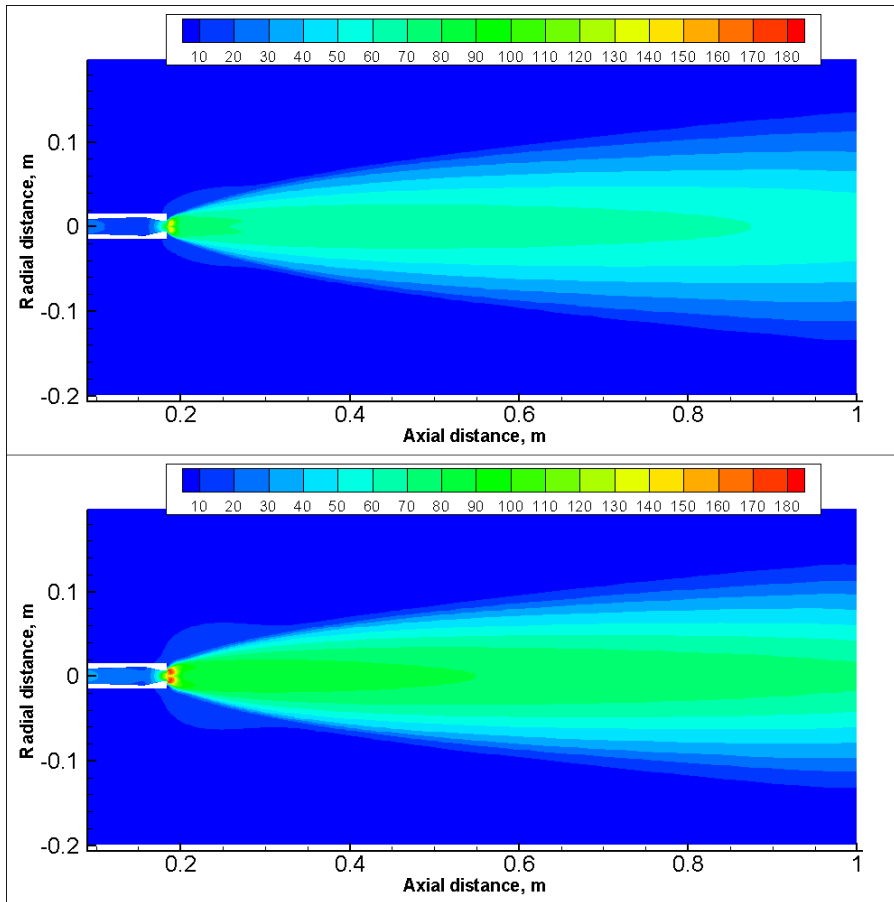


Figure 4-10. Air velocity magnitude contours (in m s^{-1}). (a) Case A1; (b) Case A2.

As discussed above, the droplets are accelerated together with the air. The droplets velocity contours are presented in Figure 4-11. Due to the much higher inertia of the droplets, they are slower to accelerate and slower to decelerate. Thus, even though their velocity follows the changes of the air velocity, the amplitudes of the changes are less. Similar to the air velocity, the droplet velocities in Case A2 are higher than in Case A1. This is caused by the higher air velocity and the interfacial momentum transfer.

Chapter 4. Gas-assisted atomization including flow through the nozzle, phase inversion, and spray dispersion

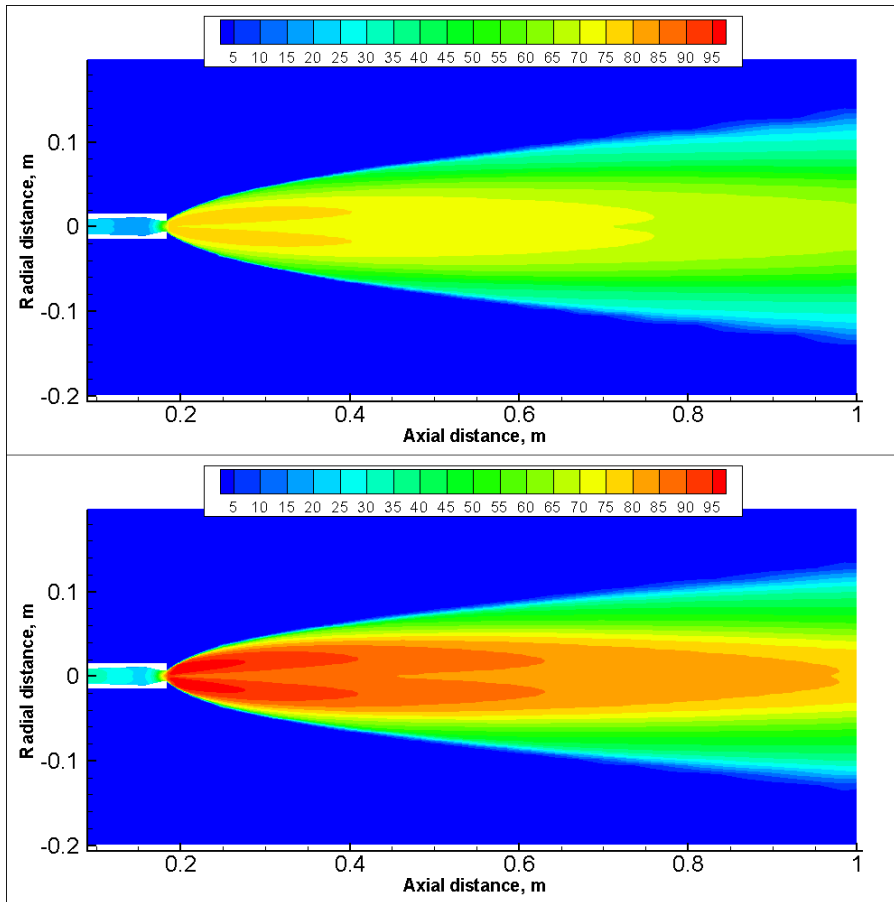


Figure 4-11. Water droplets velocity magnitude contours (in m s^{-1}). (a) Case A1; (b) Case A2.

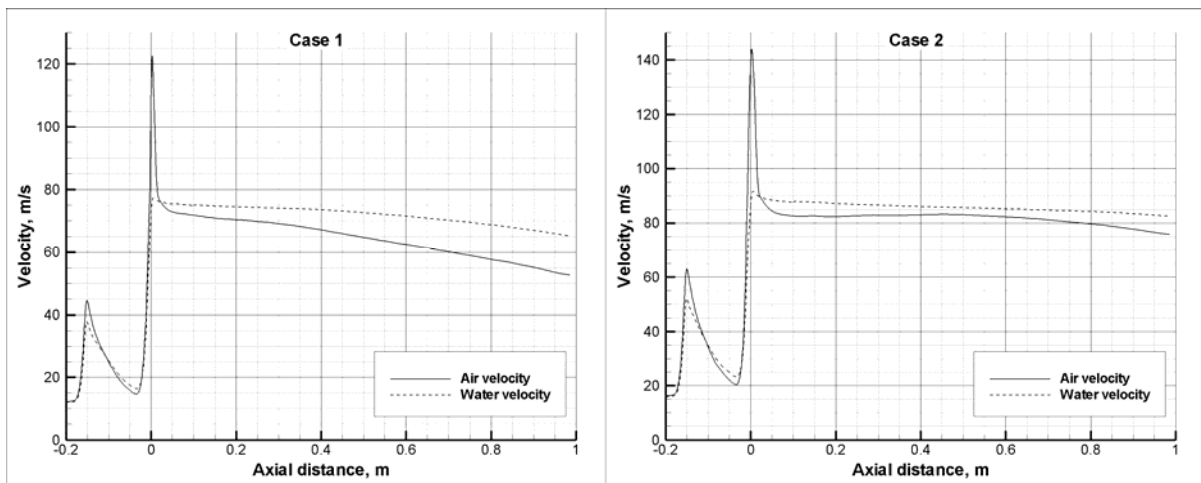


Figure 4-12. Air and droplets axial velocity profiles along the centreline for Case A1 (left) and Case A2 (right). The nozzle orifice is located at $x = 0$.

For a better understanding of the velocity variations in the spray, it is instructive to plot the phase axial velocities along the centreline on the same graph. Figure 4-12 shows this

Chapter 4. Gas-assisted atomization including flow through the nozzle, phase inversion, and spray dispersion

graph for the two cases. It illustrates the above discussion by exposing the difference between the air and droplet velocities. It can be seen that inside the nozzle, which ends at the zero axial coordinate, the velocity of the liquid follows closely that of the air. Only approaching to the exit plane (and to the phase inversion surface) do they begin to separate. Right after this plane, the air velocity spikes, causing some growth of the liquid velocity by transferring momentum to it. After the spike, the air velocity drops below the velocity of the droplets due to the higher momentum dissipation. Downstream from the points where the profiles cross, the momentum transfer is directed towards the gaseous phase keeping the air velocity from further reduction. Both velocities gradually decline, as the water jet gets dispersed. This distribution is typical for both cases; the difference is mainly in the values, which are larger for Case A2 for reasons already discussed, and in the rate of velocity decline, which is higher for Case A1 because of lower mass flow rate.

4.1.4.3. Discrete phase diameter variations

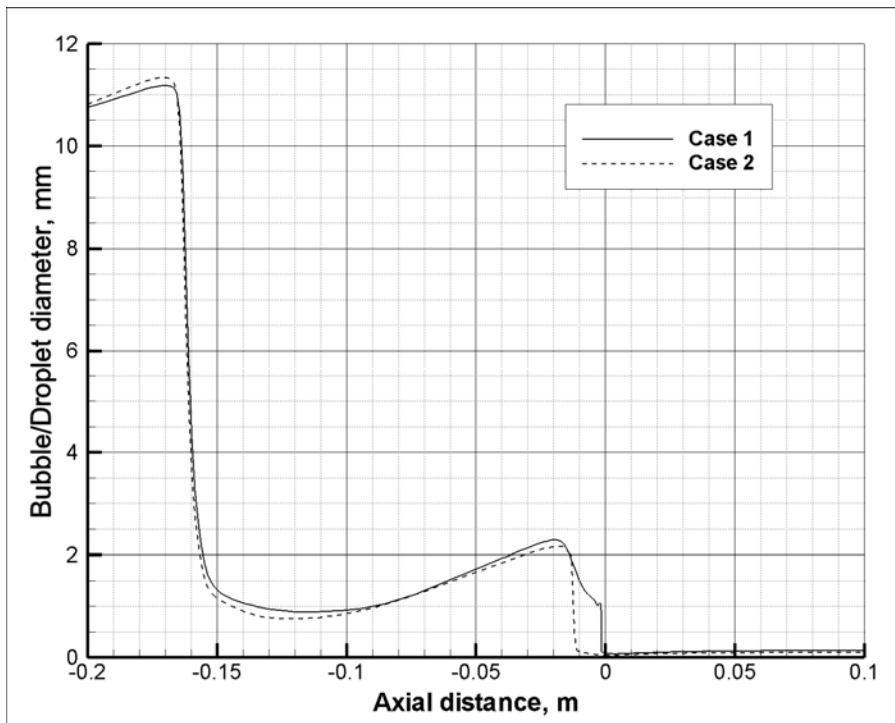


Figure 4-13. Average diameter of the discrete phase (bubbles or droplets) profiles along the centreline for both cases.

Chapter 4. Gas-assisted atomization including flow through the nozzle, phase inversion, and spray dispersion

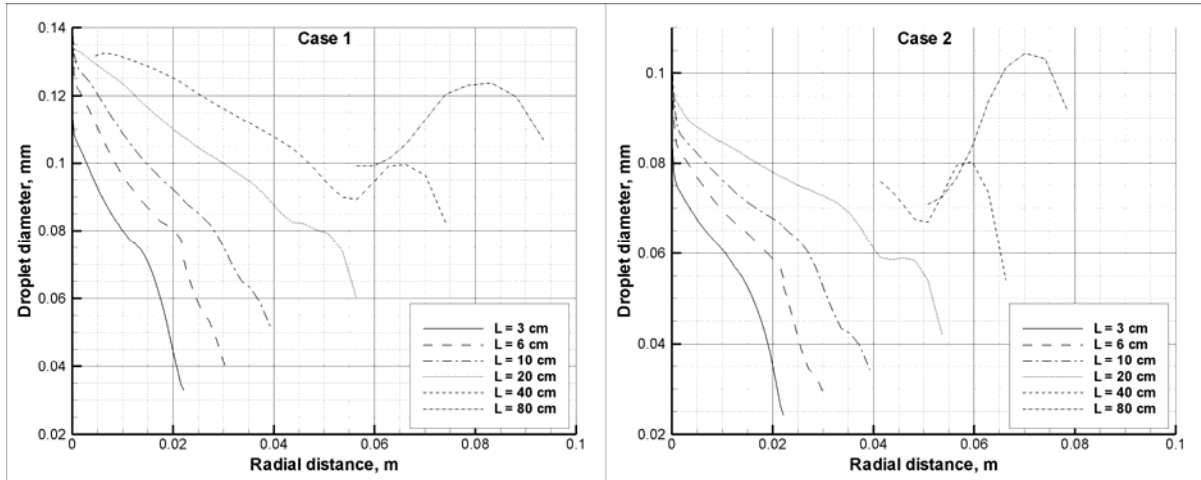


Figure 4-14. Profiles of the droplet average diameter at different distances from the nozzle orifice for Case A1 (left) and Case A2 (right). The curves are shown only if the local droplets volume fraction exceeds 0.001.

Finally, let us examine the diameter of the particles. Figure 4-13 presents profiles of the average diameter of bubbles, before the atomization, and droplets, after the atomization, for both cases. In the pipe leading to the nozzle the bubble diameter is slightly less than 10 mm which is more than one-third of the pipe diameter. Inside the nozzle the bubble diameter drops to about 1 mm after the first convergent section, then recovers somewhat to values around 2 mm. As the flow passes through the phase inversion surface, the diameter drops discontinuously, according to the assumptions made in Section 2.1.6.

$$\frac{d_{droplet}}{d_{bubble}} = \left(\frac{\alpha_d^{\max}}{1 - \alpha_d^{\max}} \right)^{\frac{1}{3}} \quad (4-1)$$

Immediately after this fall, the droplet diameter continues to decrease due to the extremely high break-up frequency. This high frequency is responsible for a relative insensitivity of the model to the prescribed values of the droplet diameter (particle number density) at the phase inversion surface. At a very short distance from the nozzle, where the rapid air expansion stops, the coalescence term begins to dominate the particle number density equation. Thus, the diameter slightly increases as the droplet travels a few centimetres from the nozzle. It is interesting to note that for both flow regimes, liquid-continuous and gas-continuous, the dominant break-up mechanism is the turbulent fluctuation of the continuous phase, as opposed to the interfacial drag. This is concluded from the analysis of the results and Eqs.

Chapter 4. Gas-assisted atomization including flow through the nozzle, phase inversion, and spray dispersion

(2-60) and (2-80). Even though the velocity difference is quite large directly after the atomization, the turbulent dissipation is also very large in the same area.

While inside the nozzle the bubble diameter does not exhibit substantial radial variation, outside the nozzle the droplet diameter changes considerably in the radial direction. Figure 4-14 shows radial profiles of the droplet diameter at different distances from the nozzle orifices for both cases. Generally, the largest diameter droplets are located near the centreline of the spray, and the smallest near the periphery. At the same time, a tendency can be seen after a certain distance for the diameter to form a second maximum closer to an outside edge of the spray. As we have already seen in Figure 4-13, the droplet diameter increases slightly due to coalescence with the particle movement away from the nozzle. This growth is more significant in the vicinity of the nozzle, where the concentrations, and hence, the coalescence rates are higher. It is clear that generally the droplet diameters in Case A2 are markedly smaller than those in Case A1. This observation provides a key to understanding the difference in spray shape between the cases (Figure 4-7 and Figure 4-8). The smaller diameter is explained by the higher interfacial friction that the droplets are experiencing from the entrained air. Therefore, the angle of the spray expansion is smaller and the shape is less dispersed.

The range of the values of the simulated bubble diameter in the nozzle (1 mm) and droplet diameter in the spray (100 μm) corresponds to the reported experimental observations. The limited comparison with the experiment does not constitute sufficient validation, which will be performed in the next section.

4.2. Study B – Droplet diameter

4.2.1. Experimental set-up

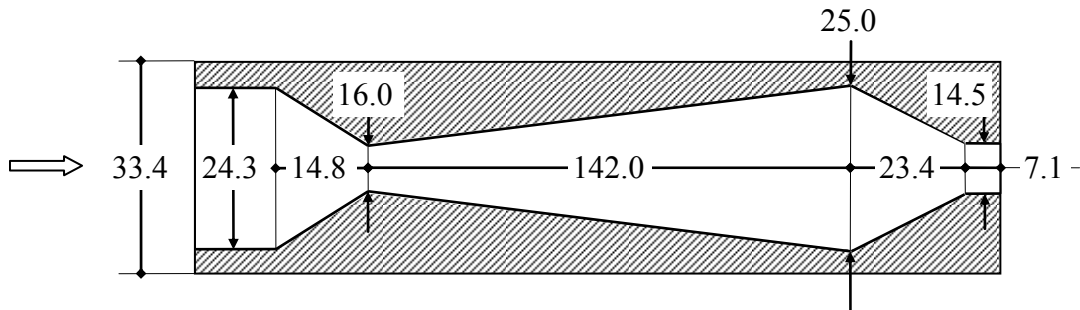


Figure 4-15. TE1.25 nozzle geometry (All dimensions are in mm; not to scale.)

A scaled-up TE1.25-type nozzle, shown in Figure 4-15, is investigated. This is a slightly larger nozzle than the one used in the liquid flow rate experiments. Otherwise, the experimental set-up and materials used (air and water) were exactly the same (see Figure 4-1). During the tests, the particle size distribution was measured using shadowgraphy, which is a non-intrusive image based method that uses background illumination. The measurements were taken at radial distances from 4 cm to 9 cm in cross-sectional planes perpendicular to the nozzle exit plane at two locations: 14'' (0.3556 m) and 24'' (0.6096 m) from the nozzle orifice. The values of the flow rates of the air and water are presented in Table 4-2.

Table 4-2. Air and water flow rates for investigated cases in droplet diameter experiments.

Case #	B1	B2	B3
Air flow rate, kg s^{-1}	0.0504	0.063	0.0758
Water flow rate, kg s^{-1}	2.52	3.15	3.79
Gas to liquid ratio, %	2	2	2

4.2.2. Interpretation of experimental results

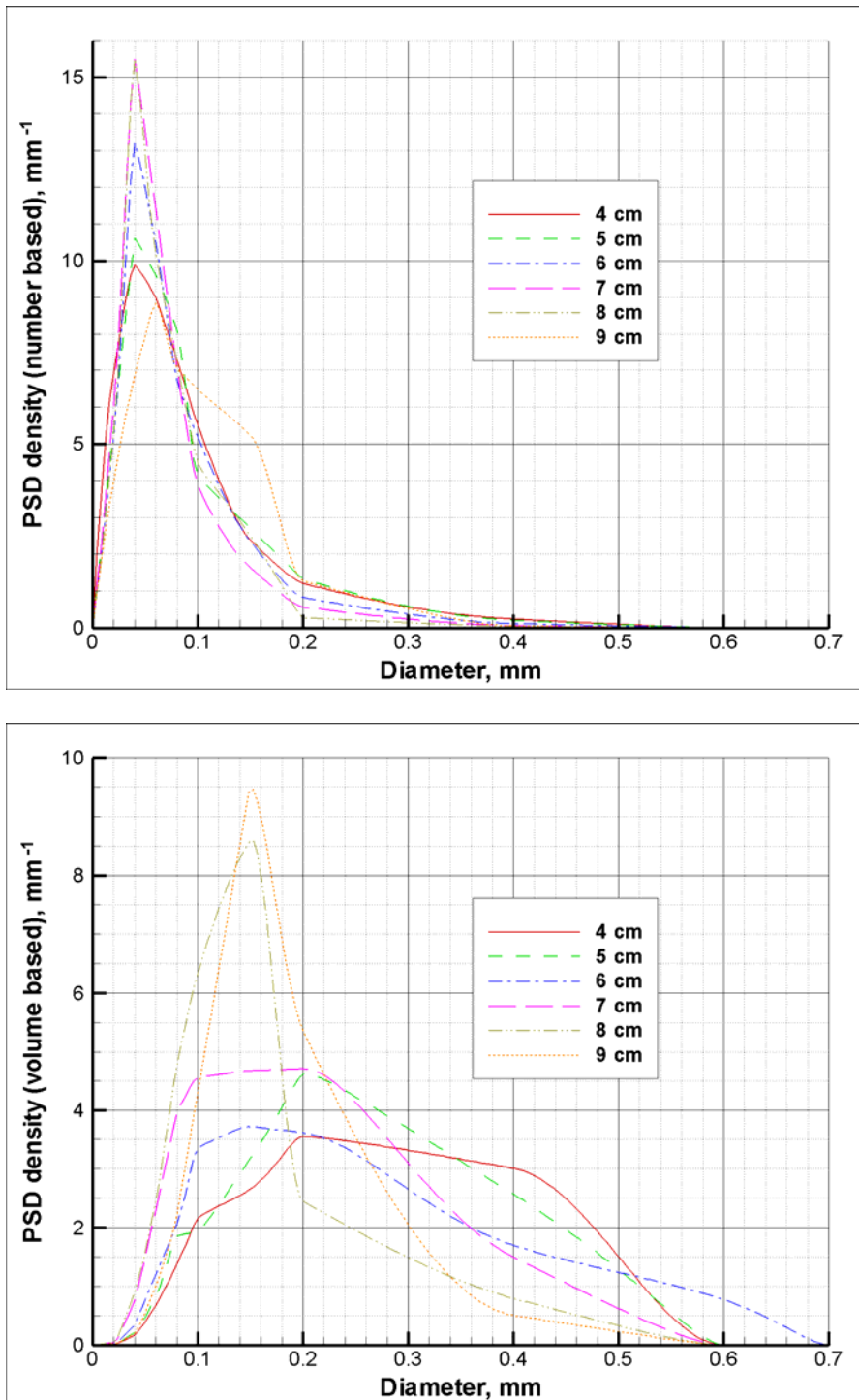


Figure 4-16. PSD density of water droplets at 0.3556 m axial distance from the nozzle orifice for Case 1 at different radial distances; number based (above), volume based (below).

Chapter 4. Gas-assisted atomization including flow through the nozzle, phase inversion, and spray dispersion

During the experiments, individual droplet diameter data were collected at various locations in the spray. Therefore, it is possible to plot Particle Size Distribution (PSD) graphs at each location. Figure 4-16 shows two such graphs for one of the investigated cases; in one of them (placed above) the density is calculated based on the number of droplets in each group, and in another (placed below), by the volume. We can see that some curves are smoother than others. It is especially visible on the volume based PSD density curves. This is the result of the variations in droplet numbers at different locations, i.e. the inherent non-uniformity of the liquid radial distribution in the spray. As investigated in Section 4.1, the maximum droplet concentration is located somewhere near the periphery of the jet; there are relatively fewer droplets in the central area, and many fewer outside the concentration peak region. Clearly, it is very difficult to draw any conclusions from these graphs, and we need some averaging procedure for spatial data analysis and for comparison with the numerical model. As we use a particle number density concept in the model, and the particles number density is defined on the volume basis (see Eqs. (2-56) and (2-57)), we need to use volume (or mass) averaging in order to be consistent. That is, the average droplet diameter has to be calculated as

$$d = \sqrt[3]{\frac{\sum_{i=1}^N d_i^3}{N}} \quad (4-2)$$

Using Eq. (4-2), we can obtain average values at different spatial locations and also at different areas that can subsequently be used for various purposes.

4.2.3. Computational domain

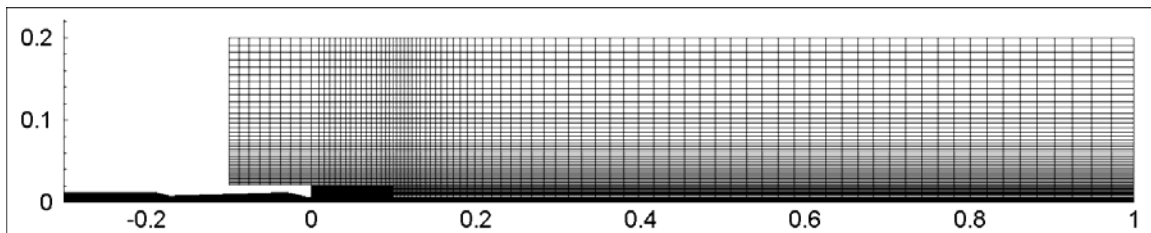


Figure 4-17. Computational grid.

Chapter 4. Gas-assisted atomization including flow through the nozzle, phase inversion, and spray dispersion

The computational domain is axisymmetric and includes the nozzle and its surrounding areas where the spray is dispersed. The domain extends axially 1 m from the nozzle exit and radially – 0.2 m from the axis. In addition, a short piece of pipe (0.1 m) with the same diameter as the nozzle inlet is added in front of it to allow for some flow development before the mixture enters the nozzle. A multi-segment curvilinear non-uniform grid, shown in Figure 4-17, is developed to provide a good resolution in the areas of high flow gradients – nozzle and its immediate vicinity – and to allow for practical computations by being relatively coarse far from the nozzle. The grid contains 10 130 grid cells. The modeling set-up and the grid distribution are very similar to the previously used ones for liquid flow rates study (see Section 4.1.1). As grid independence studies have been performed for a very similar set-up in Section 4.1.2, they are not repeated in the current work.

4.2.4. Comparison with experimental results

4.2.4.1. Model adjustment

Table 4-3. Comparison between experimental and predicted results for $C_{vel} = 3$.

Case #		B1	B2	B3
Results at 0.3556 m	Experiment, μm	95.5	96.7	94.1
	Model, μm	106.0	97.0	94.6
	Error, %	+11.0	+0.3	+1.7
Results at 0.6096 m	Experiment, μm	105.0	102.1	99.9
	Model, μm	118.1	108.3	100.0
	Error, %	+12.5	+6.1	+0.6

As was outlined in the description of the model (Section 2.1.5.2), the constant in Eq. (2-82), C_{vel} , needs to be determined based on the empirical data. To facilitate the process of finding an acceptable value, we compare the experimental and predicted values of the averaged droplet diameter at two cross-sectional planes for all three cases. That is, we average all droplets that were detected in the experiment at each cross-section, and we find a corresponding temporally and spatially average diameter from the modeling results by averaging along the radial distance from 3.5 cm to 9.5 cm. After running some parametric

Chapter 4. Gas-assisted atomization including flow through the nozzle, phase inversion, and spray dispersion

studies, it was determined that $C_{vel} = 3$ offers the best agreement between experimental and numerical results. As outlined in Table 4-3, the agreement is generally good with error below 13% for all cases. While additional “fine-tuning” of C_{vel} to further improve the agreement is possible, it is not pursued here because the obtained value already provides accuracy that falls within overall modeling errors. It has to be noted that all previous comparisons with other experimental data reported in Sections 3.1.5 still remain valid with current model development.

4.2.4.2. Average droplet diameter comparison

After the value for C_{vel} is determined, we can compare cross-sectional profiles of the average droplet diameter with experimental data points obtained by local averaging. Figure 4-18 shows this comparison for all cases. Note that the radial distances are limited by 10 cm because above this value the droplet volume fractions are very small (almost non-existent) rendering the average diameter meaningless. We can see that generally the agreement is fairly good. The trend of decreasing droplet diameter from the center to the periphery is correctly reproduced by the model. Also, in agreement with experimental evidence as shown in Table 4-3, the predicted droplet diameter decreases with the increase of the inlet flow rate. Additionally, the droplet diameter increases with increasing axial distance (which is also in accord with experimental data from Table 4-3) and the radial distribution becomes more uniform. One notable disagreement is that certain experimental values of the average diameter at 4 cm or 5 cm radial distance for a number of cases are significantly larger (two times in some instances) than model predictions. These large values appear due to the detected presence of a few considerably big droplets in the core area of the jet. Because of the volume averaging procedure, their influence becomes very substantial. We can speculate that these large droplets may result from some poor atomization localized in space and in time that takes place because of jet instabilities that are not accurately captured by the present model.

Chapter 4. Gas-assisted atomization including flow through the nozzle, phase inversion, and spray dispersion

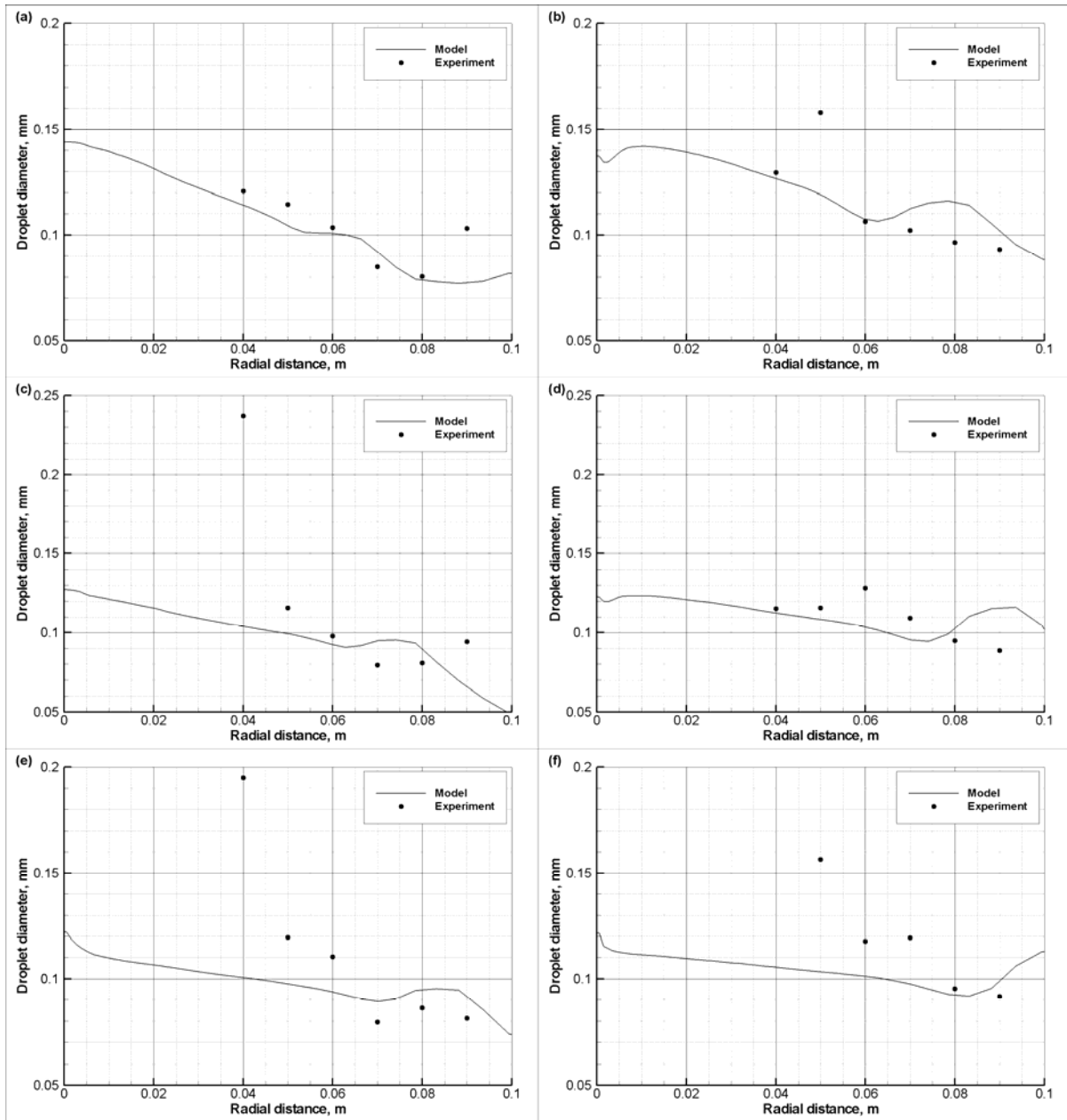


Figure 4-18. Average droplet diameter cross-sectional profile for various cases and distances from the nozzle orifice. (a) – Case B1, 0.3556 m; (b) – Case B1, 0.6096 m; (c) – Case B2, 0.3556 m; (d) – Case B2, 0.6096 m; (e) – Case B3, 0.3556 m; (f) – Case B3, 0.6096 m.

4.2.5. Flow analysis

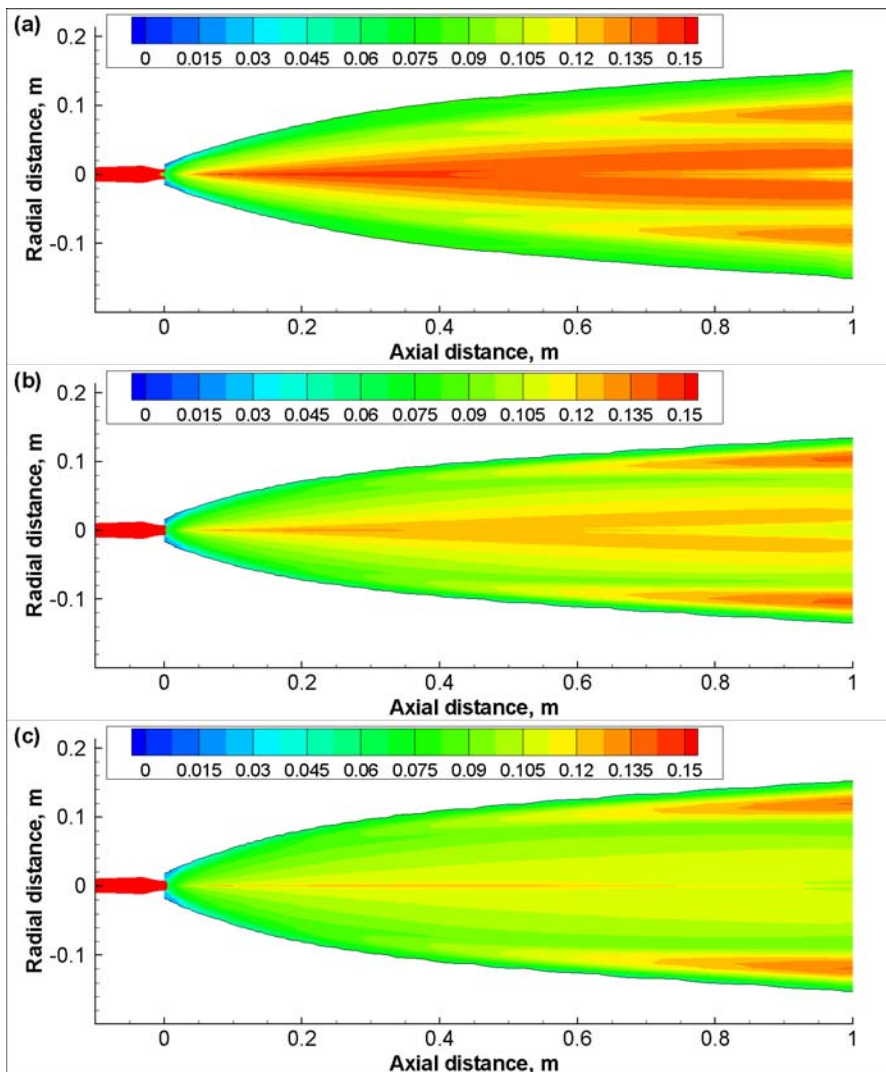


Figure 4-19. Average droplet diameter contours (in mm). (a) – Case B1; (b) – Case B2; (c) – Case B3.

While some of the distribution trends can be observed from Figure 4-18 and Table 4-3, contour plots offer better visualization. Figure 4-19 presents spatial distributions of the average droplet diameter for all investigated cases. Note that for viewing convenience, these and subsequent plots are extended to a full cross-sectional view based on the axial symmetry. Also, the areas where the droplet volume fraction is below 0.0001 are blanked out to focus on the spray only. Similar to what the experimental data and graphs in Figure 4-18 showed, the particle diameter decreases from the axis towards the circumference of the jet. This happens because of the variation in break-up frequency close to the periphery of the jet. The reason

Chapter 4. Gas-assisted atomization including flow through the nozzle, phase inversion, and spray dispersion

for this increase is that in the peripheral area there is more turbulent energy available, which in turn is convected from the edges of the nozzle. To illustrate this discussion, contours of the mixture turbulent kinetic energy are plotted in Figure 4-20. We can see that a large amount of turbulence is generated immediately after the atomization due to the high interfacial velocity. However, after a short distance, most of the energy in the core area of the jet is dissipated due to the presence of liquid particles with high inertia. At the the same time, in the periphery of the jet, where there are relatively fewer droplets initially, the energy is preserved and transported with the flow.

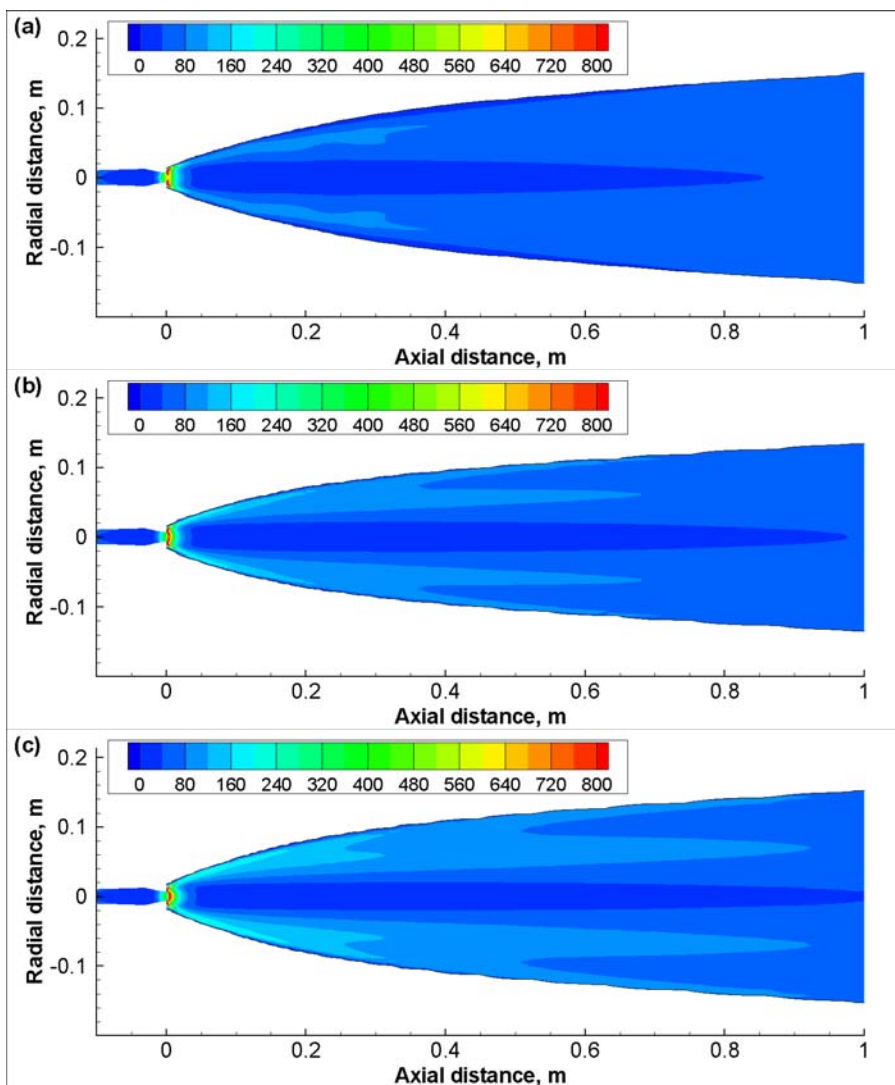


Figure 4-20. Mixture turbulent kinetic energy contours (in $\text{m}^2 \text{s}^{-2}$). (a) – Case B1; (b) – Case B2; (c) – Case B3.

Chapter 4. Gas-assisted atomization including flow through the nozzle, phase inversion, and spray dispersion

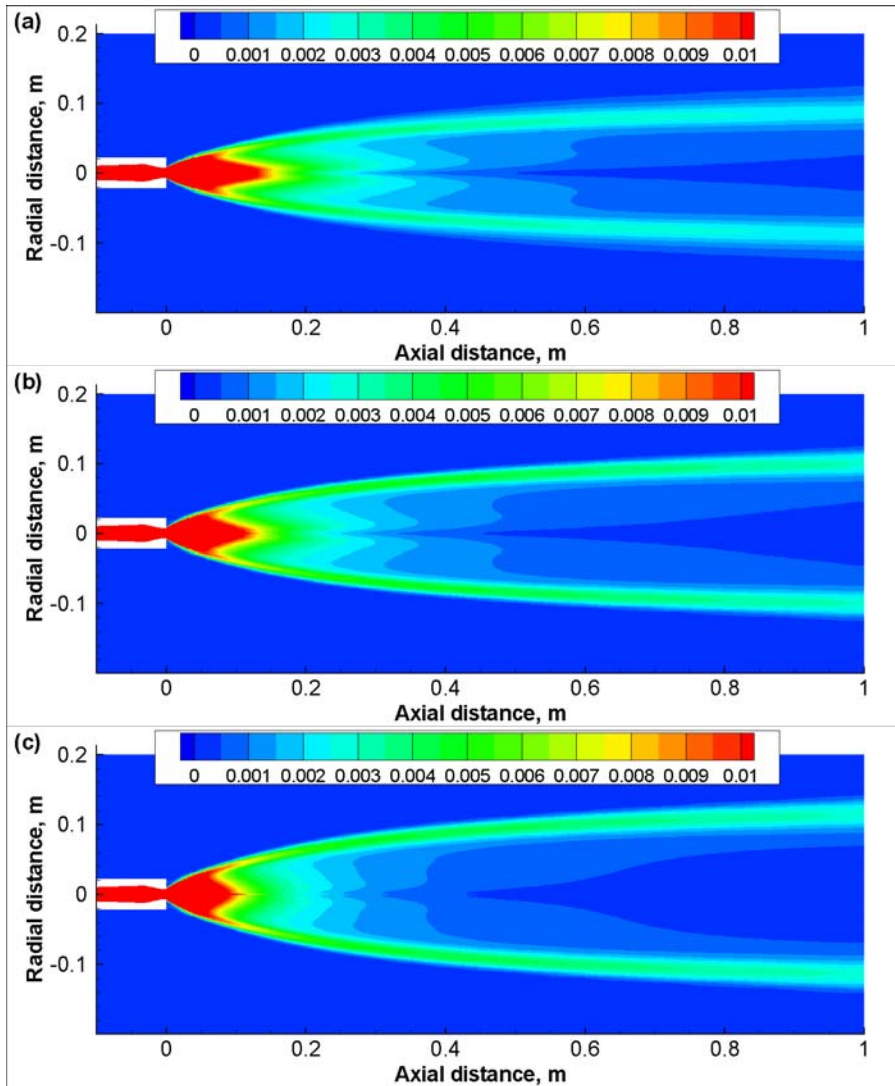


Figure 4-21. Liquid volume fraction contours. (a) – Case B1; (b) – Case B2; (c) – Case B3.

In addition, in Figure 4-19 we can also see an off-center area of an increased droplet diameter that begins to appear about 0.4 m from the nozzle exit and gets bigger further from the nozzle. It is better for this phenomenon to be analysed in connection with the liquid volume fraction distribution plots (Figure 4-21). A closer look reveals that the locations of this secondary growth area coincide with the peripheral peak areas of the jet. As the collision frequency is proportional to the volume fraction (see Eq. (2-81)), the droplets in these areas experience more coalescence than their neighbours, leading to the increase in average diameter.

Chapter 4. Gas-assisted atomization including flow through the nozzle, phase inversion, and spray dispersion

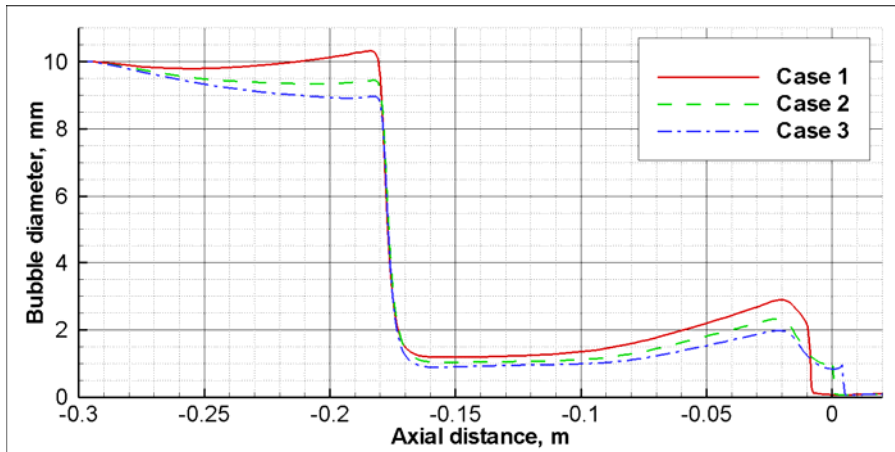


Figure 4-22. Average bubble diameter profiles along the centerline of the nozzle.

Also, we can see from Figure 4-19 that the increase of the flow rates results in the decrease of the average droplet diameter, especially in the core area. The difference is fairly substantial: 50% increase of the flow rates brings about a 50% decrease in the diameter. It becomes evident from Figure 4-20 that this takes place because more turbulence is generated by the increased flow rate, which in turn is related to the break-up frequency. This increased turbulence generation is a product of higher interfacial velocities immediately after the atomization. At the same time, the location and the average diameter value of the peripheral area of the increased diameter discussed in the previous paragraph barely changes with the flow rate variations. It is interesting to note that for the bubble diameter inside the nozzle, we have a similar phenomenon. As illustrated in Figure 4-22, the average bubble diameter decreases with the increase of the flow rate. The reason for this, however, is not turbulence, which is about the same for all cases, but the decrease of the air volume fraction because of the higher pressure drop associated with higher flow rates. Figure 4-23, showing the pressure profile along the nozzle axis for three cases, illustrates the above statement.

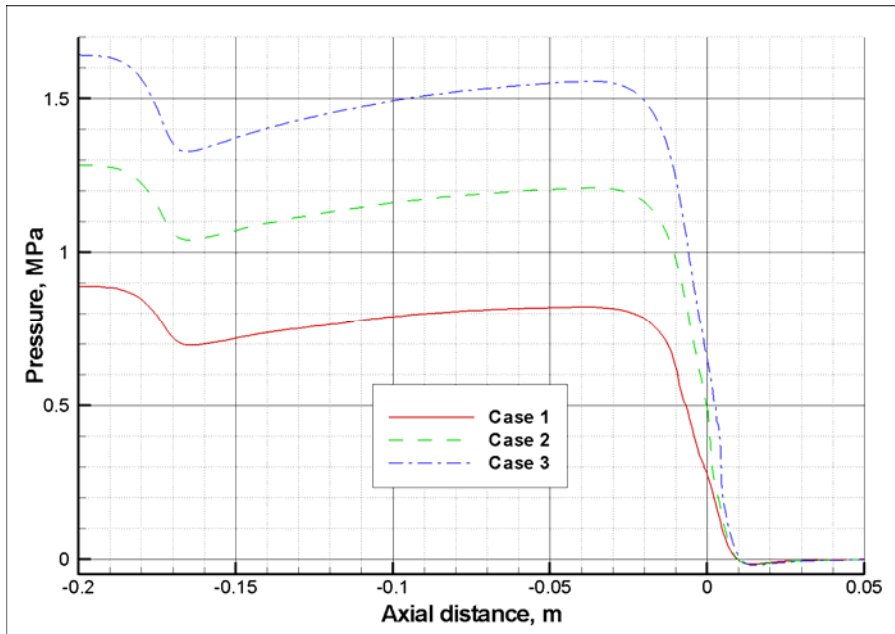


Figure 4-23. Pressure profile along the centerline of the nozzle.

4.3. Summary

A two-fluid Eulerian-Eulerian model with a catastrophic phase inversion has been applied for compressible gas-liquid mixtures that take place in the gas-assisted premixed atomization. As a simplified atomization treatment, an intuitive approach of modelling the phase inversion is proposed that depends on the local value of volume fractions. The discrete phase is assumed to be multidispersed, and the particle number density equation is solved to determine the average diameter of bubbles or droplets. The interfacial drag and the turbulence induced break-up are considered together with the coalescence of bubbles and droplets. The mixture turbulence model is adapted to liquid-continuous and gas-continuous flow regimes.

Comparison of the experimentally measured and simulated values of the pressure along the nozzle wall, the water flux, and the average droplet diameter profiles at different distances from the nozzle orifice confirms the capabilities of the model. It needs to be stressed that all the empirical and semi-empirical correlations used to close the model equations such as drag, virtual mass, break-up, etc., are used in their original form. The only parameters adjusted based on the experimental data are the critical value of the volume

Chapter 4. Gas-assisted atomization including flow through the nozzle, phase inversion, and spray dispersion

fraction which is used in the phase inversion model and the relative velocity constant. Note that their range still corresponds to scarce published values. There are no other tune ups or adjustments.

The nozzle performance analysis conducted with the model reveals a number of important trends, some of which were also experimentally observed and, most importantly, provides improved understanding and explanation of these trends.

Chapter 5. INTERACTIONS BETWEEN A GAS-LIQUID JET AND A FLUIDIZED BED

After the model was applied to the nozzle flow and to the atomization and spray dispersion in the preceding chapters, the time has come to apply the full model to the problem for which it was originally developed: the injection of spray into a fluidized bed. As the goal of this application is the verification of model performance, we chose some published experiments as an object of our simulations. The model presented in Section 2.1 is applied in its entirety. It means inclusion of all three phases, heat and mass transfer, and granular flow equations. Note that the model's two adjustable parameters have already been fixed during studies of the flow through the nozzle and the resulting spray based on the measurements of pressure, liquid flux, and droplet diameters. Therefore, there is no further adjustment specific to a fluidized bed application.

5.1. Model comparison with experiment

5.1.1. Draft tube addition (McMillan et al., 2005)

We compared model predictions with the experimental results of McMillan et al. (2005). They investigated the influence of an addition of the coaxially placed tube inside a bed downstream of the nozzle on the liquid-solid contact.

5.1.1.1. Experimental set-up and computational domain

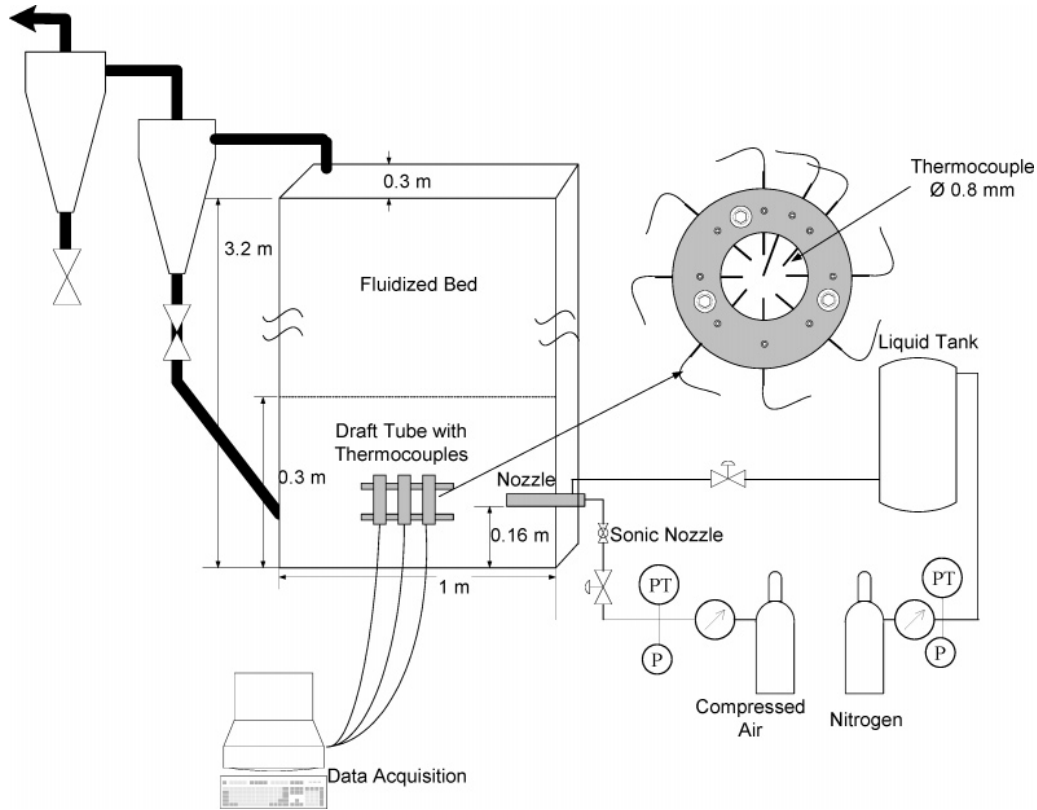


Figure 5-1. Experiment schematic (Reprinted from McMillan et al. (2005))

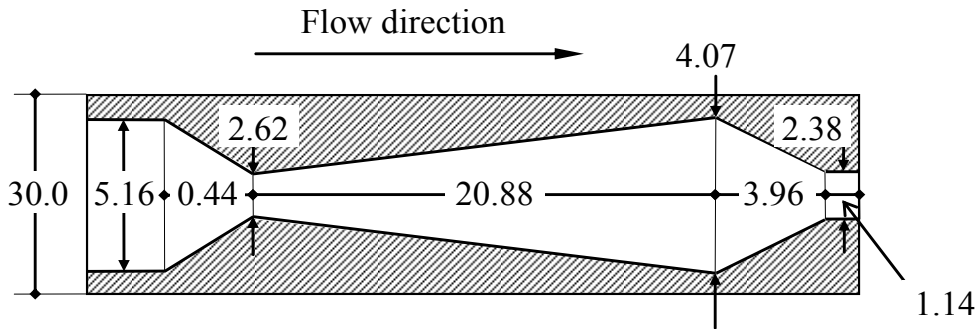


Figure 5-2. Nozzle schematics (in mm)

The model set-up follows closely the experiments conducted at the University of Western Ontario (McMillan et al., 2005) using a small scale fluidized bed, as shown in Figure 5-1. The column had a cross-section of 1 m length by 0.3 m width and was filled with coke particles ($d = 0.14$ mm, $\rho = 1500$ kg m⁻³) to a height of 0.3 m. The nozzle, shown in Figure 5-2, was a proportionally scaled down version of the one used in the commercial fluid cokers (Base et al., 1999). The nozzle was inserted into the middle of the shorter side of the

Chapter 5. Interactions between a gas-liquid jet and a fluidized bed

column at 0.16 m from the bottom gas distributor plate and its exit orifice was also at 0.16 m from the back wall. The bed is open to the atmosphere at the top and fluidized with air at the velocity 0.046 m s^{-1} . Air and ethanol were used as working fluids. The mass flow rate of air was 1 g s^{-1} and that of ethanol – 67 g s^{-1} . The mixture was injected at a lower temperature (-10°C) into the bed, heated to 40°C to enable thermocouple based measurements of the liquid to solid (L/S) ratio, a measure characterizing interactions between liquid droplets and solid particles at different axial distances. In one set of experiments, a 7 cm long draft tube with 1.9 cm diameter was installed coaxially with the nozzle and 1.27 cm downstream from its exit.

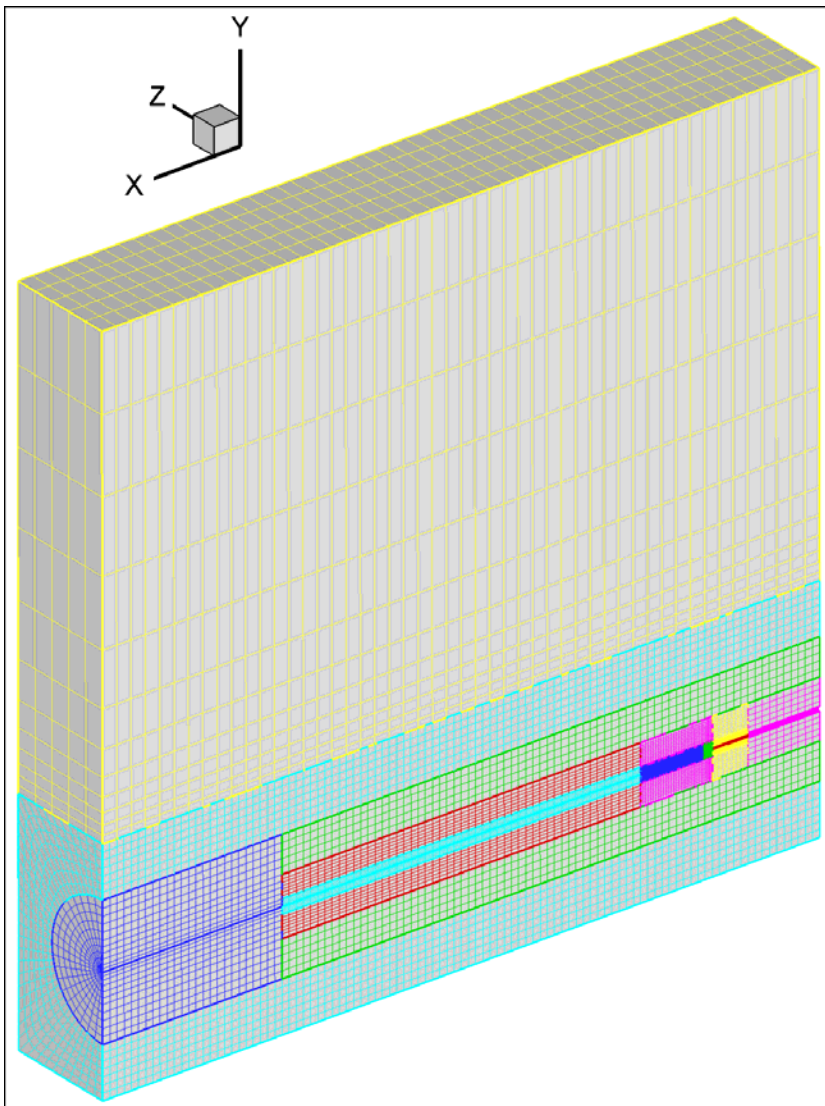


Figure 5-3. Computational grid for jet-bed interaction case.

The computational domain was chosen to satisfactorily represent experimental conditions. Only half of the fluidized bed was simulated as we assumed planar symmetry for the vertical plane cutting through the nozzle axis. This approach is justified by a high horizontal momentum associated with the nozzle flow that effectively minimizes bed random fluctuations. Another deviation from the experimental device is that we reduced the height of the freeboard region bringing the total bed height to 80 cm. This change, however, is not expected to cause any problems because the influence of the freeboard region on jet-bed interaction is minimal, if any. The curvilinear multi-segment grid shown in Figure 5-3 is quite fine inside the nozzle and in its vicinity downstream, moderately fine in the bed region, and relatively coarse in the freeboard. Somewhat skewed cells, which are inevitable for the connection of the circular nozzle into the rectangular bed for the structured grid system employed, are used at far as possible from the nozzle axis, i.e. from the area likely to be occupied by the jet. The grid contains about 90 000 cells in total, divided into 12 segments.

5.1.1.2. Computational procedure

Each simulation starts from calculating the fluidized bed only with a relatively large time step (about 3 ms), with the nozzle segment switched off. As soon as reasonable fluidization patterns are achieved, the nozzle segment is resolved, but its outlet is not connected to the bed yet. Finally, when the nozzle flow reaches steady state (or rather approaches conditions with minimal transient variations), calculations begin in the full computational domain. After a short time interval, the nozzle segment is frozen because the solution inside the nozzle, which is steady state for practical purposes, is not sensitive to the variations of bed conditions. In order to save computational time, we take advantage of the multi-scale character of the problem by introducing spatially variable time steps. This procedure was originally developed for attrition modelling in a similar geometry (see Section 7.1.2), and it allows use of smaller time steps in the segments near the nozzle with high variables gradients and larger time steps in segments that are located in the bed far from the nozzle. The computations have to run for a sufficient time to allow meaningful averaging. The introduction of this special procedure reduced the running time for a single case to about two weeks on an Intel Xeon 3.2 GHz workstation. In some instances, intermediate results for one case can be used as initial conditions for another, saving some computational time. Due

to the transient nature of the process, we obtained time averaged values of all flow parameters that will be further analysed. Note that there is no true steady state in this process, even in the average sense since liquid accumulates in the system. However, this accumulation happens relatively slowly, so that its timescale is larger than the timescale over which we can average the mechanical motion of the phases.

5.1.1.3. Grid independence

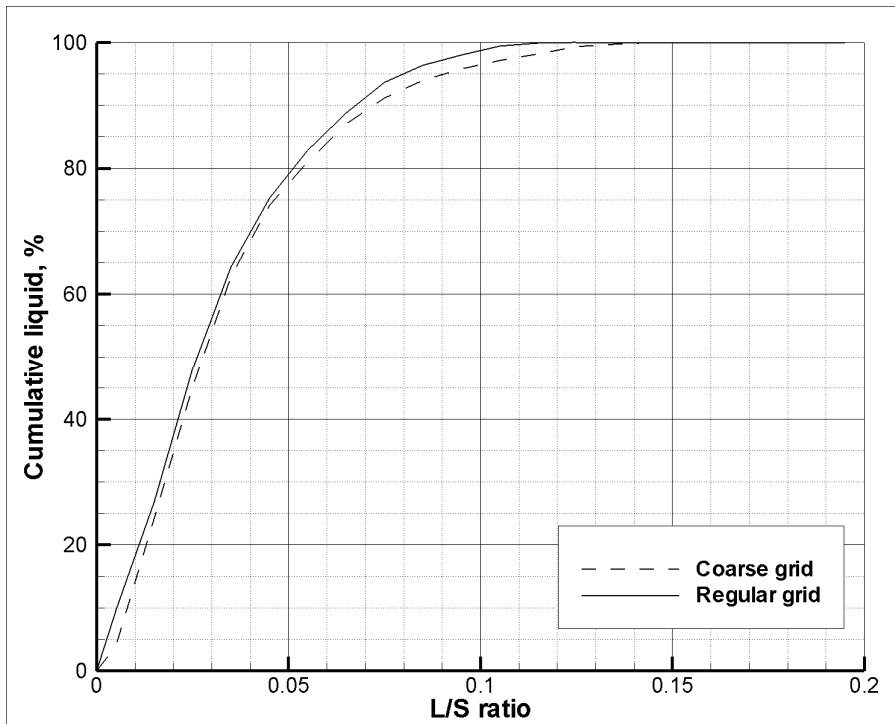


Figure 5-4. Cumulative liquid distribution profiles at 30 cm from the nozzle orifice for regular and coarse grid cases.

In order to assess grid independence, we obtained solutions on two different grids for the case without the draft tube. In addition to the main grid, which contains about 90 000 cells, we developed a coarse grid with about 75 000 cells. This coarsening was done mostly in the jet area. For ease of quantitative evaluation, we compare the data in the same format as in McMillan et al. (2005); that is, in cumulative liquid distribution. Such distribution shows how much liquid is located at places that have Liquid to Solid (L/S) ratio below a certain value. As liquid can exist in both liquid and particulate phases, we obtained L/S ratio from the mass flow rate modelling results as

$$\frac{L}{S} = \frac{\alpha_l \rho_l u_l + \alpha_p x_f \rho_p u_p}{\alpha_p x_s \rho_p u_p} \quad (5-1)$$

Figure 5-4 demonstrates a comparison between cumulative liquid distribution profiles obtained for regular and coarse grids. Evidently, the curves are reasonably close one to another to consider the solution grid independent for practical purposes.

5.1.1.4. Liquid to solid (L/S) mass ratio comparison

We start with comparison of the predicted L/S ratios with the experimentally measured ones. The L/S cumulative distribution curves can characterize the uniformity of liquid distribution: the more vertical the curve, the more uniform the distribution. Also, shifting the curve to the left indicates less liquid per solid particle, and, hence, better liquid spreading.

Figure 5-5 compares L/S ratios at different axial distances for cases with and without the draft tube. It can be seen that the qualitative agreement is quite good. The profile curves shift left with increasing distance from the nozzle orifice due to the radial liquid dispersion that occurs as the jet progresses, which is in full agreement with the experimental data points. In addition, similar to experimental observations, the draft tube case curves are always closer to the left than those obtained from the case without anything placed inside the bed, indicating that the tube insertion improves liquid-solid contact. Quantitative agreement is not as good, but still acceptable given the complexity of the problem. It is generally better for the case without a draft tube and for distances closer to the nozzle exit. The disagreement is mostly concentrated in the areas with the high L/S ratio, i.e. in the central zone of the jet. Apparently, the modelled liquid dissipation from the jet is somewhat underestimated. This can be a consequence of the moisture spreading model, the droplet-particle interaction model, the granular temperature model along with some others. Given the uncertainty of the source of the disagreement, we refrain from any adjustments, keeping the model as general as possible, even at the expense of less than perfect quantitative comparison.

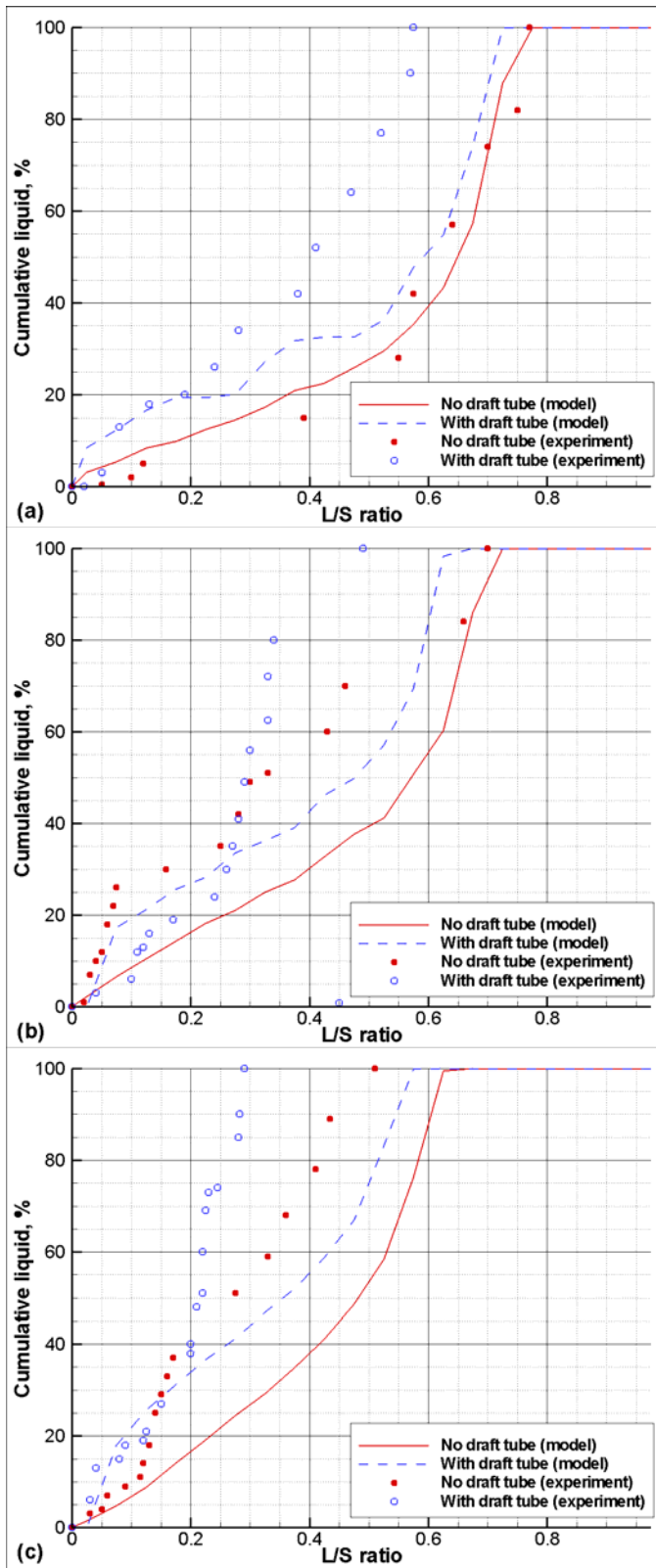


Figure 5-5. Cumulative liquid distribution profiles at various distances from the nozzle orifice obtained from model prediction and McMillan et al. (2005) experiment; (a) $l = 3.27$ cm; (b) $l = 5.27$ cm; (c) $l = 7.27$ cm.

5.1.1.5. Flow analysis

While L/S ratio profiles provided us with means for model comparison, they are not as informative regarding the flow itself. In order to gain some insights into the flow, we look at the solution in the whole domain. We start by examining time-dependent features of the flow. The case without the draft tube serves as an example, as general flow features are similar with and without the draft tube. Figure 5-6 presents the transient evolution of the particulate fraction volume phase in the bed after the jet structure is established. It can be seen as the end of the jet fluctuates irregularly, shedding bubbles. However, this phenomenon is different from the bubbles arising from the gas jet injection, e.g. Li et al. (2008), where bubbles generally move upwards after pinching off from the jet under the influence of gravity. For the gas-liquid injections presented here, there is much more momentum in the jet due to a higher liquid density transferred to solid particles resulting in strong horizontal convective flows. Trapped in these flows, the bubbles continue their movement in the direction of the nozzle axis until finally turning upwards. A careful examination of this figure reveals that the global solid circulation patterns of bed particles are dramatically influenced by the injection. Upon entrainment in the jet, particles move towards the opposite wall of the bed; then, they slowly return back mostly via the top part of the bed.

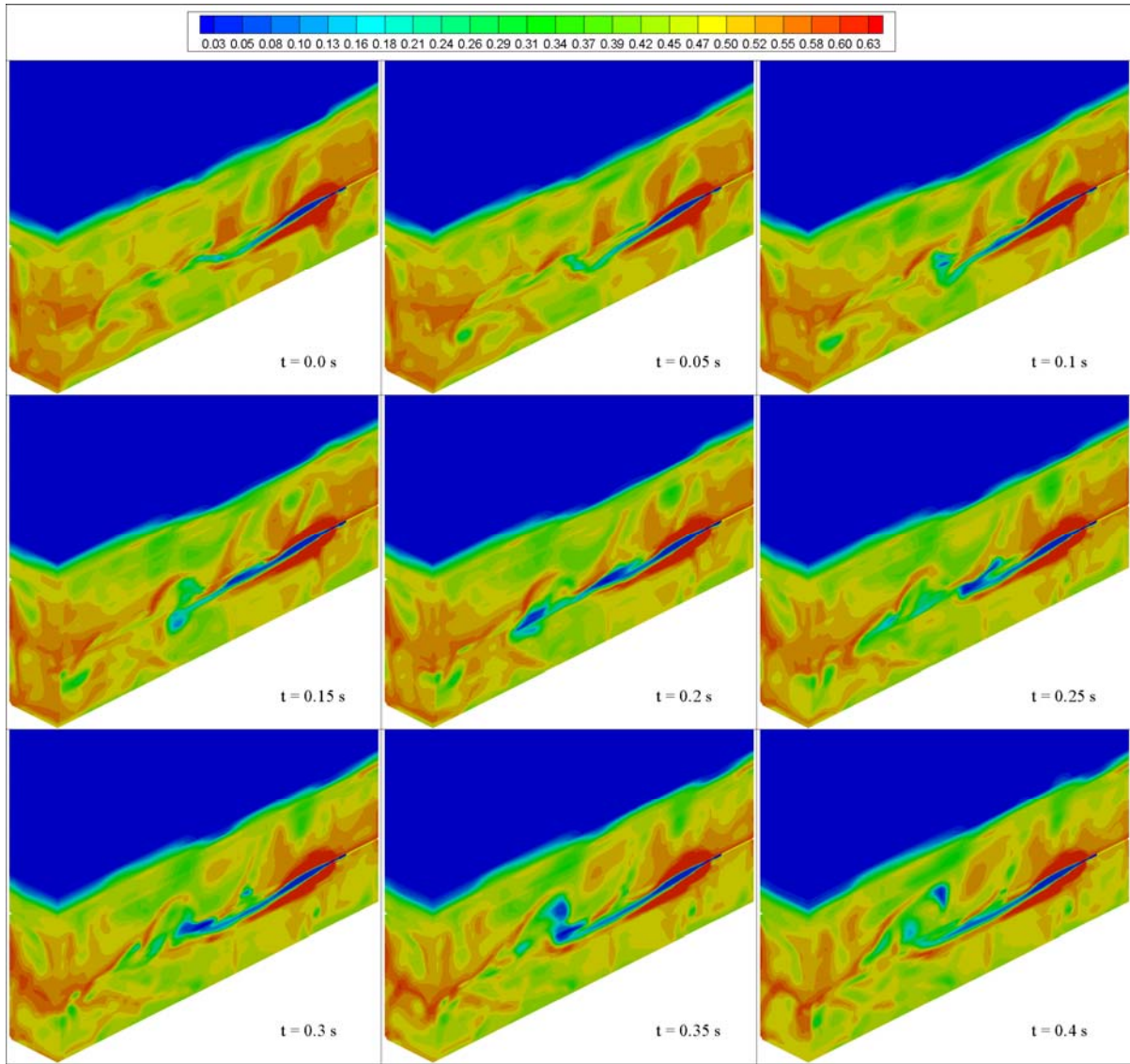


Figure 5-6. Transient variations of the particulate phase volume fraction.

To continue the analysis, we time average the results over 2 s starting from the time when the flow develops some quasi-periodical patterns. Note that, as demonstrated in Figure 5-6, there is no true periodicity in the motion of phases. Moreover, the total moisture content gradually grows as more liquid is injected. Even though the chosen averaging time is not sufficient for some bed regions far from the jet, we keep it for practical reasons of controlling computational time and because this time scale is adequate for the jet and near jet regions that are most important in our study. In addition, due to the moisture accumulation, averaging of the distant bed regions is not possible. Figure 5-7 shows volume fractions of the particulate phase for both cases considered. It can be seen that the whole fluidized bed is

under the influence of the spray injection. There is the jet area that is filled with air; also, there is the densification area around the jet that stretches from the jet boundary to the periphery of the bed, with its intensity gradually reducing. Downstream of the jet we can see the area of the decreased particulate phase volume fraction. This is the result of the bubbles separating from the jet end and continuing their horizontal motion – a phenomenon discussed in the previous paragraph. Thus, the whole wide and long region above the jet starting at about 35 cm from the nozzle exit demonstrates a somewhat reduced particulate fraction because of bubbles coming up at different distances from the nozzle during transient jet fluctuations. Also, we can see a mildly densified area close to the wall, opposite the jet. This takes place because of the jet pushing solids towards this wall and therefore a region with slightly larger concentration of particles is created. The addition of the draft tube results in a noticeably longer jet (see Figure 5-7 (b)). While generally the solids distribution is fairly similar, the jet area is narrower and longer. Evidently, the draft tube limits the radial spreading of the jet by restricting the radial momentum transport by the tube wall. The bubble trail area downstream of the jet is also more extended as a consequence. It can be also seen that for the case without the tube, the jet is slightly inclined towards the bottom. This is probably due to the global circulation patterns previously discussed. Another interesting observation is that the height of the bed is somewhat larger for the case with the draft tube. This can be the outcome of the decrease of the solid particle entrainment into the jet in the tube region because of the physical separation of the low pressure area by the tube wall. Thus, the fewer particles being bound in the densification region with high volume fraction translates to more particles in other places of the bed with smaller volume fractions. Such redistribution results in increased bed volume and hence, increased bed height.

Further examination of the near nozzle region in Figure 5-7 (a) indicates a well-defined boundary between the gas jet and the surrounding bed marked by a rapid change of the particulate phase volume fraction. It allows us to determine the initial half-angle of jet radial expansion, which is about 7.5° . This value is in good agreement with the 8° angle measured by Berruti et al. (2009) who studied jet boundaries for similar conditions with the same experimental set-up. In addition, the overall kite-like shape of the jet region, with shorter sides closer to the nozzle, qualitatively agrees with the experimentally determined

shape by the same researchers. The boundary region of this kite-like shape is very sharp at the nozzle side and becomes more diluted on the outer side.

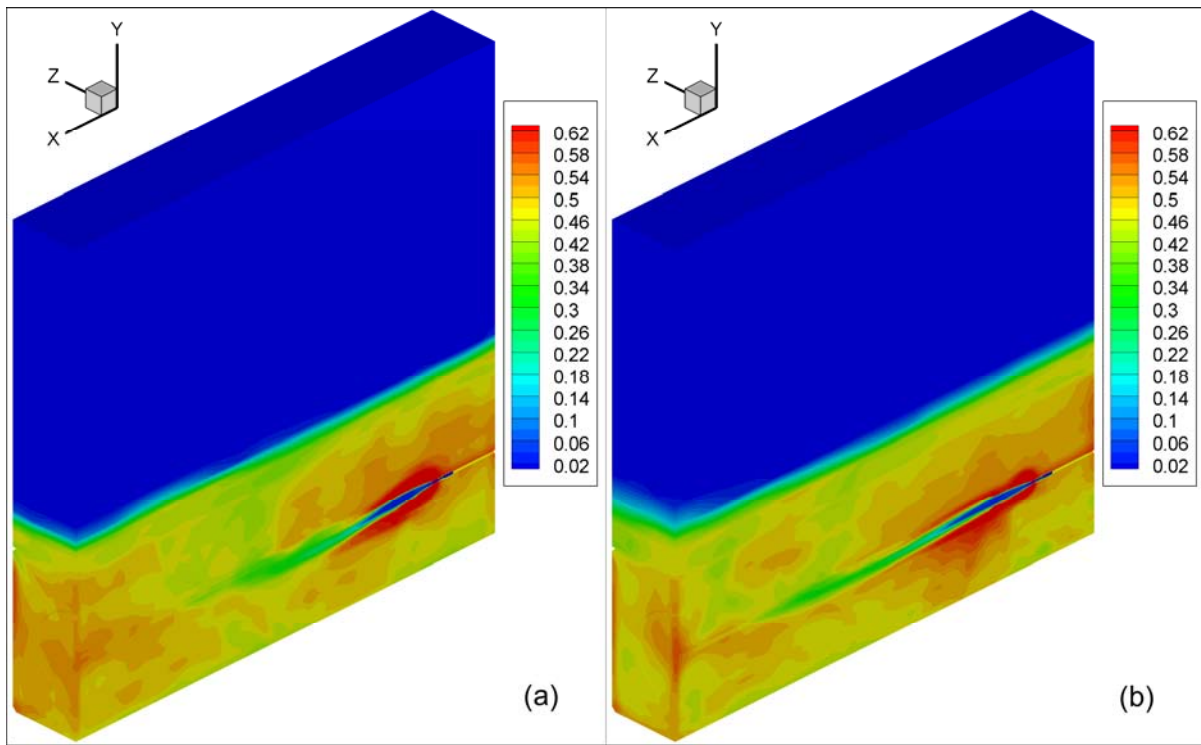


Figure 5-7. Contours of volume fraction of the particulate phase; (a) – Case without a draft tube; (b) – Case with a draft tube.

Contours of the liquid volume fractions, which include liquid droplets and a liquid layer on the particle surface, for both cases, shown in Figure 5-8, are in line with our previous observations. It is important to note that, as previously discussed, liquid spreading is a transient process. Therefore, the contours need to be interpreted in a way similar to local residence times at a certain moment. Clearly, the case without the draft tube provides a better dispersion of the liquid jet, while the case with the draft tube exhibits better penetration. As we have previously discovered in Figure 5-5, the draft tube improves liquid distribution in a near field region downstream of the nozzle. It is interesting to see what happens at further depths inside the bed. Figure 5-9 presents cumulative liquid distribution at 10 and 30 cm distances from the nozzle exit orifice. It is evident that at 10 cm the advantages of the draft tube, shown in Figure 5-5, have almost disappeared, and at 30 cm, the performance of the nozzle without the tube addition is better than with it. Therefore, it can be concluded that the draft tube provides better initial mixing of the liquid with the particles that manifests itself in

Chapter 5. Interactions between a gas-liquid jet and a fluidized bed

a more uniform liquid distribution, but further downstream from the nozzle this advantage disappears because of the limited radial expansion of the jet.

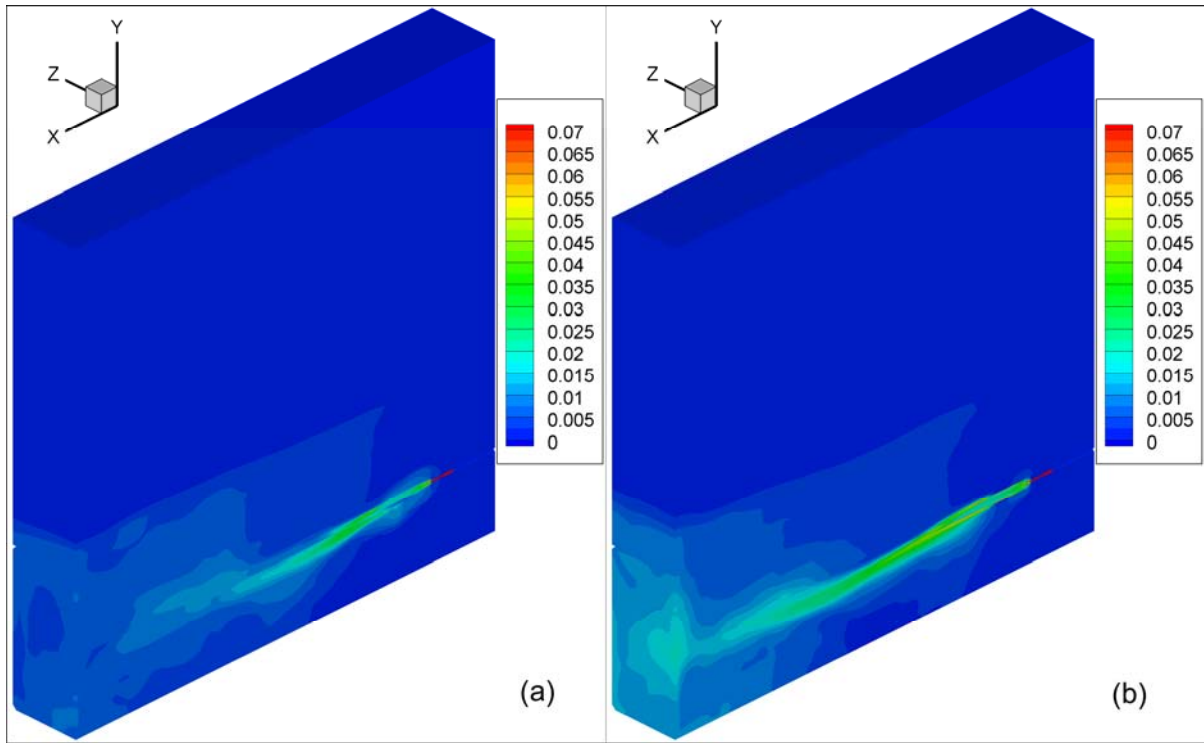


Figure 5-8. Volume fraction of liquid (droplets and liquid layer); (a) – Case without a draft tube; (b) – Case with a draft tube.

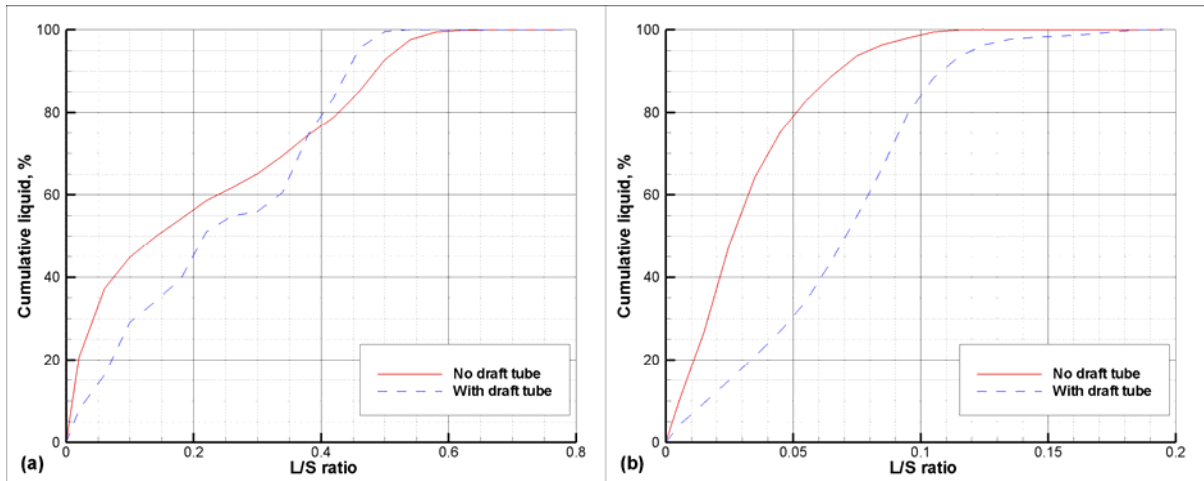


Figure 5-9. Predicted cumulative liquid distribution profiles at various distances from the nozzle orifice. (a) $l = 10$ cm; (b) $l = 30$ cm.

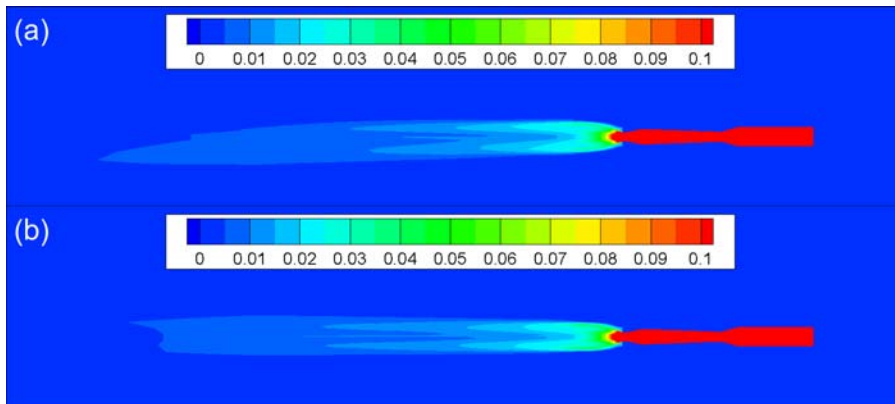


Figure 5-10. Volume fraction of droplets; (a) – Case without a draft tube; (b) – Case with a draft tube.

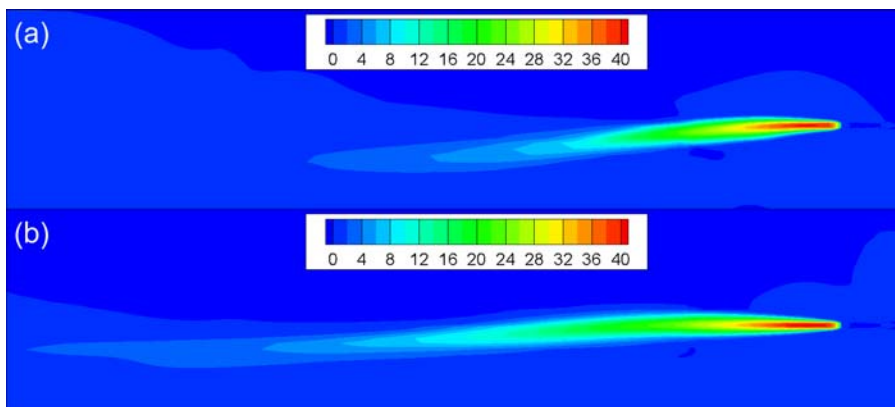


Figure 5-11. Axial velocity of the particulate phase (in m s^{-1}); (a) – Case without a draft tube; (b) – Case with a draft tube.

As we can see from Figure 5-10, individual liquid droplets do not survive for long inside the bed. It is evident that after about 10 cm from the nozzle exit, virtually no droplets are observable in the solution, as all liquid is transported to the film around the particles. It also worth noticing that there are no apparent differences in the initial droplet consumption between the cases with and without the draft tube. Thus, its role is limited to secondary moisture spreading by promoting inter-particle collisions.

As particles obtain the momentum from liquid droplets moving quickly from the nozzle outlet, their velocities can reach considerable values (up to 40 m s^{-1}). Contours of the particles axial velocity, presented in Figure 5-11, show the highest velocity in the jet region. It is important to note that the volume fraction of the particles is lowest there (see Figure 5-7). As soon as the volume fraction increases, the particle momentum begins to dissipate. As expected, the addition of the draft tube makes the velocity remain relatively high for a

longer distance. Also, we can see a jet slightly curving towards the bottom for the case without the draft tube as previously observed with the particle volume fraction contours.

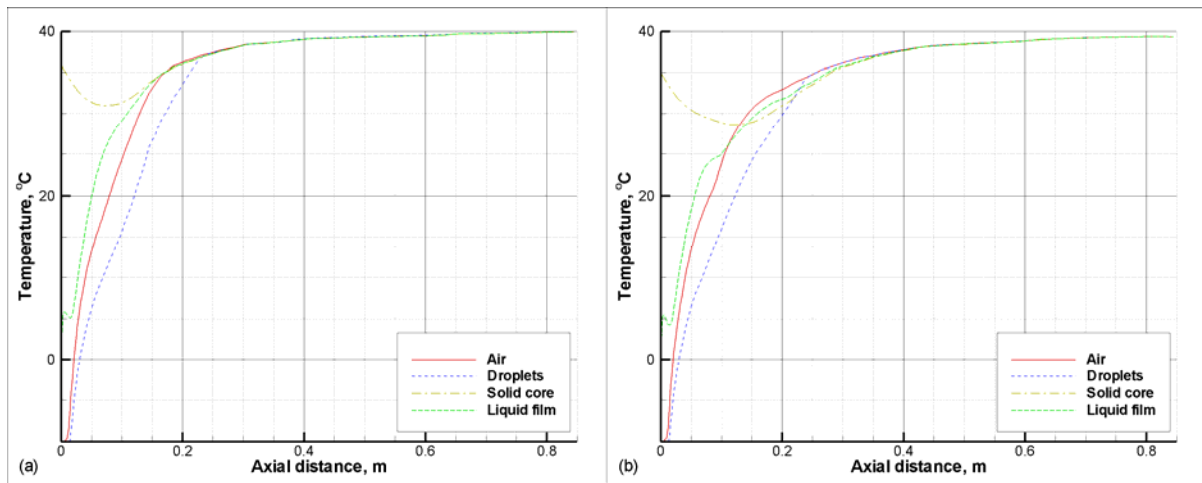


Figure 5-12. Phase and component temperature profiles along the centreline; (a) – Case without a draft tube; (b) – Case with a draft tube.

For help with the analysis of the heat transfer in the system, we plotted temperature profiles of air, droplets, solid core, and liquid film along the centreline in Figure 5-12 for both cases. Around the nozzle exit the air temperature drops slightly due to the rapid expansion, and the droplet temperature closely follows due to a very good heat transfer between the phases because of the small droplet diameter ($< 30 \mu\text{m}$ in this area) and high turbulence. As the distance increases, the air heats up due to the turbulent mixing and contact with hotter particles. Droplets, in turn, gain heat either from the air or from the interactions with the liquid layer, in which they exchange heat and momentum, but do not stick to the particles. Thus, their temperature is less than for the air. Initially, hot solid particles lose some heat after they begin to accumulate liquid film on their surface. However, this trend is soon reversed as the liquid layer temperature reaches that of the core. From this point, they both gradually gain heat from the surroundings until they reach the bed temperature. While general shapes of the curves are similar for the cases with and without a draft tube, it is evident from the comparison that the influence of the cold injection persists longer in the case where the draft tube was added. This is in agreement with a previously noticed extension of the jet length with the draft tube addition.

5.1.1.6. 2D and 3D solution comparison

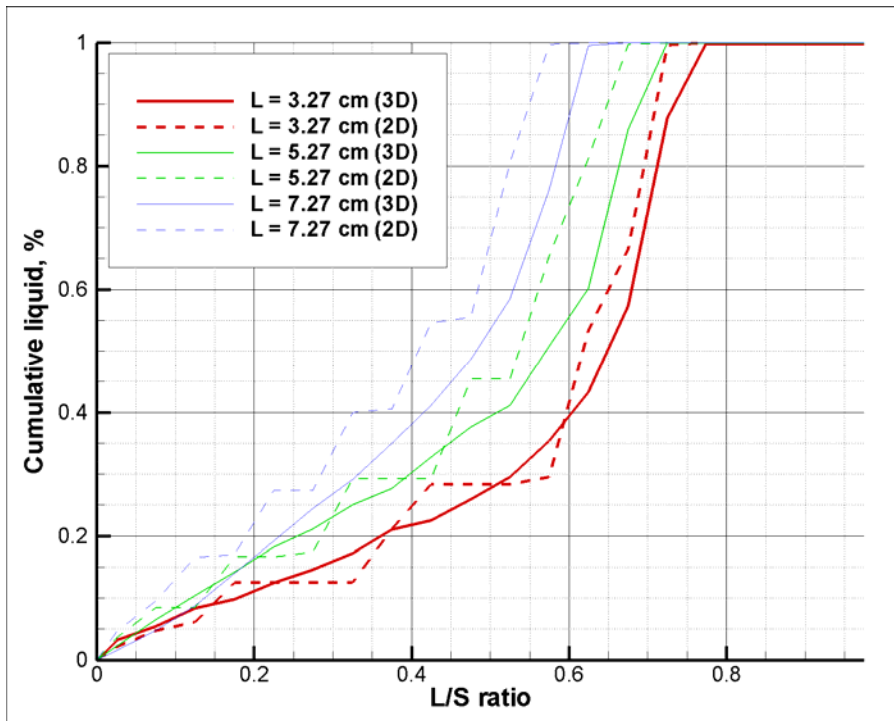


Figure 5-13. Cumulative liquid distribution for 3D and 2D axisymmetric solutions at different axial distances from the nozzle exit.

With the availability of a 3D solution, it is interesting to compare it with a 2D axisymmetric solution of the area near the nozzle orifice. After setting up a 2D case, we ran simulations until a quasi-steady state was obtained. Cumulative liquid distribution curves are plotted in Figure 5-13 together with ones previously obtained for a 3D case without a draft tube, to facilitate comparison. We can see that the axial symmetry assumption leads to somewhat better liquid dispersion compared to the 3D case. The profiles at all distances are shifted towards the left, albeit the difference is not very significant. Note that this difference grows slightly with the distance from the nozzle. It seems that some radial fluctuations in the 3D case, however minor, result in certain poorly mixed liquid parcels penetrating further, thus influencing the distribution. The results indicate that while 2D calculations give useful information about the flow and droplet-particle interactions near the nozzle exit, at more substantial distances from the nozzle, 3D effects become significant and, therefore, 3D studies are desirable.

5.1.2. Penetration distance (Ariyapadi et al., 2004)

Another way to quantify jet-bed interactions is to calculate a jet penetration distance. For gas jets, the jet boundary can be defined by a certain value of gas volume fraction. For gas-liquid jets, however, such a definition seems to be less appropriate, as liquid with a relatively high inertia can penetrate further than gas. Indeed, Figure 5-7 demonstrates that the area of jet influence extends well beyond the air bubble. It is natural to define the jet penetration length as the distance from the nozzle orifice at which the direct injection effects are still evident. Such definition still requires clarification of the effects and their quantification. Since one of our goals is model validation, we followed the available experimental techniques in choosing the effects. As described by McMillan et al. (2006), two methods fairly widely used to evaluate jet boundaries involve either thermocouples or triboelectric probes. The former relies on the temperature measurements in the bed and require the difference between the bed and jet temperatures; the latter produces a signal proportional to the flux of the solid particles. When the thermocouple is placed into the wet fluidized bed, it comes in contact with all three phases. However, the heat transfer between the solid particles and the thermocouple probe is firstly limited to a short collision time, and secondly, most of it takes place through a thin layer of either air or liquid. Liquid, on the other hand, can stick to the thermocouple surface and remains there until it is blown away or evaporates. Therefore, it seems reasonable to assume that a thermocouple placed in a wet bed would measure the locally averaged temperature of the liquid present in a form of either droplets or film. Thus, we can model it with the average liquid temperature defined from the model parameters as

$$T_l^{av} = \frac{\alpha_l \rho_l T_l u_l + \alpha_p x_f \rho_p T_f u_p}{\alpha_l \rho_l u_l + \alpha_p x_f \rho_p u_p} \quad (5-2)$$

For a triboelectric signal, we assume that it is proportional to the velocity of the particulate phase. Now we can calculate the minimum T_l^{av} and maximum $|\mathbf{V}_p|$ in each cross-sectional plane that is perpendicular to the nozzle (note that the maxima and minima may not be located at the axis) at every time instant. As an example, we show in Figure 5-14 the profiles obtained for the case without the draft tube described in Section 5.1.1 at a certain

moment of time. The remaining question is how to demarcate the penetration length from this data. Berruti et al. (2009) developed an algorithm based on a three-line model that takes advantage of the changing incline of the standard deviation curve. However, the implementation of a similar approach to our model is cumbersome and not straightforward. Thus, we decided to introduce simple cut-off values and determine the instantaneous penetration length. Then, as calculations progress, this length is time-averaged. Alternatively, we can apply cut-off values to already time-averaged data. Evidently, there is some freedom in choosing these cut-off values. While this choice would influence the absolute values, the comparison between the various cases should not depend on the cut-off selection. During our simulations, we tried three different cut-off values for temperature – 39°C, 38°C, and 37°C – and three for the velocity – 1, 2.5, and 5 m s⁻¹. After examining the results, we decided to define the cut-off temperature at 39 °C, i.e. 1 °C below the bed temperature, or 2% of the temperature difference between the bed and the spray, and the cut-off velocity at 1 m s⁻¹ in order for the predicted penetration distance to be in the same range as available experimental data, but without further fine-tuning.

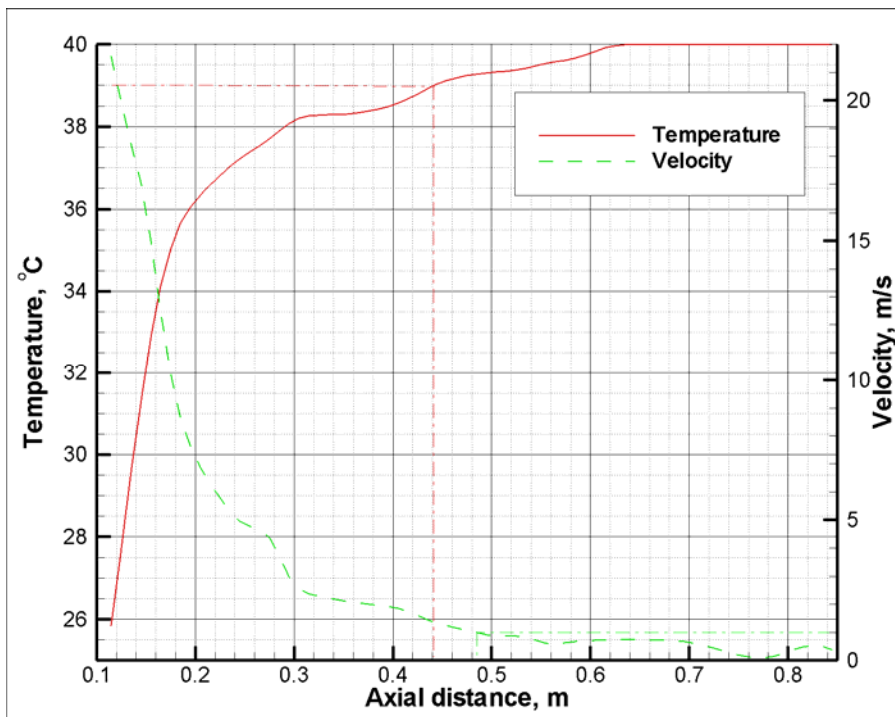


Figure 5-14. Instantaneous profiles of minimal cross-sectional liquid film temperature and maximum particle velocity with an example of penetration depth determination.

5.1.2.1. Model set-up

For comparison of model prediction of jet penetration depths, we utilized the experimental data of Ariyapadi et al. (2004), who studied jet penetration of similar nozzles. They used the same fluidized bed and experimental set-up as shown in Figure 5-1, and considered the measured temperature as a penetration indicator. The bed contained 150 μm diameter particles of density 1 400 kg m^{-3} fluidized by air with a superficial velocity of 0.1 m s^{-1} . Similar to the experiments described in Section 4.1.1, the injection temperature was -10°C and the bed temperature was 40°C . Among others, two nozzle designs that are relevant to our study were investigated: the first was the same as depicted in Figure 5-2, and the second was a scaled down version of the same geometry. An air and ethanol mixture was injected into the bed at different flow rates. The experimental conditions are summarized in Table 5-1.

Table 5-1. Nozzle diameters and flow rates for investigated cases (from Ariyapadi et al., 2004).

Case #	Nozzle exit diameter, mm	Liquid flow rate, g s^{-1}	Gas flow rate, g s^{-1}
1	2.4	57	1
2	2.4	65	1
3	2.4	71	1
4	1.6	26	0.45
5	1.6	28	0.45
6	1.6	32	0.45

After simulating these six cases, we obtained transient variations of the jet penetration distance. Figure 5-15 shows the data for the second case as an example. We can see that the two penetration distance curves, one determined by temperature and the other by velocity, follow each other fairly closely except for some minor shift. Evidently, these two methods (i.e. temperature and velocity based) capture the same physics of the flow and can be used interchangeably. It is also apparent that the time variations are rather random and a substantial time period is required for the average to be meaningful.

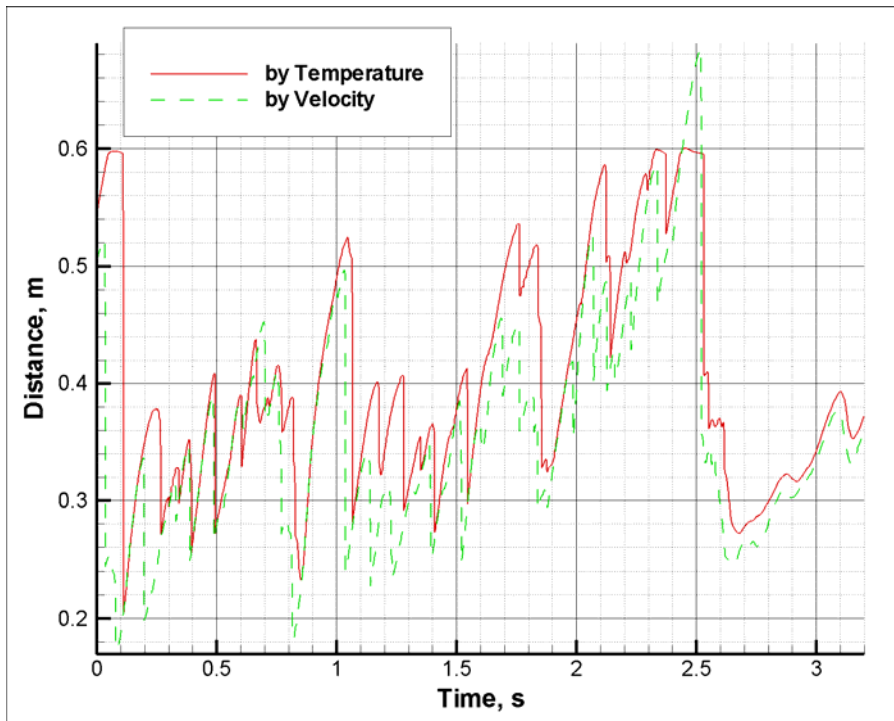


Figure 5-15. Jet penetration distance time variations for Case 2 (from Table 5-1) as determined by temperature and velocity methods.

5.1.2.2. Penetration distance comparison

Modelling predictions are presented together with the experimental results of Ariyapady et al. (2004), which were based on thermocouple measurements, in Figure 5-16. First of all, we can see that qualitative trends are reproduced correctly. The penetration length increases with the increase of liquid or gas flow rates. At the same time, there are differences in quantitative values. However, as discussed at the beginning of Section 5.1.2, the definition of the penetration length is rather “soft”, leaving an opportunity to fine-tune the model to better match the results. In addition, we note that transient variations in the penetration length are rather large, as is shown in Figure 5-15, and can be inferred from significant standard deviations in Figure 5-16. As we can see from this figure, the fluctuations increase with flow rates, even when relative values are considered. Such large fluctuations raise the question about the flow being influenced by a probe. For example, while the model shows an instantaneous temperature value, in experiments, some liquid that stuck to the probe may have remained there longer than if there had been no probe present. Thus, the results may be biased towards lower temperatures and hence, longer penetration lengths. To sum it up, while there are many uncertainties in determining the jet penetration length in modelling as well as

in experiments, both can determine a reasonable range and one can compare different cases provided the same methodology is consistently used. Therefore, we refrain from further model “fine-tuning” and keep our choice of cut-off velocity and temperature.

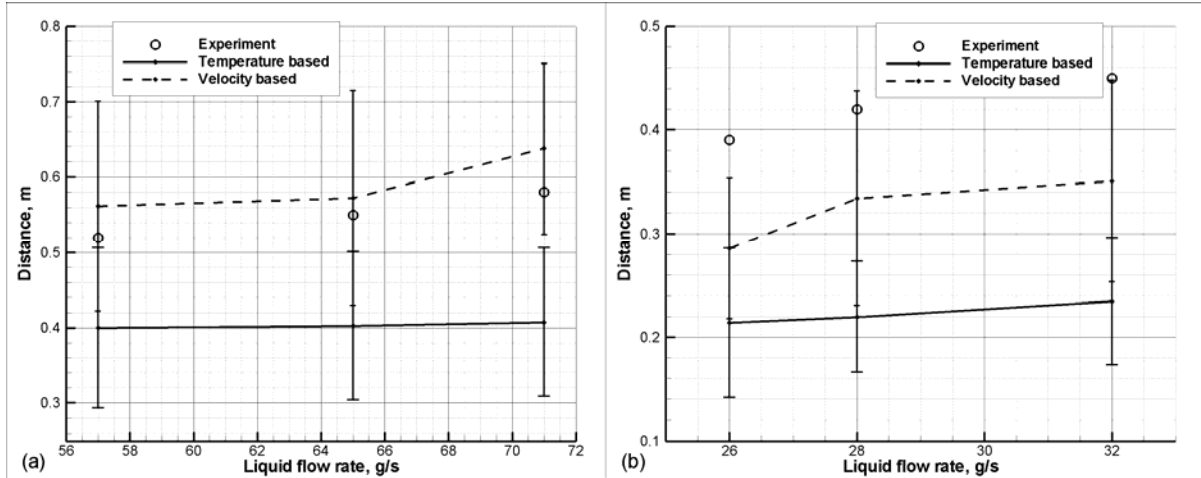


Figure 5-16. Time averaged jet penetration distance for cases from Table 5-1 compared with experimental values of Ariyapady et al. (2004). Error bars on modelling results show \pm one standard deviation. (a) lower flow rates; (b) higher flow rates.

5.1.2.3. Penetration distance for cases with and without a draft tube

Now it is possible to compare penetration distances for the cases previously considered in Section 5.1.1, i.e. to investigate the influence of the insertion of the draft tube on the penetration distance. After analysis of the transient results, we obtained the penetration values listed in Table 5-2. It can be seen that in agreement with Figure 5-7, the penetration distance increases with the addition of the draft tube. As discussed in Section 5.1.1.5, this can be attributed to restrictions placed on the radial jet momentum by the draft tube.

Table 5-2. Jet penetration distance for cases with and without the draft tube.

Case	Temperature based length, m	Velocity based length, m
No draft tube	0.448	0.554
With draft tube	0.456	0.588

Interestingly enough, in their experimental work with the same set-up as McMillan et al. (2005), Briens et al. (2009) found a reverse dependency. The addition of the draft tube slightly reduced the penetration length. They also determined that the penetration length

depends strongly on the axial location of the draft tube. This location determines the point at which wet particles make contact with the tube wall. The closer this point to the beginning of the pipe, the smaller the penetration length. That is, moving the draft tube further away from the nozzle reduces the length. This suggests that there is a loss of axial momentum during collisions of wet particles with the wall, which is not currently accounted for by the model.

5.2. Variation of superficial gas velocity

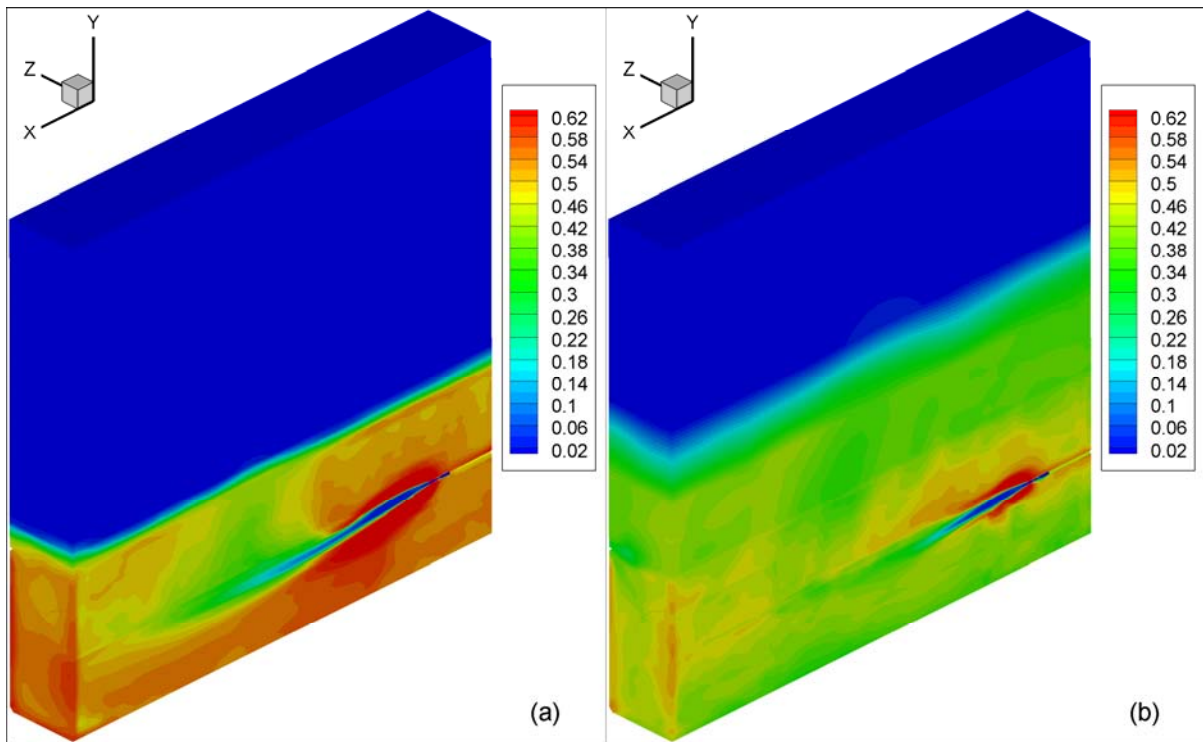


Figure 5-17. Contours of volume fraction of the particulate phase; (a) – superficial velocity 0.02 m s^{-1} ; (b) – superficial velocity 0.1 m s^{-1} .

In order to evaluate the influence of the superficial velocity on interactions between droplets and particles, we investigated two additional cases. Both have the same set-up as the case without the draft tube, as described in Section 5.1.1.1, except for the gas superficial velocity that is set at 0.02 m s^{-1} for the one case and at 0.1 m s^{-1} for the other. Note that the velocity in the baseline case (without the draft tube) is 0.045 m s^{-1} . The calculation procedure for these new cases is similar to those already discussed. Below we analyse time-averaged results.

Chapter 5. Interactions between a gas-liquid jet and a fluidized bed

Figure 5-17 presents contours of the particulate phase for new cases. (The baseline case is shown in Figure 5-7 (a).) As expected, the bed height depends on the superficial velocity. This is very evident from the plots. For a small superficial velocity, the jet issues into a very dense bed. The jet area is clearly visible and mixing is rather minimal. In contrast, for large superficial velocity, the jet blends with the surrounding bed after about 20 cm from the nozzle orifice. The case with medium velocity (Figure 5-7 (a)) lies somewhere inbetween. Thus, it seems that higher superficial velocity improves bed mixing and reduces jet length. A look at penetration distances for the cases considered confirms this suggestion. For the superficial gas velocity 0.1 m s^{-1} the distance (velocity-based) is 0.53 m, for 0.045 m s^{-1} (see Table 5-2) it is 0.55 m, and for 0.02 m s^{-1} it is about 0.8 m. The last value is approximate, as the opposite wall clearly interferes with the jet. At the same time, the part of the bed located immediately downstream from the nozzle, and which is characterised by the densification of the bed due to solid entrainment, does not appreciably change from one case to another. Evidently, the flow there is determined by the high momentum of the gas-liquid jet and not by the bed hydrodynamics.

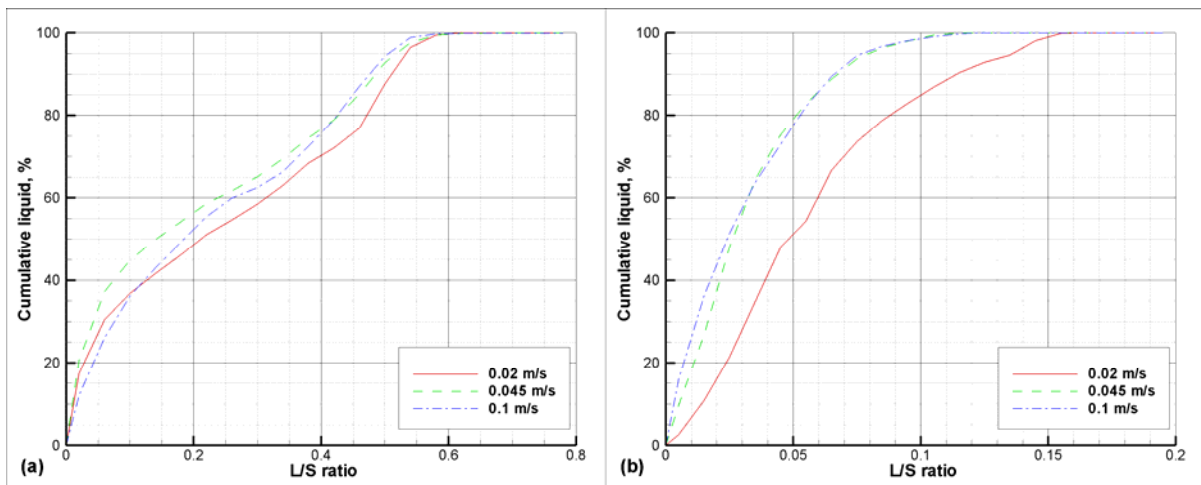


Figure 5-18. Cumulative liquid distribution profiles at various distances from the nozzle orifice for different fluidization velocities. (a) $l = 10 \text{ cm}$; (b) $l = 30 \text{ cm}$.

The above analysis also manifests itself in the profiles of the cumulative liquid distribution, which is an indication of nozzle performance, shown in Figure 5-18. Close to the nozzle exit (10 cm) all three curves are virtually the same. However, with the distance from the nozzle, the difference begins to appear. At 30 cm downstream, the case with superficial velocity 0.02 m s^{-1} demonstrates clearly very poor liquid distribution. The case

with velocity 0.1 m, on the other hand, shows somewhat better liquid dispersion than the case with velocity 0.045 m s^{-1} . However, it seems that as the superficial velocity reaches a certain value, further advantages in liquid distribution are rather minimal.

5.3. Summary

The mathematical model of the spray obtained with the gas-assisted atomization injection into the fluidized bed with droplet-particle interactions is applied to a 3D case that simulates previously published experiments. The comparison of the cumulative liquid distribution curves demonstrates good qualitative and satisfactory quantitative agreement. The modelling results reveal details of the flow that help the understanding of the jet-bed interaction phenomena.

Chapter 6. LIQUID SPRAY DISPERSION MODIFICATION BY CONICAL NOZZLE ATTACHMENTS

Liquid spray characteristics such as the droplet size and dispersion angle are determined by the atomizer design and the physical properties of the liquid and the surrounding gas. It is beneficial from the process development point of view to have some control over jet penetration and jet dispersion. Basically, the jet penetration describes how long the jet is, and the jet dispersion – how wide it is. As the momentum of the jet is conserved, the penetration and dispersion are generally inversely varying parameters. One of the means to control the jet dispersion without changing the nozzle itself is an installation of an axially aligned spray modifier attachment to the exit of the nozzle. The jet dispersion and penetration as well as other spray properties such as the droplet sizes and the liquid flux distribution, are affected by the addition of such a modifier. Even though there can be a variety of modifier shapes including the ones with azimuthal profile variations, we concentrate on the simple conical design that allows for investigation of the changes that the attachment brings to the flow and has an inherent axial symmetry that can be computationally exploited. At the same time, the results can be generalized to other configurations.

In this chapter we investigate an addition of the conically shaped attachment to the premixed gas-assisted high-pressure atomizer with the mathematical model developed in Section 2.1. While our intuition, based on the garden hose spraying, suggests that the spray simply follows the angle of the nozzle, this is not the case in the described nozzles due to a number of reasons discovered during the analysis. At first, we studied the nozzle issuing an air-water mixture into the quiescent air. We evaluated the sprays obtained with various angles of the conical expansion. As no particles are considered, only a part of the model,

similar to what is used in Chapter 4, is utilized. Next, we examined an injection of a steam-bitumen mixture into the fluidized bed of coke particles. In this part of the study, we looked at how different spraying characteristics impact jet-bed interactions for the conditions close to an industrial application. Due to the presence of particles, the full mathematical model of jet-bed interaction is employed.

6.1. Air – water spray in open air

6.1.1. Description of cases

We considered a standard TEB-type nozzle with a conical attachment, as shown in Figure 6-1. This nozzle itself was designed by Base et al. (1999) and is the same as investigated in the previous sections. While the length of the attachment is fixed, several values of its expansion angle are studied. They are listed in Table 6-1 together with a corresponding height of the attachment exit. In addition, we also include a case without an attachment, which can also be viewed as having an attachment with an expansion angle of 180° , for comparative purposes.

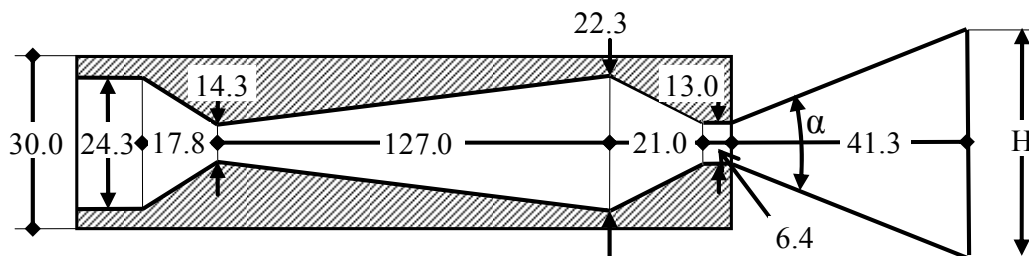


Figure 6-1. Schematic drawing of nozzle with an attachment (mm, not to scale).

Table 6-1. Attachment expansion angle and exit height of the investigated cases.

Case number	α , degrees	H, mm
1	180	0
2	10	20.2
3	20	27.6
4	40	43.1
5	60	60.7
6	80	82.3

Chapter 6. Liquid spray dispersion modification by conical nozzle attachments

Air and water are used as working fluids. The air flow rate is 0.0442 kg s^{-1} and the water flow rate is 2.2 kg s^{-1} ; this corresponds to a GLR (Gas to Liquid mass Ratio) of 2%. The room temperature, 20°C , and the atmospheric pressure, $1.013 \cdot 10^5 \text{ Pa}$, are set as the ambient conditions. All physical properties of materials, such as water surface tension (0.0727 N m^{-1}) and water density (1000 kg m^{-3}), are taken at these conditions.

6.1.2. Computational grid

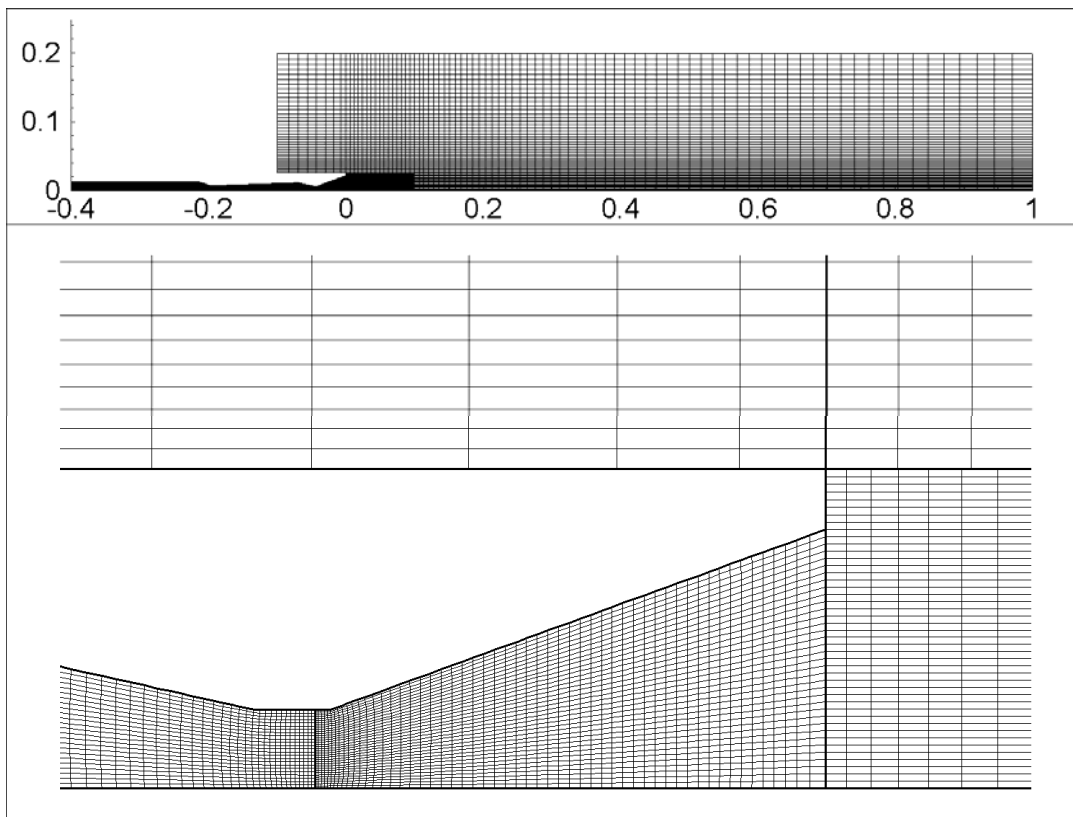


Figure 6-2. Computational grid and domain segmentation (full domain – above, and nozzle attachment area – below).

The computational domain is axisymmetric and includes the nozzle and its surrounding areas where the spray is dispersed. The domain extends axially 1 m from the nozzle exit and radially -0.2 m from the axis. In addition, a short piece of pipe (0.2 m) with the same diameter as the nozzle inlet is added in front of it to allow for some flow development before the mixture enters the nozzle.

A multi-segment curvilinear non-uniform grid, shown in Figure 6-2, is developed to provide a good resolution in the areas of high flow gradients – nozzle, attachment and its

Chapter 6. Liquid spray dispersion modification by conical nozzle attachments

immediate vicinity – and, at the same time, to allow for practical computations by coarsening elsewhere. The grid contains about 11 000 grid cells, more for the larger expansion angles, less for the smaller ones. The modeling set-up and grid density are very similar to the ones previously used in Chapter 4.

6.1.3. Transient effects

All the considered cases are simulated, and the transient converged solutions are obtained with a time step of 0.02 ms. While the solutions are time-dependant, the variations of the flow parameters in time are generally very small, rendering a steady flow for practical purposes. These minor variations have a time-scale of about 1 ms. It is interesting to note that the time-dependencies in the cases with the nozzle attachment are even less than the fairly small ones observed for the stand alone nozzle case; therefore, it follows that an attachment has some stabilizing effects. The subsequent analysis is for the results averaged during 20 ms of real time.

6.1.4. Numerical accuracy

In order to evaluate numerical accuracy we conducted a grid sensitivity analysis for a representative case. The case with 40° expansion angle (Case 4 from Table 6-1) was chosen because of the medium value of the expansion. In addition to a regular grid (10 908 cells), a coarse grid (5 438), and a fine one (22 164) were developed. If we define the average mesh size as

$$h = \sqrt{\frac{\sum_{n=1}^{NS} \sum_{i=1}^{N_n} \sum_{j=1}^{M_n} S_{nij}}{\sum_{n=1}^{NS} N_n M_n}} \quad (6-1)$$

its value for our grids would be 4.51, 6.39, and 3.16 mm correspondingly. Thus, the ratio of cell sizes would be about 1.4, which is sufficiently large for grid independence studies. We use the Richardson extrapolation method (Richardson and Gaunt, 1927) to estimate the order of convergence and evaluate an error for the liquid volume fraction. Denoting fine, medium, and coarse grids, as 1, 2 and 3, and assuming that the error is proportional to the average mesh size in some power p , we can write

$$\begin{aligned}\alpha|_1 &= \alpha + C\Delta h^p \\ \alpha|_2 &= \alpha + C\left(\frac{\Delta h}{r_{21}}\right)^p \\ \alpha|_3 &= \alpha + C\left(\frac{\Delta h}{r_{21}r_{32}}\right)^p\end{aligned}\tag{6-2}$$

Next, we take a first norm of the differences between the solutions

$$\begin{aligned}\|\alpha|_2 - \alpha|_1\| &= C\Delta h^p\left(1 - \frac{1}{r_{12}^p}\right) \\ \|\alpha|_3 - \alpha|_2\| &= C\frac{\Delta h^p}{r_{12}^k}\left(1 - \frac{1}{r_{23}^p}\right)\end{aligned}\tag{6-3}$$

After we divide one of Eq. (6-3) to another, we obtain an equation for unknown parameter p .

Finally, we can evaluate the error of the medium grid solution as

$$\|E_2\| = \|\alpha|_3 - \alpha|_2\| \frac{r_{32}^p}{r_{32}^p - 1}\tag{6-4}$$

Table 6-2. Estimated convergence order and solution error for different cut-off values of liquid volume fraction.

Cut-off value	p	Medium grid solution error
$1 \cdot 10^{-4}$	1.7	$5.7 \cdot 10^{-4}$
$5 \cdot 10^{-5}$	2.0	$4.9 \cdot 10^{-4}$
$2 \cdot 10^{-5}$	2.4	$3.0 \cdot 10^{-4}$

Before calculations, it is important to note that in some parts of the computational domain there is virtually no liquid present. Therefore, it is appropriate to limit our procedure to cells with a sufficient amount of the liquid volume fraction. Evidently, the results presented in Table 6-2 show some dependency on the cut-off selection. Nevertheless, they do confirm the expected second order of convergence. The numerical error seems to be relatively small for areas with substantial presence of the liquid. There is much more uncertainty about the areas where the liquid concentration is low; the overall importance of them, however, is also low. At the same time, it is important to understand that for models of complex problems, of which the presented model is definitely an example, numerical errors

represent only the tip of the iceberg. The modeling errors associated with uncertainties of reproducing certain phenomena play a much larger role. Unfortunately, their evaluation is not amenable to a standardized analysis. Some validation can be achieved by comparing modeling predictions and experimental results. For the presented model, such comparison was performed in Sections 3.1, 4.1.3, 4.2.4, and 5.1.1.4.

6.1.5. Flow analysis

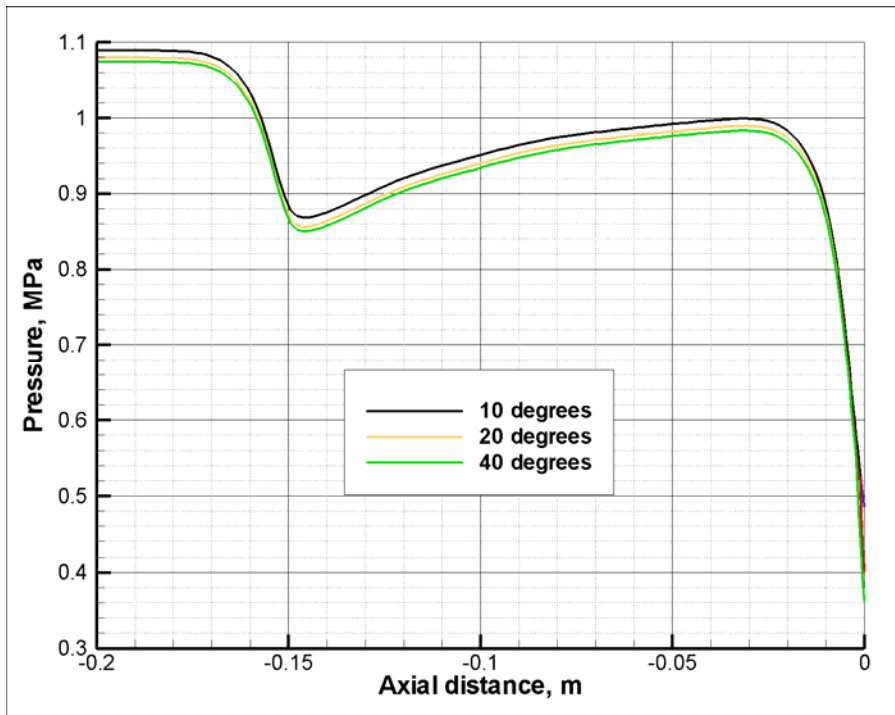


Figure 6-3. Pressure profiles along the nozzle centerline for various cases.

We start the analysis by comparing flows inside the nozzle. Figure 6-3 presents the pressure profiles along the centerline of the nozzle for several cases with a varying expansion angle. While an overall shape of the profile is very similar for all cases, quite naturally, the smaller expansion angles result in the larger pressure drops through the nozzle because of the added resistance to the flow. The difference, however, is too small (less than 1%) to have any practical consequence. Moreover, this difference rapidly decreases as the expansion angle increases: the curves for the 60° and 80° angle cases as well as for a stand-alone nozzle virtually coincide with the 40° angle case curve and are not shown in the graph. All other flow properties, such as the velocities, the bubble average diameter and the volume fractions,

exhibit even less dependence on the expansion angle or the existence of the spray modifier. Therefore, in the following we focus our attention on the flow outside the nozzle and in the spray modifier itself.

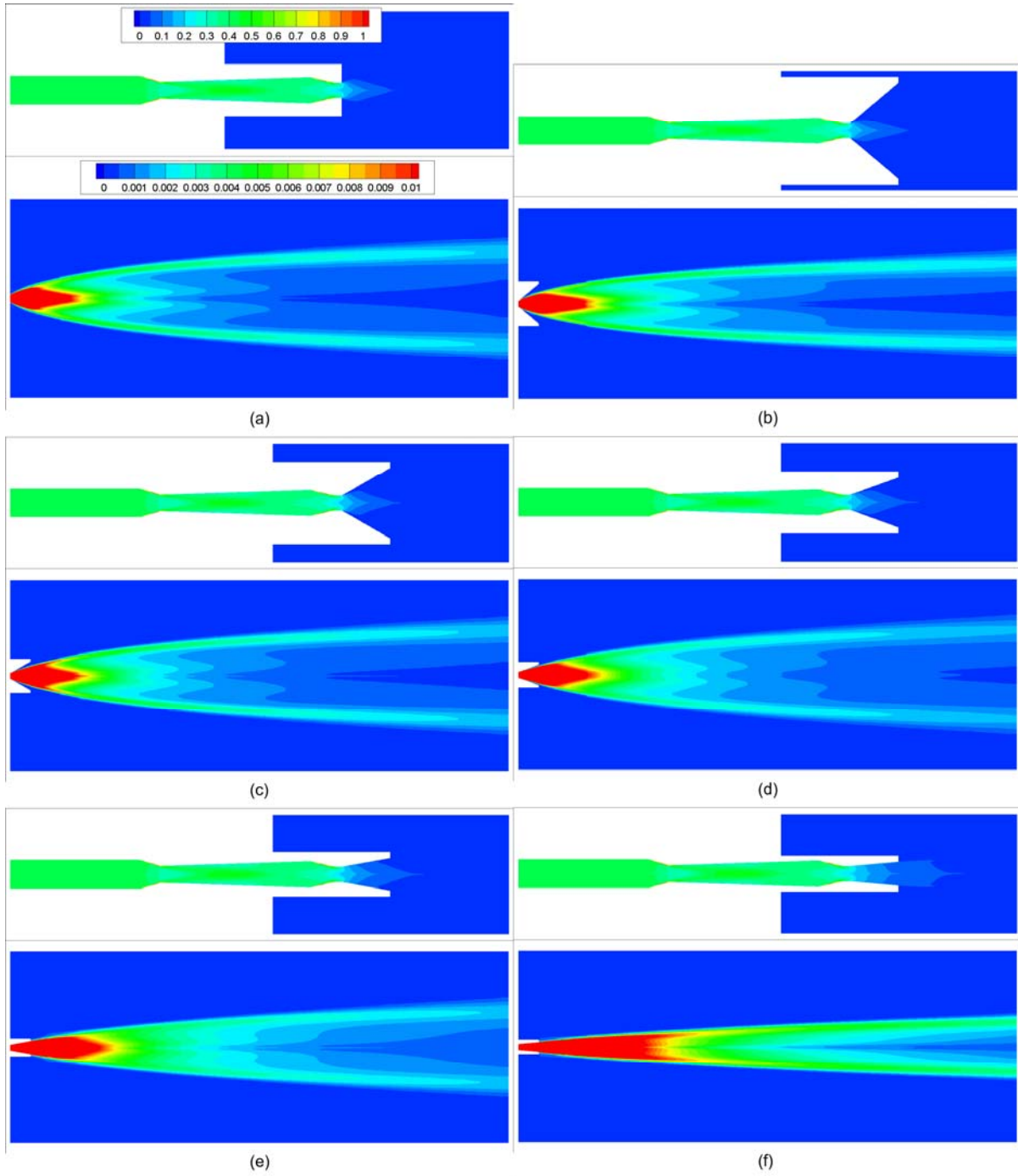


Figure 6-4. Droplets volume fraction contours in the nozzle and spray modifier (above) and in the spray area (below) for (a) - stand alone nozzle, (b) - 80°, (c) - 60°, (d) - 40°, (e) - 20°, (f) - 10°. Note the different scale for the upper and lower plots.

Chapter 6. Liquid spray dispersion modification by conical nozzle attachments

The droplet volume fraction distribution in the nozzle and in the spray is shown in Figure 6-4 for all cases. Note that in order to improve presentation, these and subsequent plots are extended to the full axial cross-section based on the axial symmetry. As already observed in the previous paragraph, inside the nozzle the volume fraction distribution does not appreciably change with the addition of the modifier. While a minor difference in the pressure does influence volume fractions, this influence is negligibly small. At the same time, immediately after the nozzle exit, the presence of the narrow modifier visibly alters the flow. We can see that for the cases with 10° and 20° angle larger volume fractions of water are present after the nozzle exit due to the delay of the air expansion by the modifier geometry. This in turn results in the delayed atomization for the narrow angle cases. Figure 6-5 shows phase inversion surfaces for all cases. Evidently, the location for the atomization moves downstream with narrowing of the expansion angle. However, for angles 40° and higher, no influence is observed. The spray structure is generally similar to that previously observed for these types of nozzles in Chapter 4. Fairly rapid initial rate of the spray dispersion decreases as the droplets move further away from the nozzle. It is evident that the addition of the narrow angle attachments significantly modifies the spray. The cases with 10° and 20° angle demonstrate visibly less dispersion than others, the stand-alone nozzle case included. We can see that for the narrow attachments, the maximum jet dispersion angle approximately coincides with the angle of the nozzle attachment. Thus, addition of the attachment with a narrow cone angle produces the less dispersed and hence, more penetrating jets. The reverse, however, is not true. As soon as the expansion angle reaches about 40° , the spray stops changing and the droplet spatial distribution looks very similar for the cases 40° , 60° , 80° , and for the stand-alone nozzle. It looks as if there is a natural expansion angle, which is achieved in a stand-alone nozzle that cannot be exceeded. Another interesting observation pertains to the rate of the jet expansion. We can see that for the stand-alone nozzle and for the nozzles with wide attachments the expansion rate is relatively large at the beginning and then decreases as the liquid moves further from the nozzle. For the nozzles with narrow attachments, on the other hand, the jet expansion rate remains almost steady throughout the computational domain for the 10° case, and variation is barely noticeable for the 20° case. This phenomenon will be explained later, after we examine droplet size variations.

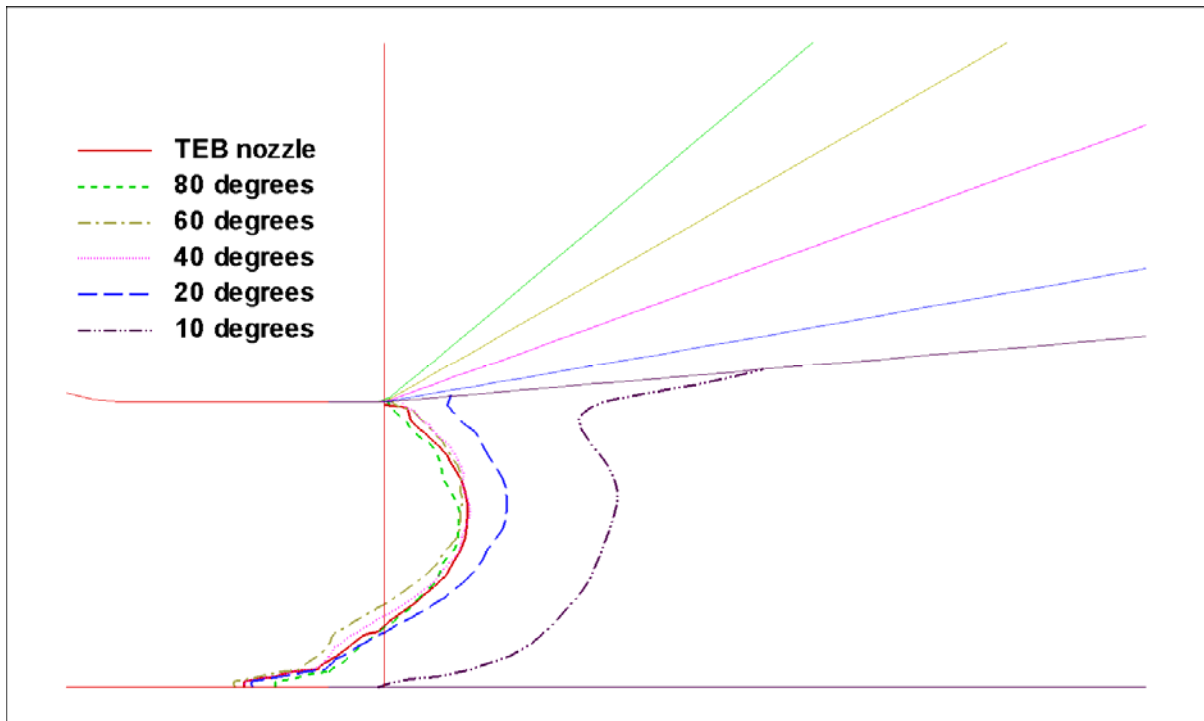


Figure 6-5. Phase inversion surfaces for all investigated cases.

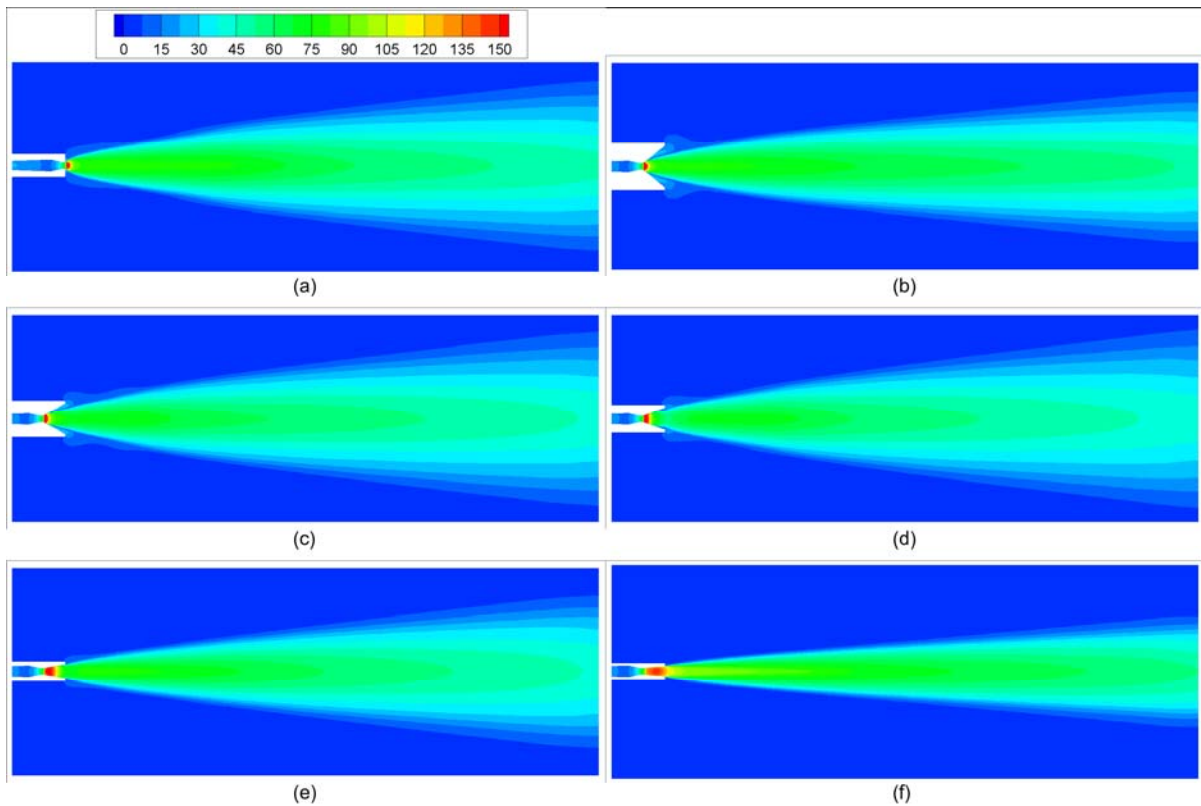
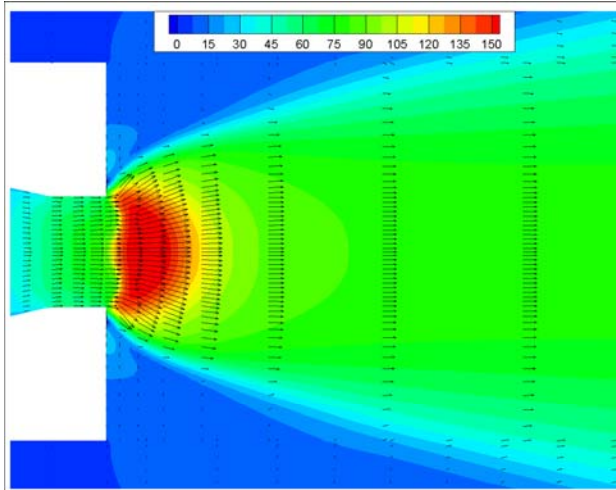


Figure 6-6. Air velocity magnitude contours in the spray area for (a) - stand alone nozzle, (b) - 80°, (c) - 60°, (d) - 40°, (e) - 20°, (f) - 10° (in m s^{-1}).

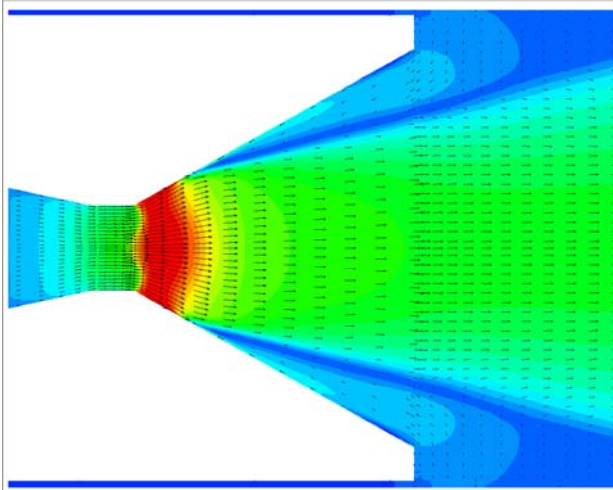
Chapter 6. Liquid spray dispersion modification by conical nozzle attachments

Figure 6-6 shows the air velocity magnitude for all cases. Evidently, the velocity is largest for the smallest expansion angle case, reconfirming our conclusion about the larger jet penetration for the narrower attachments. These plots also show a high velocity area (red) that immediately follows the atomization. The origin of this area lies in the dramatic difference of the interfacial drag and virtual mass forces between liquid and bubbles and between gas and droplets. Therefore, the atomization results in a significant reduction of the interfacial forces; thus, gas can accelerate allowing the slip velocity, which is the difference between the gas and liquid velocities, to grow. However, this growth is not limitless and at some distance downstream the new equilibrium conditions are reached. This zone, as well as the whole liquid-continuous area preceding it, is characterized by the high interfacial momentum exchange. It is there that the spray droplets obtain the momentum to continue along their trajectories.

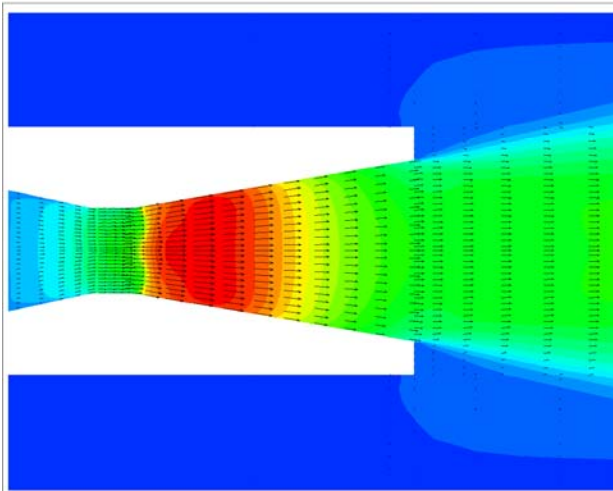
We looked closer into this area by plotting the velocity vectors in this region in three representative cases (Figure 6-7). It can be seen that while in the stand-alone nozzle case there is a rapid increase of the radial velocity, in the case with 10° expansion angle, the radial velocity changes are rather small. The reason is that without an attachment the jet expands freely in the open air. With the nozzle attachment, however, the expansion takes place inside the spray modifier, and it is restricted by its walls. Thus, in the narrow attachment cases the radial velocity is limited by the expansion angle. In the case of the wide attachment angle, shown in Figure 6-7 (b), the air radial velocity initially grows so that the jet fills the entire area. However, soon after, the radial velocity reduces and the jet detaches from the wall. That probably occurs because of the presence of the droplets (which can have a spatial variation of volume fraction as any discrete phase) with relatively large inertia that makes them unable to follow small radius bends in the gas streamlines. Because the droplets transfer their momentum to the gas through the interfacial forces, we can observe a recirculation bubble forming near the wall of the expanding section. Note that the recirculation takes place only for the air – the droplets do not really occupy this area (see Figure 6-4 (c)), and the existing few continue their movement in the flow direction.



(a)



(b)



(c)

Figure 6-7. Air velocity vectors and magnitude contours in the nozzle exit area for (a) – stand-alone nozzle, (b) - 60°, (c) - 20° (in m s^{-1}).

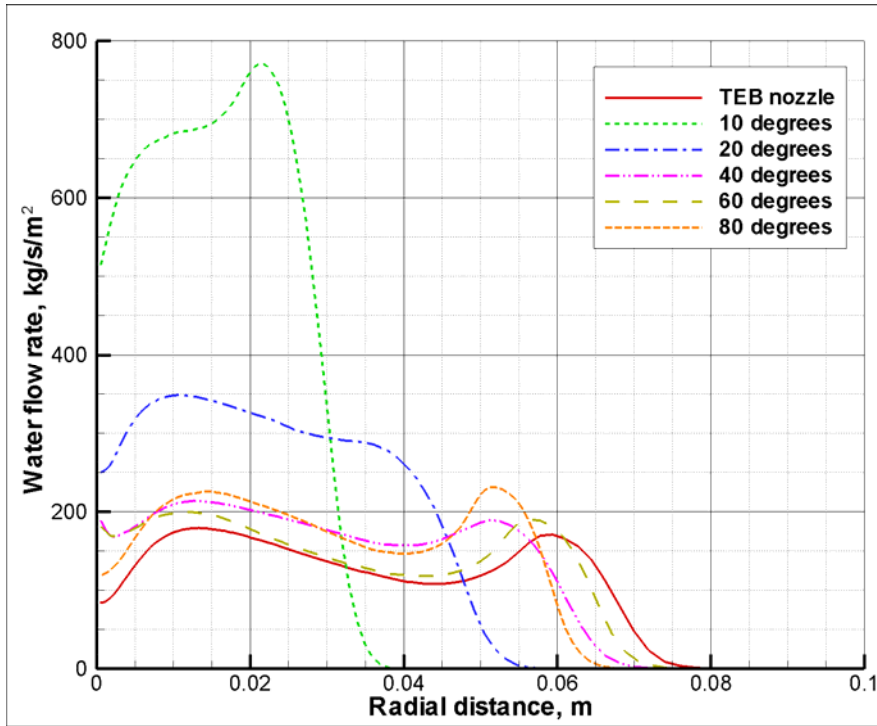


Figure 6-8. Water flow rate profiles in a radial cross-sectional plane located at 0.3048 m from the nozzle exit.

Next, we look at the radial distributions of the liquid flow rates, which are defined as $\varepsilon_i \rho_i \mathbf{V}_i \cdot \mathbf{k}$, for all cases. Figure 6-8 presents water flow rate variations at 0.3048 m (1 ft) distance from the nozzle exit orifice. As expected, we observe higher flow rates and less dispersion for jets obtained with a narrow nozzle attachment. For the case with a 10° angle, the maximum flow rate increases more than three times compared with the stand-alone nozzle. What is interesting in this graph is that while almost all cases seem to follow the pattern just described – the reduction of the jet dispersion and the increase in maximum flow rate – the case with 80° angle produces a narrower jet than that obtained with a 60° modifier. In order to explain such behavior, we examine the droplet diameter variations in the spray.

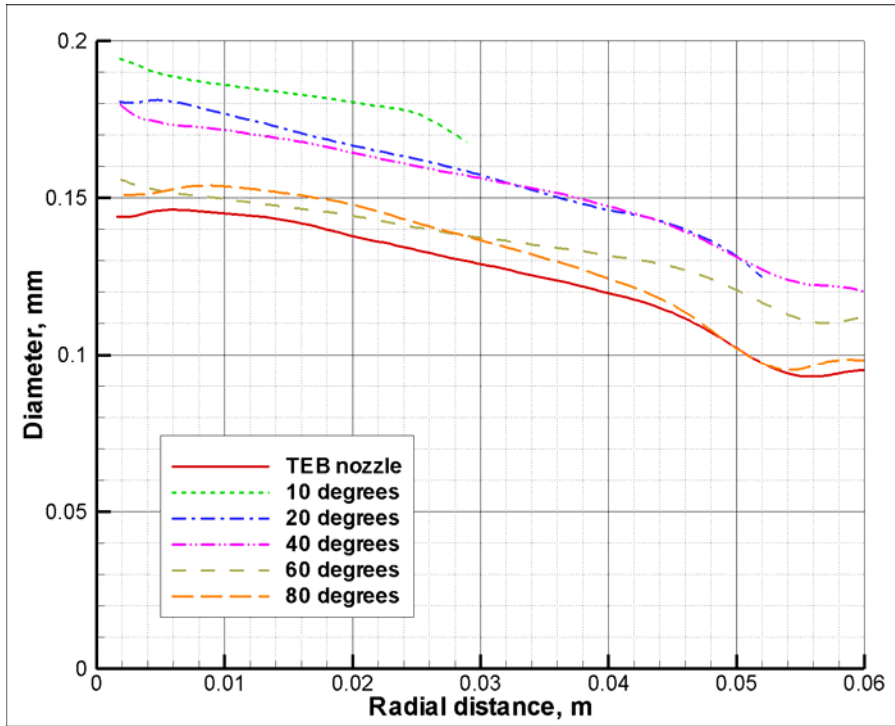


Figure 6-9. Average droplet diameter variation in a radial cross-sectional plane located at 0.3048 m from the nozzle exit.

Figure 6-9 shows the local average droplet diameter profiles at a 0.3048 m distance from the nozzle exit. First of all, we can see that for all of the cases the average droplet diameter decreases from the axis towards the periphery of the jet. The addition of the spray modifier does not change this trend. Second, the nozzles with the narrow attachments (10° – 40° angle) produce larger droplets than the nozzles with the wide attachments or without any attachments at all. This explains the difference in the spray expansion rate noticed during the analysis of water volume fractions. The reduction of the spray expansion rate as it moves further out from the nozzle is caused by the interfacial friction between the droplets and the air entrained into the jet to preserve the total volume continuity. Therefore, the radial momentum of the droplets is reduced. However, the interfacial friction depends on the droplet size – the larger the droplet, the smaller the friction force. Thus, the sprays with the larger droplets exhibit less momentum exchange, and hence, less reduction of the expansion rate. Third, we can see that for the 80° angle case, the average droplet diameters at the periphery of the jet are smaller than for all other cases, including the stand-alone nozzle case. As just analyzed, these smaller diameters result in a larger reduction of the jet expansion rate and, ultimately, in a narrower spray. That is in agreement with our earlier

observation regarding a perceived anomaly of a somewhat narrower spray for the 80° angle case.

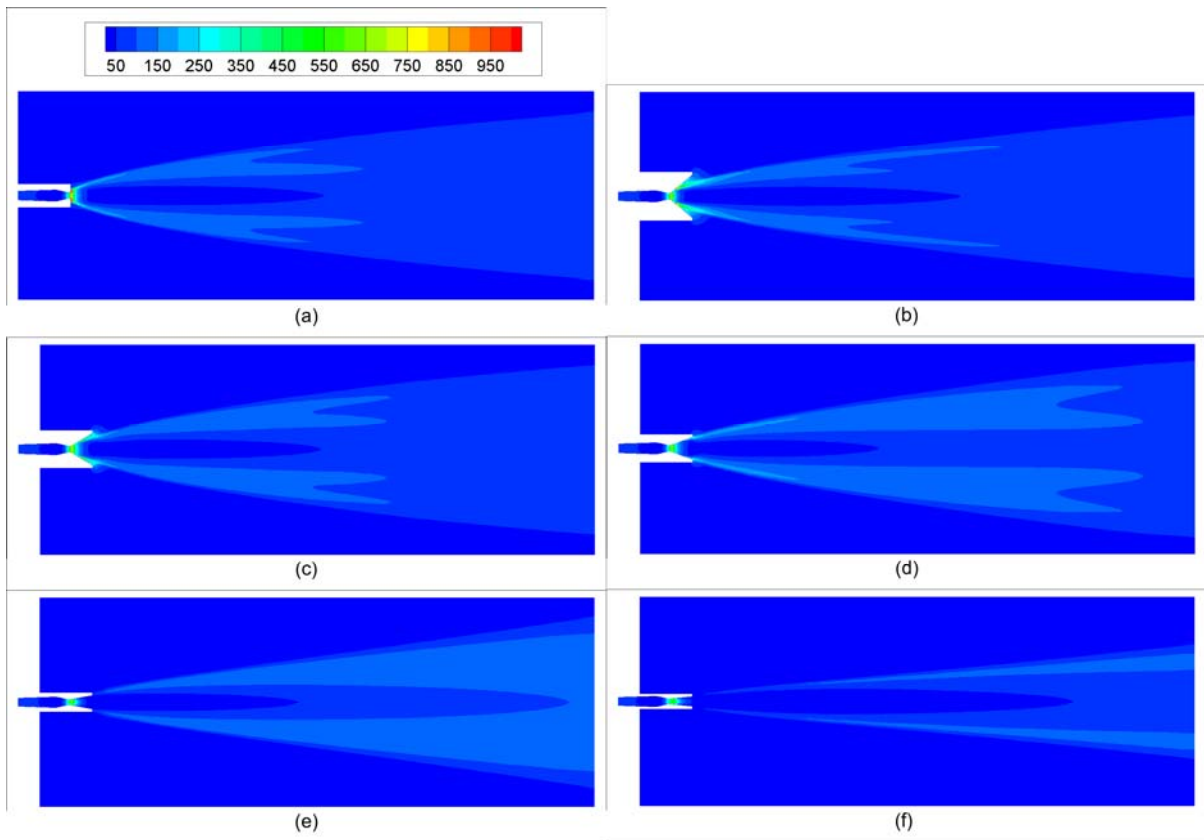


Figure 6-10. Turbulence kinetic energy contours in the spray area for (a) - stand alone nozzle, (b) - 80°, (c) - 60°, (d) - 40°, (e) - 20°, (f) - 10° (in $\text{m}^2 \text{s}^{-2}$).

To understand the mechanisms underlying the droplet diameter distribution, we need to recall that (a) the droplets are born after the phase inversion surface, and (b) they undergo break-up and coalescence. As the flow in the nozzle is essentially the same for all cases, the average bubble diameter leading to the phase inversion is also essentially the same. Therefore, the initial droplet diameters are also almost the same for all cases. Thus, the differences between the cases appear because of the different break-up rates for the cases with different nozzle attachments. In our model, the break-up takes place due to either the interfacial shear or the turbulence fluctuations. Previous analysis in Chapter 4 confirmed that the dominant breakage mechanism in this type of spray is the turbulence induced break-up. Therefore, to understand the differences in the break-up rates, we plot contours of the turbulent kinetic energy in Figure 6-10. In all of the cases, we can see substantial turbulence

generated near the nozzle exit that propagates downstream, dissipating along the way. One can observe that the turbulence is much less for the narrow attachment cases. Probably, this is a consequence of the phase inversion taking place in the restricted environment where the shearing motion induced by the jet is constrained. With smaller turbulence, the break-up frequency is also smaller, and as a result, the droplets are larger.

In addition, we can see a significant amount of turbulence generated in the expansion section of the 80° angle case. This turbulence is generated because of the significant air recirculation that takes place near the modifier walls (see Figure 6-7 (b)); such recirculation is absent in the stand alone nozzle case. Even though in the stand-alone nozzle much turbulence is generated around the sharp angles surrounding the nozzle orifice, at the periphery of the jet it is still less than what is generated by the strong recirculation in the 80° angle case. This is the cause of the smaller droplets being present at the outer side of the jet and of the unexpected trend of the liquid flow rates for the 80° angle case.

6.2. Steam-bitumen spray injected into a fluidized bed

6.2.1. Description of cases

We investigate the same nozzle configurations described in Section 6.1.1 and shown in Figure 6-1. As shown in Section 6.1, sprays obtained with a wider angle of attachment behave very similarly to the sprays produced by a standard TEB nozzle. Therefore, we limit our investigation to the attachments with expansion angles of 10°, 20°, and 40°. Also, we include the nozzle without any attachments for comparative purposes. That is, we consider cases 1 – 4 from Table 6-1. While physical properties of steam are widely available, bitumen values are more difficult to obtain. While at low temperatures bitumen exhibit some shear thinning behaviour (Bazyleva et al., 2010), at temperatures above 50°C it can be safely approximated as Newtonian liquid. Aminu et al. (2004) investigated properties of an Athabaska vacuum residue that can be representative of fluid coking process conditions. Even though the focus of their research was on finding variation of properties with the progress of chemical reactions, we can still extract some data related to unreacting bitumen

that is required for this work.³ Because liquid does not have time to be substantially heated up in our domain of interest, variation of liquid properties with temperature is not currently supported by the model. Therefore, we are looking at bitumen properties at the injection temperature, i.e. 350°C. The surface tension does not show significant variations with temperature (nor with chemical reactions), and it can be extrapolated based on values at 400°C (0.014 N m⁻¹) and at 503°C (0.0058 N m⁻¹). Thus, the surface tension at 350°C is estimated to be 0.018 N m⁻¹. The viscosity, on the other hand, demonstrates more significant variations with temperature (and with chemical reactions), which make extraction of data more difficult. We know from measurements presented by Aminu et al. (2004) that bitumen viscosity at 180°C is 0.15 Pa s and at 270°C is 0.03 Pa s. As can be seen, not only the variation of values is rather large, but the extrapolating interval is also large. Simple linear extrapolation, which was sufficient for surface tension, would result in clearly unphysical negative viscosity values at our temperature of interest. Therefore, we try a more sophisticated interpolation procedure. Seeton (2006) developed a viscosity-temperature correlation that is applicable to hydrocarbons, albeit for ones with lower carbon content than bitumen. This correlation takes the following form

$$\ln(\ln(\nu + 0.7 + e^{-\nu} K_0(\nu + 1.244067))) = A - B \ln(T) \quad (6-5)$$

where K_0 is the zero order modified Bessel function of a second kind and A and B are fitting parameters. We determine these parameters based on known viscosity at lower temperature points and then extrapolate the viscosity according to Eq. (6-5). This procedure results in a viscosity value of 0.0122 Pa s at 350°C. It is interesting to note that a simple exponential extrapolation

$$\mu = \mu_0 e^{-AT} \quad (6-6)$$

gives viscosity about 0.007 Pa s. Given a large number of uncertainties in bitumen viscosity values, we set it at 0.01 Pa·s in our computations. Other properties, such as bitumen density (851 kg m⁻³), heat capacity (1000 J kg⁻¹ K⁻¹), and thermal conductivity (0.17 W kg⁻¹ K⁻¹), are

³ Since we consider only the initial distribution of liquid inside the bed that takes place immediately after leaving the nozzle, chemical reactions do not have sufficient time to alter liquid properties.

less critical and varied less with temperature. We assume that all coke particles have the same diameter that is equal to 0.15 mm. The coke density is 1500 kg m^{-3} , heat capacity – $850 \text{ J kg}^{-1} \text{ K}^{-1}$, and thermal conductivity $0.05 \text{ W kg}^{-1} \text{ K}^{-1}$. The same computational grid as for the open air cases (see Figure 6-2) is utilized for simulating fluidized bed injections.

6.2.2. Steam dispersion without particles

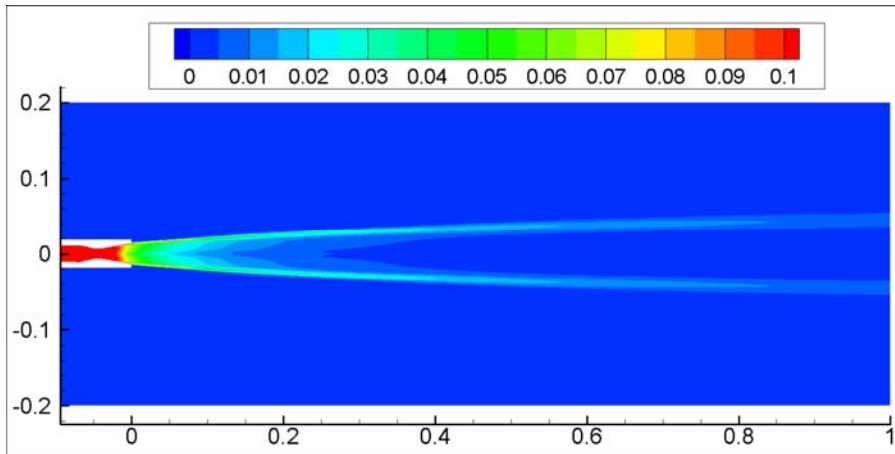


Figure 6-11. Droplet volume fraction contours for the case with 20° attachment angle.

We start the analysis by considering cases without the presence of solid particles. While they are generally similar to those investigated in Section 6.1, in this section we utilize industrially relevant process conditions described in the previous section. All simulated cases produced solutions that can be considered steady state for practical purposes, i.e. any transient variations are negligibly small. A typical solution is presented in Figure 6-11 for the case with 20° attachment angle. Note that for better presentation in this and subsequent contour plots, the solution is extended to a full axial cross-section based on the axial symmetry. We can see that the spray follows the shape of the attachment with maximum droplet concentration being near the periphery of the spray. As the attachment angle increases, the spray expansion angle reaches its maximum value and does not increase any further, confirming the conclusion obtained in Section 6.1. This can be observed by plotting cross-sectional profiles of liquid flow rates. From Figure 6-12, it is clear that the solutions for the cases with the attachment angle 40° and larger are practically the same. Interestingly enough, the solution for a stand alone TEB nozzle differs from the one obtained for the cases with large attachment angles, albeit slightly. It seems that the spray obtained from the TEB

nozzle has somewhat less dispersion. It can be hypothesized that the nozzle cone reduces the outside air entrainment at the nozzle exit where the spray starts to develop, and as a result, droplets can keep their radial momentum for a little longer time. This phenomenon was not observed previously for air-water cases (see Figure 6-8) because they generally had a wider overall dispersion over a longer distance, and as a consequence, the initial radial spreading was less important.

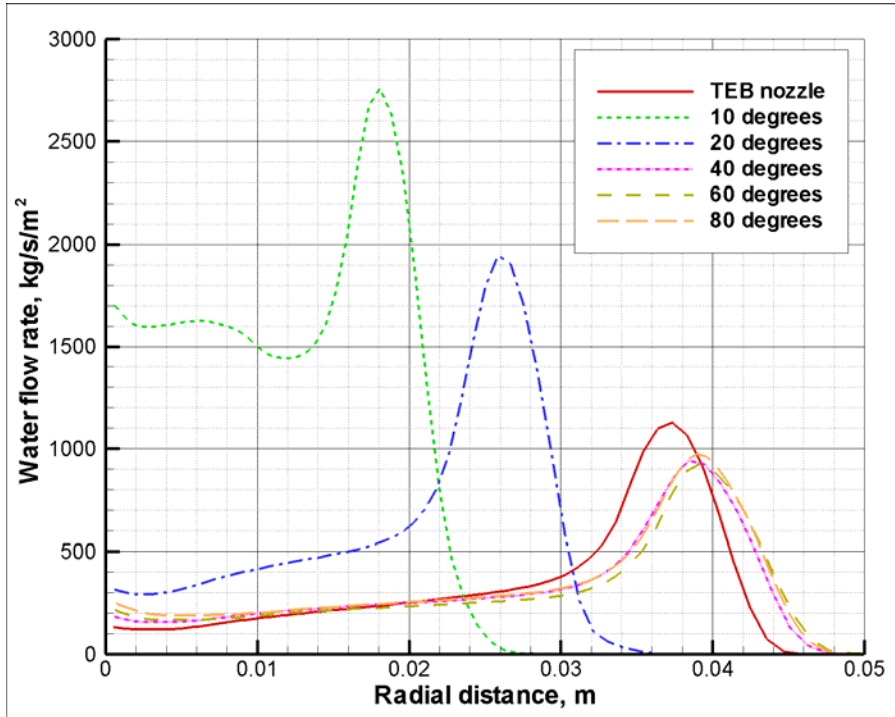


Figure 6-12. Water flow rate profiles in a radial cross-sectional plane located at 0.3048 m from the nozzle exit.

6.2.3. Steam dispersion in a fluidized bed

6.2.3.1. Transient behaviour

The presence of solid particles makes flow in all cases markedly unsteady. In Figure 6-13, we present typical snapshots of the solutions for all cases (the animations showing time-dependent behaviour are provided as supplementary materials). The wavy interface that demarcates the jet and bed areas is evident in all plots. Its fluctuations are quite periodic. It seems that their mechanism is similar to Kelvin-Helmholtz instability as there is a considerable difference of velocities across the jet-bed “interface”. There are also notable differences between the cases. For the cases with a small attachment angle, the onset of

instabilities takes place further downstream than for the cases with a large attachment angle, including the case with a stand alone nozzle. While the behaviour of the cases with 80° and 60° attachment angles is rather similar, the case with a 40° angle exhibits boundary fluctuations beginning right from inside the attachment area. Also, the start of the fluctuations is slightly delayed for a stand-alone nozzle, compared with the cases with large attachment angles. As will be subsequently shown, this transient phenomenon is mostly responsible for the observed characteristics of the interactions between spray droplets and solid particles.

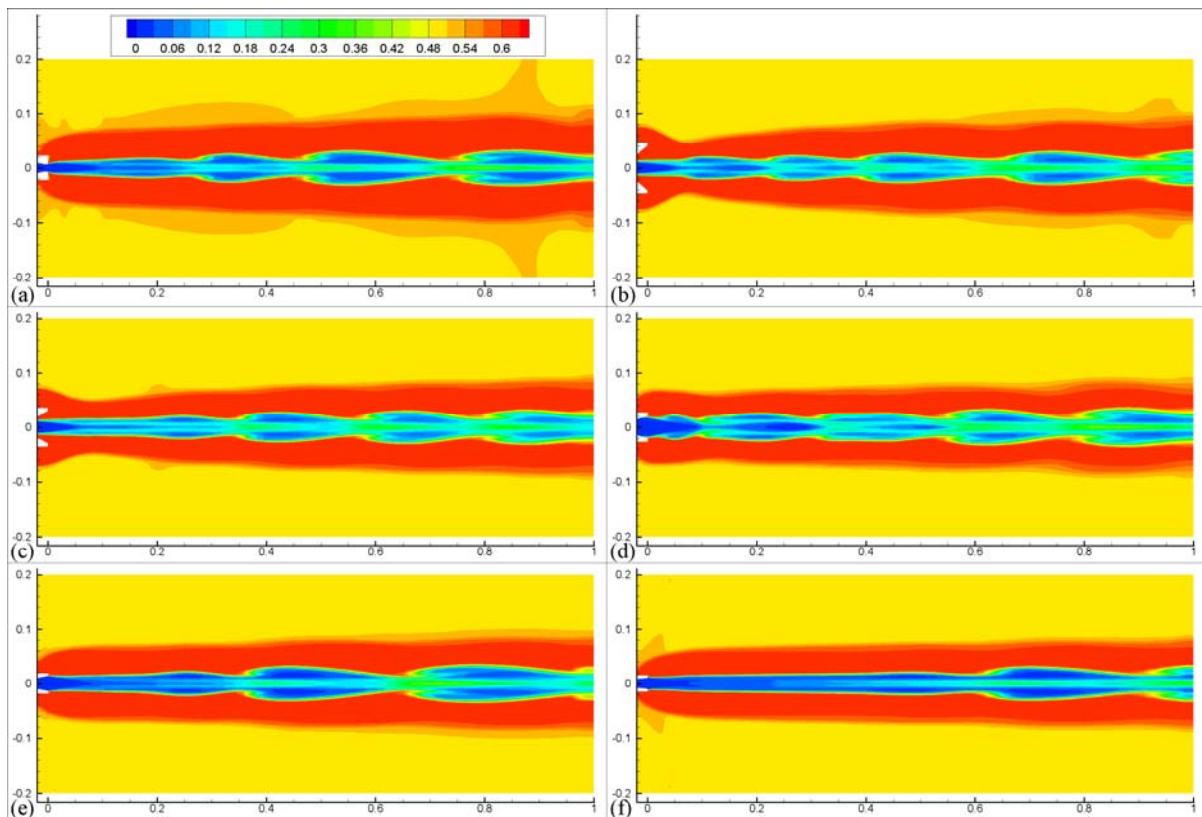


Figure 6-13. Snapshots of volume fraction of the particulate phase; (a) - TEB nozzle, (b) - 80°, (c) - 60°, (d) - 40°, (e) - 20°, (f) - 10°.

6.2.3.2. Flow analysis

To facilitate further analysis, we average in time the solution for all cases. Contours of time-averaged volume fractions of the particulate phase are presented in Figure 6-14. It can be seen that the jet boundary changes from sharp to vague, depending on whether some fluctuations are present in the specific area. All of the plots show the expected densification area around the jet due to the gas entrainment. In the case of a stand-alone nozzle, this area is

visibly larger than in all other cases. This is probably the result of the attachment impeding the entrainment of the outside gas that was discussed above. Also, we can see that for the cases with large attachment angles, solid particles penetrate into the cone of the attachment.

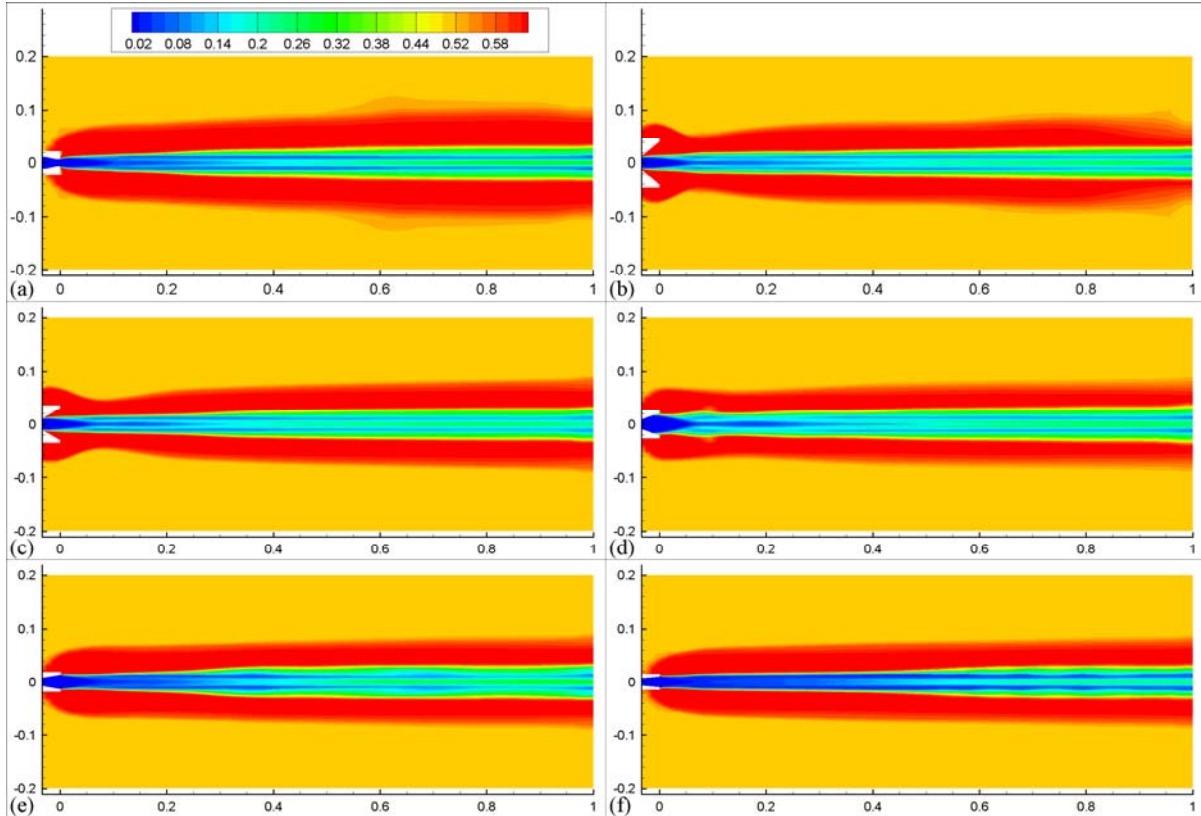


Figure 6-14. Time-averaged particulate phase volume fraction contours; (a) - TEB nozzle, (b) - 80°, (c) - 60°, (d) - 40°, (e) - 20°, (f) - 10°.

Next, we look at the bitumen droplet volume fraction contours plotted in Figure 6-15. We can see that these plots differ dramatically from what was observed without the particles present (see Figure 6-11). Instead of spreading out radially after leaving the nozzle, the droplets are confined by the solid particles to the narrow axial area. We can even see a notable increase of the droplet volume fraction downstream of the nozzle for some cases. Evidently, for cases with a small attachment angle (10°, 20°) many droplets leave the domain without attaching to the solid particle. This happens because the spray from these cases has a low initial dispersion (see Figure 4) that reduces the jet contact area with the particles, and most importantly, the relatively stable jet-bed interface does not promote liquid-solid contact. Similar conclusions (however, to a smaller degree) apply to the case without an attachment. The cases with large attachment angles, on the other hand, demonstrate that all droplets

become consumed after about 2/3 of the length of the domain. The main reason for this is a good mixing promoted by the jet instability.

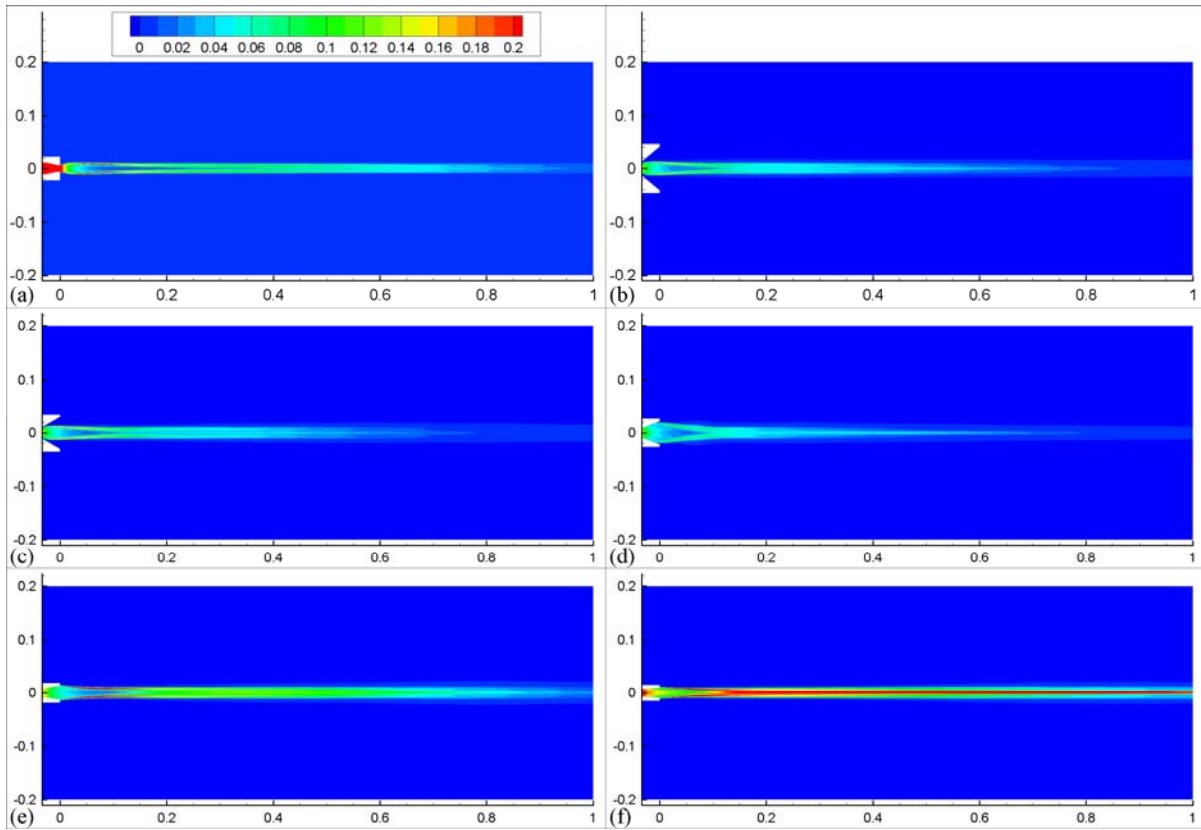


Figure 6-15. Bitumen droplets volume fraction contours; (a) - TEB nozzle, (b) - 80°, (c) - 60°, (d) - 40°, (e) - 20°, (f) - 10°.

A look at the volume fraction of the liquid film, calculated as $\alpha_f = x_f(\rho_f/\rho_p)$ and presented in Figure 6-16, confirms our previous observations. The cases with a small attachment angle show poor bitumen distribution among coke particles. For these cases, liquid starts to accumulate on solid particles only after a certain distance downstream of the nozzle; apparently, this is due to the lack of mixing and high interfacial velocity. In contrast, the plots for cases with a large attachment angle reveal that the jet-bed interactions result in the formation of wet particles right after the nozzle exit and inside the attachment. We can see that the solids entrained into the attachment provide a mechanism for early radial bitumen spreading. Another mechanism is the previously discussed fluctuations of the jet-bed interface that expose more dry particles to the moving droplets. Note that the case with a

stand-alone nozzle exhibits a performance which is somewhere in the middle of the two discussed limits.

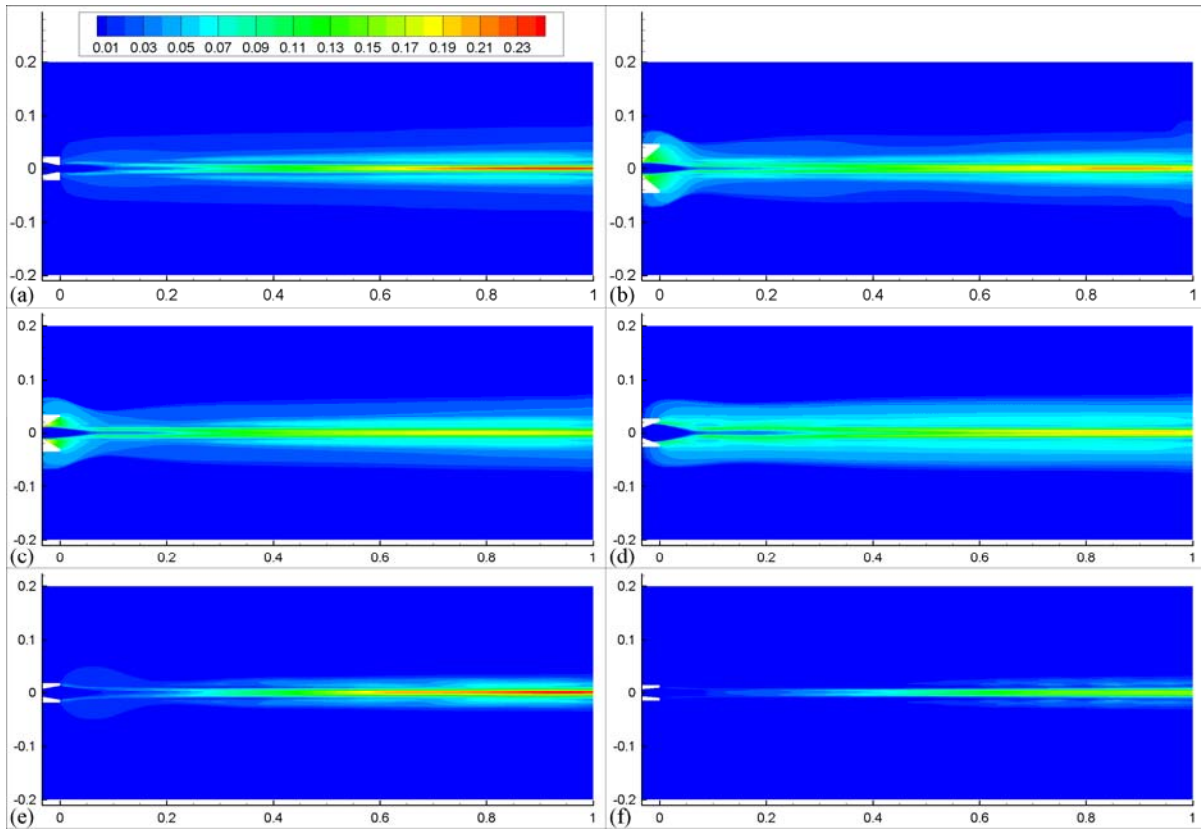


Figure 6-16. Bitumen film volume fraction; (a) - TEB nozzle, (b) - 80°, (c) - 60°, (d) - 40°, (e) - 20°, (f) - 10°.

In order to quantify jet-bed interactions, in Figure 6-17 we present plots for cumulative liquid distribution variation with liquid to solid (L/S) mass ratio, defined by

$$\frac{L}{S} = \frac{\alpha_l \rho_l u_l + \alpha_p x_f \rho_p u_p}{\alpha_p x_s \rho_p u_p} \quad (6-7)$$

The nozzle performance can be judged based on how close the curve is located to the left side of the graph, where more liquid in the system is characterized by a low L/S ratio, indicating wider liquid distribution as the total volumetric flux remains the same in all cases.

In agreement with the presented analysis, the case with the 10° attachment angle demonstrates the markedly worst performance. The best performance is obtained in the case with the 40° attachment. Evidently, this is the outcome of boundary fluctuations, which are limited for the former case, but are most pronounced for the latter. There is no significant

difference between the cases with 60° and 80° attachments; all of them provide second best liquid distribution. The performance of a stand-alone nozzle without attachments is somewhere inbetween. The conclusions of the analysis are in agreement with an experimental study conducted by House et al. (2008), who investigated nozzle design influence on liquid-solid contact. They noted positive improvements to liquid distribution obtained with the addition of a conical attachment to a small-scale nozzle. Apparently, the expansion angle of their attachment was sufficiently large to produce such results.

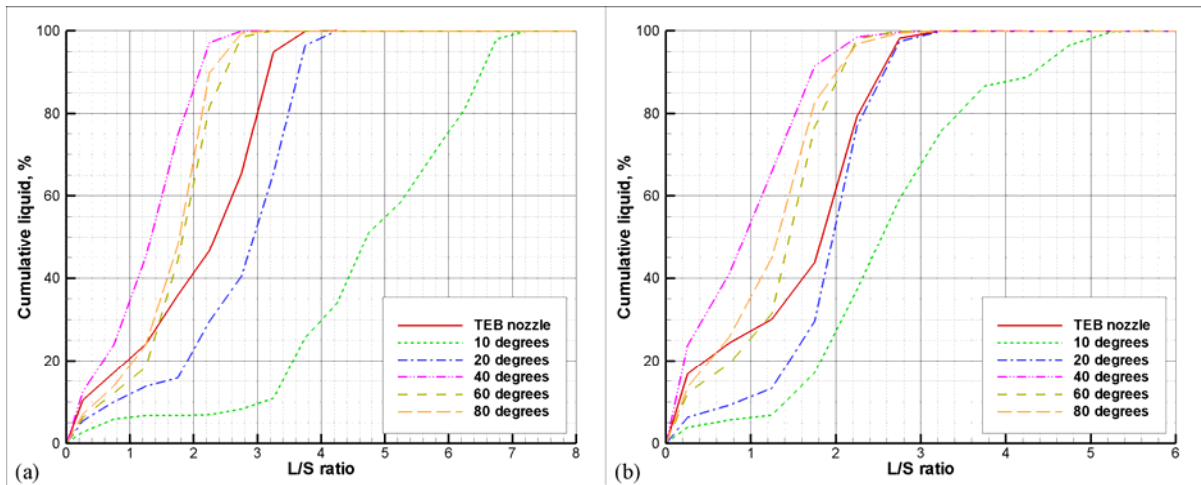


Figure 6-17. Cumulative liquid distribution profiles at 10 cm (a) and at 30 cm (b) from the nozzle exit.

Undoubtedly, the major factor in the performance of the nozzle attachments is the instability of the jet and resulting fluctuations of the jet-bed interface. Whether each particular configuration impedes or amplifies fluctuations determines whether nozzle performance is improved or deteriorated. The advantages or disadvantages of a certain configuration do not change with distance: the curves at 10 and 30 cm downstream from the nozzle orifice have the same relative positions, even though the absolute values of L/S ratio expectedly decrease with moving further away from the nozzle exit. It is important to note that in the industrial case where the gravity is present, after a certain distance in the axial direction, the solution deviates from what is presented in this section. However, this does not change the differences in primary dispersion observed in this study.

6.2.3.3. Grid independence

In order to assess grid independence of the solution, we chose a typical case – the case with 20° attachment – and computed it additionally for coarser and finer grids. The

coarse grid has 6 876 cells, the fine grid has 18 800 cells, and the regular grid has 10 548 cells. To quantify the comparison, we plotted cumulative liquid distribution at 30 cm downstream from the nozzle orifice for three different grids in Figure 6-18. It can be seen that while the coarse grid profile differs considerably from the other two, the profiles obtained on the medium and fine grid are approximately the same. Therefore, we can conclude that the solution is sufficiently grid independent, and the medium grid is adequate for our simulations.

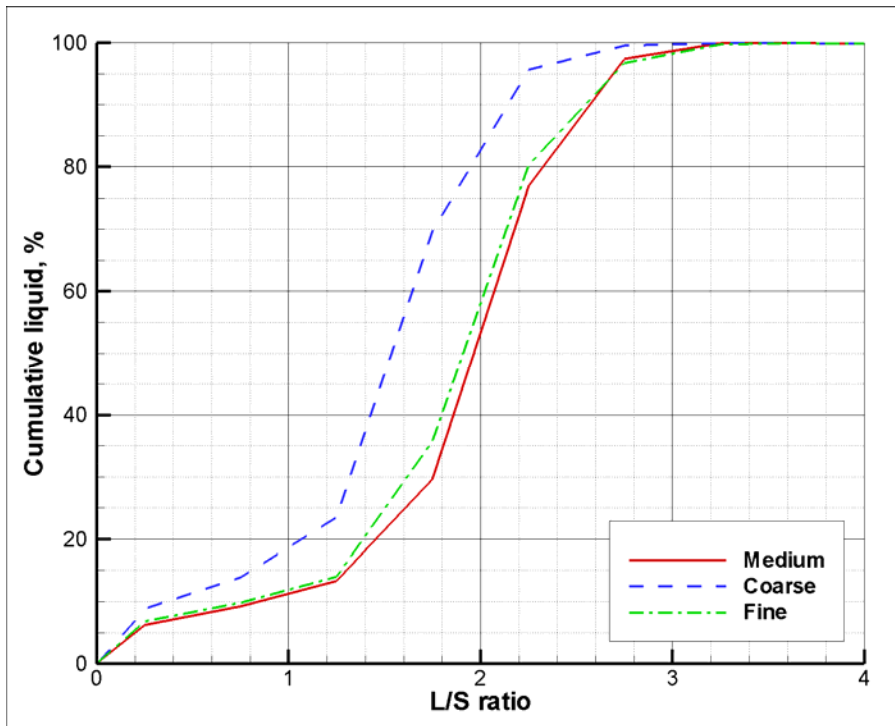


Figure 6-18. Cumulative liquid distribution profile for the case with 20° attachment at 30 cm from the nozzle exit for three different grid resolutions.

6.3. Summary

The influence of the addition of the spray modifiers to the standard TEB-type nozzle was investigated numerically for air-assisted water spraying into open air and for steam assisted bitumen spraying into a fluidized bed of coke particles. Conical modifiers with varying expansion angle were chosen for our study. The simulation conditions were relevant to the industrial application – a fluid coking reactor. We examined the effects that the attachments have on spray dispersion, liquid flux distribution, droplet size distribution, and on the interactions between droplets and bed particles. The modelling confirmed that while

Chapter 6. Liquid spray dispersion modification by conical nozzle attachments

certain types of attachments can substantially modify both the spray itself and its interaction with a fluidized bed, others can have a significant influence on spray-bed interaction only without having an impact on the spray. Our analysis also demonstrated that there is an optimal expansion angle of about 40° for a conical attachment.

Chapter 7. PARTICLE ATTRITION

In this chapter the attention is shifted from gas-liquid injections into a fluidized bed to high speed gas injections. These gas injections are used to promote collisions between bed particles and, as a result, induce breakage. The process is called particle attrition, and it serves as a means to reduce particle size and break down agglomerates. A mathematical model of particle attrition developed in Section 2.2 is applied to simulate the experiments in a small scale fluidized bed for model validation purposes and also to investigate the attrition phenomena in industrial settings.

7.1. Small scale fluidized bed

7.1.1. Grinding efficiency model

In this study the grinding “efficiency”⁴ model differs somewhat from the one described in Section 2.2.7.4. Because the attrition rates are relatively low, it is possible to relax one of the model assumptions and to account for particles being split into two unequal parts. We do it only for the purposes of calculating grinding efficiency.

Following McMillan et al. (2007b), let us introduce a symmetry coefficient, ψ , which is a ratio of the volumes of small and large daughter particles.

$$\psi = \frac{V_{small}}{V_{large}} \quad (7-1)$$

Then, the diameters of the small and large daughter particles are

⁴ As previously noted, we continue using the terminology, introduced by McMillan et al. (2007a, 2007b) related to the particle surface area increase per mass of the injected gas, to be consistent with already published literature.

$$d_{small} = \frac{d}{\sqrt[3]{1+1/\psi}}, \quad d_{large} = \frac{d}{\sqrt[3]{1+\psi}} \quad (7-2)$$

The change of the surface area after the breakage of a single particle can be found as

$$\Delta S_{part} = S_{small} + S_{large} - S_0 = \pi d^2 \frac{1 + \psi^{\frac{2}{3}} - (1 + \psi)^{\frac{2}{3}}}{(1 + \psi)^{\frac{2}{3}}} \quad (7-3)$$

Next, a total change of the surface area per unit volume can be calculated

$$\Delta S = \Delta S_{part} N \quad (7-4)$$

In the simulations, the value of ψ is set to 0.8 as was suggested by McMillan et al. (2007b). It is interesting that the difference in the increase of the particle surface area between $\psi = 1$ (equally split particles) and $\psi = 0.8$ is only 0.7%. Note, however, that this approach make an implicit assumption that the particle can break up only once within each computational cell. That is, the number of collisions resulting in breakage cannot be more that twice the number of particles. This condition was generally satisfied during the small scale computations for small flow rates and moderate inlet pressure values reported in this section.

7.1.2. Calculation procedure

Due to the size and the complexity of the model, it is necessary to develop an efficient calculation procedure to ensure that simulations can be completed in reasonable time. Clearly, the time scale is substantially different between the high Mach number regions inside and near the attrition nozzle and in the rest of the fluidized bed. Moreover, inside the nozzle the flow is single phase and can be approximated as steady state, while outside, the flow is two-phase and highly transient. Therefore, in order to take advantage of these features, the computational domain is partitioned into several segments so that they can be treated separately. The simulation can be divided into two stages. The preliminary stage precedes the main computations by creating suitable initial conditions of the jet issuing into the fluidized bed. The main stage runs the model for sufficient time to obtain time-averaged results for the flow and the grinding efficiency. Following the solution initialization with a

Chapter 7. Particle attrition

constant value of the solid fraction in a lower portion of the bed, the computations proceed with a fairly high value of the time step (~ 1 ms) to obtain a reasonable solid distribution inside the bed. During this stage, the equations in the nozzle segments are not solved. This stage lasts for about 6 s of real time. Next, the solution in most of the fluidized bed is frozen, and only the nozzle segments together with the one directly downstream of the nozzle are computed with a small time step (1 μ s). After the solution inside the nozzle reaches steady state (judged by comparing the inlet and outlet flow rates), the nozzle segments are switched off and the rest of the bed is calculated. During this period, the time step is different in the various segments: near the nozzle it is 0.01 - 0.05 ms (depending on the case), and everywhere else it is 0.5 ms. This stage continues for about 1 s of real time and concludes the preliminary phase. Next, the main simulation starts with the same solution parameters, and the results from each time step are collected to calculate the time-averaged flow variables and the total value of the grinding efficiency. The calculations continue until the grinding efficiency stops changing within the accepted accuracy. The real time required is about 1 - 2 s. Computations are done on an Intel Xeon 2.6 GHz workstation, and it takes about one week of computational time on a single CPU to complete one case. Note that some cases can be started from an intermediate point of the preliminary stage by utilizing the results from similar cases already computed to shorten the overall computational time required.

7.1.3. Model comparison with experiments

7.1.3.1. Experimental set-up

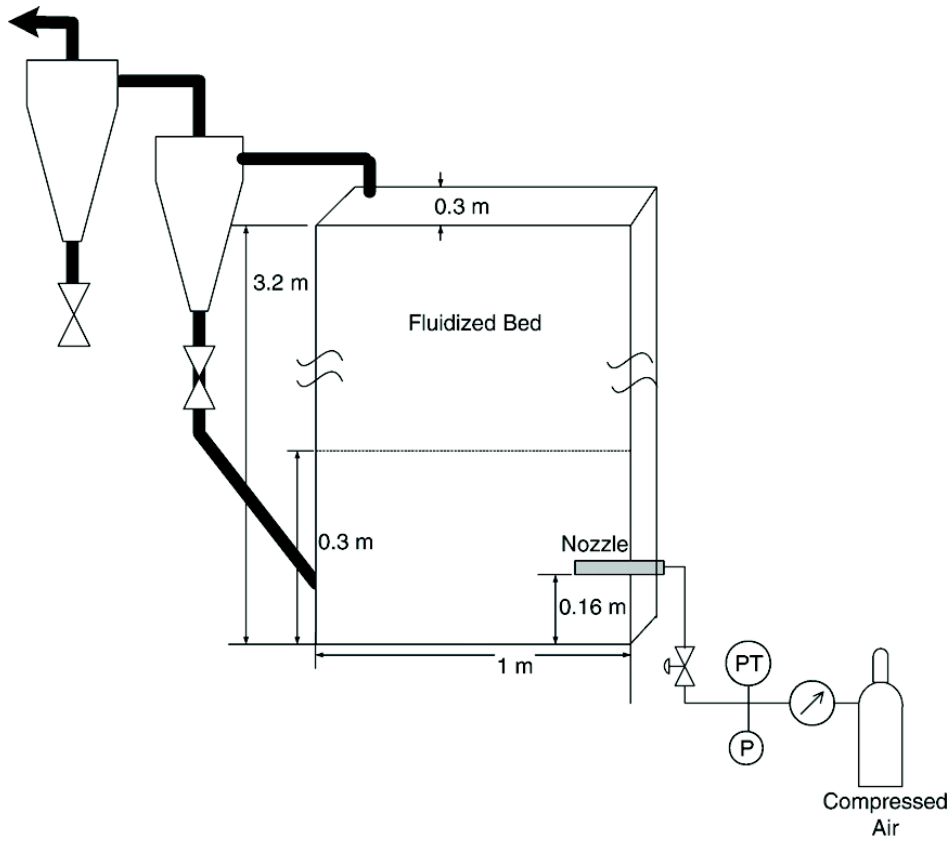


Figure 7-1. Schematic of the experiment (Reprinted from McMillan et al. (2007a) with permission from Elsevier).

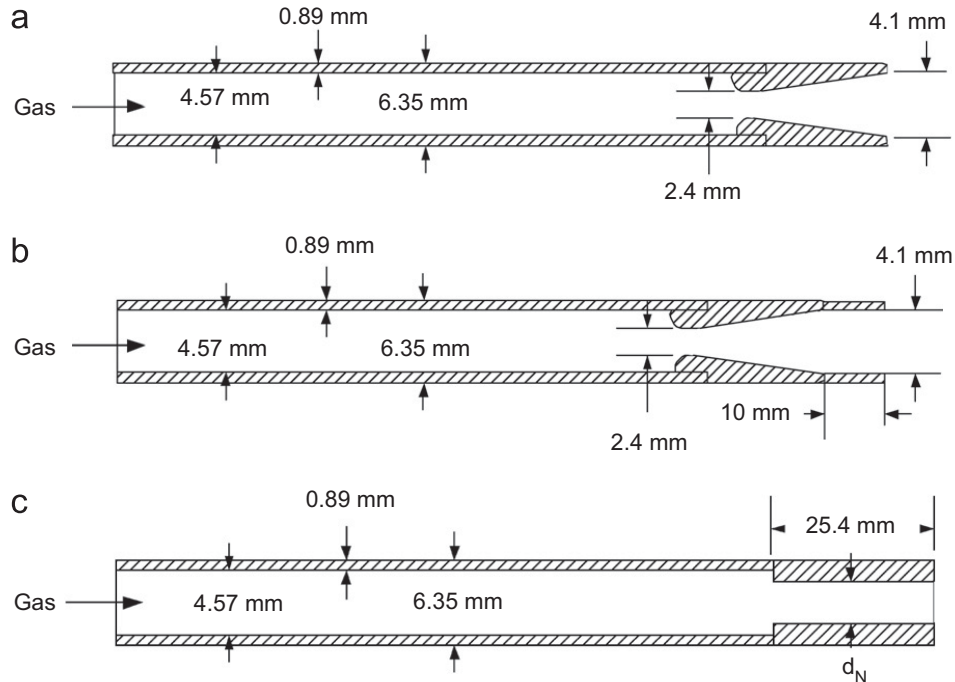


Figure 7-2. Investigated nozzle geometries (Reprinted from McMillan et al. (2007b) with permission from Elsevier).

Model performance is evaluated by comparing its prediction with the experimental data of McMillan et al. (2007a), who investigated high pressure air injections into a fluidized bed through several nozzle geometries. The experimental set-up is schematically shown in Figure 7-1. A nozzle is inserted 10 cm into the rectangular fluidized bed 16 cm above the bottom air distributor. Gas pressure in the nozzle inlet is varied from 100 psi (0.689 MPa) up to 300 psi (2.07 MPa). Only silica sand is considered in the simulations, while two different types of solid materials were tested: coke and silica sand. As the model focuses on the hydrodynamic behaviour of the mixture, the different solid materials would result in different values of the empirically defined C_{br} in Eq. (2-192), without adding much to the understanding of the flow behaviour. A sample of solid particles was taken from the bed before and after the run to obtain the new surface area created by attrition and to calculate the grinding efficiency. Three different nozzle configurations shown in Figure 7-2 were examined. Nozzles A and B are convergent-divergent nozzles and nozzle C is a convergent-only nozzle (a forward step). While nozzle C has four different values of d_N , only three are considered in this work – 2.4 mm, 1.7 mm, and 1.2 mm; they are referred subsequently as nozzles C2.4, C1.7, and C1.2 correspondingly.

7.1.3.2. Computational domain, initial and process conditions

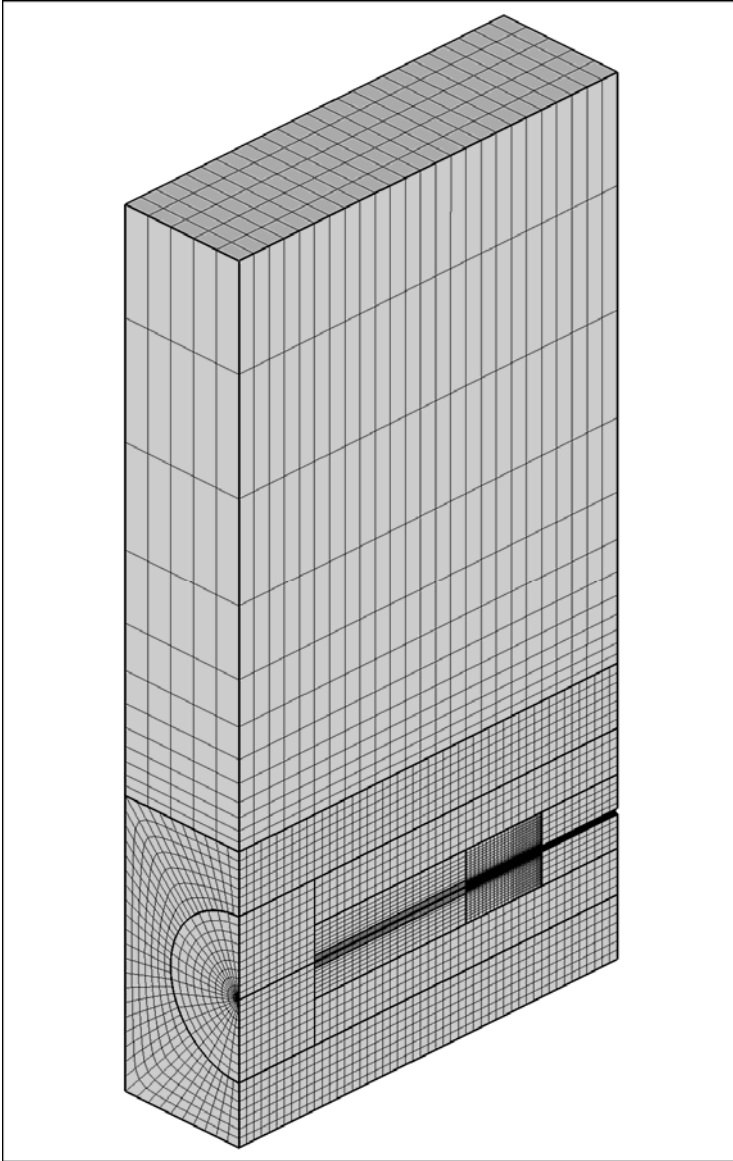


Figure 7-3. Computational domain with grid.

The choice of the computational domain and the grid system is guided by two objectives: first, to represent the attrition phenomenon truthfully; and second, to ensure the computations can be completed in reasonable time. The computational domain closely follows the described experimental set-up with a few exceptions. First, the height of the freeboard is substantially reduced: the total bed height is 0.8 m instead of 3.2 m used in the experiments. However, as the height of the actual space occupied by solid particles is about 0.3 – 0.4 m, the reduction of the open area above the bed is not expected to influence the

Chapter 7. Particle attrition

attrition results. Second, the width of the bed (measured along the direction of the high speed gas injection) is reduced from 1 m to 0.5 m. This reduction is possible because McMillan et al. (2007b) showed that for the flow conditions investigated, the attrition rates did not change with a similar reduction of the bed width. Additionally, it will be subsequently shown that the penetration of the jet is less than 0.5 m, and the portion of the bed located beyond the jet reach does not directly participate in attrition. Third, we assume that there is planar symmetry about the vertical plane passing through the nozzle axis that allows us to consider only half of the whole system. The computational domain is discretized by a structured curvilinear grid shown in Figure 7-3. The grid contains about 45 000 grid cells divided into 11 or 12 segments, depending on the particular nozzle configuration. The segmentation is done to ensure a high resolution in the area of the jet and to avoid unnecessary grid density in the areas where the gradients of the flow variables are relatively low. In addition, the segmentation has to allow for the calculation procedure outlined in the Section 7.1.2. Note that even though it is not shown in the Tecplot rendering, all edges of the grid are represented by second order splines for purposes of calculating areas, volumes, and curvilinear transformation coefficients to ensure accurate reproduction of the nozzle geometry.

The solution is initialized in a way that maintains the same bed height and bulk density of sand as in the experiments. That is, the bed is filled with sand to a depth of 0.3 m with a volume fraction of 0.63 that represents the random packing of spheres. The sand density and the initial diameter are $2\,650\text{ kg m}^{-3}$ and $1.9\cdot 10^{-4}\text{ m}^2$ respectively; the superficial velocity is 0.065 m/s. The incoming air is at room temperature— 20°C —when at rest.

As noted in Section 2.2.7.3., the model contains a single empirical parameter, C_{br} , that needs to be established. After a series of trial runs with the selected nozzle configurations and different values of C_{br} , it is determined that the best overall agreement is obtained when its value is $0.21\text{ m}^3\text{ s}^{-2}$. This value is used in all simulations reported below.

7.1.3.3. Comparison with experimental results

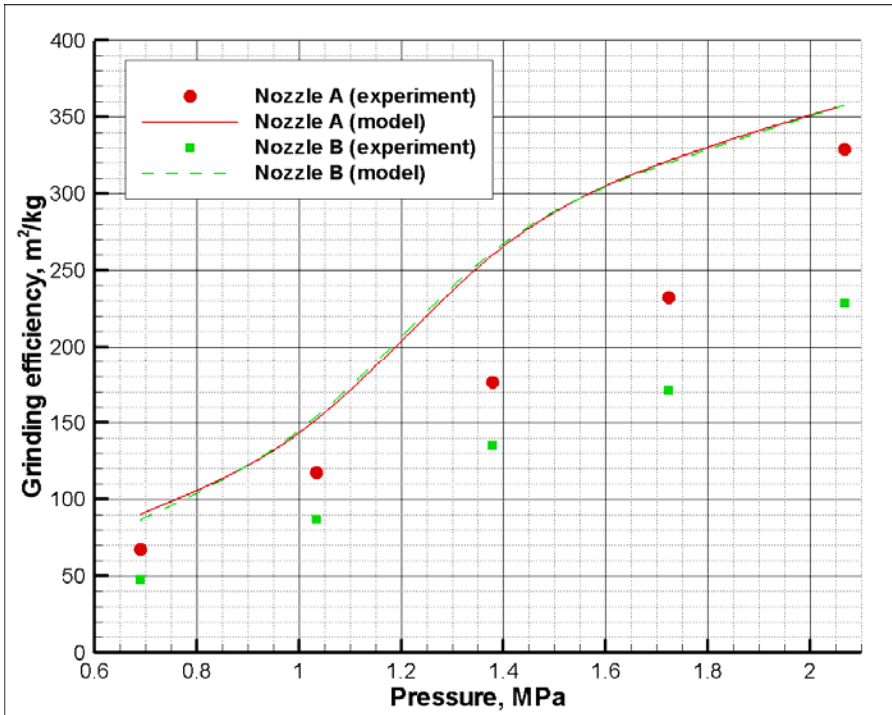


Figure 7-4. Variation of the predicted grinding efficiency with the inlet pressure for A and B nozzle configurations together with experimentally measured values (McMillan et al., 2007a).

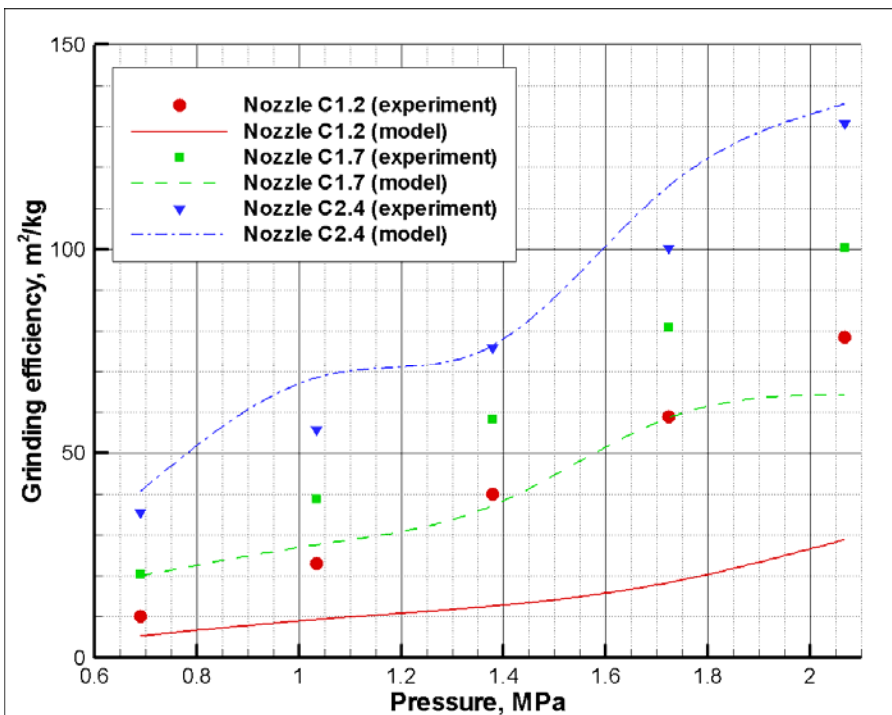


Figure 7-5. Variation of the predicted grinding efficiency with inlet pressure for C nozzle configurations with different exit diameters together with experimentally measured values (McMillan et al., 2007a).

The predicted grinding efficiencies are plotted together with the experimental data points in Figure 7-4, for nozzles A and B, and in Figure 7-5, for the variations of nozzle C with different exit diameters. It can be seen that qualitatively the results agree very well with the experiment, except the model does not predict any difference in performance for nozzles A and B that was observed during the experiment. In all of the nozzle cases, an improvement in the grinding efficiency as the inlet pressure is increased is correctly demonstrated. Reduction of the nozzle exit diameter in the C nozzle results in the decrease of the grinding efficiency. Also, the nozzle C demonstrates poorer performance than nozzles A and B with the same exit diameter. However, the difference observed in the experiments between the A and B nozzles does not appear in the simulation results: the values of the grinding efficiency for these two nozzle configurations are equal within the error margin. It can be seen that while most of the qualitative trends are predicted correctly, quantitative results show noticeable deviation from the experimental data. The calculated efficiencies for A and B nozzles are consistently higher than the experimentally measured one. At the same time, the quality of the prediction of the efficiency of the C nozzles depends on the exit diameter: for the C2.4 nozzle, the efficiency is slightly over-predicted, and for the other C nozzles with smaller diameters, it is under-predicted. It is very likely that the model cannot account fully and accurately for the complex physics involved, leading to quantitative discrepancies between the model and experiment. Nevertheless, these quantitative deficiencies do not preclude the model from being useful. All the main modelling objectives, such as gaining understanding of the phenomenon and evaluation of various arrangements and process conditions in order to improve the efficiency, can be achieved provided that the model correctly represents the physics involved. One can be optimistic about this given the correct qualitative trends. Keeping in mind the complexity of the problem, we can conclude that the numerical model represents particle attrition by the high speed gas jet reasonably well.

7.1.3.4. Numerical accuracy

In order to evaluate the numerical accuracy of the solution, we repeat computations for a selected case (Nozzle A, 200 psi (1.379 MPa)) on the refined grid. The refined grid has about 96 000 cells, which is more than twice the number of the standard grid discussed above. Moreover, most of the refinement is done in the jet area where the attrition is more

likely to take place. The simulations performed on this grid predict an attrition efficiency of $271 \text{ m}^2 \text{ kg}^{-1}$. Comparison with the result obtained on the standard grid ($260 \text{ m}^2 \text{ kg}^{-1}$) reveals that the difference is about 4%. This is small compared with the uncertainties associated with various sub-models employed in the calculations and indirectly reflected in some deviations between modelling and experimental results.

7.1.4. Flow analysis

7.1.4.1. Transient features of the flow

The injection of the gas results in the formation of a jet inside the bed with a very small solid content. The highly transient nature of the flow is demonstrated in Figure 7-6 showing particle volume fraction contours in the vertical cross-sectional plane that passes through the nozzle axis at different time intervals. Nozzle C2.4 at 150 psi (1.034 MPa) inlet pressure serves as an example because the general features of the flow are similar for all nozzle configurations and inlet pressures considered in this work. It can be seen that the jet widens and narrows periodically as it attempts to shed a bubble. However, the bubbles are not completely formed, most likely due to the insufficient bed height as they burst through the top of the bed. Nevertheless, the bubble shedding dynamics are similar to what has been observed in the simulations of Li et al. (2008) for lower speed jets. In contrast, the jet area is much longer and the bubbles begin to detach further downstream than for the cases investigated by Li et al. (2008). Clearly, this difference is a consequence of the higher jet momentum associated with the supersonic jets. Note that some visual discontinuity in the plume area slightly above the jet surface results from the boundary between the finer and coarser grid (see Figure 7-3). The plotted volume fraction is actually a value at the cell centre closest to the boundary; with coarsening of the grid, this distance changes by a factor of two, producing the described outcome.

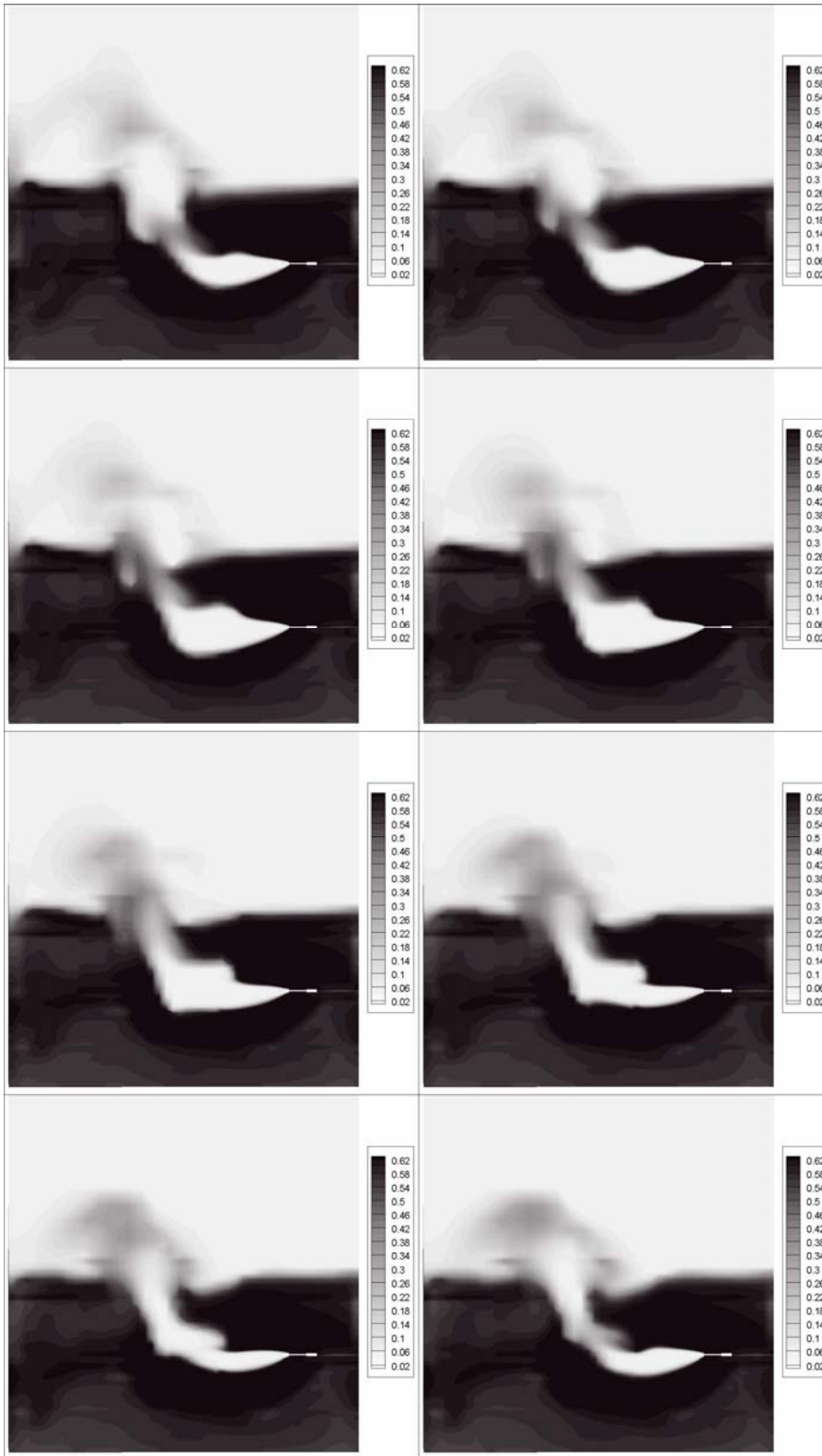


Figure 7-6. Particulate phase volume fraction contours in the axial cross-sectional plane passing through the axis for the C2.4 nozzle at 150 psi (1.034 MPa) inlet pressure. Plots are arranged in a time sequence left to right and top to bottom. Time interval between each successive plots is 25 ms.

Chapter 7. Particle attrition

Figure 7-6 illustrates one completed bubble-detachment cycle. While all the cycles are similar, they are not exactly the same due to random variations. Apparently, the bubble shedding cycle is also related to the fluidization conditions in the surrounding bed. These variations mean that the flow is not strictly periodic, and a reasonable number of cycles is required to obtain the correct time-averaged solution. In addition, this figure also illustrates the separation of time scales: the fluidized bed far from the jet does not change much while the jet area undergoes a complete cycle.

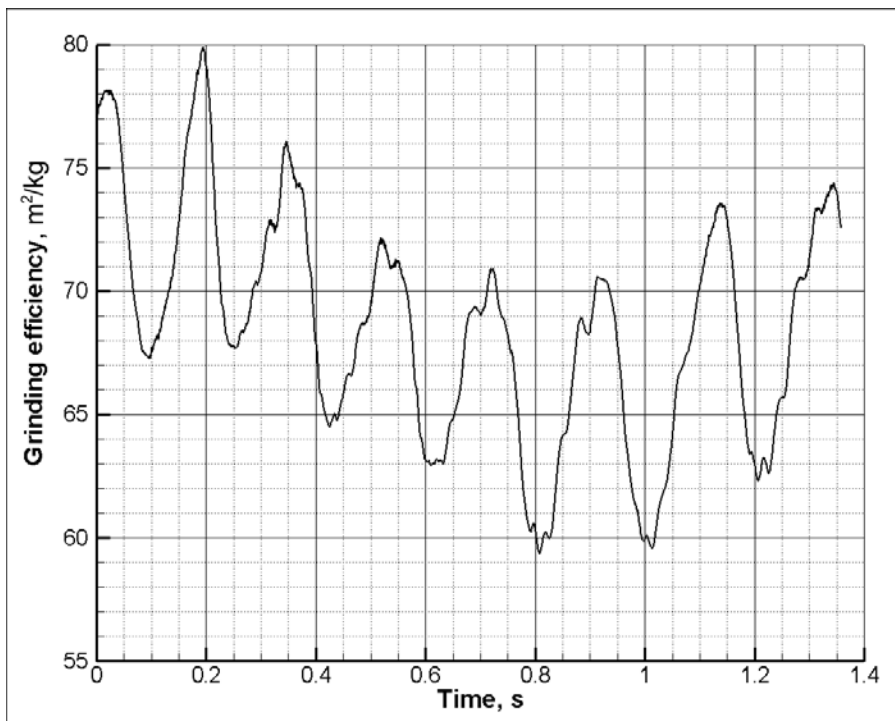


Figure 7-7. Grinding efficiency variation with time for the C2.4 nozzle at 150 psi (1.034 MPa).

Considering the cyclic nature of the flow, it comes as no surprise that the grinding efficiency also varies with time. Figure 7-7 shows the time-evolution of the efficiency for nozzle C2.4 as an example. We can observe that the efficiency increases and decreases periodically; however, the variations are not smooth as they are combined with seemingly random fluctuations especially near the peaks. It is interesting to note that the quasi-periodic variation of the grinding efficiency coincides with the bubble-detachment cycle – about 0.2 s (see Figure 7-6). The efficiency is highest when the jet area is narrow and small, and lowest when the jet area is wide and large. This is rather intuitive as the small area means that the particles entrained in and accelerated by the jet soon encounter other particles and collide

with them, resulting in breakage. Alternatively, in the wide jet area, part of the particle energy can dissipate due to drag before collision, thus reducing the breakage rate.

7.1.4.2. Time-averaged solution

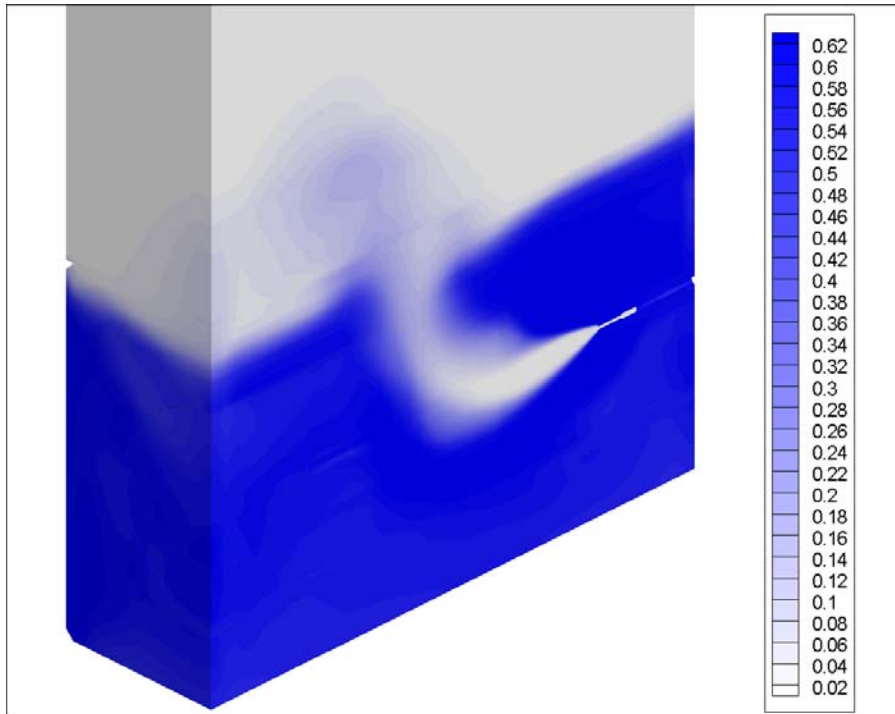


Figure 7-8. Time-averaged volume fraction contours of the particulate phase for nozzle C2.4 at 150 psi (1.034 MPa) inlet pressure.

To facilitate further analysis, the results are time-averaged according to the procedure outlined in Section 7.1.2. Figure 7-8 demonstrates the averaged contours of the particulate phase volume fraction for the same case as was used before as an example (C2.4 nozzle at 150 psi (1.034 MPa)). It can be seen that the jet penetrates about half of the bed, then bends upward and forms a fairly short plume. Contours of the average particle diameter, shown in Figure 7-9, reveal that the diameter is smallest in the jet area from the nozzle exit to the tip of the jet. Evidently, the particles entrained in the jet experience multiple collisions due to high turbulence (granular temperature) in this area.

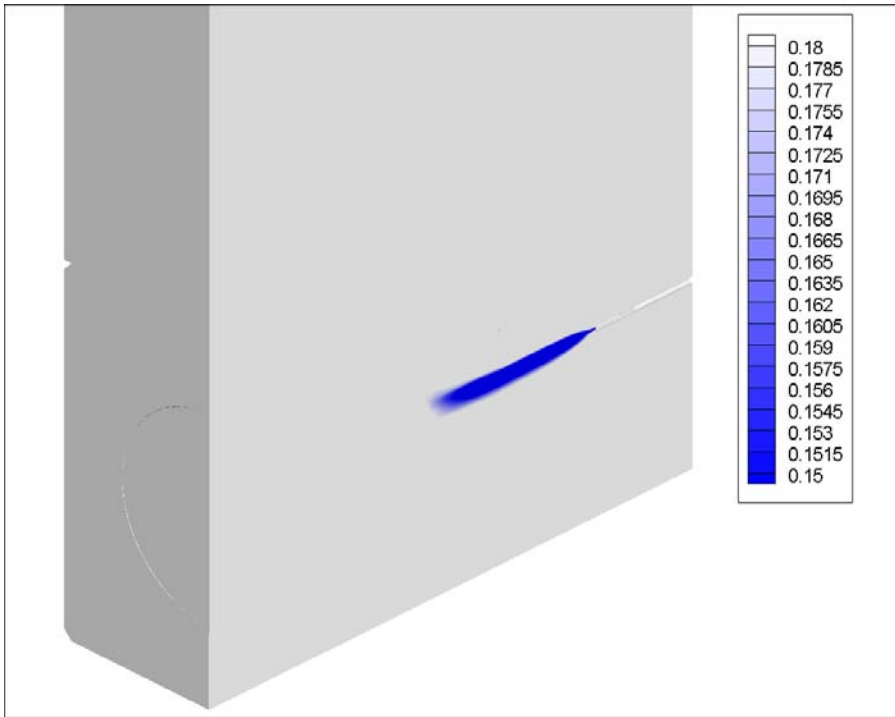


Figure 7-9. Time-averaged particle diameter contours for the nozzle C2.4 at 150 psi (1.034 MPa) inlet pressure (in mm).

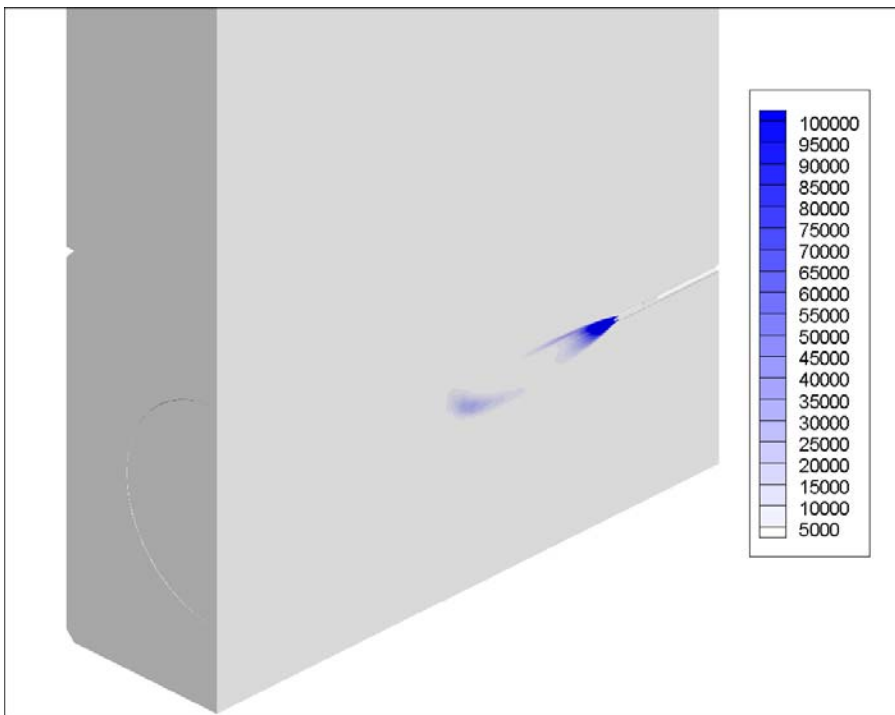


Figure 7-10. Time-average increase of the particles surface area (in $\text{m}^2 \text{s}^{-1}$) due to breakage for nozzle C2.4 at 150 psi (1.034 MPa) inlet pressure.

Chapter 7. Particle attrition

To quantify the particle breakage, in Figure 7-10 we plot the increase of the particle surface area per unit volume and per unit time (ΔS from Eq. (7-4)). The largest increase in particle surface area happens close to the nozzle exit; another distinctive area of substantial particle surface area increase is located near the tip of the jet, although it is not as large as the first one. The physical mechanisms of the attrition in these two zones identified in this figure are notably different. Immediately downstream from the nozzle, the attrition is the result of the random high speed collisions between solid particles entrained into the gas jet and have a high fluctuating velocity component. On the other hand, near the end of the jet, most of the collisions happen between the fast particles in the jet and the slower particles of the surrounding bed, in a manner suggested by McMillan et al. (2007b). It is difficult to judge the importance of the described areas in overall attrition performance from the essentially cross-sectional plot. Even though the surface area increases significantly larger in the zone located at the beginning of the jet, the volume of this zone is less than the volume of the other one due to the distance from the axis. When the volume is factored in, the total surface area reduction are of the same order in both zones. Thus, we can conclude that both attrition mechanisms are similarly important and both need to be taken into consideration during the process analysis.

7.1.4.3. Comparison between cases

It has been consistently seen in the modelling as well as in the experiments that nozzles A and B, which are convergent-divergent, perform significantly better than the C nozzles, which are convergent only, for the same pressure and exit diameter. This difference in performance has two explanations. First, the C nozzles have a step change in diameter, resulting in the flow negotiating a sharp corner. This means that the effective diameter, *vena contracta*, would be less than the actual diameter. Thus, nozzle C2.4 has a smaller throat diameter than nozzles A and B. However, this is not the only reason for the performance change. The second reason that the convergent-divergent nozzles perform better originates from the difference in the flow at the nozzle exit. This difference can be illustrated by the contours of the Mach number. Figure 7-12 shows Mach number contours for nozzles A and C2.4 at 100 psi (0.689MPa) pressure. While nozzles A and B are over-expanded, i.e. the exit pressure is less than atmospheric pressure, nozzle C is under-expanded, i.e. the exit pressure

Chapter 7. Particle attrition

is larger than atmospheric pressure. Thus, upon exit from nozzles A or B, the jet contracts, showing oblique shocks arranged in a diamond pattern.⁵ In contrast, downstream from nozzle C, there is an area of rapid jet expansion that terminates with the Mach disc, which is a shock wave perpendicular to the flow. It is very likely that the initial contraction helps to promote the entrainment of the bed particles into the jet, while the expansion prevents such entrainment. Indeed, Figure 7-12 demonstrates the difference up to about 20% in the solid phase concentration right after the nozzle exit. The entrained particles are quickly accelerated, and more particles in the jet area translates into higher collision rates and, therefore, better attrition performance.

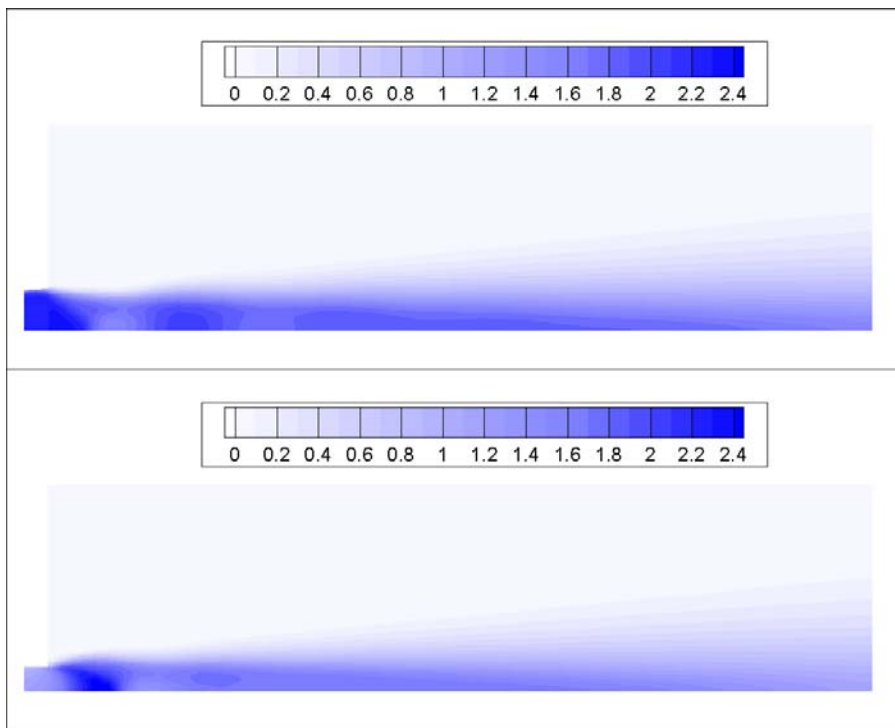


Figure 7-11. Contours of the Mach number for the nozzle A (top) and the nozzle C2.4 (bottom) at 100 psi (0.689 MPa).

⁵ Interested reader is referred to Adamson and Nicholls (1959) for detailed analysis of sonic jets structure.

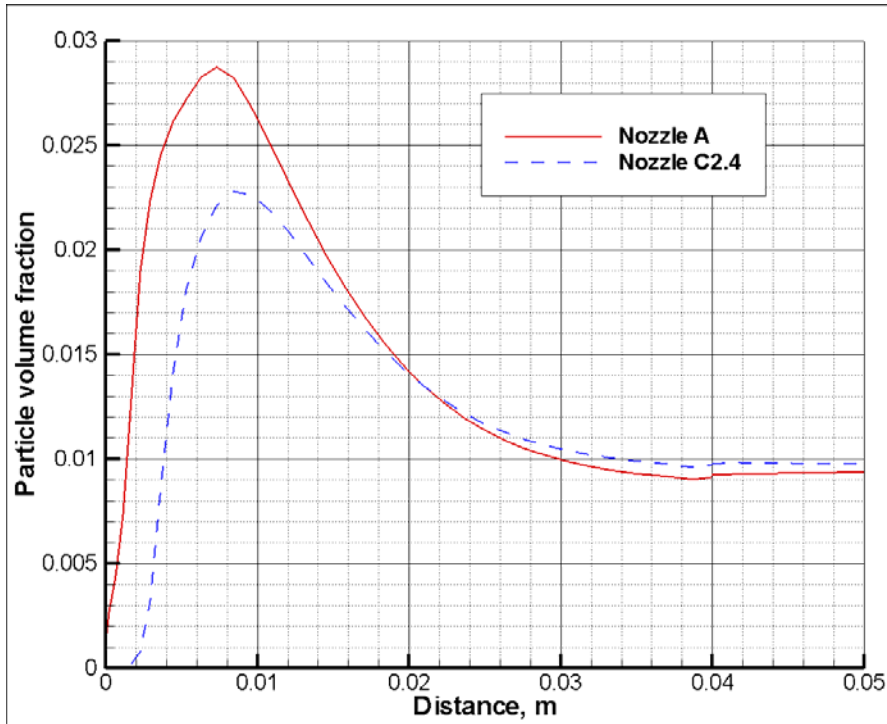


Figure 7-12. Particle volume fraction along the centreline for the nozzles A and C2.4.

To continue with the analysis, we estimate the jet penetration lengths from the average simulation results. In order to be specific, we follow Li et al. (2008) and demarcate the boundary of the jet as corresponding to a solid volume fraction value of 20%. This value is rather arbitrary and serves as a reference point for comparison. With a change in the jet boundary definition, all length values would be shifted. Figure 7-13 shows the variation of the jet penetration length with the inlet pressure for all types of nozzles investigated. Note that due to the jet proximity to the top of the bed, in some of the cases with higher pressure, the jet reaches the bed surface before exhausting its horizontal momentum. Thus, these cases are excluded from the graph. For comparison, we also plot the jet penetration values obtained from the Benjelloun et al. (1995) empirical correlation:

$$L = 5.52D \left(\frac{\rho_g U_g^2}{(\rho_s - \rho_g)gD} \right)^{0.27} \quad (7-5)$$

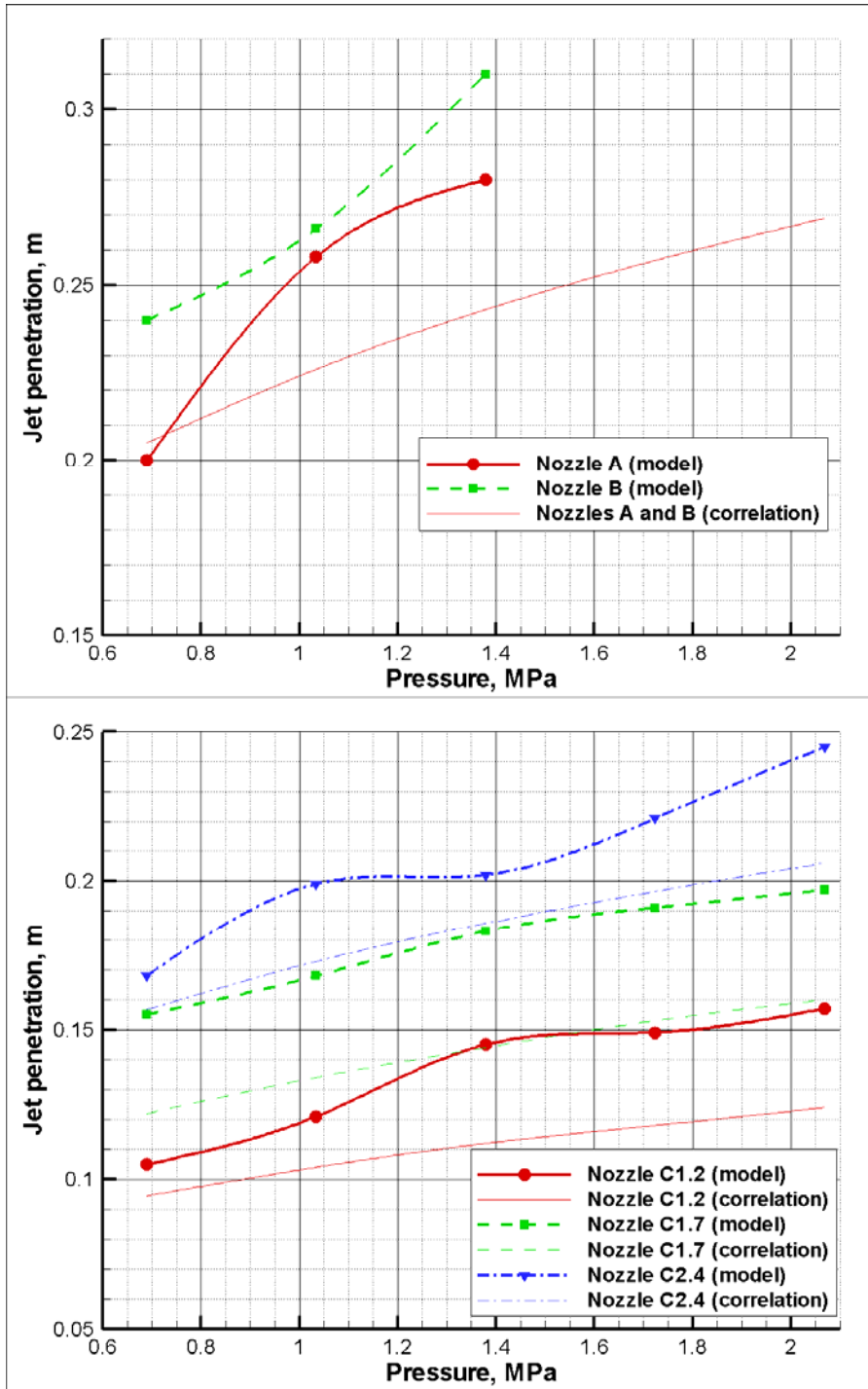


Figure 7-13. Variation of jet penetration length with pressure for the nozzles A and B (top) and for the nozzles C (bottom) together with the estimated values from Benjelloun et al. (1995) empirical correlation.

This particular correlation is chosen because it provides a better fit for jets with issuing velocity larger than 100 m s^{-1} (see Li et al., 2008). In the above equation all parameters are evaluated at the nozzle exit. To use the correlation independently from the

numerical analysis, isentropic flow formulae are used to calculate the gas exit density and velocity from the known inlet pressure. The numerical results agree reasonably well with this empirical correlation for the range of parameters investigated. Apparently, the uncertainties with demarcation of the jet boundary resulted in the numerical results being slightly shifted upward. At the same time, note that the empirical correlation is used outside the range for which it was developed; therefore, it serves as an illustration only and not as a validation for the numerical model.

It can be seen that in all investigated cases the jet penetration increases with increasing inlet pressure. This is due to the increased gas mass and momentum through the nozzle and is in agreement with many previous observations. In addition, the jet penetration also increases with an increase in the nozzle exit diameter for nozzle C. The reason is also due to an increased gas mass and momentum; however, in this case the increase takes place because of the enlargement of the area and not as a result of an increase in the gas density. It is evident that nozzles A and B have noticeably larger penetrations than the C nozzles. It can be speculated that in nozzles A and B a larger part of the gas momentum is directed horizontally because the jet expands inside the nozzle, therefore putting some limitation on the radial velocity. In addition, the compression right after the nozzle further limits the radial spread. Alternatively, the expansion of the gas after the exit from nozzle C distributes a significant portion of the momentum radially. After comparison with Figure 7-4 and Figure 7-5, it is apparent that the penetration length is correlated with the attrition efficiency. That is, an increase of pressure and nozzle exit diameter increases the attrition efficiency. The only exception is for nozzles A and B: while nozzle A penetrates slightly less than nozzle B, their attrition efficiencies are approximately the same.

7.2. Industrial scale attrition

In this section, we apply the numerical model to investigate industrially relevant flow conditions. We consider attrition of coke particles by a supersonic steam jet.

7.2.1. Model calibration

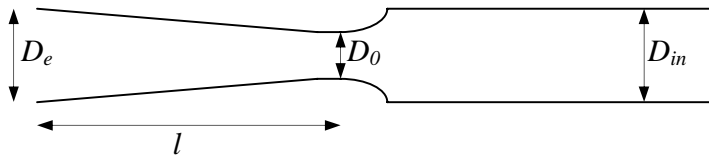


Figure 7-14. Nozzle schematic.

The model employs a single empirical parameter, C_{br} , which is solid material dependent. During the small-scale attrition work (Section 7.1), its value was established for silica sand particles. In order to determine this parameter for industrially-used particles, we simulate another set of experimental data from McMillan et al. (2007b) that describes attrition by an air jet in a small air-fluidized bed. For these simulations, we use the original set-up previously described in Section 7.1.3.1. Nozzle A, sketched in Figure 7-14 with $D_{in} = 4.57$ mm, $D_0 = 2.4$ mm, $D_e = 4.1$ mm, $l = 13.61$ mm, issues into a bed shown in Figure 7-1.

Table 7-1. Process parameters for small-scale computations.

Particle density, kg m^{-3}	1500
Particle diameter, μm	135
Ambient pressure, MPa	0.1301
Ambient temperature, $^{\circ}\text{C}$	20
Superficial gas velocity, m s^{-1}	0.065
Initial bed height, m	0.3
Initial particles volume fraction	0.63

Computational domain, simulation set-up and calculation procedure are identical to those described in Section 7.1. Table 7-1 lists all process parameters used in the computations. After performing several trial runs for different nozzle inlet pressures, we determined that $C_{br} = 0.75 \text{ m}^3 \text{ s}^{-2}$ provides the best fit to the experimental data. This value is used in all subsequent computations for the industrial scale attrition simulations. Final results showing grinding efficiency variation with pressure are presented in Figure 7-15 (a). It is interesting to see that attrition efficiency fluctuations, which can be analysed by a standard deviation shown by the error bars, increase with the increase of the pressure. In relative

Chapter 7. Particle attrition

terms, the fluctuations grow from about 5% to 12%. In addition, we analyse solution sensitivity to the chosen breakage constant. Figure 7-15 (b) compares grinding efficiency profiles obtained with the selected value of C_{br} with two other profiles obtained with C_{br} equals 0.7 and 0.8. It can be seen that the attrition efficiency is rather sensitive to the selection of C_{br} , as its 6% change brings about 25% change of the efficiency. It is not surprising, though, as C_{br} is located under the exponent (see Eq. (2-192)). In addition, as shown in Eq. (2-193), this constant depends on the Young's modulus to the power of minus four. Therefore, it varies rather dramatically with the material change; at the same time, its variation for a particular material is limited.

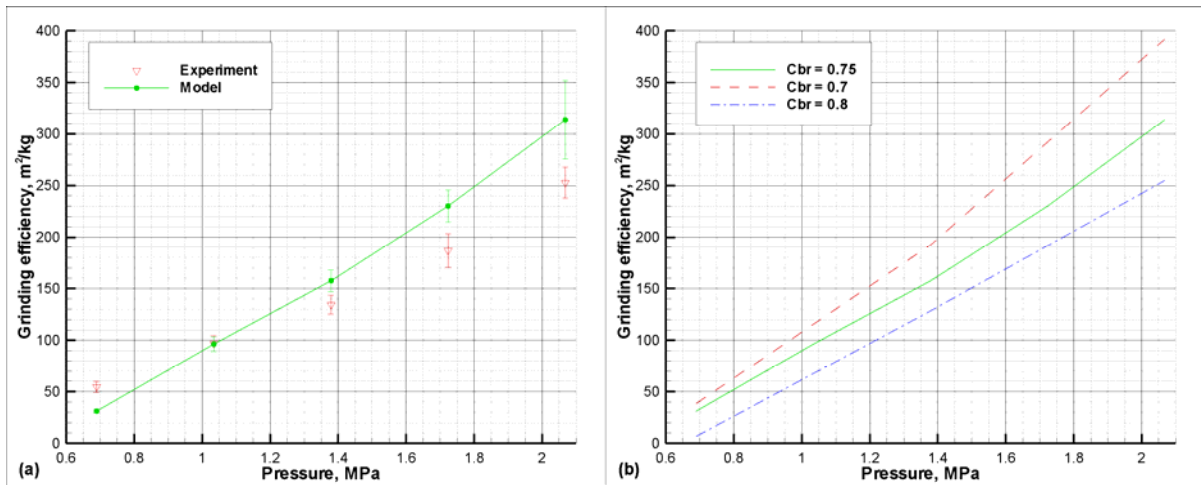


Figure 7-15. Grinding efficiency variation with pressure in a small scale fluidized bed. Error bars show \pm one standard deviation for modelling results and for experimental data. (a) Comparison with experimental values; (b) Parametric study for different breakage constants.

7.2.2. Computational domain

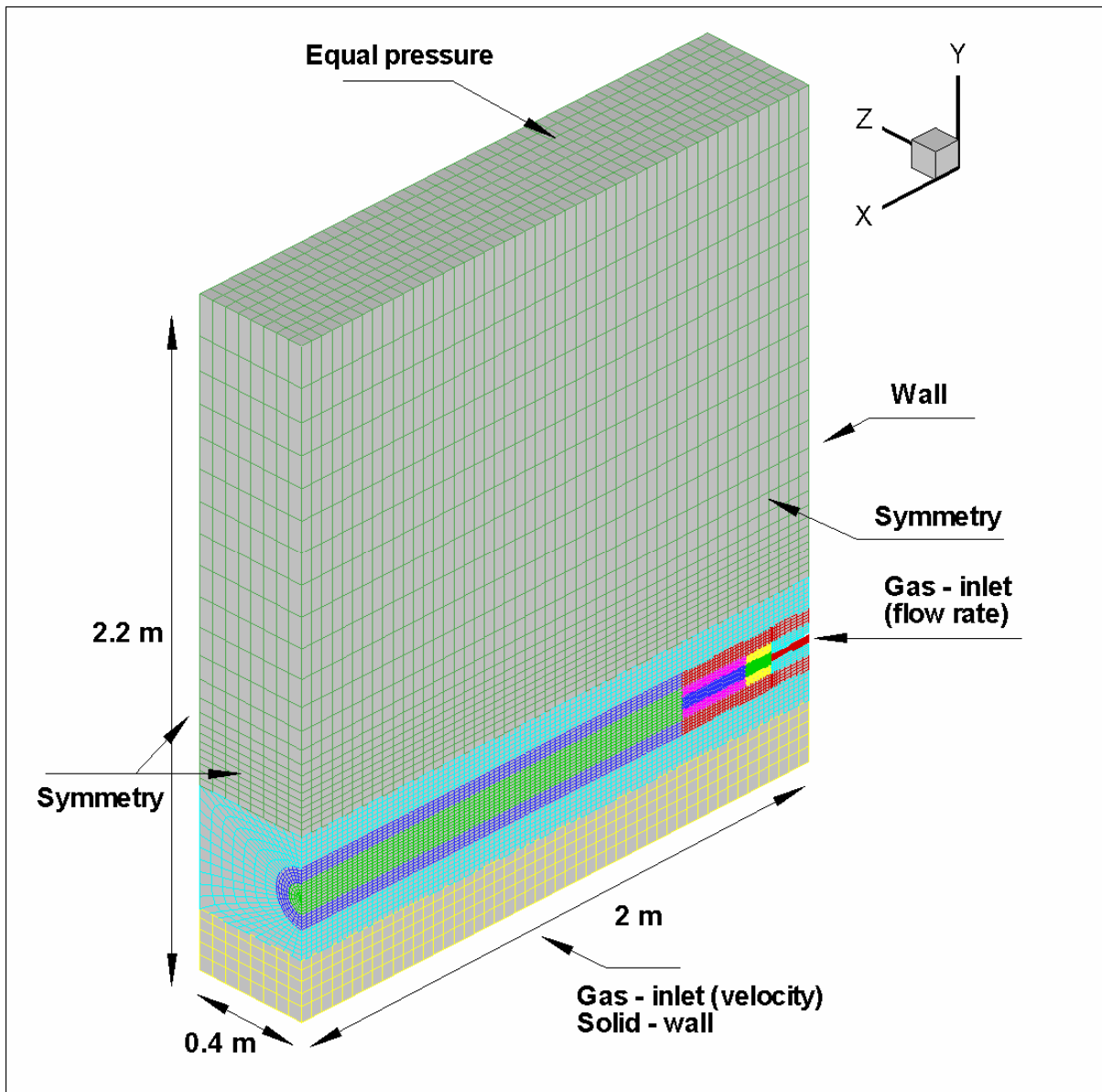


Figure 7-16. Domain segmentation, computational grid and boundary conditions (nozzle walls not shown here are treated as walls).

As mentioned in Section 1.1.2, there are many attrition nozzles in the reactor. However, modelling all (or even a substantial fraction) of them with the spatial resolution required for reliable grinding efficiency calculations is impractical. Therefore, we need to make some simplifications to the problem. First, we assume that the attrition nozzles do not influence one another because the attrition happens in the direct vicinity of the nozzle, and the distance between neighbouring nozzles is relatively large. Second, we place the nozzle

into a sufficiently large fluidized bed to provide conditions similar to what is encountered in the actual reactor. And third, we assume planar symmetry across the vertical plane passing through the axis of the nozzle. Even though there is generally no symmetry in fluidized beds—bubbles are born, move, and burst at random without isotropy—in our case we have a strong momentum transferred from the nozzle in the horizontal direction. This momentum transfer limits fluctuations in the vicinity of the nozzle making flow around it more stable as we have already seen in Section 7.1.4. At the same time, this is the area we are most interested in because it was demonstrated in Figure 7-10 that the most particle breakage takes place there. Thus, under the circumstances of our investigation, the symmetry assumption is appropriate and strikes a balance between accuracy and practicality. The dimensions of the bed and boundary conditions are marked in Figure 7-16. The nozzle is inserted into the bed at a distance of 0.15 m from the wall. Variations in the average solid volume fraction in the surrounding area can be modelled by changing the velocity of the steam supplied from the bottom to fluidize the bed. Also, we exploit the planar symmetry present in the geometry of the problem that allows for the investigation of only half the nozzle.

As the process proceeds, the mean particle size in the bed is reduced due to attrition. For small scale tests investigated previously in Section 7.1, such reduction was generally minor and did not appreciably influence bed hydrodynamics. For conditions presented in this section, however, the diameter reduction is substantial and the time-scale of this reduction is comparable with that required to obtain averaged grinding efficiency results. In the actual reactor, there is always an exchange of particles due to bed mixing between different zones. Thus, the particle diameter around the attrition area is maintained in an average sense. In lieu of the natural mixing, we apply the following procedure in our simulations. As soon as the particle moves vertically from the nozzle axis more than a predetermined distance (0.2 m), its diameter is regenerated, i.e. it is returned to its original value.

The computational domain is divided into 12 segments (see Figure 7-16) because of two main considerations: first, to ensure different structured curvilinear grid density in the various parts of the domain – fine close to the nozzle where the spatial gradients of flow variables are higher, coarse far from it; and second, to facilitate the implementation of a segment-variable time step, a special procedure to speed up the computations. While the

equations in the nozzle segment and those directly downstream are solved for every time step, the segments further away from the nozzle are solved only every second, tenth, or twentieth time step because the time gradients there are relatively small.

7.2.3. Grid independence

In order to assess solution grid independence, in addition to the main grid that contains about 53 000 computational cells, we also develop a finer grid that contains about 70 000 cells. Even though the difference seems to be fairly small, the refinement is done only for the segments near and directly downstream from the nozzle, i.e. the ones where the attrition is taking place. Thus, the actual grid density for these segments is twice the original one. Only one representative case—Case 2 from Table 7-2—is calculated on the fine grid due to substantially longer running time. The comparison of the grinding efficiency results between the fine and the standard grid reveals a difference of 3.4%. This value is very small compared with modelling errors that are inevitable for such complex simulations that require many constitutive equations. Thus, it can be concluded that the solution sensitivity to the numerical grid is minimal, and can be considered grid independent for practical purposes.

7.2.4. Flow analysis

7.2.4.1. Influence of nozzle area ratio

Table 7-2. Nozzle dimensions for various cases.

Case number	D_{in} , mm	D_0 , mm	D_e , mm	l , mm	Area ratio
1	24.31	12.95	12.95	0.00	1
2	24.31	12.95	17.02	33.22	1.727
3	24.31	12.95	21.82	72.39	2.839
4	24.31	12.95	27.03	115.06	4.357

We start our investigations of the nozzle design with determining the optimal area ratio (exit area to throat area) of the nozzle. That is, we are to find out whether it is better to have an under-, perfectly-, or over-expanded jet. Four different nozzle cases are considered. The general nozzle geometry is shown in Figure 7-14 and dimensional values are listed in Table 7-2. Case 1 represents the under-expanded jet, Case 2 – the perfectly expanded, and

cases 3 and 4 – the over-expanded jets that differ by the degree of overexpansion. Note that the expansion angle is the same (7°) for all nozzles considered. The process parameters presented in Table 7-3 were chosen for their similarity to typical industrial conditions.

Table 7-3. Process parameters for industrial scale cases.

Parameter	Value
Particle density, kg m^{-3}	1500
Particle diameter, μm	150
Reactor pressure, MPa	0.41
Reactor temperature, $^\circ\text{C}$	525
Steam at the nozzle temperature, $^\circ\text{C}$	375
Superficial gas velocity, m s^{-1}	0.305
Fluidizing steam temperature, $^\circ\text{C}$	525
Inlet flow rate, kg s^{-1}	0.48

Similar to what was observed in small scale simulations presented in Section 7.1.4.1, all cases exhibit transient jet behaviour with bubbles pinching off near the tip of the jet. However, the shape of the jet fluctuates from the average position significantly more than for the smaller nozzles. The consequences are that relatively longer time periods (around 3 s of real time) are necessary to obtain average results. Even after such a time, the proper averages are obtained only for the areas surrounding the jet. Far from the jet inside the bed, the timescale is larger, and even longer time is required for averaging. However, as our main concern is with the attrition and it is known that it takes place in and around the jet, the spatially incomplete averages are sufficient for the purposes of our analysis.

Figure 7-17 shows average particle volume fraction contours in a vertical cross-sectional plane passing through the nozzle axis for Case 1. This case is chosen to represent all others because the general flow features are very similar for all nozzle designs considered. We can see a jet that bends upwards closer to its tip due to gravity and the densification area around the jet created by the solid entrainment. Also, near the free-slip wall (symmetry boundary) opposite the nozzle entrance, we can observe some accumulation of particles that are pushed by the jet. While it cannot be directly seen from this figure, there are distinctive global patterns of the solid movement. The particles accelerate with the jet around it, then

slow down and start their upward motion; in the upper part of the bed they drift towards the nozzle side of the bed and slowly move downwards. Next, they enter the dense area during the turn towards the jet direction and, finally, accelerate again with the jet. A similar, but significantly smaller, circulation also takes place below the jet.

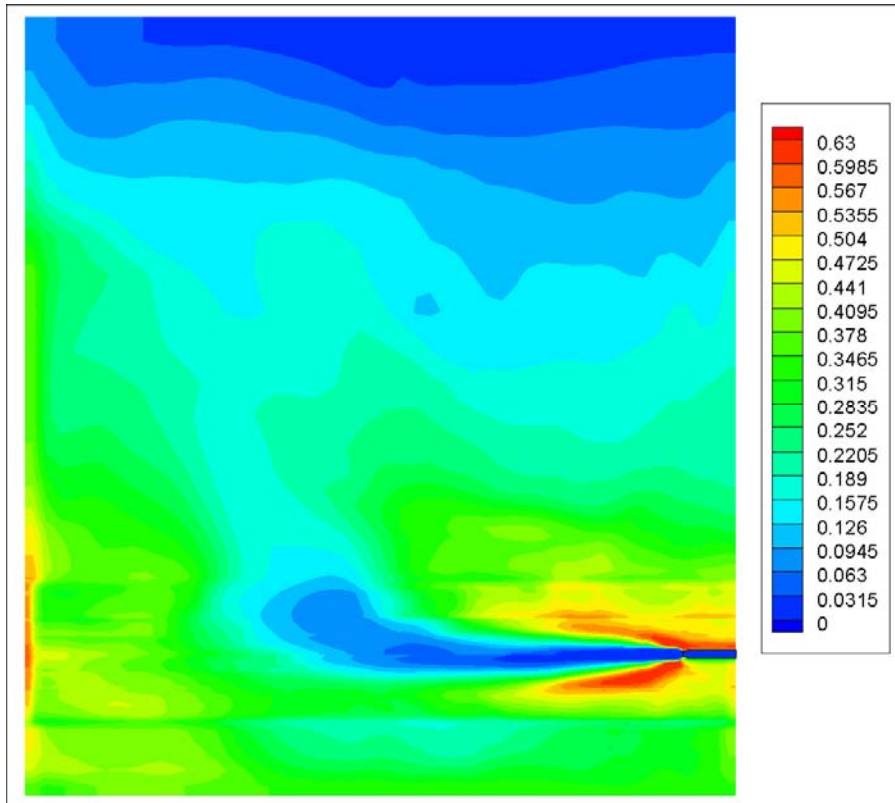


Figure 7-17. Average particle volume fraction contours for Case 1.

Variation of steam temperature is presented in the upper part of Figure 7-18. It can be seen that the temperature drops during the jet expansion, then quickly recovers and continues to increase until the steam approaches the bed temperature close to the end of the jet. While it is possible for condensation to occur as the jet expands, in our case this does not happen because the steam temperature is always above the saturation value for a local pressure multiplied by 0.96 – a coefficient commonly used in steam nozzle calculations that reflects the delay of condensation due to rapid velocity (Cengel and Boles, 2006). Note that this conclusion extends to all other cases presented in this section. From the lower part of this figure, it is evident that the heat transfer between the phases is very good: the interfacial temperature difference ($T_s - T_g$) is appreciable only in the immediate vicinity of the nozzle.

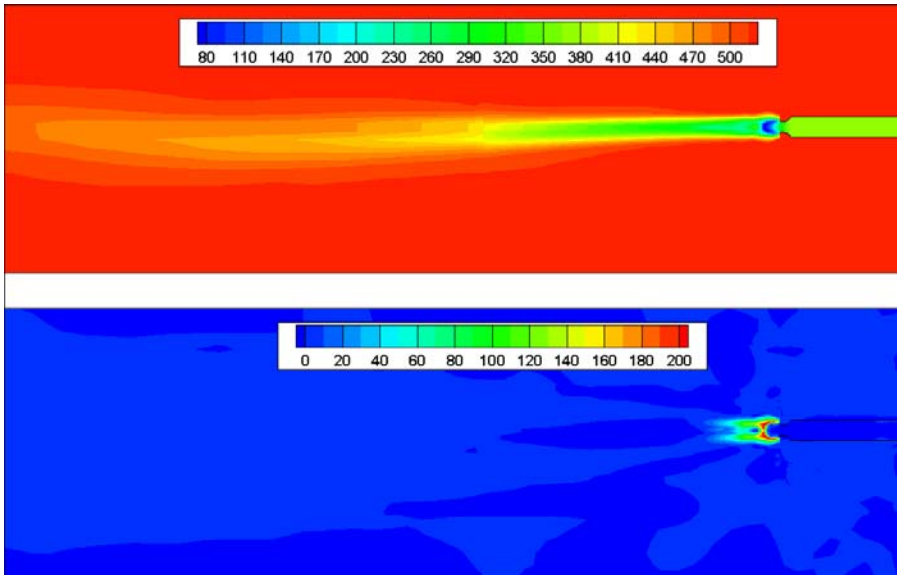


Figure 7-18. Contours of steam temperature ($^{\circ}\text{C}$) (above) and temperature difference between particles and steam ($^{\circ}\text{C}$) (below).

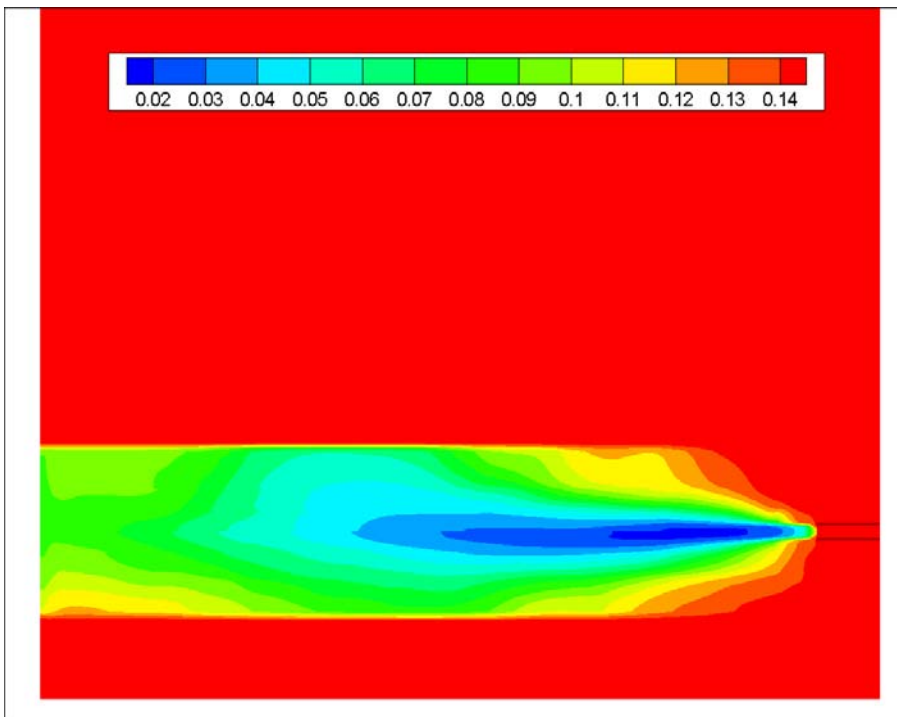


Figure 7-19. Contours of average particle diameter for Case 1 (mm).

The variations of the particle diameter are presented in Figure 7-19. It shows that the particles entrained into the jet undergo break-up and their average diameter is diminished.

Chapter 7. Particle attrition

Around the jet the predicted average particle diameter is approximately 0.1 mm, a 33% reduction from the initial value of 0.15 mm. Note that above and below the jet are the regeneration zones discussed in Section 2.3 where the diameter is set to a constant 0.15 mm. Analyzing this figure, we have to keep in mind that even though inside the jet the average particle diameter is very small, the particle volume fraction is also very small (see Figure 7-17). Therefore, similar to our previous observation (see Section 7.1.4), the majority of particle attrition happens near the boundaries of the jet.

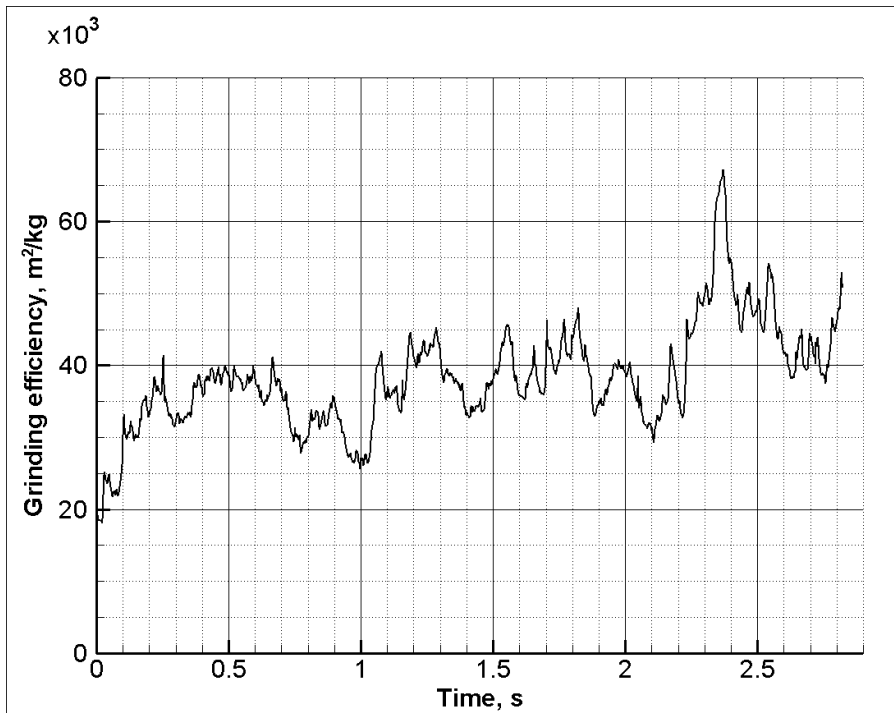


Figure 7-20. Grinding efficiency variation with time for Case 1.

The variation of the grinding efficiency with time, shown in Figure 7-20 for Case 1, is also typical for other cases. The curve is much more “rugged” than those obtained previously for smaller nozzles (see Figure 7-7), in agreement with an observation made already in this section regarding more intense nozzle fluctuations. In order to compare the cases, we calculate the time-averaged grinding efficiency for each nozzle design.

Figure 7-21 shows variation of grinding efficiency with nozzle area ratio, which is defined as the nozzle exit cross-sectional area divided by the cross-sectional area at the nozzle throat. This figure demonstrates that the best grinding efficiency is achieved for the perfectly expanded nozzle (Case 2). At the same time, a slightly over-expanded jet (Case 3)

exhibits approximately the same grinding efficiency; however, it decreases with a further increase in the over-expansion ratio. The variation of the grinding efficiency between the cases is rather significant, about two times. In order to gain insights into the reasons for such nozzle performance, further analysis is conducted.

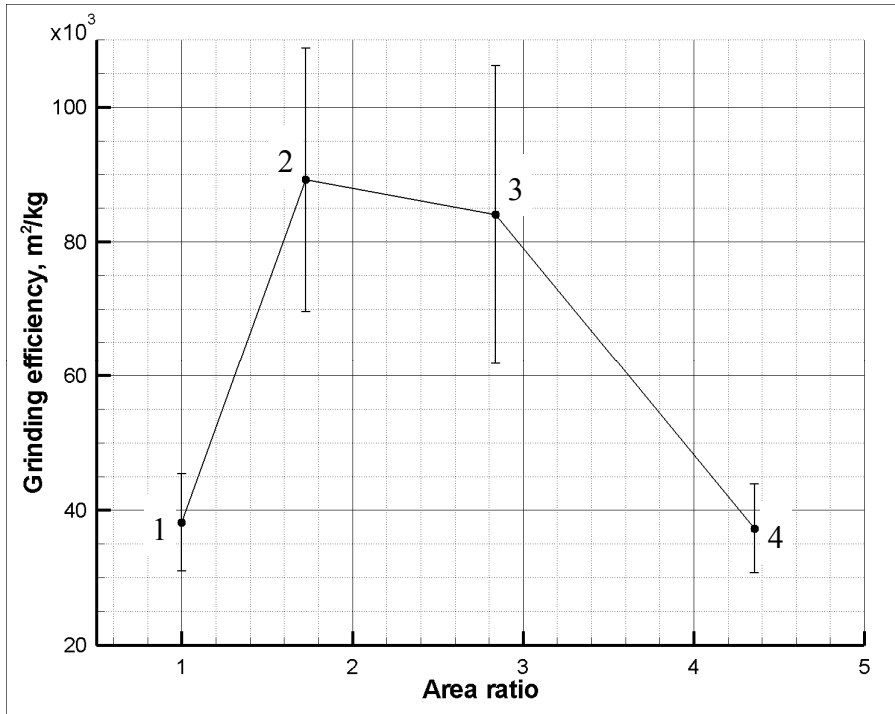


Figure 7-21. Grinding efficiency variation with nozzle area ratio. Error bars show \pm one standard deviation.

It is helpful to estimate the entrainment of solid particles into the jet. However, while there is a common understanding of the meaning of the jet entrainment, this property lacks a standard formal definition. The definition varies from one researcher to another, driven mostly by experimental or computational convenience. For example, Briens et al. (2008) defined solid entrainment as the quantity of solid particles driven through a hole located a certain distance from the nozzle orifice concentric with a jet. Clearly, the solid entrainment defined in such a way is dependent on the hole diameter and the distance from the tip of the nozzle to the hole. Therefore, such definitions cannot be generally extended from one set of conditions to another, and a more universal definition is required. We propose to define the solid entrainment in a rather intuitive way, as a maximum flow rate through the cross-sectional plane (perpendicular to the nozzle) of solid particles that have a velocity above a certain value, which separates the jet and non-jet regions of the bed. Such a definition still

requires knowledge of this borderline velocity; however, it is not dependent on the geometry or additions to the system. To select an appropriate value for this velocity, we plot the variation of solid flow rates with the distance from the nozzle exit for different borderline velocities (from 2 m s^{-1} to 20 m s^{-1}) in Figure 7-22. It can be seen that for velocities above 14 m s^{-1} the curves attain a similar pattern. The initial increase reflects more solids being entrained into the jet, followed by a decline due to particles entrained into the jet colliding with bed particles and dissipating their momentum. The curves obtained for velocities below this value exhibit a somewhat different profile that suggests some effects of fluidization contaminate the solid fluxes transported by the jet. Therefore, it seems appropriate to select the borderline velocity as 15 m s^{-1} . This value will be used in all consequent simulations presented in this section. It is also important to note that the solid entrainment results do depend on the choice of the velocity. However, this dependency would influence only absolute values still allowing for meaningful comparison of cases.

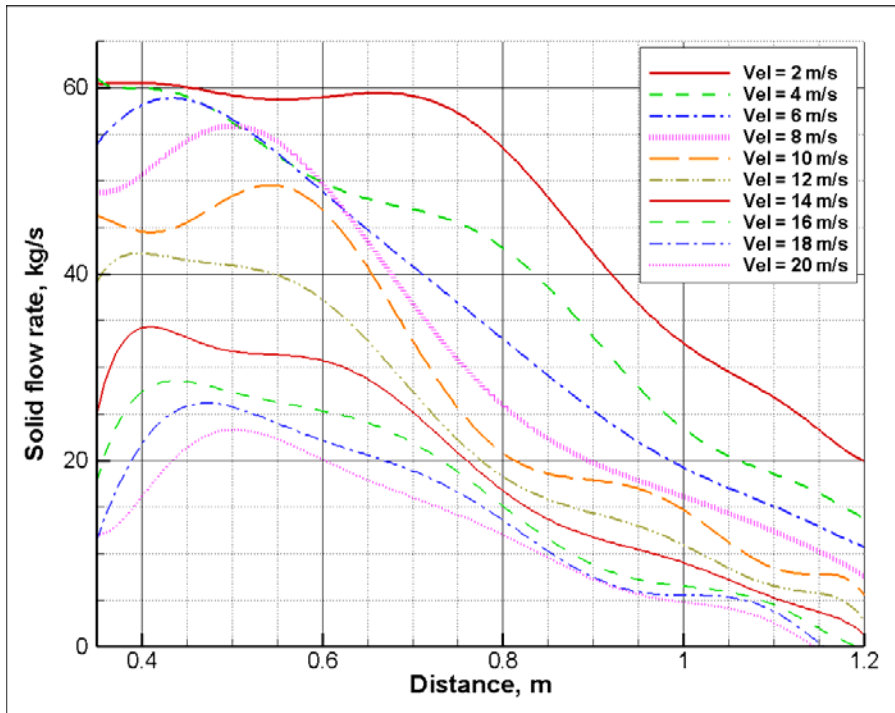


Figure 7-22. Solid flow rate dependence on the borderline velocity definition.

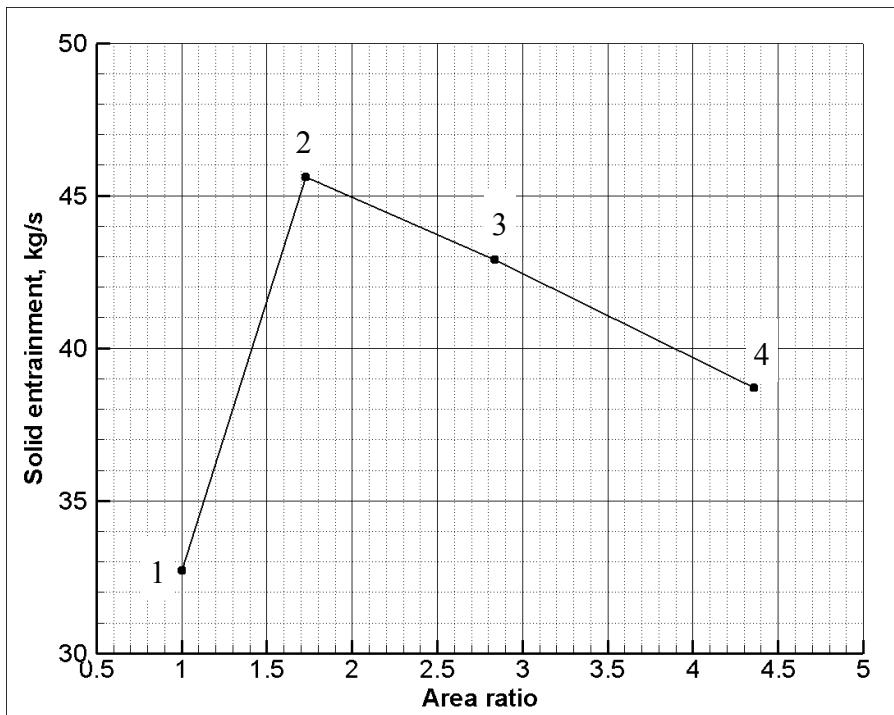


Figure 7-23. Solid particle entrainment for nozzles of different exit areas.

Figure 7-23 shows solid entrainments for nozzles with different area ratios. We can see that the perfectly expanded nozzle (Case 2) has the maximum solids entrainment, and it gradually reduces with under- (Case 1) or over- (Cases 3 and 4) expansion. To better understand the mechanisms responsible for such behaviour, we plot velocity contours for steam and particles near the nozzle for the cases considered.

Figure 7-24, showing steam velocity contours, demonstrates classical patterns expected from isentropic flow analysis. In the under-expanded case (Case 1), we can see a rapid jet expansion and a formation of the Mach disc. In the perfectly expanded case, the flow continues without any waves. In the over-expanded cases, some jet contraction is noticeable and a diamond-shaped shock wave pattern appears. Obviously, due to the limitations in spatial resolution, these features are not as sharp as if they were obtained on a finer grid. In addition, the presence of the particles with high inertia also smoothes the velocity distribution. What is important is that the perfectly expanded case seems to have the longest jet penetration. The steam keeps its momentum further downstream compared to other cases. It can be speculated that in cases other than the perfectly expanded one, part of the energy of the jet is dissipated due to the presence of the shock waves instead of being

used for the momentum transfer in the axial direction. Additionally, for the under-expanded case, substantial radial momentum is generated, which manifests itself in a relatively wide jet, thus reducing the axial momentum that could have been used for attrition.

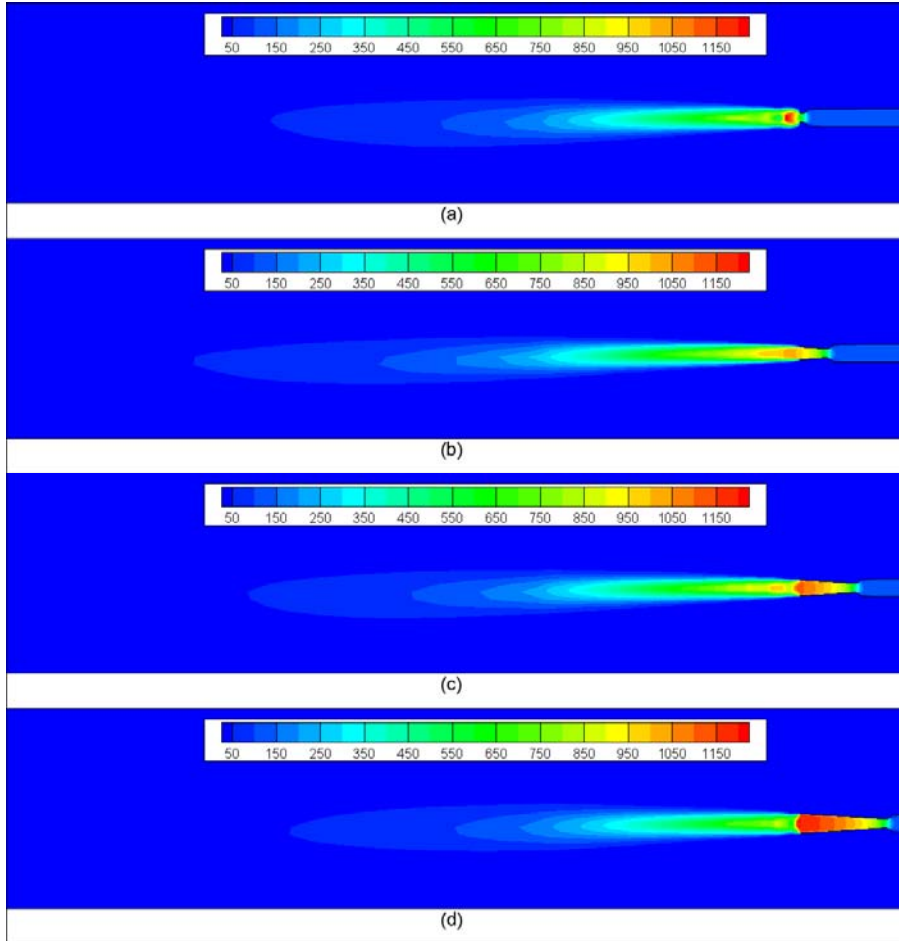


Figure 7-24. Steam velocity contours (m/s) for Cases 1 – 4. (a) – Case 1, (b) – Case 2, (c) – Case 3, (d) – Case 4.

As the solid particles gain their momentum from the steam, it comes as no surprise that the trends observed in steam velocity are closely followed by particle velocity. Figure 7-25 shows that in the perfectly expanded case (Case 2) the particles accelerate further downstream from the nozzles than in other cases. Also, we can see that the axial velocity is the largest for the perfectly expanded case. This makes the pressure in the jet core area the lowest. As solid entrainment is driven by the pressure difference between the jet and surrounding area, the relationship shown in Figure 7-23 follows from our analysis.

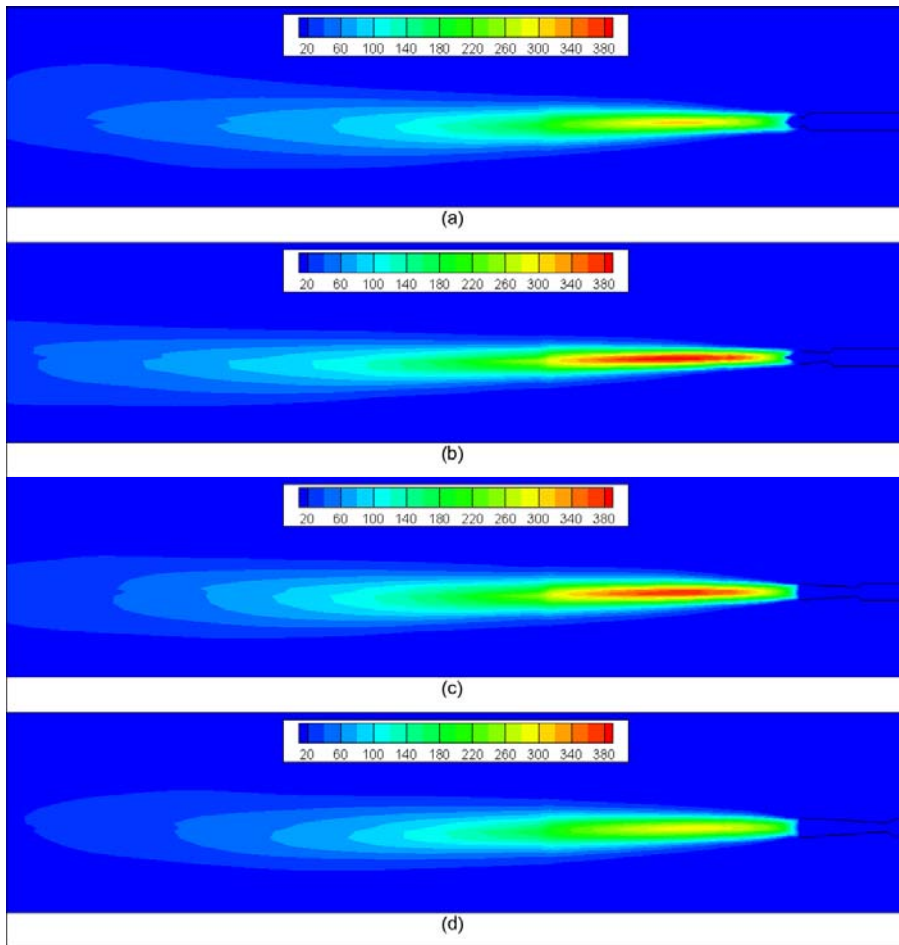


Figure 7-25. Particle velocity contours for Cases 1 – 4. (a) – Case 1, (b) – Case 2, (c) – Case 3, (d) – Case 4 (in m s^{-1}).

We can also see from Figure 7-26 that, in agreement with velocity contours, the perfectly expanded jet results in the largest penetration distance. Note that we used Li's et al. (2008) definition of the penetration distance as the average length of the jet boundary demarcated by 20% solid volume fraction. Similar to our previous findings reported in Section 7.1.4, the largest penetration distance corresponds to the highest grinding efficiency.

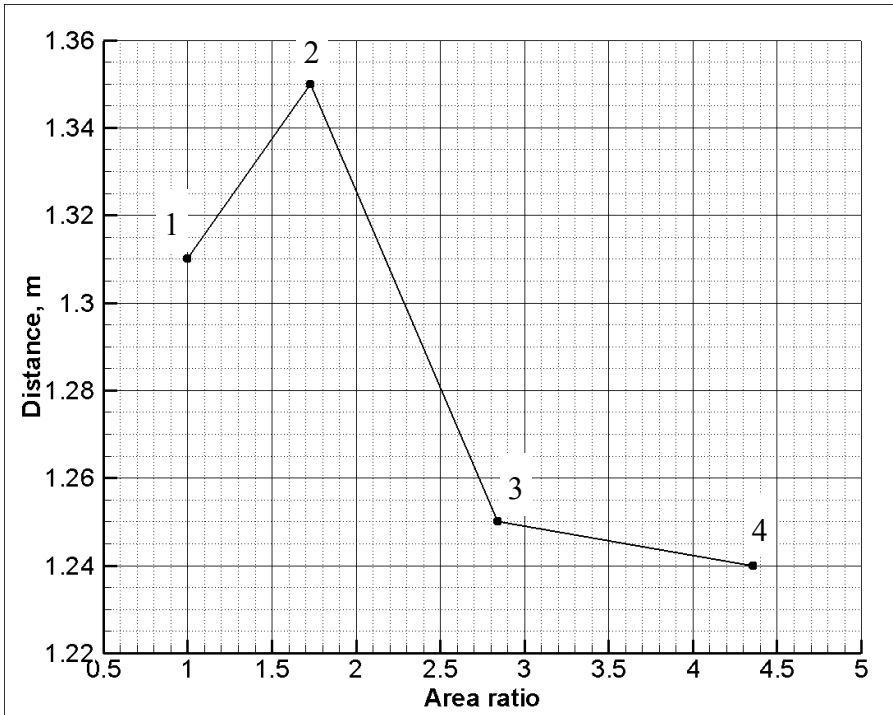


Figure 7-26. Jet penetration distance for nozzles of different exit areas.

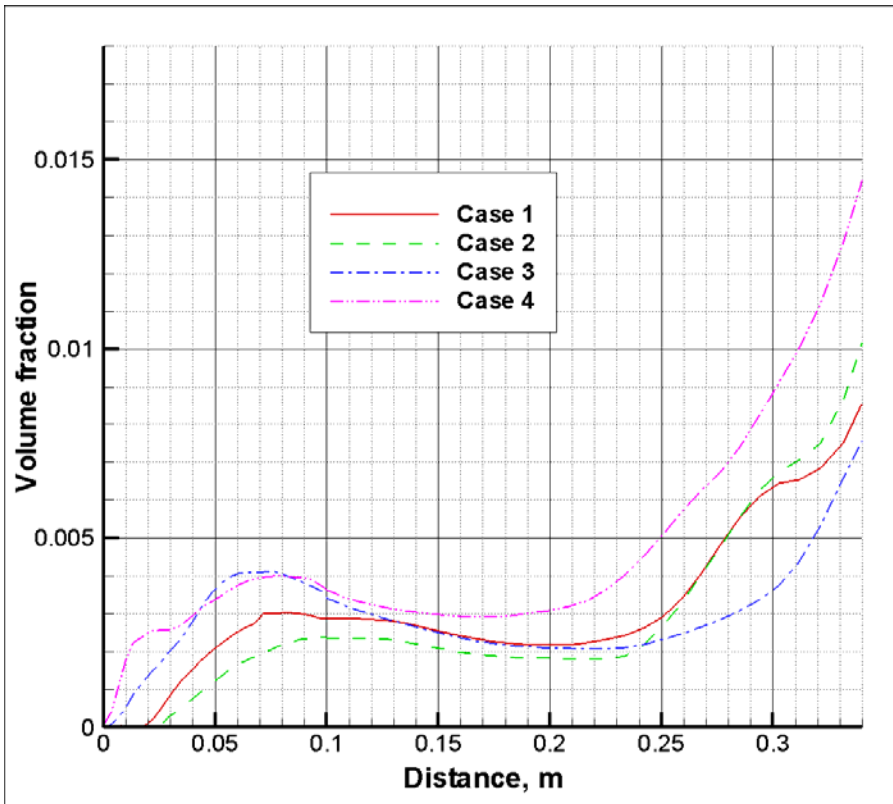


Figure 7-27. Particle volume fraction variations along the axis for Cases 1 – 4.

Previously, during the analysis of small scale jets, we concluded that the contraction of the jet that follows the release of the under-expanded jet is beneficial to attrition as it improves solid entrainment by creating radial flows directed towards the axis (see Section 7.1.4). However, that seems not to be the case for the large-scale jets studied in this section, as over-expanded nozzles (Cases 3 and 4) demonstrate poorer attrition performance than the perfectly expanded one (Case 2). To understand this seeming contradiction, we plot the variation of the particle volume fraction along the centreline for all cases (Figure 7-27). It is easy to see that the over-expanded cases have indeed a sharp increase in solid volume fraction immediately downstream of the nozzle orifice. However, this increase is relatively short-lived and ceases to be appreciable after about 10 cm downstream. This distance is rather minor compared to the overall length of the jet (see Figure 7-26). For small scale jets, however, that have much lower penetration distances (~ 25 cm), the high solid volume fraction region represents a substantial portion of the jet. It is important also to note that the solid entrainment depends not only on the volume fraction, but on the velocity as well, because it is generally a flow rate, i.e. volume fraction multiplied by velocity. Thus, while there are some advantages of using over-expanded nozzles, better overall performance is still obtained with the perfectly expanded nozzle.

7.2.4.2. Influence of nozzle expansion angle

In addition to the expansion angle of 7° , used in all of the cases previously investigated, we examine two other expansion angles – 2° and 20° for the perfectly expanded nozzle. The new nozzles have the same area ratio as the original one, but different expansion angles that result in a different nozzle length (l in Figure 7-14). All other process parameters are kept at the same values. Figure 7-28 reveals that the grinding efficiency decreases with the increase of the expansion angle. It is interesting that the variation is very close to linear. Evidently, such dependency occurs because of the increase in jet dispersion with the widening of the nozzle, which results in a larger portion of the total momentum being directed radially and already noted during the discussion of the under-expanded case, this radial momentum is not very useful in generating high impact inter-particle collisions. At the same time, the higher expansion angle results in the increase of solid entrainment into the jet (shown in the same figure) due to the total mass continuity. Even though there are more

particles available for attrition, it is still far from sufficient to reverse the trend of decreasing grinding efficiency. This conclusion is in agreement with a recent study by Cruz et al. (2010) who also studied various nozzle designs, albeit in small laboratory scale testing facilities. Therefore, it is beneficial to have as small an expansion angle as practical. Note, however, that a very small angle may result in a very long expansion section, so that the wall friction can reach appreciable values and increase inlet pressure requirements.

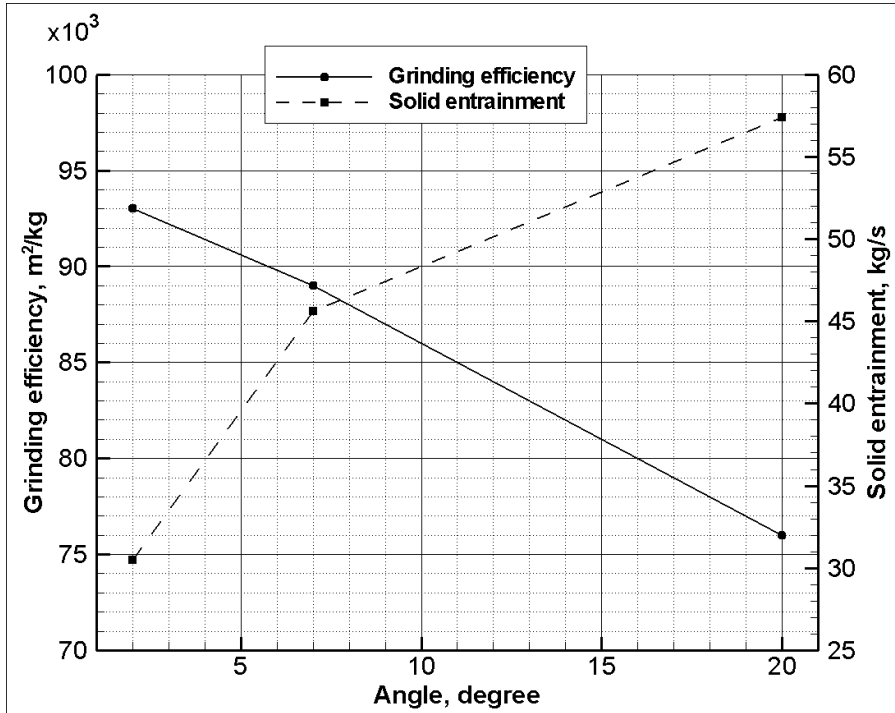


Figure 7-28. Grinding efficiency variation with nozzle expansion angle.

7.2.4.3. Influence of superficial gas velocity

Next, we investigate the influence of the superficial velocity. In addition to the original superficial velocity— 0.3048 m s^{-1} —we consider two others: one lower (0.2 m s^{-1}) and one higher (0.5 m s^{-1}). The simulations are conducted for the perfectly expanded nozzle geometry (Case 2). All other process parameters (except the velocity) are kept the same as in the original computations. The variation of the grinding efficiency with the superficial velocity is presented in Figure 7-29. The grinding efficiency increases modestly with the increase in velocity, as shown in the graph. Similar to the expansion angle variation, this dependency is also almost linear. This phenomenon is in qualitative agreement with observations of McMillan et al. (2008b) for sand attrition by an air jet in a small scale

fluidized bed. In addition, as also shown in Figure 7-29, solid entrainment decreases with higher superficial gas velocities. Higher superficial velocities produce lower average particle volume fractions in the bed that, in turn, results in the transfer of jet momentum to fewer particles; but these particles have a higher velocity and their collisions are more likely to result in breakage.

Variations of the superficial velocity can be linked to different zones of the industrial reactor: high velocities correspond to the central core area with lower particle concentrations, and low velocities correspond to the peripheral area with higher particle content (Song et al., 2004). Therefore, it seems more beneficial to inject steam closer to the central region to improve grinding efficiency. However, the gain from this improvement is only about 3% for a velocity increase from 0.2 m s^{-1} to 0.5 m s^{-1} .

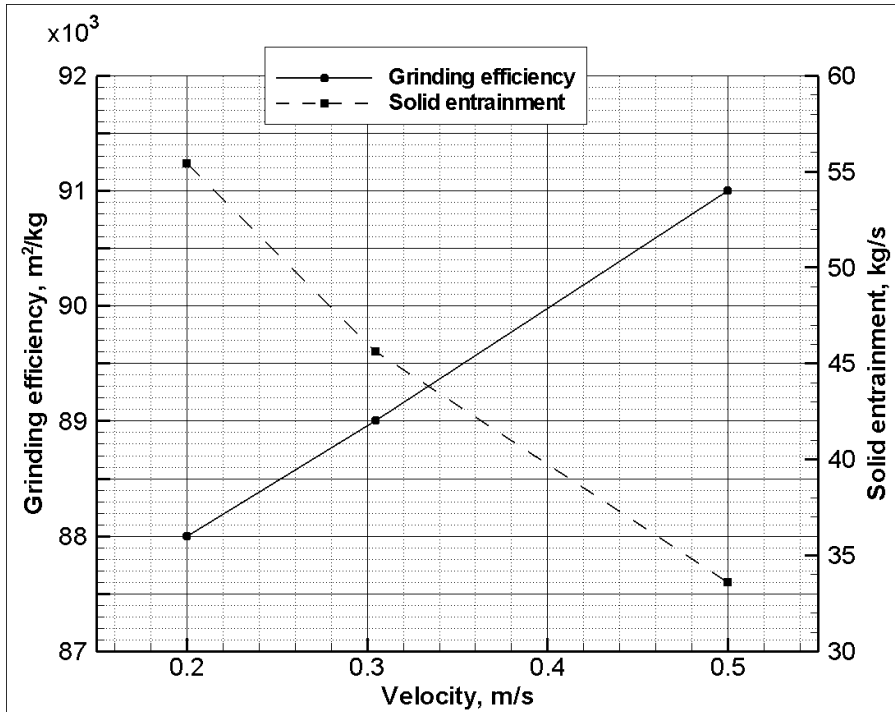


Figure 7-29. Grinding efficiency variation with superficial gas velocity.

7.3. Summary

The mathematical model for particle attrition developed in Section 2.2 is applied for two situations, first a small-scale fluidized bed, and second an industrial scale process. Based on the results provided by the model, it is possible to estimate the grinding efficiency, and

Chapter 7. Particle attrition

therefore evaluate the nozzle attrition performance and compare various configurations and flow rates. The model is applied to a large number of cases that have also been investigated experimentally. The comparison between the modelling predictions and experimental data demonstrates reasonably good agreement. Even though there are some apparent quantitative discrepancies, the modelling results reveal the correct trends in this very complex problem. For an industrial-sized nozzle, we analysed the influences of nozzle area ratio, nozzle expansion angle, and bed superficial velocity.

Chapter 8. CONCLUSIONS AND RECOMMENDATIONS

In this chapter major original research contributions are summarized together with practical conclusions from the conducted studies. In addition, possible directions for future research pertaining to the improvement of the current models and building up from the presented work are outlined.

8.1. Main contributions

The most important outcome of this research is the development of the mathematical models for

- Gas-assisted atomization including two-phase flow through a variable cross-section nozzle followed by spray dispersion and its interaction with a fluidized bed.
- Particle attrition by a supersonic gas jet.

These models advance the understanding of the physics and can be applied to optimization of industrial processes.

8.1.1. Jet-bed interactions

The jet-bed interaction model simulates the flow of the gas-liquid mixture through the convergent-divergent nozzle, gas assisted atomization of liquid, spray dispersion, droplet interactions with solid particles, and liquid spreading throughout the bed. The model does not require the knowledge of the issuing spray characteristics because the nozzle itself is incorporated into the model. The only required boundary conditions are the inlet flow rates of liquid and gas. Based on the Eulerian treatment for each phase, the model contains a large

Chapter 8. Conclusions and recommendations

number of sub-models to close the main flow equations. Variation of bubble and droplet sizes is represented by the particle number density approach that takes into account both break-up and coalescence. While many of the sub-models are taken from the published literature, some have been developed and implemented in the course of this work. These newly developed models are listed below.

- *Atomization model.* In Section 2.1.6, the atomization is proposed to be treated as a catastrophic phase inversion triggered by local values of the volume fraction. The intuitive considerations provide for a simple transfer of variables, including the particle diameter, through the phase inversion surface and, as a result, for smooth solutions without any internal jump conditions.
- *Multiphase wall functions.* An extension of wall functions, which are used to close the turbulence model at the near wall cells to multiphase flow, are developed in Section 2.1.12.1 and are used in a framework of the mixture turbulence model. They are applied at wall boundaries to liquid continuous flow with bubbles through the leading pipe and through the nozzle.
- *Moisture and heat transport by wet particle collisions.* A new relationship based on the granular kinetic theory is derived in Section 2.1.10 in order to determine the contribution to the diffusion coefficient due to the liquid redistribution between the particles during their collisions.
- *Heat conduction in a solid core of the particulate phase.* As described in Section 2.1.9, the assumption of an infinitely high heat conductivity of the solid particle, i.e. uniform temperature from centre to surface, would lead to erroneous results when large temperature gradients are present. Therefore, a special model was developed that accounts for finite conduction in a practical way which involves an algebraic correlation between the average and surface temperatures of the solid core.
- *Virtual mass coefficient correction.* In order to be applicable to liquid continuous flows with high gas volume fractions, the previously obtained

Chapter 8. Conclusions and recommendations

correlation for the virtual mass coefficient is augmented to limit the results within physically acceptable bounds.

The majority of the sub-models utilize adjustable coefficients in one form or another. We tried to use correlations with their published coefficients and preferred not to tune the model in order to preserve as much generality as possible. That sometimes entailed the extrapolation of the applicability range of some correlations. At the end, only two undetermined coefficients remained in the model.

The model overall performance is evaluated by comparison with four sets of experiments:

- Pressure measurements along the nozzle wall for air-water mixture.
- Liquid flow rate measurements at different axial distances in the radial direction of the water spray in the open air.
- Droplet diameter measurements at different axial distances in the radial direction of the spray in the open air.
- Cumulative liquid distribution in the air fluidized bed of coke particles with and without the draft tube for ethanol assisted by air.

The agreement between model predictions and experimental measurements is within reasonable limits. Most of the time the numerical results are within 20% of the experimental data. For a problem with extremely rich physics that cannot be simulated directly, this is the best that can be realistically achieved. It is important to underline that the qualitative behaviour of the system is always very well reproduced.

8.1.2. Particle attrition

The particle attrition model simulates particle breakage in a fluidized bed by a supersonic gas jet. The numerical model is formulated in a way that allows for a solution of a compressible flow (provided the Mach number is not very large) together with the fluidized bed hydrodynamics. This model also contains a number of sub-models. One of them is developed during the course of the research specifically for this problem.

- *Breakage frequency.* The relationship for breakage frequency that is used in the particle number density equation as a source term is derived based on the granular kinetic theory and collision mechanics.

This model involves a single empirical coefficient that depends on the particle's material properties. The value of this parameter is determined based on the published experimental results. The experiments are also used to evaluate overall attrition model performance. The following experimental set-up is simulated.

- Grinding efficiency measurement in a fluidized bed of silica sand particles for different inlet pressures and nozzle designs.

The comparison reveals a good agreement with most of the trends predicted correctly. However, similar to the jet-bed interaction model, exact agreement is not achieved, nor can it be expected.

8.2. Research findings

During multiple model applications to various conditions described in the research chapters of this work, a number of observations that are worthy of our attention are made.

8.2.1. Jet-bed interactions

The influence of the gravity force on the flow through the nozzle is evaluated. It is concluded that even though some top to bottom non-symmetry in the bubbles distribution in the flow occurs at the end of the entrance pipe, it almost completely disappears after passing through the nozzle. The pressure drop through the nozzle is not influenced by the gravity force. It is observed that the model is insensitive to the initial bubble diameter provided that the entrance pipe is of sufficient length. Modelling results provide the insight on the flow features inside the nozzle. It is also concluded that the virtual mass force plays an important role in the high speed dispersed bubble flow with a relatively high average bubble diameter. This role necessitates an implicit discretization of the virtual mass term; otherwise, the problem becomes numerically unstable.

The model application to sprays obtained by gas-assisted atomization through the investigated nozzle device, enables us to analyse the flow features and understand the reasons

Chapter 8. Conclusions and recommendations

for the developing droplet distribution pattern. The nozzle performance analysis conducted with the model reveals a number of important trends, some of which were also experimentally observed and, most importantly, provides improved understanding and explanation of these trends. An expected “tulip” shape of the plume appears in the numerical results. Moreover, they allow explaining the reason for such a shape – the entrainment of the surrounding gas. The appearance of the peripheral maxima of droplet mass flow rate after a certain distance downstream of the nozzle also has a similar physical nature, i.e. gas entrainment into the jet. It is interesting to note that this phenomenon had been discovered in modelling results before it was confirmed experimentally. It is found that the droplet diameter decreases from the axial area to the periphery of the jet because of the turbulence being dissipated in the core region. Along the axial direction, the diameter increases slowly with the distance from the nozzle, and the radial distribution becomes more uniform. Also, we found an additional area of the increased droplet diameter located near the periphery of the jet that starts to develop after about 0.4 m downstream from the nozzle orifice and increases gradually in size.

The influence of the addition of the conical spray modifiers to the standard TEB-type nozzle is investigated numerically for water spraying assisted by air. It is discovered that the spray modifiers act as spray limiters by reducing the spray’s natural expansion angle. Also, the droplets produced by the nozzle with an addition tend to be larger than the ones obtained with a stand alone nozzle. The largest droplets ($\sim 190 \mu\text{m}$) are generated by the smallest modifier angle considered – 10° . With the increase of the modifier angle, the spraying characteristics become closer to the ones of the stand alone nozzle. It can be concluded that the conical shape of the modifiers with a relatively small angle may be used when a higher jet penetration and a lower dispersion is desirable. The modifiers with the larger angles do not offer a substantial difference from the non-modified nozzle. Another important conclusion is that the dispersion of the jet is determined by the radial momentum provided to the liquid before and immediately after the phase inversion takes place. Thus, for improved dispersion, the place where the phase inversion occurs should not be restricted. An additional interesting observation is that the case with 80° expansion angle differs slightly from the others in terms of the jet expansion and droplet sizes due to the large turbulence generated in the air recirculation area confined within a modifier cone.

Chapter 8. Conclusions and recommendations

The investigation of the conical spray modifiers is continued with the study of steam assisted bitumen spraying into the fluidized bed of coke particles. While the attachments with smaller angles continue to act as spray limiters, the introduction of a fluidized bed brought out new phenomena connected with the stability of the issuing jet. We discovered that the attachment may stabilize or destabilize the interface between the jet and the bed, depending on the expansion angle. Generally, small angles have a stabilizing effect, while large ones – destabilising. It is interesting that the most unstable configuration involves the 40° attachment angle; in this case, boundary fluctuations start right inside the attachment because the solids are periodically drawn in and expelled. As a result of these fluctuations, the best liquid distribution is achieved for the 40° case, followed by cases with larger angles. The worst distribution is obtained for the 10° case, followed by the 20° case. The performance of a stand alone nozzle without attachments is somewhere inbetween.

The full model application to a 3D case provides a wealth of information relevant to jet-bed interactions. The modelling results reveal the details of the flow, such as field distribution of volume fractions, phase velocities, temperatures, turbulence and granular flow parameters, etc., that helps understand the jet-bed interaction phenomena. The analysis of two cases, with and without a draft tube, reveals that while the draft tube improves initial mixing and distribution of liquid inside the bed, further downstream from the nozzle this advantage disappears. In addition, a developed methodology allows the determination of the jet penetration length – an important parameter that characterizes a jet impact on the bed. The investigation of the influence of the superficial gas velocity shows that the increase of this parameter shortens the jet by enhancing solids mixing in the bed. At the same time, the area close to the nozzle exit is not affected by the superficial gas velocity. We quantify this dependency by plotting cumulative liquid distribution profiles for the cases with a different superficial velocity.

8.2.2. Particle attrition

The particle attrition model is applied to a number of cases that have also been investigated experimentally. Simulations demonstrate that an increased nozzle inlet pressure or a larger exit diameter for a forward step nozzle results in improved grinding efficiency. In addition, the convergent-divergent nozzle is more efficient in breaking the particles than the

nozzle that contains only the convergent section. It is also shown that the jet penetration length correlates with the grinding efficiency; that is, the larger penetration results in better efficiency.

The numerical analysis of several nozzle designs and operating conditions conducted with the mathematical model adapted for use in the industrial scale conditions reveals that the best grinding efficiency for the same flow rate and inlet pressure is obtained by the perfectly expanded nozzle as compared with the under- and over-expanded cases. Also, the increase in the nozzle expansion angle results in a decrease in grinding efficiency. Moreover, higher bed superficial velocities, which correspond to the lower particle average volume fractions in the central zone of the reactor, slightly improve the grinding efficiency. Therefore, it can be recommended for industrial attrition application in a reactor to use the perfectly expanded nozzle with the narrowest possible expansion angle and to position it close to the central core area of the reactor.

8.3. Future research directions

The presented work demonstrated a developed framework for numerical investigation of gas-assisted atomization and spray injections into the fluidized bed together with particle attrition by a supersonic gas jet and provided answers to some practical questions. However, it also uncovered many new questions, exposed problems that were not evident from the beginning, and branched into adjacent areas that may benefit from the presented methods or, alternatively, may provide some insights into the problems under consideration. Thus, it can be suggested, that this work has a potential to open up a large research program. Some possibilities of building on this study are outlined below.

8.3.1. Model application to cases of practical and/or research interest

One extension of the work is to continue model application to investigate various conditions of interest. These applications can be either for a full model or for certain parts of the model. This work would be a continuation of what we have started in Sections 6.2 and 7.2. The jet-bed interaction model can be employed to study various nozzle designs, injection arrangements, and gas and liquid flow rates. The influence of various material properties, such as density, viscosity, surface tension, thermal conductivity, heat capacity, and solid

particle diameter, together with process properties, such as pressure and temperature, can be examined. Similarly, the attrition model can be used to investigate the variety of nozzle designs and arrangements, attriting gas properties, and operating conditions.

The model can be used to investigate churn-turbulent flows with large gas volume fractions in pipes or other more complex geometries. Different designs of gas-assisted atomizers can potentially be analysed. While the model is not an ideal tool to investigate sprays — the Lagrangian approach is more suitable for this — there might be situations where its application is warranted. Spraying over the liquid surface can be an example of such situations. The catastrophic phase inversion concept may also be applied to other processes. For example, flushing of high pressure liquid through a relief valve may have a similar physics. A multitude of spray and gas injections into the fluidized bed can be amenable to the presented modelling approach. The model's ability to handle compressible flow extends its range of applicability to include high velocity jet injections.

8.3.2. Improvements of existing model

It has been stated several times that the model relies on a number of sub-models that are sometimes extrapolated outside their established range of applicability. The decision to extrapolate the sub-models was based on the unavailability of specific empirical data. Therefore, there is great value in conducting targeted experiments that aim at particular phenomena. Some of the most apparent choices are outlined below.

Gas-dispersed flow in variable cross-section pipes with high values of gas volume fraction can be studied with some imaging techniques to visualize phases and velocities distribution in order to obtain reliable interfacial drag and virtual mass correlations. Also, bubble behaviour in a highly turbulent flow can be analyzed in order to improve break-up and coalescence closures

The gas assisted atomization by a catastrophic phase inversion is another area that may benefit from a more in depth experimental study. The process of breaking liquid films between neighbouring bubbles during the transition from one continuous phase to another is not trivial and probably depends on other variables neglected in the current approach. This investigation has a potential to verify or improve assumptions involved in our modelling.

Chapter 8. Conclusions and recommendations

While droplet break-up and coalescence are fairly well studied for single droplets, the increase of droplet concentration may have an influence on the process other than a currently assumed proportionality of the collision frequency. Thus, a study of multiple droplets behaviour may be warranted.

Also, the turbulence theory in multiphase flows has not yet settled. Modern phase velocity measurement techniques may be able to detect instantaneous phase velocities at different types of the flow of interest, such as inside the pipe, through the nozzle, near atomization, and in the spray. These measurements can provide verification data for a turbulence response coefficient and, as a result, to the appropriateness of the chosen mixture turbulence model.

Modelling of droplet collisions with solid particles relied on some earlier empirical correlations to determine a fraction of liquid that sticks to the particle. Due to certain shortcomings discussed in Section 2.1.8, there is a need for a more focused and detailed study to develop a more physically based relationship that is appropriate for a targeted application.

The theoretically obtained relationship of the heat and moisture propagation in the fluidized bed due to inter-particle collisions needs to be verified experimentally. It can possibly be achieved by adding some liquid to the bed and monitoring moisture content at several locations.

The attrition model can benefit from a study aimed at collisional cracking of coke or other particles of interest. The influence of the particle diameter can be material dependent and thus, needs to be experimentally evaluated to confirm or modify model assumptions.

In addition, for some investigations there is a possibility of employing a numerical experiment, i.e. using direct numerical simulation, in order to gain insights into the flow behaviour and to help in development of macro-scale closures. While currently it may not be practical due to the high Reynolds numbers involved, in the future the necessary tools will become available.

8.3.3. Further development

There are two main ways of taking the model further. First, it can grow in complexity to become more accurate; and second, it can become applicable to more complex problems losing some features along the way.

The model can be improved by relaxing some of the assumptions. It is suggested that one of the first assumptions to reconsider is a monodispersed droplet/bubble size distribution and the corresponding particle number density equation. By substituting it with a full population balance approach that allows different sizes of particles to coexist locally, we may be able to account for variation of behaviour associated with large and small particles that quite possibly play a role in the process. Similarly, in the attrition model, the variety of sizes of bed particles resulting from the breakage can be better represented by applying a population balance method. Another possibility is to solve turbulence equations for each phase, instead of assuming proportionality between the fluctuating velocities. While these improvements should in theory improve model performance, the comparison with original results may show that the improvement is only marginal. However, the studies proposed above would still have an important role by gaining more confidence in a model because of its minor sensitivity to material assumptions.

Modelling of the granular flow inside the bed can be improved by accounting for a change of collision dynamics resulting from the liquid layer. Varying of the restitution coefficient with the liquid layer volume fraction is suggested. Another area of model development is connected to the phenomenon not addressed in the current study, namely particle agglomeration. At some point wet particles may stick together and form agglomerates. These agglomerates may grow in size attracting more particles, or may break up under the flow shear or multiple collisions. The importance of the agglomeration to the performance of the coking reaction is extremely high. Therefore, a systematic study can be of a great value. A population balance approach applied to the bed particles is suitable to study agglomeration; however, specific closures, or kernels, reflecting process physics need to be developed. Also, the agglomeration may be studied separately from the model by a more detailed Discrete Element Method (DEM) that allows for collisional mechanics to be directly

simulated. The application of this method can help in the closure development for a population balance approach.

The next avenue of potential research progress comes from our original goal of improving the fluid coking reactor. While a single nozzle study can and does provide a wealth of information to help guide the industry when there is a need to make design and operation choices, the large-scale questions related to the whole reactor or to interactions between multiple nozzles remain unanswered. It is proposed to develop a model that allows for multiple nozzles; such a model would in principle be applicable to an entire reactor. Evidently, numerical solution for each and every nozzle is computationally unaffordable. Therefore, based on the observations that the flow in the vicinity of the nozzle does not depend significantly on surrounding bed conditions, it is possible to replace the nozzles by either source terms or patched flow variables. The values for this substitution should come from a detailed model of a single nozzle. The final large scale model may include not only flow hydrodynamics, but also chemical reactions and the material properties variation associated with them. The described approach of dealing with multiscale problems is not dissimilar to what we have applied earlier (Pougatch et al., 2007; Stropky et al., 2007) during the study of the mechanical aerator placement in a large wastewater lagoon.

Finally, our current numerical tool — a structured multi-segment curvilinear code — developed in-house is in a need of further development. Its parallelization can dramatically decrease simulation time, making computations more practical. Also, the introduction of unstructured grids would make the model more easily adaptable to more complex geometries that would benefit many practical applications.

REFERENCES

- Adamson Jr, T.C., Nicholls, J.A., 1959. On the structure of jets from highly underexpanded nozzles into still air. *Journal of Aerospace Science* 26, 16-24.
- Akunov, V. I., 1966. Jet mills. *Glass and Ceramics* 23, 482-485.
- Aminu, M.O., Elliott, J.A.W., McCaffrey, W.C., Gray, M.R., 2004. Fluid properties at coking process conditions. *Industrial Engineering and Chemistry Research* 43, 2929-2935.
- Andrews, M.J., O'Rourke, P.J., 1996. The multiphase particle-in-cell (MP-PIC) method for dense particulate flows. *International Journal of Multiphase Flow* 22, 379-402.
- Ariyapadi, S., Berruti, F., Briens, C., McMillan, J., Zhou, D., 2004. Horizontal penetration of gas-liquid spray jets in gas-solid fluidized beds. *International Journal of Chemical Reactor Engineering* 2, A22.
- Ariyapadi, S., Berruti, F., Briens, C., Knapper, B., Skwarok, R., Chan, E., 2005. Stability of horizontal gas-liquid sprays in open-air and in a gas-solid fluidized bed. *Powder Technology* 155, 161-174.
- Ashgriz, N., Poo, J.Y., 1990. Coalescence and separation in binary collisions of liquid drops. *Journal of Fluid Mechanics*, 221, 183-204.
- Base, T., Chan, E., Kennett, R., Emberly, D., 1999. Nozzle for atomizing liquid in two phase flow. U.S. Patent 6003789.
- Batchelor, G.K., 1956. *The Theory of Homogeneous Turbulence*. Cambridge University Press.
- Bazyleva, A. B., Hasan, A., Fulem, M., Becerra, M., Shaw, J.M., 2010. Bitumen and heavy oil rheological properties: reconciliation with viscosity measurements. *Journal of Chemical Engineering Data* 55, 1389-1397.

References

- Becher, R.-D., Schlunder, E.-U., 1997. Fluidized bed granulation: gas flow, particle motion and moisture distribution. *Chemical Engineering and Processing* 36, 261-269.
- Beck, J.C., Watkins, A.P., 2003. Simulation of water and other non-fuel sprays using a new spray model. *Atomization and Sprays* 13, 1-26.
- Behzadi, A., Issa, R.I., Rusche, H., 2004. Modelling of dispersed bubble and droplet flow at high phase fractions. *Chemical Engineering Science* 59, 759-770.
- Benjelloun, F., Liegeois, R., Vanderschuren, J., 1995. Penetration length of horizontal gas jets into atmospheric fluidized beds. In *Fluidization VIII: Proceedings of the Eighth Engineering Foundation Conference on Fluidization*, Large, J-F., Laguerie, C., Eds., Engineering Foundation, N.Y.
- Bentham, A.C., Kwan, C.C., Boerefin, R., Ghadiri, M., 2004. Fluidized-bed jet milling of pharmaceutical powders. *Powder Technology* 141, 233-238.
- Benz, M., Herold, H., Ulfik, B., 1996. Performance of a fluidized bed jet mill as a function of operating parameters. *International Journal of Mineral Processing* 44-45, 507-519.
- Birkby, P., Page, G.J., 2001. Numerical predictions of turbulent underexpanded sonic jets using a pressure-based methodology. *Proceedings of the Institution of Mechanical Engineers, Part G: Journal of Aerospace Engineering* 215, 165-173.
- Bentham, A.C., Kwan, C.C., Boerefin, R., Ghadiri, M., 2004. Fluidized-bed jet milling of pharmaceutical powders. *Powder Technology* 141, 233-238.
- Berruti, F., Dawe, M., Briens, C., 2009. Study of gas-liquid jet boundaries in a gas-solid fluidized bed. *Powder Technology* 192, 250-259.
- Besnard, D.C., Harlow, F.H., 1988. Turbulence in multiphase flow. *International Journal of Multiphase Flow* 14, 679-699.
- Boisson, N., Malin, M.R., 1996. Numerical prediction of two-phase flow in bubble columns. *International Journal for Numerical Methods in Fluids* 23, 1289-1310.
- Brauer, H., 1992. Fluid flow around accelerated and decelerated particles. *Waerme- und Stoffuebertragung* 27, 93-101.

References

- Briens, C., Berruti, F., Felli, V., Chan, E., 2008. Solids entrainment into gas, liquid, and gas-liquid spray jets in fluidized beds. *Powder Technology* 184, 52-57.
- Briens, C., Dawe, M., Berruti, F., 2009. Effect of a draft tube on gas-liquid jet boundaries in a gas-solid fluidized bed. *Chemical Engineering and Processing: Process Intensification* 48, 871-877.
- Cengel, Y.A., Boles, M.A., 2006. *Thermodynamics: an engineering approach*, fifth edition, McGraw Hill Higher Education, New York, NY.
- Chapman, S., Cowling, T.G., 1970. *The mathematical theory of non-uniform gases*. Cambridge University Press, Cambridge.
- Chawla, J.M., 1985. Atomization of liquids employing the low sonic velocity in liquid/gas mixtures. ICLASS-85: 3rd International Conference of Liquid Atomization and Spray Systems, London, England, pp. LP/1A/5/1- LP/1A/5/7.
- Chen, P., Sanyal, J., Dudukovic, M.P., 2005. Numerical simulation of bubble columns flows: effect of different breakup and coalescence closures. *Chemical Engineering Science* 60, 1085-1101.
- Chesters, A.K., 1991. The modeling of coalescence processes in fluid-liquid dispersions. *Transactions of the Institution of Chemical Engineers* 69, 259-270.
- Cheung S.C.P., Yeoh, G.H., Tu, J.Y., 2007. On the modelling of population balance in isothermal vertical bubbly flows – average bubble number density approach. *Chemical Engineering and Processing* 46 (8), 742-756.
- Chisholm, D., 1968. Critical conditions during flow of two-phase mixtures through nozzles. *Thermodynamics and Fluid Mechanics Convention* 182 (Part 3H), 145-151.
- Cocco, R., Arrington, Y., Hays, R., Findlay, J., Karri, S.B.R., Knowlton, T.M., 2010. Jet cup attrition testing, *Powder Technology* 200, 224-233.
- Copan, J., Balachandar, R., Berruti, F., 2001. Droplet size-velocity characteristics of sprays generated by two-phase feed nozzles. *Chemical Engineering Communications* 184, 105-124.

References

- Cruz, N., Briens, C., Berruti, F., 2010. Supersonic attrition nozzles in gas-solid fluidized beds. *Chemical Engineering and Processing* 49, 225-234.
- Darabi, P., Pougatch, K., Salcudean, M., Grecov, D., 2009. A novel coalescence model for binary collision of identical wet particles. *Chemical Engineering Science* 64, 1868-1876.
- Das, A. K., De Wilde, J., Heynderickx, G. J., Marin, G. B., Vierendeels, J., Dick., E., 2004. CFD simulation of dilute phase gas-solid riser reactors: Part I – a new solution method and flow model validation. *Chemical Engineering Science* 59, 167-186.
- Deichsel, M., Winter, E.R.F., 1990. Adiabatic two-phase pipe flow of air-water mixtures under critical flow conditions. *International Journal of Multiphase Flow* 16, 391-406.
- Deux, E., Sommerfeld, M., 2006. Modelling of turbulent atomization combining a two-fluid and a structure function approach. *Atomization and Sprays* 16, 103-125.
- De Wilde, J., Heynderickx, G.J., Vierendeels, J., Dick, E., Marin, G.B., 2002. An extension of the preconditioned advection upstream splitting method for 3D two-phase flow calculations in circulating fluidized beds. *Computers and Chemical Engineering* 26, 1677-1702.
- Drew, D.A., Passman, S.L., 1999. *Theory of Multicomponent Fluids*. Springer-Verlag, New York.
- Dubrovskiy, V.V., Podvysotskiy, A.M., Shraiber, A.A., 1984. An experimental investigation of the dynamic interaction of droplets with solid particles. *Promyshlennaya Teplotekhnika* 6, 52-54.
- Dukowicz, J.K., 1980. A particle-fluid numerical model for liquid sprays. *Journal of Computational Physics* 35, 229-253.
- Eskin, D., Voropayev, S., Vasilkov, O., 1999. Simulation of jet milling. *Powder Technology* 105, 257-265.
- Gunn, D. J., 1978. Transfer of heat or mass to particles in fixed and fluidized beds. *International Journal of Heat and Mass Transfer* 21, 467-476.

References

- Ghadiri, M., Zhang, Z., 2002. Impact attrition of particulate solids. Part I: A theoretical model of chipping. *Chemical Engineering Science* 57, 3659-3669.
- Gidaspow, D., Bezburuah R., Ding, J., 1992. Hydrodynamics of circulating fluidized beds: kinetic theory approach, in *Fluidization VII. Proceedings of the 7th Engineering Foundation Conference on Fluidization*, May 3-8, Brisbane, Australia.
- Gidaspow, D., 1994. *Multiphase Flow and Fluidization: Continuum and Kinetic Theory Descriptions*. Academic Press, San Diego, CA, USA.
- Garnier, C., Lance, M., Marié, J.L., 2002. Measurement of local flow characteristics in buoyancy-driven bubbly flow at high void fraction. *Experimental Thermal and Fluid Science* 26, 811-855.
- Goldhirsch, I., 2008. Introduction to granular temperature. *Powder Technology* 182, 130-136.
- Goldschmidt, M.J.V., Beetstra, R., Kuipers, J.A.M., 2002. Hydrodynamic modelling of dense gas-fluidised beds: Comparison of the kinetic theory of granular flow with 3D hard-sphere discrete particle simulations. *Chemical Engineering Science* 57, 2059-2075.
- Gosman, A.D., Lekakou, C., Politis, S., Issa, R.I., Looney, M.K., 1992. Multidimensional modelling of turbulent two-phase flow in stirred vessels. *AIChE Journal* 38, 1946-1956.
- Gray, M.R., Le, T., McCaffrey, W.C., Berruti, F., Soundararajan, S., Chan, E., Huq, I., Thorne, C., 2001. Coupling of mass transfer and reaction in coking of thin films of an Athabasca vacuum residue. *Industrial and Engineering Chemistry Research* 40, 3317-3324.
- Gray, M.R., 2002. Fundamentals of bitumen coking processes analogous to granulation: a critical review. *Canadian Journal of Chemical Engineering* 80, 393-401.
- Han, T., Kalman, H., Levy, A., 2002. DEM simulation of particle comminution in jet milling. *Particulate Science and Technology* 20, 325-340.

References

- Heinrich, S., Morl, L., 1999. Fluidized bed spray granulation – a new model for the description of particle wetting and of temperature and concentration distribution. *Chemical engineering and Processing* 38, 635-663.
- Hench, J.E., Johnston, J.P., 1972. Two-dimensional diffuser performance with subsonic, two-phase, air-water flow. *Journal of Basic Engineering* 94, 105-121.
- Hibiki, T., Ishii, M., 1999. Interfacial area transport of air-water bubbly flow in vertical round tubes. *Proceedings of the 33rd National Heat Transfer Conference*, Albuquerque, New Mexico.
- Hinze, J.O., 1955. Fundamentals of the hydrodynamic mechanism of splitting in dispersion process. *AIChE Journal* 1, 289-295.
- House, P. K., Briens, C.L., Berruti, F., Chan, E., 2008. Effect of spray nozzle design on liquid-solid contact in fluidized beds. *Powder Technology* 186, 89-98.
- House, P.K., Saberian, M., Briens, C.L., Berruti, F., Chan, E., 2004. Injection of a Liquid Spray into a Fluidized Bed: Particle-Liquid Mixing and Impact on Fluid Coker Yields. *Industrial and Engineering Chemistry Research* 43, 5663-5669.
- Hsiau, S.S., Hunt, M.L., 1993. Kinetic theory analysis of flow-induced particle diffusion and thermal conduction in granular material flows. *Journal of Heat Transfer* 115, 541-548.
- Hunt, M.L., 1997. Discrete element simulations for granular material flows: effective thermal conductivity and self diffusivity. *International Journal of Heat and Mass Transfer* 40, 3059-3068.
- Issa, R.I., 1986. Solution of implicitly discretized fluid flow equations by operator-splitting. *Journal of Computational Physics* 62, 40-65.
- Iveson, M.S., Litster, J.D., Hapgood, K., Ennis, B.J., 2001. Nucleation, growth and breakage phenomena in agitated wet granulation processes: a review. *Powder Technology* 117, 3-39.
- Ishii, M. and Zuber, N., 1979. Relative motion and interfacial drag coefficient in dispersed two-phase flow of bubbles, drops and particles. *AIChE Journal*, 25, 843-855.

References

- Jenkins, J.T., Savage, S.B., 1983. A theory for the rapid flow of identical, smooth, nearly elastic, spherical particles. *Journal of Fluid Mechanics* 130, 187-202.
- Jiang, X., Zhou, L., Liu, L., Han, X., 2009. A model on attrition of quartzite particles as a bed material in fluidized beds. *Powder Technology* 195, 44-49.
- Jimenez, T., Turchiuli, C., Dumoulin, E., 2006. Particles agglomeration in a conical fluidized bed in relation with air temperature profiles. *Chemical Engineering Science* 61, 5954-5961.
- Johnson, D.L., Avidan, A.A., Schipper, P.H., Miller, R.B., 1994. New nozzle improves FCC feed atomization, unit yield patterns. *Oil and Gas Journal* 92, 80-86.
- Kapur, P.C., Pande, D., Fuerstenau, D.W., 1997. Analysis of single-particle breakage by impact grinding. *International Journal of Mineral Processing* 49, 223-236.
- Karki, K.C., Patankar, S.V., 1988. Calculation procedure for viscous incompressible flows in complex geometries. *Numerical Heat Transfer* 14, 295-307.
- Kataoka, I., Serizawa, A., 1989. Basic equations of turbulence in gas-liquid two-phase flow. *International Journal of Multiphase Flow* 15, 843-855.
- Kocamustafaogullari, G., Smits, S.R., Razi, J., 1994. Maximum and mean droplet sizes in annular two-phase flow. *International Journal of Heat and Mass Transfer* 37, 955-965.
- Kolev, N.I., 2002a. *Multiphase Flow Dynamics 1. Fundamentals*. Springer-Verlag, Berlin.
- Kolev, N.I., 2002b. *Multiphase Flow Dynamics 2. Thermal and Mechanical Interactions*. Springer-Verlag, Berlin.
- Kolmogorov, A.N., 1949. On the disintegration of drops in a turbulent flow. *Doklady Akademii Nauk SSSR* 66, 825-828.
- Krishna, R., Urseanu, M.I., van Baten, J.M., Ellenberger, J., 1999. Influence of scale on the hydrodynamics of bubble columns operating in the churn-turbulent regime: experiments vs. Eulerian simulations. *Chemical Engineering Science* 54, 4903-4911.
- Kuipers, J.A.M., Prins, W., van Swaaij, W.P.M., 1992. Numerical calculation of wall-to-bed heat transfer coefficients in gas-fluidized beds, *AIChE Journal* 38, 1079-1091.

References

- Lahey, R.T., Jr, Cheng, L.Y., Drew, D.A., Flaherty, J.E., 1980. The effect of virtual mass on the numerical stability of accelerating two-phase flows. *International Journal of Multiphase Flow* 6, 281-294.
- Lamb, H., 1932. *Hydrodynamics*. Cambridge University Press, Cambridge, UK.
- Lasheras, J.C., Villermaux, E., Hopfinger, E.J., 1998. Break-up and atomization of a round water jet by a high speed annual air jet. *Journal of Fluid Mechanics* 357, 351-379.
- Laurien, E., Niemann, J., 2004. Determination of the virtual mass coefficient for dense bubbly flows by direct numerical simulation. In: 5th International Conference on Multiphase Flow, Yokohama, Japan, paper No. 388.
- Lee, C.S. and Reitz, R.D., 2001. Effect of liquid properties on the breakup mechanism of high speed liquid drops. *Atomization and Sprays* 11, 1-19.
- Legendre, D., Magnaudet, J., 1998. The lift force on a spherical bubble in a viscous linear shear flow. *Journal of Fluid Mechanics* 368, 81-126.
- Li, T., 2009. Numerical investigation of the gas/spray jet interaction with fluidized beds. Ph.D. thesis. University of British Columbia, Vancouver, Canada.
- Li, T., Pougatch, K., Salcudean, M., Grecov, D., 2008. Numerical simulation of horizontal jet penetration in a three-dimensional fluidized bed. *Powder Technology* 184, 89-99.
- Li, T., Pougatch, K., Salcudean, M., Grecov, D., 2009. Numerical simulation of a spouted bed with a draft tube with and without liquid spray. *Canadian Journal of Chemical Engineering* 87, 237-251.
- Li, T., Pougatch, K., Salcudean, M., Grecov, D., 2010. Numerical simulation of an evaporative spray in a gas-solid crossflow. *International Journal of Chemical Reactor Engineering* 8, A43.
- Lun, C.K.K., Savage, S.B., Jeffrey, D.J., Chepurnyi, N., 1984. Kinetic theories for granular flow: Inelastic particles in Couette flow and slightly inelastic particles in a general flowfield. *Journal of Fluid Mechanics* 140, 223-256.
- Ma, D., Ahmadi, G., 1986. An equation of state for dense rigid sphere gases. *The Journal of Chemical Physics* 84, 3449-3450.

References

- Martinez-Bazan, C., Montanes, J.L., Lasheras, J.C., 1999. On the breakup of an air bubble injected into a fully developed turbulent flow. Part 1. Breakup frequency. *Journal of Fluid Mechanics* 401, 157-182.
- Maxwell, T.T., Maples, G., Dyer, D.F., 1975. Thrust of and air-augmented waterjet with a converging-diverging nozzle. *Journal of Hydronautics* 9, 154-159.
- McMillan, J., Briens, C., Berruti, F., Chan, E., 2007a. High velocity attrition nozzles in fluidized beds. *Powder Technology* 175, 133-141.
- McMillan, J., Briens, C., Berruti, F., Chan, E., 2007b. Particle attrition mechanism with a sonic gas jet injected into a fluidized bed. *Chemical Engineering Science* 62, 3809-3820.
- McMillan, J., Zhou, D., Ariyapadi, S., Briens, C., Berruti, F., 2005. Characterization of the contact between liquid spray droplets and particles in a fluidized bed. *Industrial and Engineering Chemistry Research* 44, 4931-4939.
- McMillan, J., Zhou, D., Saberian, M., Briens, C., Berruti, F., 2006. Measurement techniques to characterize the contact between injected liquid and circulating solids in a downer mixing chamber. *Powder Technology* 161, 175-184.
- Meier, M., John, E., Wieckhusen, D., Wirth, W., Peukert, W., 2009. Generally applicable breakage functions derived from single particle comminution data. *Powder Technology* 194, 33-41.
- Monahan, S.M., Vitankar, V.S., Fox, R.O., 2005. CFD predictions for flow-regime transitions in bubble columns. *AIChE Journal* 51, 1897-1923.
- Nasr, G.G., Yule, A.J., Bendig, L., 2002. *Industrial Sprays and Atomization*. Springer-Verlag, London.
- Nayak, S.V., Joshi, S.L., Ranade, V.V., 2005. Modeling of vaporization and cracking of liquid oil injected in a gas-solid riser. *Chemical Engineering Science* 60, 6049-6066.
- Nijdam, J.J., Guo, B., Fletcher, D.F., Langrish, T.A.G., 2006. Lagrangian and Eulerian models for simulating turbulent dispersion and coalescence of droplets within a spray. *Applied Mathematical Modelling* 30, 1196-1211.

References

- Nowak, Z.P., Salcudean, M., 1996. Turbulent flow calculations by the nonlinear multi-grid method. *ZAMM – Journal of Applied Mathematics and Mechanics* 76, 463-469.
- Nowak, P., Pougatch, K., Salcudean, M., 2010. Simulation of the steam-bitumen jet in the fluidized bed of coke particles using the Eulerian-Lagrangian splitting method. *The Journal of Computational Multiphase Flows* 2, 59-72.
- Okasha, F., Miccio, M., 2006. Modelling of wet jet in fluidized bed. *Chemical Engineering Science* 61, 3079-3090.
- Palaniandy, S., Azizli, K.A.M., Hussin, H., Hashim, S.F.S., 2008. Effect of operational parameters on the breakage mechanism of silica in a jet mill. *Minerals Engineering* 21, 380-388.
- Pan, Y., Dudukovic, M.P., Chang, M., 1999. Dynamic simulation of bubbly flow in bubble columns. *Chemical Engineering Science* 54, 2481-2489.
- Pan, Y., Suga, K., 2005. Numerical simulation of binary liquid droplet collision. *Physics of Fluids* 17, 082105.
- Papadopoulos, D.G., Teo, C.S., Ghadiri, M., Bell, T.A., 1998. Impact attrition of common table salt. *World congress on Particle Technology* 3, paper 156, Brighton, UK, July 7-9.
- Pilch, M., Erdman, C.A., Reynolds, A.B., 1981. Acceleration induced fragmentation of liquid drops, harlottesville, VA: Department of Nuclear Engineering, University of Virginia, NUREG/CR-2247.
- Podvysotskiy, A.M., Dubrovskiy, V.V., 1986. Mass transfer of collision of droplets with a solid spherical particle. *Heat Transfer – Soviet Research* 18, 136-140.
- Politano, M.S., Carrica, P.M., Converti, J., 2003. A model for turbulent polydisperse two-phase flow in vertical channels. *International Journal of Multiphase Flow* 29, 1153-1182.
- Portoghese, F., Ferrante, L., Berruti, F., Briens, C., Chan, E., 2008. Effect of injection-nozzle operating parameters on the interaction between a gas-liquid jet and a gas-solid fluidized bed. *Powder Technology* 184, 1-10.

References

- Pougatch, K., Salcudean, M., Gartshore, I., Pagoria, P, 2007. Computational modelling of large aerated lagoon hydraulics. *Water Research* 41, 2109-2116.
- Rajniak, P., Dhanesekharan, K., Sinka, C., MacPhail, N., Chern, R., 2008. Modeling and measurement of granule attrition during pneumatic conveying in a laboratory scale system. *Powder Technology* 185, 202-210.
- Ranz, W.E., Marshall, W.R., Evaporation from drops, Part I. *Chemical Engineering Progress* 48, 141-146.
- Richardson, L.F., Gaunt, J.A., 1927. The deferred approach to the limit. Part I. Single lattice. Part II. Interpenetrating lattices. *Proceedings of Royal Society London, Ser. A* 226, 299-361.
- Romstedt, P., Werner, W., 1986. Numerical analysis of critical two-phase flow in a convergent-divergent nozzle. *Nuclear Science and Engineering* 92, 71-83.
- Saad, Y., 1996. *Iterative Method for Sparse Linear Systems*. PWS publishing, New York.
- Sanders, W.C., Winkel, E.S., Dowling, D.R., Perlin, M., Ceccio, S.L., 2006. Bubble friction drag reduction in a high-Reynolds-number flat-plate boundary layer. *Journal of Fluid Mechanics* 552, 353-380.
- Santiso, E., Muller, E.A., 2002. Dense packing of binary and polydisperse hard spheres. *Molecular Physics* 100, 2461-2469.
- Sarkar, S., Erlebacher, G., Hussaini, M.Y., 1991. The analysis and modelling of dilatational terms in compressible turbulence. *Journal of Fluid Mechanics* 227, 473-493.
- Sato, Y., Sekoguchi, K., 1975. Liquid velocity distribution in two-phase bubble flow. *International Journal of Multiphase Flow* 2, 79-95.
- Savage, S.B., Jeffrey, D.J., 1981. The stress tensor in a granular flow at high shear rates. *Journal of Fluid Mechanics* 110, 255-272.
- Schiller, L. Naumann, A.Z., 1935. *Zeitschrift des Vereiner der Deutschen Ingenieur* 77, 318-320.
- Schaeffer, D.G., 1987. Instability in the evolution equations describing incompressible antigranulocytes flow. *Journal of Differential Equations* 66, 19-50.

References

- Seeton, C.J., 2006. Viscosity-temperature correlation for liquids. *Tribology Letters* 22, 67-78.
- Sha, Z., Laari, A., Turunen, I., 2006. Multi-phase-multi-size-group model for the inclusion of population balances into the CFD simulation of gas-liquid bubbly flows. *Chemical Engineering and Technology* 29, 550-558.
- Shamlou, P.A., Liu, Z., Yates, J.G., 1990. Hydrodynamic influences on particle breakage in fluidized beds. *Chemical Engineering Science* 45, 809-817.
- Shi, H., Kleinstreuer, C., 2007. Simulation and analysis of high-speed droplet spray dynamics. *Journal of Fluid Engineering* 129, 621-633.
- Schmidt, A., Renz, U, 1999. Eulerian computation of heat transfer in fluidized beds, *Chemical Engineering Science* 54, 5515-5522.
- Simonin, O., He, J., 1992. Eulerian prediction of the particle behaviour in a turbulent boundary layer. EDF – Electricite de France, Clamart, France.
- Sinclair, J.L., Jackson, R., 1989. Gas-particle flow in a vertical pipe with particle-particle interactions. *AIChE Journal* 35, 1473-1486.
- SLATEC Common Mathematical Library, 1993. <http://www.netlib.org/slatec>
- Song, X., Bi, H., Lim, C. J., Grace, J., Chan, E., Knapper, B., McKnight, C., 2004. Hydrodynamics of the reactor section in fluid cokers. *Powder Technology* 147, 126-136.
- Spalding, D.B. (1980) Numerical computation of multiphase flow and heat transfer, in: Taylor, C., Morgan, K. (Eds.), *Recent Advances in Numerical Methods in Fluids*, vol 1. Pineridge Press, Swansea, pp.139-168.
- Stropky D., Pougatch K., Novak, P., Salcudean, M., Pagoria, P., Gartshore, I., Yuan, J., 2007. RTD (Residence Time Distribution) predictions in large mechanically aerated lagoons. *Water Science and Technology* 55, 29-36.
- Taitel, Y., Dukler, A.E., 1976. A model for predicting flow regime transitions in horizontal and near horizontal gas-liquid flow. *AIChE Journal* 22, 47-55.
- Thornton, C., Ning, Z., 1998. A theoretical model for the stick/bounce behaviour of adhesive, elastic-plastic spheres. *Powder Technology* 99, 154-162.

References

- Troshko, A.A., Hassan, Y.A., 2001a. Law of the wall for two-phase turbulent boundary layers. *International Journal of Heat and Mass Transfer* 44, 871-875.
- Troshko, A.A., Hassan, Y.A., 2001b. A two-equation turbulence model of turbulent bubbly flows. *International Journal of Multiphase Flow* 27, 1965-2000.
- Vaessen, G.E.J., Visschers, M., Stein, H.N., 1996. Predicting catastrophic phase inversion on the basis of droplet coalescence kinetics. *Langmuir* 12, 875-882.
- Vallet, A., Burluka, A.A., Borghi, R., 2001. Development of a Eulerian model for the “atomization” of a liquid jet. *Atomization and Sprays* 11, 619-642.
- Vinokur, M., 1974. Conservative equations of gas dynamics in curvilinear coordinate system. *Journal of Computational Physics* 14, 105-125.
- Viollet, P.L., Simonin, O., 1994. Modelling dispersed two-phase flows: closure validation and software development. *Applied Mechanics Reviews* 47 (6, part 2), S80-S84.
- Von Berg, E., Edelbauer, W., Alajbegovic, A., Tatschl, R., Volmajer, M., Kegl, B., Ganippa, L.C. 2005. Coupled simulations of nozzle flow, primary fuel jet breakup, and spray formation. *Journal of Engineering for Gas Turbines and Power* 127, 897-908.
- Wang, T., Wang, J., Jin, Y., 2005. Theoretical prediction of flow regime transition in bubble columns by the population balance model. *Chemical Engineering Science* 60, 6199-6209.
- Weibull, W., 1939. A statistical theory of the strength of materials. *Ingeniors Vetenskaps Akademien – Handlingar* 151.
- Wells, M.R., Stock, D.E., 1983. The effects of crossing trajectories on the dispersion of particles in a turbulent flow. *Journal of Fluid Mechanics* 136, 31-62.
- Werther, J., Xi, W., 1993. Jet attrition of catalyst particles in gas fluidized beds. *Powder Technology* 76, 39-46.
- Wilcox, D.C., 1998. *Turbulence Modelling for CFD*. DCW Industries, La Canada, California.

References

- Yashima, S., Kanda, Y., Sano, S., 1987. Relationships between particle size and fracture energy or impact velocity required to fracture as estimated from single particle crushing. *Powder Technology* 51, 277-282.
- Zhang, D.Z., Prosperetti, A., 1994. Ensemble phase-averaged equations for bubbly flows. *Physics of Fluids* 6, 2956-2970.
- Zhu, C., Wang, X., Liu, G., 2002. Numerical Simulation of Coaxial Evaporating Spray in Nozzle Region of Circulating Fluidized Reactor. *Proceedings of the ASME Joint US-European Fluids Engineering Conference*, Montreal, Quebec, Canada, July 14-18.